UC Santa Cruz

UC Santa Cruz Electronic Theses and Dissertations

Title

The Quest for Active Galactic Nuclei Feedback in Local and Distant Galaxies

Permalink

https://escholarship.org/uc/item/6qw3s9kx

Author

Yesuf, Hassen Mohammed

Publication Date

2016

Copyright Information

This work is made available under the terms of a Creative Commons Attribution License, availalbe at https://creativecommons.org/licenses/by/4.0/

Peer reviewed|Thesis/dissertation

eScholarship.org Powered by the California Digital Library
University of California

UNIVERSITY OF CALIFORNIA
SANTA CRUZ

THE QUEST FOR ACTIVE GALACTIC NUCLEI FEEDBACK IN LOCAL AND DISTANT GALAXIES

A dissertation submitted in partial satisfaction of the
requirements for the degree of

DOCTOR OF PHILOSOPHY

in

ASTRONOMY AND ASTROPHYSICS
with an emphasis in STATISTICS

by

Hassen Mohammed Yesuf

September 2016

The Dissertation of Hassen Mohammed Yesuf
is approved:

Professor Sandra M. Faber, Chair

Professor David C. Koo

Professor J. Xavier Prochaska

Dean Tyrus Miller
Vice Provost and Dean of Graduate Studies

Copyright © by

Hassen Mohammed Yesuf

2016

Table of Contents

List of Figures

List of Tables

Abstract

The Quest for Active Galactic Nuclei Feedback in Local and Distant Galaxies

by

Hassen Mohammed Yesuf

The mechanisms for quenching star formation in galaxies are not yet well understood. Identifying these mechanisms is one of the paramount endeavors in the current state of Astrophysics. The fundamental requirement for quenching is that the cold gas that fuels star formation must be depleted or removed, or heated. AGN feedback is one of the hypothesized quenching agents. In this dissertation, we present our observational studies on AGN feedback.

In chapter 2, we will identify very rare galaxy candidates going through a rapid merger evolutionary sequence from disturbed starbursts, followed by fading and relaxed AGN, and to eventually young and quiescent post-starburst galaxies. Most nearby galaxies today are evolving slowly. The era of major galaxy mergers and rapid black hole growth is almost over. However, post-starbursts (PSBs) are rapidly evolving from the blue cloud to the red sequence today. Although they are rare today, integrated over time they may be an important pathway to the red sequence. The transition PSBs have stellar properties that are predicted for fast-quenching starbursts and morphological characteristics that are already typical of early-type galaxies. The active galactic nucleus (AGN) fraction, as estimated from optical line ratios, of these post-starbursts is about three times higher ($\gtrsim 36\% \pm 8\%$) than that of normal star forming galaxies of the same mass, but there is a significant delay between the starburst phase and the peak of nuclear

optical AGN activity (median age difference of 200 ± 100 Myr). We also find that starbursts and post-starbursts are significantly more dust obscured than normal star forming galaxies in the same mass range. The time delay between the starburst phase and AGN activity suggests that AGNs do not play a primary role in the original quenching of starbursts but may be responsible for quenching later low-level star formation by removing gas and dust during the post-starburst phase.

In chapter 3, we study the cold gas contents of PSBs. We undertook new CO (2–1) observations of 24 Seyfert post-starburst galaxies and together with our data analyzed about 100 previously studied PSBs. When combined with the other samples, our sample is indispensable in sampling the entire starburst-AGN-quenched post-starburst evolutionary sequence. Unlike the previous studies, we find that both star-formation and molecular gas evolutions in PSBs are rapid. These galaxies do not need to linger in the green valley for a longer period of time as previous studies suggested. We find a significantly lower molecular gas detection rate (25%) in our sample than do previous PSBs studies (50-90%). The distribution of gas fraction in Seyfert PSBs is significantly different from young star-forming galaxies. We observe a rapid decline in gas fraction around 0.7 Gyr after the starburst. We interpret this far removed event from the peak of the starburst as evidence for a delayed AGN feedback.

A key physical manifestation of active galactic nuclei (AGN) feedback is predicted to be powerful galactic winds. However, the relative roles between AGN activity and star formation in driving such winds remain largely unexplored at redshifts $z \sim 1$, near the peak of cosmic activity for both. In chapter 4, we study

winds in 12 X-ray AGN host galaxies at $z \sim 1$ in the CANDELS fields using deep Keck rest-frame UV spectroscopy. We use the low-ionization Fe II λ2586 absorption profile in their stacked spectrum to trace the cool gas kinematics. Our wind model accounts for both the galactic self-absorption and wind absorption imprinted on the absorption profile. We find that the AGN show a median centroid velocity shift of -124 $\mathrm{km\,s^{-1}}$ and a median velocity dispersion of 106 $\mathrm{km\,s^{-1}}$. For comparison, a star-forming, non-AGN sample at a similar redshift, matched roughly in stellar mass and galaxy inclination, show the outflows to have a median centroid velocity of -148 $\mathrm{km\,s^{-1}}$ and a median velocity dispersion of 168 $\mathrm{km\,s^{-1}}$. Thus, winds in the AGN are similar in velocities to those found in star-formation-driven winds, and are too weak to escape and expel substantial cool gas from galaxies. Thus, we do not find evidence to support bulk velocities having greater than 500 $\mathrm{km\,s^{-1}}$ predicted by some AGN feedback models. Future studies of winds in older and less star-forming AGN than the current sample will be useful to discriminate between delayed AGN wind gas removal or gas heating by AGN and will tell us how the AGN feedback operates.

To my family and friends,

for their love and support.

Acknowledgments

I am profusely thankful to my advisors Prof. Sandra M. Faber and Prof. David C. Koo. I would not have completed this work without their unwavering support, unstinted guidance, wise advice, creative minds, and contagious passion for science. I am very grateful for the opportunity and the privilege of working with them. They gave me utmost independence, showed me unbelievable kindness and care, and made a better person and scientist. I am also very grateful to my committee member Prof. J. Xavier. Prochaska for his continued support and inputs to my scholarly growth.

I thank all graduate students and post-doctoral researchers, faculty and staff members that I have had the pleasure to meet and work with during my time in Santa Cruz. I am particularly grateful for Tuguldur Sukhbold, John Forbes, Morgan MacLeod, Anna Rosen, Srikar Srinath, Jerome Fang, Edmond Cheung, Eric Lopez, Emily Cunningham, Jonathan Trump, Yicheng Guo, Guillermo Barro, Dale Kocevski, and Maria Sliwinski for their help, advice and encouragement.

I am very indebted to all my friends outside Santa Cruz. Without their support and friendship, I would not have made it this far. For a practical purpose, I will acknowledge the few friends that came to mind as I am rushing to finish this dissertation. I thank Eyob Demeke, Aswab Ali, Kalid Amiru, Ali Sheikh, Nasir Ahmed, Nebiyu Demissie and his brothers, Hagos Salih, Sedik Awelu, Edris Degu and Yuchen Zhang for their wonderful friendship and for their encouragements to keep going.

I thank my parents and five siblings for their love, patience, and for supporting me to pursue my passion and dream very far away from home. I know they

probably do not fully understand the work I did and why I did spend more than ten years away from home. But I hope they know that I am really happy with how I spent my time away from home, and with what I have learned thereby the way I see the world. This is a wonderful and worthy experience. I hope millions of young students from the developing world, where I came from, get the opportunity to see the beautiful world through the cosmic perspective, free from the shackles of the mundane search and struggle for food and shelter.

I am very grateful for my inspiring teachers I had in high school and college (Princeton University). Without them, I would not have dreamt of exploring the Universe and know how beautiful it is. I thank Michael Strauss, Richard Gott, Neta Bahcall, Daniel Kwapong, Chris Hamper, Brian Kern, Malkamu Gebeyehu, Girma Ali, Kebedachew Zegeye, and Belay Ayfokru for making me a better student, developing my curious mind, and for just making learning fun and enjoyable. I also thank all those who supported my education from high school to graduate school. Special thanks to Shelby Davis and his family for their incredible philanthropy and support for international education. The journey that has culminated in this dissertation would not have been possible without the dedicated work of the Ethiopian UWC National Committee. I thank Rita Pankhurst, Gary Campbell and other committee members for believing in me and sending me to UWC in Norway representing Ethiopia for the last two years of high school education.

I thank all my research collaborators including Fengshan Lui, Vivian Wild, Christopher Hayward, Raja Guhathakurta, Alison Coil, Decker French, Ann Zabludoff for their contributions, comments and suggestions. The quality of my work would not have reached the current level if it were not for their inputs. I hope we

keep working together in the future.

The text of this dissertation includes reprints of the following previously published material: Yesuf, H. M., Faber, S. M., Trump J. R., Koo, D. C., Fang, J. J., Liu, F. S., Wild, V., & Hayward, C. C. 2014, ApJ, 792, 84. One of the co-authors listed in these publications (S. M. Faber) directed and supervised the research which forms the basis for this dissertation. I am the first author on the paper. The content of this publications makes up chapters 2 of this dissertation. The content of chapter 3 or chapters 4 either has just been submitted or will be submitted for a publication in the near future. I will be the first author in these two papers. Almost all of the analyses presented in this dissertation are my own work, including the text, figures, and tables (except for the introductory figures in Chapter 1). I also played a major role in putting together existing data, or collecting and reducing new data, that are used throughout the dissertation.

Chapter 1

Introduction:

"We shall not cease from exploration, and the end of all our exploring will be to arrive where we started and know the place for the first time."

— T. S. Eliot

"It is hard to think of practical applications of the black hole. Because practical applications are so remote, many people assume we should not be interested. But this quest to understand the world is what defines us as human beings."

— Yuri Milner

One hundred years ago, our understanding of the cosmos was very limited. We did not even know for sure that the Universe extended beyond the bounds of our own Milky Way galaxy. In 1920, there was a great debate between two astronomers, Heber Curtis and Harlow Shapley, about the nature of "spiral nebulae", which we now know are external galaxies. Curtis was a researcher at our own UCO Lick Observatory while Shapley was at the Mount Wilson Observatory at the time, and later became the director of the Harvard College Observatory.

Shapley argued that "spiral nebulae" were simply part of the Milky Way while Curtis thought that the Andromeda and other such nebulae were external galaxies. The debate was soon resolved by observations of Edwin Hubble who conclusively showed that these spiral nebulae were actually faraway galaxies beyond the bounds of the Milky Way. Hubble used pulsating stars called Cepheid variables, which have well-defined periods and brightnesses, as benchmarks for distances to these external galaxies.

I think the ultimate reason that we are interested in studying external galaxies is to gain a cosmic perspective and understand humanity's place in the Universe: who we are, where we come from, and where are we going. Because light travels at finite speed, $3 \times 10^5\,\mathrm{km\,s^{-1}}$, it takes a long time for the light to traverse the large distances between the external galaxies and the Earth. The light that reaches us today was actually emitted long time ago. In this dissertation, we will look back in time to study external galaxies about one billion years ago in chapter 2 & 3, and then venture even farther in chapter 4 to study distant galaxies as they were 8 billion years ago.

Today, unlike hundred years ago, we have the privilege of exploring the vast expanse of the Universe to the first moment of creation, the big bang, and to the moment the first stars and galaxies were born. The all-sky surveys such as the Sloan digital Sky Survey (SDSS) have provided us with a wealth of information on millions of galaxies in the nearby Universe while the small-area but very deep surveys such as the Cosmic Assembly Near-infrared Deep Extragalactic Legacy Survey (CANDELS), using the Hubble Space Telescope, have endowed us with the chronicles of tens of thousands galaxies from the distant Universe. As a result, our

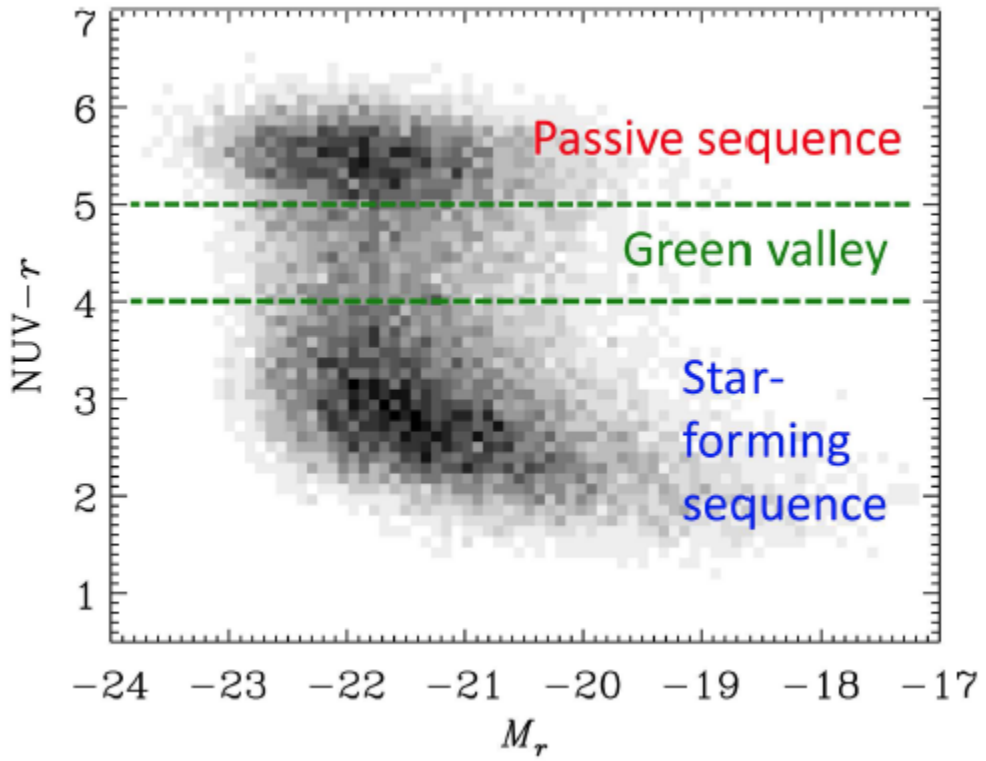

Figure 1.1:. Ultraviolet-optical color magnitude diagram showing a bimodal distribution of galaxies corresponding to active star-forming galaxies and passive galaxies (Salim et al., 2007; Salim, 2014). The figure is based on the sample of galaxies at redshift $z < 0.22$ (a look back time of 2.7 billion years). The horizontal axis shows the absolute brightnesses (proxies for masses) of galaxies increasing from the right to the left while the vertical axis shows the colors (proxies for ages) of galaxies getting redder from the bottom to the top.

understanding of how galaxies form and evolve has begun to matured significantly. Thanks to these dedicated surveys, we now have the general outline, if not close to the whole picture, of how galaxies form and evolve.

When galaxies are sorted by their absolute brightnesses (or masses) and colors, they exhibit a remarkable two-peaked distribution shown in Figure 1.1 (e.g., Strateva et al., 2001; Baldry et al., 2004; Bell et al., 2004; Faber et al., 2007; Salim, 2014). Galaxies in the "blue cloud" are young and actively forming stars, while galaxies located in the "red sequence" have stopped forming stars. The

"green valley" is inhabited by a transiting population between the blue and red galaxies. The transition time of these galaxies must be a fairly rapid in order to produce the dearth of objects in the green valley (Faber et al., 2007; Martin et al., 2007). Galaxy number counts going back in time have shown that the number of red galaxies around $L_\star$ luminosity has at least doubled since 8 billion years ago while the number of blue galaxies has remained substantially constant (Faber et al., 2007), suggesting that blue cloud galaxies are quenched, causing them to migrate to the red sequence, but while the blue cloud itself is replenished by similar number of newly formed galaxies.

The reason why galaxies cease forming stars and transition from blue to red is an active and ongoing area of research. As illustrated in Figure 1.2, one popular hypothesis is that the titanic collisions between galaxies triggers intense star formation and powerful black hole activity at the centers of the merger remnants. These intensely bright supermassive black hole environs at the centers of galaxies are called active galactic nuclei (AGN). The brightest AGN are called quasars. The merger-induced, intensely star-forming galaxies are known as starbursts. Their star formation rates often reach 10–100 times that of the normal star-forming galaxies. It is thought that the starburst and AGN in concert consume and destroy the cold gas which otherwise would fuel future star formation in the galaxies (Sanders et al., 1988; Hopkins et al., 2006). This process is called stellar or AGN feedback.

AGN feedback is a relatively young topic. Many details of how and when it operates are unclear. In this dissertation, we will focus on studying observational signatures of AGN feedback with the aim to test nascent theories of galaxy evo-

lution and to provide insights that will aid future developments of more refined theories. Most nearby galaxies are evolving relatively slowly compared to the more distant galaxies. The era of major galaxy mergers and rapid black hole growth is mostly over today. In this dissertation, we will identify very rare galaxy candidates undergoing through a rapid merger evolutionary sequence extending all the way from disturbed starbursts, followed by fading and relaxed AGN, and to eventually young and quiescent post-starburst galaxies, which resemble the red sequence galaxies in many ways. In chapter 2, we will quantify the AGN fraction and the AGN activation time in these candidates to ascertain if the AGN are responsible for the rapid evolution observed in these galaxies. In chapter 3, we will further examine the molecular gas properties of these candidate post-starburst galaxies to test if AGN destroy the molecular gas, thereby suppress residual star formation at the end of the starbursts. The cold gas destruction by the AGN could be by heating or expulsion from the galaxies. In chapter 4, we will investigate if AGN in distant galaxies expel their gas through powerful AGN-driven galactic winds.

In the rest of this section, I briefly give a general context and summarize the key findings of the dissertation. Further detailed background to the topics in each chapter can be found in their corresponding introduction. I started this chapter with a poetic quotation that asserted that "the end of all our exploring will be to arrive where we started and know the place for the first time." In the reminder of this section, I will discuss some of the observations of the Milky Way to emphasize that our own Galaxy likely underwent through similar processes explored in this dissertation but using observations of external galaxies. At the end of reading this dissertation, I hope the reader marvels at the fact that the same processes

explored in the external galaxies may be connected to the past or the future of our home galaxy.

1.1 A supermassive black hole in the Milk Way and its wind relics

Supermassive black holes (SMBHs) are large mass concentrations at centers of galaxies. They weigh from one million to ten billion times the mass of the sun. Currently their origin is not well-understood. It is believed that they might have formed from seed black holes in the early universe from either remnants of massive first generation stars or direct collapse of dynamically unstable dense gas in proto-galaxies or dynamical interactions in first dense nuclear clusters (see a review by Volonteri, 2010). The seed black holes grow through a series of galaxy mergers and are incorporated into larger and larger dark matter halos as time progresses. At each merger incident, the seeds accrete gas in their merger remnants and coalesce at the end of the merger. Through successive gas accretions and black hole-black hole merging, the seeds eventually become supermassive black holes.

The most compelling observational evidence we have for SMBH is at the center of our Milk Way galaxy, near the radio source known as Sgr A*. The Galactic center hosts a supermassive black hole weighing 4.4 million solar masses (Ghez et al., 2008; Gillessen et al., 2009). Due to the proximity of the Galactic center, which is only 8.3 kpc (27,000 light years) away, the mass of the supermassive black hole could be estimated directly by following the orbits of individually resolved stars around Sgr A*, using Adaptive Optics technology on Keck and VLT tele-

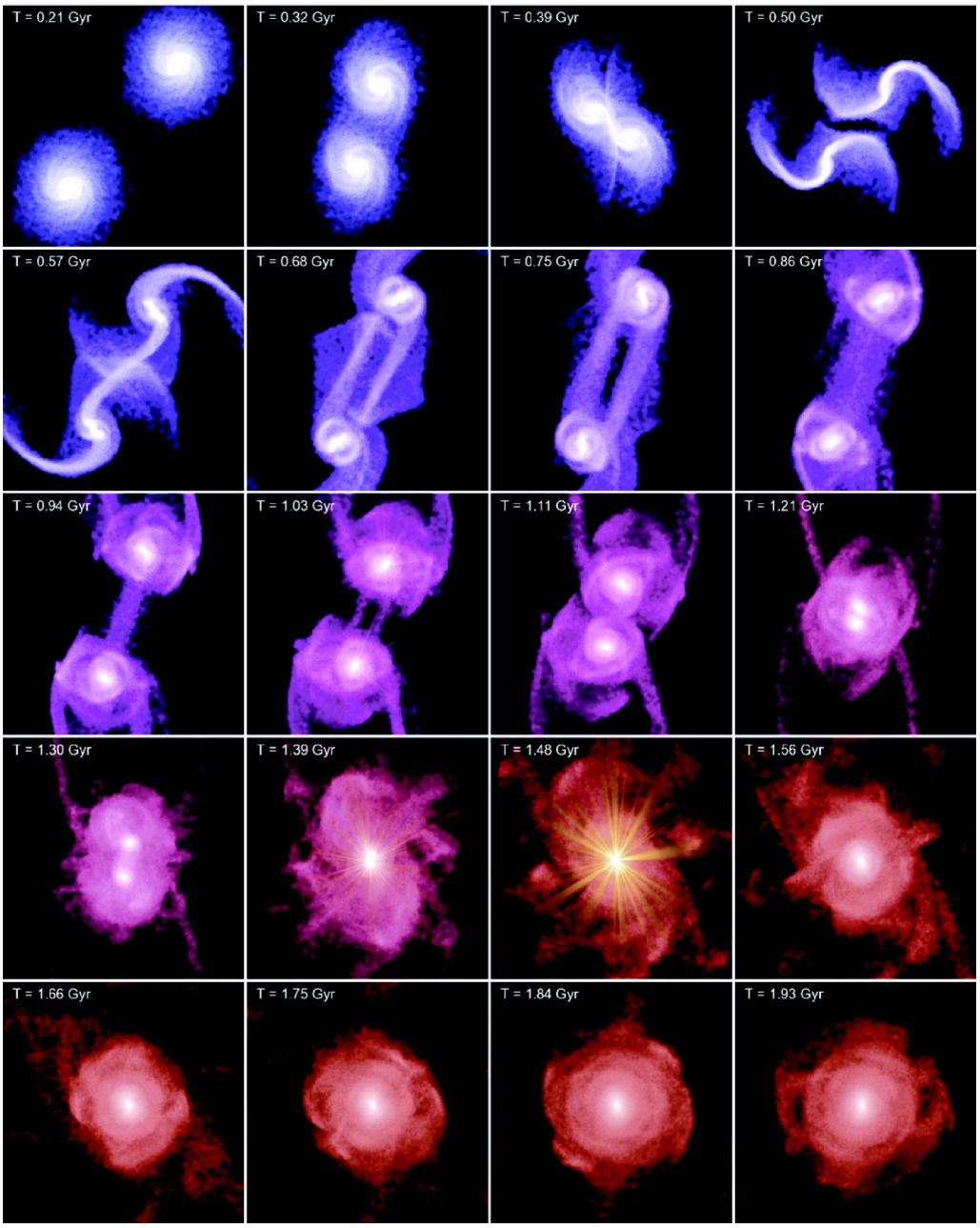

Figure 1.2:. Time sequence of a galaxy merger simulation with initial gas fraction of 20% (Hopkins et al., 2006). Each panel is 80 h^{-1} kpc on a side and shows the simulation time in the upper left corner. Brightness of the image is scaled to the logarithm of the projected stellar mass density, while color indicates the gas fraction, from 20% (blue) to less than 5% (red). Merging of galaxies which triggers an intense starburst and a black hole activation is one of the ways galaxies may evolve from blue to red.

scopes (Figure 1.3). The most recent, highest-resolution measurement indicates that the angular diameter for Sgr A* is of 37μas (Doeleman et al., 2008), which means that all the observed mass is concentrated in a region less than half of the distance between the Earth and the Sun. The Schwarzschild radius, inside which even light cannot escape, for the SMBH at center of the Galaxy is about 10μas.

The galactic center is currently quiescent. Sgr A* does qualify as an AGN. It is substantially less luminous than weak AGN which we customarily observe in external galaxies. However, there is relic evidence that the SMBH in the Galaxy was once active. The Fermi Gamma-ray Space Telescope recently discovered two large gamma-ray bubbles, which extend about 10 kpc above and below the Galactic center (disk). Hydrodynamic simulations show that the bubbles may be relics of a recent powerful AGN jet activity a few million years ago (Guo & Mathews, 2012). Zubovas et al. (2011) argued that Sgr A* likely had a brief but very bright quasar phase associated with the recent star formation observed in the inner nuclei of the Galaxy. The authors also argued that the observed highly symmetrical lobes are unlikely to have originated from an AGN jet but from an isotropic nearly-spherical AGN-driven wind. They predict that the outermost parts of the lobes should still be expanding at $\sim 1000\,\mathrm{km\,s^{-1}}$. Fox et al. (2015) used background quasar light to probe the velocity of one of the bubbles (Figure 1.4). The quasar light pocking through the bubble would be absorbed at velocity corresponding outflow velocity. The authors reported two high-velocity metal absorption components at radial velocities of -235 and $+250\,\mathrm{km\,s^{-1}}$. These two velocity components might originate from the front and back side of an expanding biconical outflow launched from the Galactic center. Their wind model suggested that the true wind velocity, ac-

counting for the projection effect, is $\gtrsim 900$, which is consistent with the theoretical prediction. It is possible that other galaxies also produce similar structures like the Fermi bubbles but their faintness in gamma rays will make their detection difficult in external galaxies. However, as we will discuss later, galactic winds, probed using other methods, are very common in other galaxies. By exploring AGN feedback in other galaxies, we hope to understand better the past and the future of our home galaxy.

1.2 Simple energetic argument for AGN feedback

I wrote the previous section, with a non-astronomer readers in mind, this selection is technical, and such readers can skip this section and get the summary of the dissertation in the next section.

A simple energetic argument of comparing the radiative accretion energy of a SMBH with the binding energy of its host galaxy leads to the conclusion that the black holes may have profound effects on their host galaxies (Fabian, 2012). The binding energy of the galaxy $\mathrm{E_{gal}}$, with a stellar mass $\mathrm{M_{gal}}$, and a velocity dispersion σ, is $\mathrm{E_{gal}} \approx \mathrm{M_{gal}}\sigma^2$ and the energy radiated, $\mathrm{E_{BH}}$, by accretion onto the black hole of mass $\mathrm{M_{BH}}$, with a radiative efficiency η, is $\mathrm{E_{BH}} = \eta \mathrm{M_{BH}} c^2$, where c is the speed of light and η is about 0.1. Equating the two energies and using the observed ratio $\mathrm{M_{BH}}/\ \mathrm{M_{bulge}} \sim 3 \times 10^{-3}$ (e.g., Kormendy & Ho, 2013) and a bulge-to-total mass ratio of 0.5, results in $\mathrm{E_{BH}}/\ \mathrm{E_{gal}} \gtrsim 84\,(\eta/0.1)(400\,\mathrm{km\,s^{-1}}/\sigma)^2$. The approximate equality is only achieved for the most massive galaxies, as most

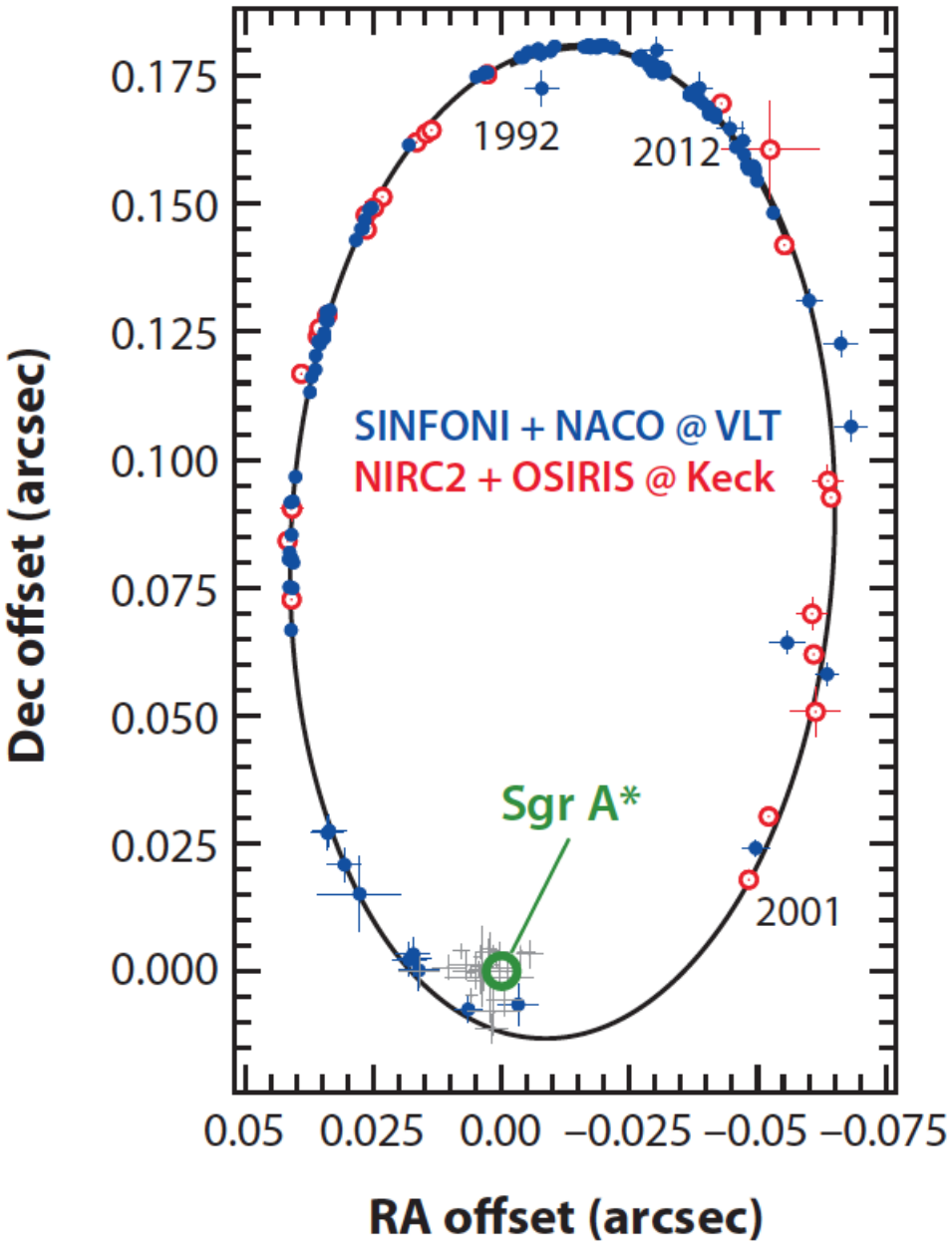

Figure 1.3:. The orbit of star S2 around the black hole at the center of Milk Way (Ghez et al., 2008; Gillessen et al., 2009). The figure is taken from Kormendy & Ho (2013).

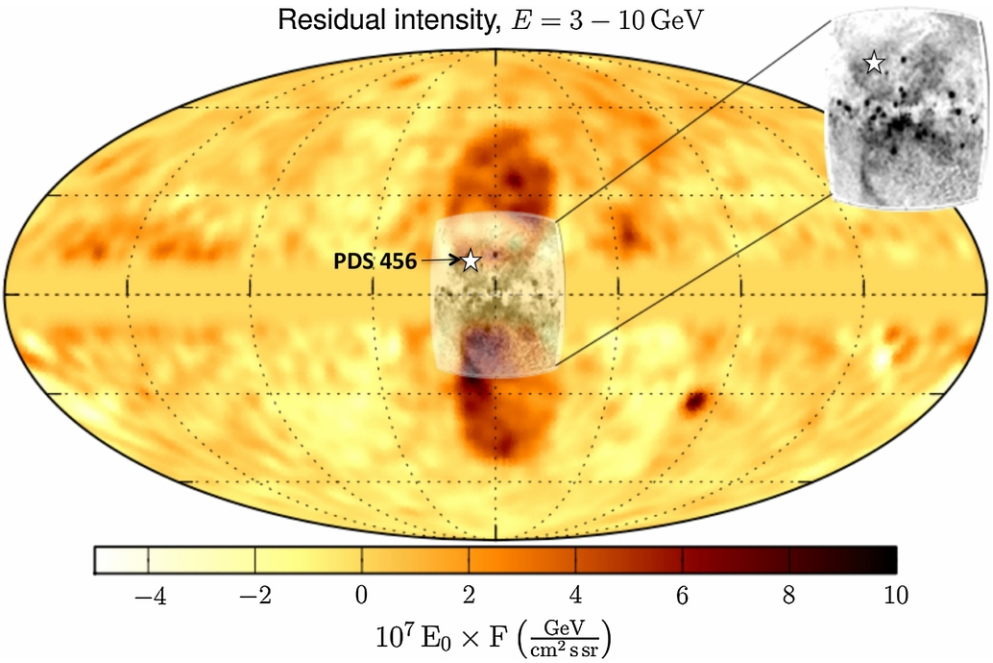

Figure 1.4:. The Fermi Gamma-ray Telescope discovered a pair of enormous gamma-ray-emitting bubbles extending from the Galactic center. The yellow/orange map is an all-sky Fermi image of the residual gamma-ray intensity (Ackermann et al., 2014). The Fermi Bubbles are the twin lobes in dark orange at the center of the figure. Superimposed in gray-scale is the ROSAT 1.5 keV X-ray emission map. The inset on the right is a zoom-in on the X-ray data. The star is the background quasar used to probe the bubble. The figure is taken from Fox et al. (2015).

galaxies have $\sigma < 400\,\mathrm{km\,s^{-1}}$. Therefore, the black hole has the potential to disrupt the entire galaxy.

In the following discussion, I present the condition required for momentum-driven AGN winds to unbind galactic gas, following Silk & Nusser (2010). These authors argued, from the condition they derived, that AGN cannot supply enough momentum in radiation to drive the gas out galaxies. My slightly different derivation shows that AGN are capable of removing gas once the molecular gas fraction is below about 8%, perhaps explaining the delayed AGN molecular gas destruction we observe in this work, and the minor role of AGN in quenching starbursts we infer in chapter 2.

Let us assume an isothermal sphere galaxy with a radius r, so that its mass is $\mathrm{M_{gal}} = 2\sigma^2 r/G$, where G is Newton's gravitational constant. The total gas fraction is $f_g = \mathrm{M_{gas}/M_{gal}} = (\mathrm{M_{HI}}+\mathrm{M_{H_2}})/\mathrm{M_{gal}} = 4f_{\mathrm{H_2}}$, since $\mathrm{M_{HI}} \approx 3\mathrm{M_{H_2}}$ (Saintonge et al., 2011). The Eddington luminosity is $\mathrm{L_{Edd}} = 4\pi G M_{\mathrm{BH}} m_{\mathrm{p}} c/\sigma_{\mathrm{T}}$. If the the radiation pressure force balances and gravitational force, $\mathrm{L_{Edd}/c = GM_{gal}M_{gas}}/r^2 \implies \mathrm{M_{BH}} = 4f_{\mathrm{H_2}} \frac{\sigma_{\mathrm{T}}}{m_p} \frac{\sigma^4}{\pi G^2}$, which has similar scaling as the observed $\mathrm{M_{BH}} - \sigma$ relation. The total energy radiated by the black hole, $\mathrm{E_{out}}$, in driving the gas out of its host galaxy with radius r_e by the radiation pressure is $\mathrm{E_{out}} = \mathrm{L}\int_r^{r_e} 1/v(r)dr > \mathrm{L}\times(r_e - r)/v_e(r)$, where $v_e(r)$ is the escape speed at the radius r. For an isothermal sphere truncated at the virial radius, R_v, $v_e(r) = 2\sigma\sqrt{(}1 + \ln \mathrm{R}_v/r)$. The work done by radiation pressure in moving the gas from r to r_e must be greater than the kinetic energy required for the gas to the escape at each radius, $\mathrm{L}(r_e - r)/c > 1/2 M_{\mathrm{gas}} v_e^2(r)$. Thus, $\mathrm{E_{out}} > c/2 M_{\mathrm{gas}} v_e(r) > M_{\mathrm{gas}} c\sigma > 4f_{\mathrm{H_2}}\mathrm{M_{gal}}\ \mathrm{c}\sigma$. The accretion energy of the black hole must also satisfy $\eta \mathrm{M_{BH}} c^2 > 4f_{\mathrm{H_2}}\mathrm{M_{gal}}\ \mathrm{c}\sigma$. Di-

viding both sides by M_{gal} leads to the condition $f_{H_2} < \frac{\eta}{4}\frac{M_{BH}}{M_{bulge}}\frac{M_{bulge}}{M_{gal}}\frac{c}{\sigma}$. Using the observed ratio $M_{BH}/M_{bulge} \sim 3 \times 10^{-3}$, M_{bulge}/M_{gal}=0.5, $\sigma = 150\,\mathrm{km\,s^{-1}}$, $f_{H_2} \lesssim 0.08(\eta/0.1)(M_{bulge}/M_{gal}/0.5)(\frac{\sigma}{150\,\mathrm{km\,s^{-1}}})$. These values are reasonable for post-starburst galaxies. Therefore, the condition implies that that AGN feedback may be effective in post-starbursts after the molecular gas fraction is below 8%. Normal star-forming galaxies have gas fractions of 10%, while starbursts have molecular gas fractions of 20–30%.

1.3 Summary of the dissertation

As I have mentioned before, the dissertation focuses on studying the observational signatures of AGN feedback. AGN feedback is one of the mechanisms invoked in cosmological simulations of galaxy evolution to suppress star formation in massive galaxies. Without feedback, the theoretical models fail to reproduce even basic properties of galaxies. However, observational constraints on AGN feedback are few.

In chapter 2, we study the AGN prevalence and activation time in 159 transition post-starburst galaxies. These galaxies recently underwent starbursts but they still have some star formation and AGN activity. They are very rare galaxy candidates on the rapid merger evolutionary sequence of starbursts and fading AGN. One of the major achievements of the work presented in chapter 2 is to identify them for the first time. With the new sample, we study the connection between the cessation of star formation and AGN activity. We find that AGN are more commonly hosted by post-starburst galaxies than by normal galaxies. Post-starburst AGN hosts make up 36% of the transiting post-starbursts. Despite

the high frequency of AGN in post-starbursts, we find that the clear presence of AGN is significantly delayed from the peak of starbursts by about 200 million years. We also find that starbursts and transition post-starburst galaxies are significantly more dust-obscured than normal galaxies and quiescent post-starbursts. There is indirect evidence that AGN may remove left-over dust and gas at the end of the starburst.

In chapter 3, we study the molecular gas evolution of 126 nearby post-starburst galaxies, of which 24 have new observations undertaken by us while the rest are compiled from previously published works. We use the carbon monoxide (CO) emission in radio frequency as a surrogate for molecular hydrogen gas. The galaxies in the new sample are selected as green valley galaxies. Most post-starburst galaxies in previous samples are bluer and younger than our sample. we find that as the post-starbursts age, both the star formation rate and molecular gas fraction decrease with time, and eventually PSBs attain low gas contents observed in quiescent galaxies within one billion years after experiencing a starburst. Therefore, the evolution of molecular gas in post-starburst galaxies is rapid compared to normal galaxies. Even though they used part of the data analyzed in chapter 3, previous works did not find rapid evolution of gas in post-starburst galaxies. Therefore, we find the first evidence that AGN feedback can destroy the molecular gas in post-starburst galaxies, thereby suppress residual star formation and facilitate the rapid transition of these galaxies to the red sequence.

In chapter 4, we study galactic winds in 12 distant galaxies hosting low-luminosity AGN. The light travel time from these galaxies is about 8 billion years. Our AGN are the most distant objects of their kind to be studied in (wind) absorp-

tion to date. We use the near UV Fe II λ2586 absorption line profile in the average spectrum of these AGN to trace the movement of cool gas entrained in the winds. The stellar lights in the galaxies get absorbed by the intervening winds surrounding the galaxies and the wind motions are imprinted on the average Fe II λ2586 absorption profile. We find an average velocity shift of about -125 $\mathrm{km\,s^{-1}}$. The wind velocities in these AGN are significantly lower than the velocities needed to escape from the galaxies, and they are also similar to the velocities observed in star-forming non-AGN galaxies at a similar redshift. Thus, we do not find evidence for wind-driving AGN feedback in the distant low-luminosity AGN host galaxies. There is one similar and complementary work which studied winds in ten AGN host galaxies at look back times of 5 billion years (Coil et al., 2011) and this study also did not find evidence for AGN feedback.

Chapter 2

From Starburst to Quiescence: Enhanced AGN Fraction and Delayed AGN Appearance in Rapidly Quenching Local Post-Starburst Galaxies.

2.1 Introduction

Galaxies show bimodality in their colors, morphologies, and star formation rates both locally and at high redshift (e.g., Strateva et al., 2001; Baldry et al., 2004; Bell et al., 2004; Brammer et al., 2009). It is thought that star formation quenching causes "blue cloud" galaxies to migrate to the "red sequence" (Bell

et al., 2004; Faber et al., 2007). A wide variety of quenching mechanisms have been proposed to explain the observed bi-modal galaxy properties (e.g., Di Matteo et al., 2005; Kereš et al., 2005; Croton et al., 2006; Dekel & Birnboim, 2006; Hopkins et al., 2006; Somerville et al., 2008; Martig et al., 2009). These mechanisms quench star formation by heating up gas in the galaxy (halo), stabilizing it against collapse, or (rapidly) using it up or expelling it from the galaxy. These quenching mechanisms can be classified broadly into two modes: fast and slow. The slow mode occurs when star formation gradually fades, probably due to simple gas exhaustion over timescales longer than $\gtrsim 1$ Gyr, and it does not require any special triggering event such as mergers (e.g., Noeske et al., 2007; Fang et al., 2013). On the other hand, rapid quenching is often identified with a triggering event associated with a merger-induced starburst and the resulting feedback (from either the starburst or from an associated AGN) that rapidly removes or exhausts the gas (e.g., Sanders et al., 1988; Hopkins et al., 2006). This work focuses on rapidly quenching or recently quenched galaxies.

(Quenched) post-starburst galaxies, also known as K+A or E+A [1]galaxies (e.g., Dressler & Gunn, 1983; Zabludoff et al., 1996; Quintero et al., 2004), offer a unique view into galaxy evolution because they are believed to be recently quenched starbursts rapidly transitioning from the blue cloud to the red sequence. They may contain lingering signatures of a quenching process imprinted on their

[1]The term "K+A" refers to a galaxy with significant populations of both (old) K stars and (young) A stars, indicative of rapidly quenched recent star formation. The term "post-starburst" traditionally refers to a K+A galaxy that was necessarily preceded by a starburst. We use the terms K+A and post-starburst interchangeably. We often use the term K+A in a general sense when we refer to related past studies. We avoid the term "E+A" which refers to a quenched galaxy with early-type morphology and a young stellar population, because we show that many starburst galaxies already have compact and early-type morphologies before quenching into post-starbursts.

spectral and structural properties. The fact that these galaxies have unusually large A-star populations but lack younger stars has been interpreted as evidence for recently quenched starbursts.

Theoretically, post-starburst galaxies might be the end-product of galaxy mergers (Hopkins et al., 2006, 2008; Bekki et al., 2001, 2005; Snyder et al., 2011). In gas-rich model mergers, tidal torques channel gas to galaxy centers and power intense nuclear starbursts (Barnes & Hernquist, 1991, 1996). The gas channeled to the centers may also lead to the onset of obscured nuclear AGN activity (Di Matteo et al., 2005; Hopkins et al., 2006). At the end of the starburst, after gas has been exhausted by the starburst itself and/or expelled by stellar feedback, the leftover gas and dust obscuring the active galactic nucleus (AGN) are cleared out due to feedback from the AGN (Springel et al., 2005a,b; Hopkins et al., 2006; Kaviraj et al., 2007; Hopkins et al., 2008; Snyder et al., 2011; Cen, 2012). Consequently, star formation and further black hole growth are halted. Then the galaxies pass through the quenched post-starburst phase before they passively age and become "red and dead". This work aims to test this hypothesis in detail.

Using galaxy merger simulations, Snyder et al. (2011) have constrained the typical K+A life-time of merger-induced post-starbursts to be $\lesssim 0.1 - 0.3\,\mathrm{Gyr}$ (cf. Falkenberg et al., 2009; Wild et al., 2009). They find that the presence of AGN makes almost no difference to the evolution of the post-merger spectrum in their simulation without diffuse dust. However, with diffuse dust, they find that including AGN accretion results in a longer K+A phase with stronger Balmer absorption lines than without this accretion. Their interpretation of this result is that AGN feedback does not itself directly shut off a starburst but rather serves

to remove the leftover obscuring dust around the post-starburst population in the nucleus, thereby enhancing the Balmer absorption features.

Consistent with the merger origin, past observational studies of morphology and kinematics of K+A galaxies in the field hint that they are merger remnants on the way to becoming early-type galaxies (Norton et al., 2001; Quintero et al., 2004; Goto, 2007). As such, they display both early-type morphologies and signs of interactions (Schweizer, 1982; Zabludoff et al., 1996; Quintero et al., 2004; Balogh et al., 2005; Yang et al., 2008; Pracy et al., 2009). Similarly, many post-starburst galaxies are observed to be blue-centered with positive color gradients and have central (within $\sim 4\,\mathrm{kpc}$) A star populations (e.g., Yamauchi & Goto, 2005; Goto et al., 2008; Yang et al., 2008; Swinbank et al., 2012).

Identifying the mechanisms responsible for quenching star formation in post-starbursts is still an outstanding problem after thirty years since their discovery. The rest of this section highlights special problems that plague post-starburst studies and have consequently hampered progress in understanding feedback in these systems. A brief discussion of how these problems are addressed in this work is also presented. The key novel feature of this work is that it broadens the definition of post-starburst using multi-wavelength galaxy colors and spectral indices and thereby identifies AGN in post-starbursts more completely and consistently.

2.1.1 Finding a more complete sample of post-starbursts

Post-starbursts are rare galaxies, especially at low red-shift (Wild et al., 2009). They comprise $\lesssim 1\,\%$ of all galaxies at $z \sim 0.1$ (Wong et al., 2012). Furthermore, these galaxies tend to evolve through regions of parameter space populated by nor-

mal galaxies. For these two reasons, post-starbursts are hard to distinguish from the underlying, slowly quenching normal galaxies. Because of this difficulty, the conventional definition of post-starburst is restricted to quenched post-starbursts with weak or no emission lines. The problem is that this definition excludes any transiting (quenching) post-starbursts with on-going star formation or strong AGN activity, which may be a key link between starbursts and the quenched post-starbursts.

In this work, we strive to directly link starbursts and post-starbursts by using a variety of novel yet plausible criteria to identify a more complete sample of objects that are in transit between the starburst phase and the fully quenched post-starburst phase. Wild et al. (2010) traced the evolution of local bulge-dominated galaxies during the first 600 Myr after a starburst using principle component analysis of stellar continuum indices around the 4000Å break.

Our work is complementary to Wild et al. (2010) in some of its main results but it is quite different in its overall methodology and analysis. For instance, we take a multi-wavelength approach: while we use stellar continuum indices to define some post-starbursts, we also apply additional constraints, such as the dust-corrected global near-UV to optical colors or near-UV to mid-IR colors. The continuum indices are SDSS values measured in a $3''$ aperture and may not be representative of a galaxy as a whole. They are also not sufficient to identify heavily dust-obscured post-starbursts, which happen to overlap with normal galaxies in their spectral indices. To identify such objects we find that mid-IR colors are useful augmentation.

Finally, one of the methods used in this work is to identify common mem-

bers of the starburst sequence in a narrow mass slice around $\log M(M_{\odot}) \sim 10.5$. This value corresponds to the transition mass in the color-mass diagram where both star-forming and quiescent galaxies are presently observed (Kauffmann et al., 2003b). A narrow mass window approximately captures galaxies on the starburst evolutionary sequence because the quenching timescale ($\lesssim$ 1 Gyr; Martin et al., 2007; Snyder et al., 2011) is much faster than the merging timescale (a typical local galaxy has a major merger rate of $\lesssim 0.05\,\mathrm{Gyr}^{-1}$ (Hopkins et al., 2010)). Therefore, the precursors of post-starbursts are unlikely to grow in mass via multiple mergers in the time it takes them to quench. The burst fraction (amount of new stars formed) in a merger is typically $< 20\%$ of the total mass (Norton et al., 2001; Balogh et al., 2005; Kaviraj et al., 2007; Wild et al., 2009; Swinbank et al., 2012). Hence, it also does not significantly contribute to the mass increase on the starburst sequence. Even though a galaxy can be linked to its immediate progenitors by its mass, mass by itself is not a sufficient predictor of galaxy properties. Recent studies show that structural parameters that combine mass and radius (i.e., stellar mass surface density, μ_* or velocity dispersion, σ) are better tracers of galaxy quenching (Kauffmann et al., 2006; Franx et al., 2008; Cheung et al., 2012; Wake et al., 2012; Fang et al., 2013). This work will examine whether μ_* and σ of starbursts and post-starbursts are indicative of quenching in these galaxies.

2.1.2 Finding all AGN, including a population of highly obscured AGN.

Most previous studies on post-starburst galaxies excluded strong AGN because they adopted a restrictive definition of post-starbursts as galaxies with weak or no emission lines. Wild et al. (2010) attempted to improve this by defining post-starbursts using spectral indices only, bypassing the need for (weak) emission line requirements. However, heavily dust-obscured post-starbursts and broad-line AGN are still excluded or missing from their sample. This work attempts to include dust-obscured post-starbursts as part of the starburst sequence. It also constrains the star formation rates of broad-line AGN and investigates whether they are preferential to a specific stage in the merger sequence (e.g., Hopkins et al., 2006). We use GALEX and WISE photometery in our selection criteria of obscured post-starbursts, and we use the WISE 12 μm luminosity as a proxy for star formation rates (upper limits) of broad-line AGN. In a follow up work, we plan to do further study on the star formation rates of broad-line AGN using far-infrared data.

Past studies of quenched post-starburst galaxies hint that AGN are more common in these galaxies than in normal galaxies (Yan et al., 2006; Georgakakis et al., 2008; Brown et al., 2009). However, these past studies were explicitly biased against strong AGN (Seyferts) since they excluded emission-line galaxies from their post-starburst samples. These studies also cannot exclude the possibility that the weak AGN signatures in their post-starbursts are from "LINER-like" emission unrelated to AGN activity (Cid Fernandes et al., 2011; Yan & Blanton, 2012; Singh et al., 2013). Regardless, Yan et al. (2006) have found that 95% of

their K+A galaxies have LINER-like line ratios. Using a sample of 44 K+A galaxies at $z \sim 0.8$, Georgakakis et al. (2008) have found a higher fraction of X-ray sources in post-starbursts ($\sim 15\%$) than in normal red sequence galaxies ($\sim 5\%$). These sources are mostly low luminosity AGN at best and have a hard mean stacked X-ray spectrum suggesting moderate levels of obscured AGN activity in the bulk of this population. Similarly, Brown et al. (2009) have found that a third (8/24) of their K+A galaxies at $z \sim 0.2$ are X-ray sources with luminosities of $\sim 10^{42}$ erg s^{-1}.

To improve on these previously incomplete estimates of the AGN fraction in post-starbursts, we assemble a large and less biased sample of post-starbursts which includes emission-line galaxies to robustly identify AGN. This enables us to estimate the AGN fraction in transiting post-starbursts for the first time. We will infer the relationship between AGN and recent quenching in post-starbursts from the AGN fraction, and the time interval between the peak of starburst to the peak of AGN activity. If the AGN fraction is low, it indicates that AGN and quenching of starbursts are likely not related. A significant AGN delay might indicate a non-causal or secondary relationship (e.g., a common fueling mechanism or later additional quenching) between starbursts and AGN even if AGN are more common in post-starbursts than in normal galaxies.

The rest of this chapter is structured as follows. Section 2.2 describes the multi-wavelength data. Section 2.3 presents the sample selection. Starbursts and the different classes of post-starbursts are defined in this section. Section 2.4 investigates the AGN properties of post-starbursts. Section 2.5 presents the bulge properties of post-starbursts as an independent check on our sample selection.

Section 2.6 presents a discussion on the importance of post-starbursts in the build-up of the red sequence. This section also summarizes the main results of this work. Throughout this chapter, an $(\Omega_m, \Omega_\Lambda, h) = (0.27, 0.73, 0.7)$ cosmology is used. All magnitudes and colors are on the AB system unless indicated otherwise.

2.2 Data and Measurements

In the first three subsections, we will briefly describe the SDSS, GALEX and WISE data used. In the later subsections, we will describe the dust correction, galaxy structural parameters and stellar population modeling employed in the following sections.

2.2.1 SDSS

The Sloan Digital Sky Survey (York et al., 2000, SDSS) is a large photometric and spectroscopic survey. It has mapped out about a third of the celestial sphere with its five filter band-passes, *ugriz* (Fukugita et al., 1996). The parent sample (§ 2.3.1) used in this chapter comes from SDSS Data Release 8 (DR8, Aihara et al., 2011). The SDSS DR8 has more value-added quantities essential for this chapter.

As described in Aihara et al. (2011), DR8 includes various galaxy physical parameters such as stellar masses. Briefly, the stellar masses are estimated from *ugriz* photometery using the Bayesian methodology to calculate the likelihood of each model star formation history (SFH) given the data (Kauffmann et al., 2003a). The mass estimate assumes that the SFH is approximated by a sum of discrete bursts and uses templates over a wide range in age and metallicity. Thus,

there should be no concern over systematic differences between the stellar mass estimates of starbursts, post-starbursts and normal galaxies. In addition, the masses of these galaxies are dominated by their old pre-burst stellar populations as the contribution to the total mass from newly formed stars in a burst is only $3-20\%$ of the total mass (Norton et al., 2001; Balogh et al., 2005; Kaviraj et al., 2007; Wild et al., 2009; Swinbank et al., 2012).

DR8 also provides spectral indices and emission line measurements (Tremonti et al., 2004; Aihara et al., 2011). To measure the nebular emission lines of a galaxy, the continuum is modeled as a non-negative linear combination of single stellar population (SSP) template spectra generated using the Bruzual & Charlot (2003) (hereafter BC03) population synthesis code, and the best fitting model is subtracted from the galaxy spectrum.

2.2.2 GALEX

We use UV data from the Galaxy Evolution Explorer (GALEX, Martin et al., 2005) to exploit the greater sensitivity of its near-UV ($m_{\rm NUV} < 20.8$) band to recent star formation. The near-UV (1771 - 2831Å) imaging data have a spatial resolution of 6-8$''$ and 1$''$ astrometry. The data come from the cross-matched catalog between GALEX GR6 against SDSS DR7. This catalog is available through the GALEX CASJobs interface[2]. At fainter UV magnitudes, GALEX loses red galaxies because they drop below the GALEX detection threshold. About 82% ($\sim$ 220,000) of galaxies in SDSS spectroscopic sample ($m_r < 17.77$), in the redshift of interest for this work ($0.03 < z < 0.1$), have a GALEX counterpart within

[2]http://galex.stsci.edu/casjobs/

$5''$. Adopting brighter r-band limit gives higher completeness ($\gtrsim 90\%$) but excludes significantly more post-starbursts (see Wyder et al. (2007) for a discussion of GALEX completeness relative to SDSS). Since post-starbursts (including dust-obscured ones) are mainly in the blue cloud and green valley, the GALEX incompleteness is less likely to affect our results significantly. Furthermore, about 10% of the post-starburst galaxies have multiple GALEX matches within $5''$. Although the GALEX photometery for post-starbursts with multiple matches may not be accurate, we do not exclude them lest we systematically exclude merging systems. About 90% of these post-starbursts are significantly dust obscured compared to normal galaxies. The exclusion of these post-starbursts does not significantly alter any of our main results.

2.2.3 WISE

The Wide-field Infrared Survey Explorer (WISE, Wright et al., 2010) performed an all-sky survey with photometery in the $3.4\,\mu$m, $4.6\,\mu$m, $12\,\mu$m, and $22\,\mu$m bands. We used the Infrared Science Archive (IRSA)[3] to match SDSS galaxies with the closest WISE sources within a $5''$ radius. About 99 (92)% of SDSS galaxies with $5''$ ($2''$) GALEX matches have corresponding matches in WISE. We use WISE data to study obscured star formation and AGN properties of post-starburst galaxies.

[3]http://irsa.ipac.caltech.edu/Missions/wise.html

2.2.4 Dust correction

The main purpose of the dust correction is to reduce the number of dusty obscured emission-line galaxies, which otherwise masquerade as post-starbursts. We use the Balmer decrements, Hα/Hβ, with the physically motivated two-component dust attenuation model of Charlot & Fall (2000) to correct for attenuation of the nebular emission lines by dust. In the two-component model, the diffuse dust accounts for 40% of the optical depth at 5500Å while the denser birth-cloud dust accounts for the other 60% (Wild et al., 2011b). The optical depth of the dust is assumed to be a power-law of the form $\tau_\lambda \propto \lambda^{-0.7}$ for the diffuse dust and $\tau_\lambda \propto \lambda^{-1.3}$ for the birth-cloud dust. We adopt this model because it has a physical basis and is broadly consistent with observations (Wild et al., 2011b).

In addition, we correct the continuum fluxes (i.e., integrated magnitudes) using the empirical relationship between the emission line and continuum optical depths found in Wild et al. (2011a) and their empirical stellar attenuation curve. They found that Balmer emission lines experience two to four times more attenuation than the continuum at 5500Å. We apply the dust correction only on galaxies whose Hα and Hβ lines are well measured (with signal-to-noise ratio (SNR) > 1). Galaxies with undetected or low signal-to-noise Balmer emission lines are not dust-corrected and their observed quantities are used as the intrinsic ones. We assume the dust-free Case B recombination ratio of Hα/H$\beta = 2.86$ for H II regions (Osterbrock, 1989) and Hα/H$\beta = 3.1$ for type 2 AGN (Veilleux & Osterbrock, 1987).

The Balmer decrements are measured within the 3″ fiber and do not reflect the galaxy-wide values, as there are dust gradients across galaxies (Muñoz-Mateos

et al., 2009; Wild et al., 2011a). We make an approximate correction for this effect following Wild et al. (2011a).

We also correct for Galactic extinction of optical fluxes using the catalog values provided in SDSS DR8 and of the NUV fluxes assuming a ratio $A_{\rm NUV}/E(B-V) = 8.2$ (Wyder et al., 2007), where $A_{\rm NUV}$ is the NUV Galactic extinction and $E(B-V)$ is the $B-V$ color excess.

More details on the dust correction can be found in Appendix 5.1.1, where it is shown that our post-starburst selection does not significantly depend on the detailed assumptions of the dust correction described above. For instance, using single foreground screen model for dust distribution Calzetti et al. (2000), we recover 85% of PSBs selected using the two-component dust attenuation model. However, the single-component model identifies $\sim 15-25\%$ more PSB candidates, which may also be dusty contaminants. Throughout the thesis, the subscript 'dc' on a given quantity denotes dust-correction. For example, $\rm W_{H\alpha,dc}$ denotes a dust-corrected Hα equivalent width ($\rm W_{H\alpha}$).

2.2.5 K-correction

In addition to the dust correction, all galaxy magnitudes and colors used in this work are k-corrected to $z = 0$ using the public *kcorrect* IDL code (Blanton & Roweis, 2007). The GALEX NUV magnitude and the five SDSS *ugriz* magnitudes are used in estimating the k-correction.

2.2.6 Structural parameters

This section describes three structural parameters used to study the relationship between star formation quenching and bulge growth.

The stellar surface mass density is defined as the ratio of half the total stellar mass to the half-light Petrosian z band area, $\mu_* = M_*/2\pi R^2_{50,z}$. Kauffmann et al. (2006) found that μ_* is inversely proportional to the consumption time of the accreted gas from a galaxy halo (i.e, the burst decline time). They suggested that a high stellar surface mass density may be connected to bulge formation through a nuclear starburst and quenching of star formation. However, Fang et al. (2013) showed that the mass surface densities as defined above may exaggerate structural differences between blue and red galaxies because they use a light-profile based radius as opposed to mass-profile based radius. We use μ_* as defined above only to show that starbursts and post-starbursts are both bulge-dominated galaxies, unlike most normal star-forming galaxies.

The velocity dispersion, σ, corrected to 1/8 of the effective radius, $r_{\rm e}$, is estimated from the velocity dispersion measured within the $1.5''$ radius fiber, $\sigma_{1.5}$, using the relation: $\sigma = \sigma_{1.5}(8 \times 1.5'' / {\rm r_e})^{0.066}$ (Cappellari et al., 2006). $\sigma_{1.5}$ is measured by the SDSS *idlspec2d* pipeline using broadened stellar PCA templates (Aihara et al., 2011). For $r_{\rm e}$, we use the weighted average of the circularized r-band radi of the de Vaucouleurs profile ($r_{\rm e,dev}$) and exponential profile ($r_{\rm e,exp}$) : $r_{\rm e} = f_{\rm dev} \times r_{\rm e,dev}\sqrt{b/a} + (1 - f_{\rm dev}) \times r_{\rm e,exp}\sqrt{b/a}$, where $f_{\rm dev}$ is a coefficient that characterizes a galaxy image as a linear combination of a de Vaucouleurs profile and an exponential profile (available in the SDSS catalog).

The color gradient, $\nabla_{\rm color}$, is defined as the difference between the $g-r$ galaxy-

wide color and the $2''$ $g-r$ aperture color. The $2''$ aperture magnitudes are available in SDSS DR8. The global galaxy colors are derived from model magnitudes by fitting the galaxy light with either de Vaucouleurs or exponential profile.

Previous studies have used color gradients defined based on $3''$ apertures (Roche et al., 2009; Bernardi et al., 2011). We define $\nabla_{\rm color}$ using the $2''$ aperture instead to better probe galaxy centers. For instance, about 90% of galaxies in the parent sample have half-light r-band areas that are twice the $2''$ aperture areas at the corresponding redshifts. In comparison, only $\sim 60\%$ of the galaxies have half-light areas that are twice the $3''$ aperture areas. We note that this is the only time we use a quantity measured within a $2''$ aperture.

Positive $\nabla_{\rm color}$ means blue-centered (young bulge), negative $\nabla_{\rm color}$ means red-centered (old bulge) and $\nabla_{\rm color} \sim 0$ means a uniform color throughout a galaxy.

2.2.7 Stellar population modeling

To illustrate how a starburst evolves in some of our diagrams, we overplot Bruzual & Charlot (2003) model tracks on these diagrams. To do so, we model SFHs of a post-starburst as a superposition of an old stellar population initially starting to form at time $t = 0$ and following a delayed exponential SFH of the form $\psi \propto t \exp(-t/\tau_1)$ with e-folding time $\tau_1 = 1$ Gyr (cf. Kriek et al., 2011) plus a young stellar population formed in a recent burst at $t = 12.5\,{\rm Gyr}$ ($z \sim 0.1$) with exponentially declining SFH, $\psi \propto \exp(-t/\tau_2)$ and $\tau_2 = 0.1\,{\rm Gyr}$ (cf. Kaviraj et al., 2007; Falkenberg et al., 2009). The SSP models assume Chabrier (2003) IMF, a solar metallicity for SFH before the recent burst, and 2.5 solar metallicity for the recent burst. A superposition of the two SFHs with varying burst mass

fraction ($bf \sim 3\% - 20\%$) generally describes the starburst to post-starburst evolution. Because of the well-known burst mass-age degeneracy, the ages of the post-starbursts depend on the assumed decay timescale. In Appendix 5.1.2, we quantify the effect of using different decay timescales ($\tau_2 = 0.05\,\mathrm{Gyr}$ or $\tau_2 = 0.2\,\mathrm{Gyr}$) instead of our adopted one. The model tracks overplotted on the data in some of our figures mainly serve to facilitate the interpretation of the data, and our post-starburst selection is purely empirical: it does not explicitly use the models.

2.2.8 Galaxy merger simulation

To further justify our selection of dust-obscured post-starburst galaxies, we use results from the M2M2 simulation presented in Lanz et al. (2014) and Hayward et al. (2014b), which is an equal-mass merger of two disk galaxies. Each disk galaxy is composed of a dark matter halo, gaseous and stellar exponential disks, and a bulge. The progenitor galaxies each have a stellar mass of $1.1 \times 10^{10} M_\odot$ and a gas mass of $3.3 \times 10^9 M_\odot$. See Lanz et al. (2014) for full details of the specific simulation used.

The merger was simulated using the smoothed-particle hydrodynamics code Gadget-3 (Springel et al., 2005a). The simulation includes models for star formation and stellar feedback (Springel & Hernquist, 2003) and black hole accretion and AGN feedback (Springel et al., 2005b). In post-processing, the three-dimensional dust radiative transfer code Sunrise (Jonsson et al., 2006; Jonsson et al., 2010) was used to calculate synthetic UV–mm SEDs of the simulated merger at various times throughout the merger. Sunrise uses the stellar and AGN particles from

the GADGET-3 simulation as sources of radiation and calculates the effects of dust absorption, scattering, and re-emission as the radiation propagates through the dusty ISM of the simulated galaxies. SUNRISE calculates SEDs and images from arbitrary viewing angles. For clarity, we show only results from a single viewing angle in this work. See Jonsson et al. (2010) and Hayward et al. (2011) for further details of the SUNRISE calculations.

2.3 Sample Selection

This section presents the parent sample, and details on how starbursts and post-starbursts are selected from this sample.

2.3.1 The Parent Sample

The basic sample selection is shown Figure 2.1. The sample consists of a SDSS/GALEX/WISE-matched volume-limited sample ($0.03 < z < 0.1$) in a narrow stellar mass range of $\log M(M_{\odot}) = 10.3 - 10.7$. We call this sample of $\sim 67,000$ galaxies the parent sample. The chosen mass range roughly corresponds to the transition mass in the color-mass diagram (Figure 2.1b) from lower-mass star-forming blue galaxies to higher-mass quiescent red galaxies (Kauffmann et al., 2003b). We located the center of the mass bin on the lower end of the transition mass because post-starbursts are preferentially found in smaller-mass galaxies, unlike slowly transitioning galaxies which dominate at higher masses (see also Wong et al., 2012). Moreover, restricting the redshift to be less than 0.1 ensures higher GALEX completeness of the parent sample to red sequence galaxies. As discussed in § 2.1, the starburst-to-post-starburst evolution is followed in the narrow mass-

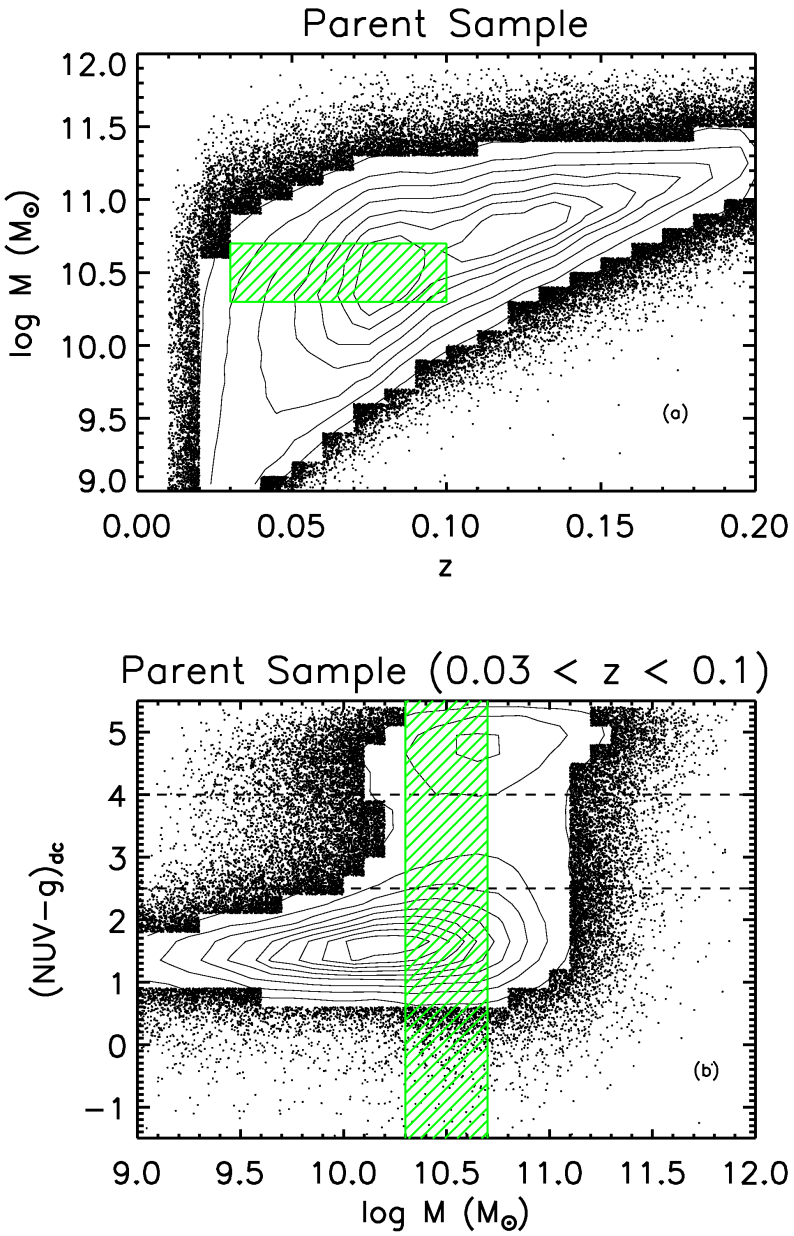

Figure 2.1:. Panel a): Redshift versus stellar mass. The black points are galaxies in the SDSS-GALEX-WISE-matched catalog. Panel b): Dust-corrected NUV-g color versus stellar mass for galaxies in redshift range $0.03 < z < 0.1$. This study uses a volume-limited parent sample of galaxies in a narrow mass slice around the transition mass between the blue cloud and the red sequence. The hatched regions in both panels define the parent sample ($\log\ M(M_{\odot}) = 10.3-10.7$ and $0.03 < z < 0.1$). It is known that quenched post-starburst preferentially occupy the low-mass end of the green valley (Wong et al., 2012). Hence, we chose the lower mass end of the transition mass. The horizontal dashed lines approximately demarcate the blue cloud, the green valley and the red sequence.

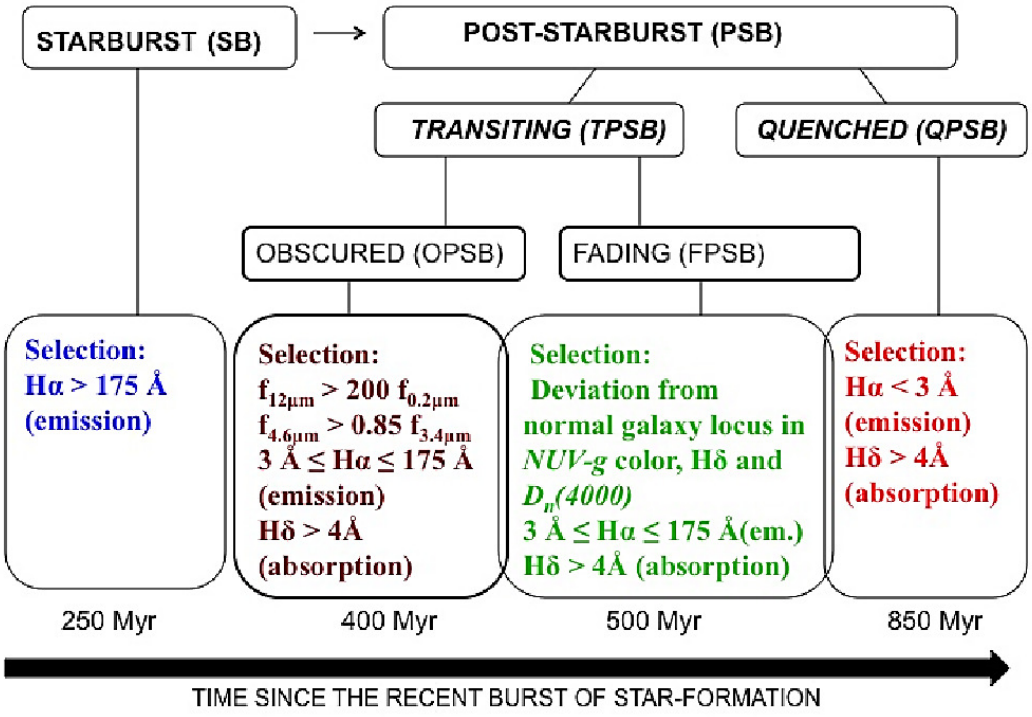

Figure 2.2:. Schematic outline of our starburst and post-starburst selection. Identifying a reasonably complete transiting post-starburst population between the starbursts and the quenched post-starbursts is the major new aspect of this work. The TPSBs are identified by combining their GALEX and/or WISE photometery with with their optical photometery and spectral indices.

slice because mass likely does not increase significantly more than a factor of 2 along the starburst sequence.

As schematically outlined in Figure 2.2, the next three subsections describe in detail the selection of starbursts and post-starbursts from the parent sample. Starbursts are selected to have Hα emission equivalent width above 175Å. The selection of post-starbursts generalizes the conventional definition to encompass both quenching and quenched objects. The conventional post-starbursts, which are characterized by weak or no emission lines but strong Balmer absorption lines, are termed as "Quenched Post-starbursts (QPSBs)" in this thesis. Transit-

ing post-starburst (TPSB) galaxies, which precede quenched post-starbursts but come after the starbursts, are selected in two ways. The first selection is based on the distinctive evolutionary path that starbursts and post-starbursts follow in the 3D parameter space defined by dust-corrected NUV-g color, Hδ equivalent width and the 4000Å break. Objects in this first class are called "Fading Post-starbursts (FPSBs)". They are clearly offset from normal galaxy locus in the parameter space that defines them. The second selection of TPSBs uses GALEX and WISE photometery to identify dust-obscured transiting post-starbursts, which are simply referred as "Obscured Post-starbursts (OPSBs)". We will later show that both classes of transiting post-starbursts have similar properties (e.g., morphology) and that OPSBs generally precede the FPSBs.

The above discussion has isolated four classes of SB and PSB galaxies, we now proceed to explain how the four classes are selected.

2.3.2 Starbursts

A starburst has been defined in at least three ways (Knapen & James, 2009). The definition we adopt considers a starburst as a galaxy with a temporarily higher current SFR than its past average by a factor of $2-3$ (e.g., Brinchmann et al., 2004; Kennicutt et al., 2005). This can be quantified by a threshold in the equivalent width of Hα ($W_{H\alpha}$). Galaxies with ratios of current to past average SFR greater than two or three have (dust-extincted) $W_{H\alpha} \gtrsim 80-110$ Å (Lee et al., 2009; McQuinn et al., 2010).

We define a starburst as a galaxy with dust-corrected $W_{H\alpha,dc} > 175$Å . This threshold corresponds to $\gtrsim 2\,\sigma$ deviation from the mean $W_{H\alpha,dc}$ distribution of

star-forming galaxies in the parent sample (star-forming galaxies are objects below the maximum starburst boundary of Kewley et al. (2001) in the BPT diagram). We note that a starburst with $W_{H\alpha} \gtrsim 80 - 110$Å and nebular extinction $A_V = 1$ will have $W_{H\alpha,dc} \gtrsim 125 - 175$Å if the continuum is extincted less than the gas by a factor of two, as observed in starbursts (Calzetti et al., 2000). Our starbursts have a median A_V of 2.3 and (fiber) SFR of about $10\,M_\odot\,yr^{-1}$ (specific SFR of about $10^{-9}\,yr^{-1}$). For comparison, the typical SFR of a normal star-forming galaxy in the parent sample is about $1\,M_\odot\,yr^{-1}$.

2.3.3 Quenched Post-Starbursts (QPSB)

The conventional post-starburst galaxies are characterized as having no detectable or weak current star formation, but with significant star formation in their recent past (< 1 Gyr). These two underlying characteristics have been quantified using various spectral signatures. The lack of ongoing star formation is inferred from weak Hα and/or O II emission lines. The episode of significant recent star formation is inferred from the presence of strong Balmer absorption lines ($H\delta \gtrsim 4$Å), indicative of intermediate-age stars (A stars) or from the relative ratio of young to old stars or from the comparison of Balmer absorption lines to 4000Å break strength (e.g., Zabludoff et al., 1996; Balogh et al., 1999; Blake et al., 2004; Poggianti et al., 2004; Quintero et al., 2004; Yang et al., 2004; Goto, 2007; Wild et al., 2007; Yan et al., 2009).

Figure 2.3 shows the dust-corrected equivalent width $W_{H\alpha,dc}$ in emission versus $W_{H\delta}$ in absorption, after the emission line infill correction. This diagram is used to define QPSBs, which will help us motivate and explore how such a conventional

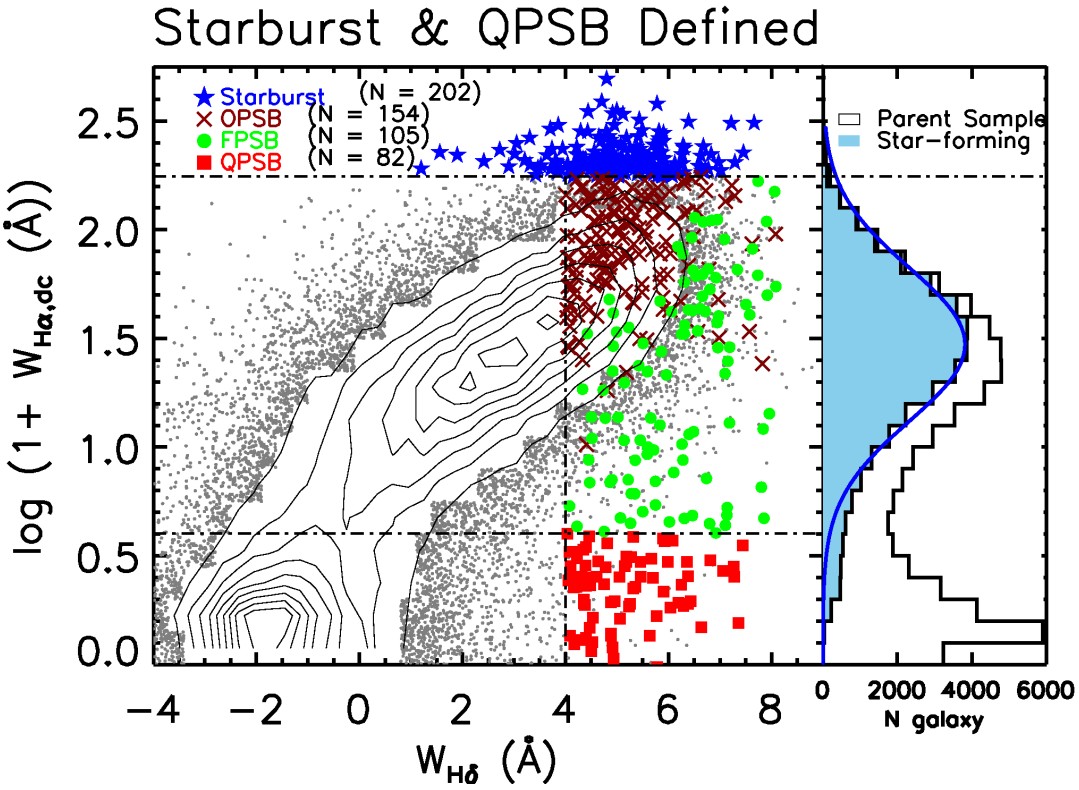

Figure 2.3:. The dust-corrected Hα emission equivalent width ($W_{H\alpha,dc}$) against Hδ_A absorption strength($W_{H\delta}$) for the galaxies in the parent sample (grey), starbursts (blue stars), fading post-starbursts (FPSBs; green circles), obscured post-starbursts (OPSBs; brown Xs), and quenched post-starbursts (QPSBs; red squares). This diagram defines starbursts and QPSBs only, as galaxies lying above the upper horizontal line and below the lower horizontal line; FPSBs and OPBS are defined by the next figures. The definition for each class is given in §3 and the number of galaxies in each class is indicated on the plot. The histograms show distributions of the Hα EW for star-forming galaxies with well-measured emission lines (shaded sky-blue histogram) and the parent sample. As shown by the blue curve, the distribution of Hα EW for star-forming galaxies is well fit by a log-normal distribution with $\mu = 1.5$ and $\sigma = 0.35$. We define starbursts as objects with $W_{H\alpha,dc} > 175$Å, which is more than $2\,\sigma$ from the mean.

definition of post-starburst can be improved on to include emission line galaxies (AGN or star-forming post-starbursts).

The grey points in the figure represent all galaxies in the parent sample. For the majority of galaxies, $W_{H\alpha,dc}$ and $W_{H\delta}$ are well-correlated with some scatter. Normal[4] star-forming galaxies form an elongated concentration above $W_{H\alpha} \gtrsim 10$Å and $W_{H\delta} \gtrsim 2$Å while quiescent galaxies clump below $W_{H\alpha,dc} \lesssim 3$Å,and $W_{H\delta} \lesssim 1$Å. Galaxies undergoing starburst or rapid quenching move vertically in this diagram (e.g., Shioya et al., 2001; Quintero et al., 2004). Galaxies undergoing strong starburst lie above the star formation sequence, while recently quenched post-starbursts lie below the sequence.

We define quenched post-starbursts as galaxies with $W_{H\alpha,dc} < 3$Å and $W_{H\delta} > 4$Å. We consider only QPSBs with well-measured $W_{H\delta}$ (SNR > 3) and $W_{H\alpha}$ (contaminants with bad Hα equivalent width measurements due to spectral gaps around Hα are excluded). QPSBs are denoted by (red) squares and are found in the lower-right corner of Figure 2.3. The (blue) stars in the top-right corner represent the starburst galaxies selected in the previous subsection ($W_{H\alpha,dc} > 175$Å). A large gap exists between starbursts and QPSBs, which must contain many transiting objects if the basic picture of aging starbursts in this chapter is correct. Identifying these transiting post-starbursts is the next goal of this chapter. The (green) circles and the (brown) Xs represent the two types of transiting post-starbursts that are found in the next subsection.

[4]The adjective "normal" is used throughout the chapter to describe galaxies that have not undergone a large burst ($> 10\%$) of star formation recently (< 1 Gyr).

2.3.4 Transiting Post-starbursts (TPSB)

This subsection will describe our two ways of identifying TPSBs. Because of its similarity to that of previous works, the selection of FPSBs is described first for convenience, but FPSBs actually come after the OPSBs in time.

2.3.4.1 Fading Post-starbursts (FPSB)

Figure 2.3 illustrates the point made in the introduction that it is difficult to identify the transiting post-starburst population without additional constraints because they mostly overlap in this figure with the normal (non-bursty) star-forming galaxy sequence. However, it is possible to find these transiting objects by using other combinations of colors and spectral indices. For this purpose, Figure 2.4 shows 2D projections of the 3D parameter space defined by the 4000Å break, $D_n(4000)_{\rm dc}$, $\rm W_{H\delta}$, and $\rm (NUV\text{-}g)_{dc}$.

$D_n(4000)_{\rm dc}$ and $\rm W_{H\delta}$ are often used to distinguish recent star formation histories dominated by bursts from those that are more continuous (Kauffmann et al., 2003a; Martin et al., 2007; Wild et al., 2007). $D_n(4000)$, probes the mean temperature of the stars responsible for the continuum and is a good indicator of mean stellar population age (Bruzual A., 1983; Kennicutt, 1998; Balogh et al., 1999). It is also much less sensitive, but not impervious, to dust effects (MacArthur, 2005). We correct for (possibly small) dust effects on $D_n(4000)$ using the average attenuation in the narrow wavelength range in which it is defined.

The $\rm (NUV\text{-}g)_{dc}$ color is sensitive to young massive stars and as a result it evolves rapidly in rapidly quenching galaxies. It provides an additional lever arm that can be used to cleanly separate galaxies that are rapidly quenching from the

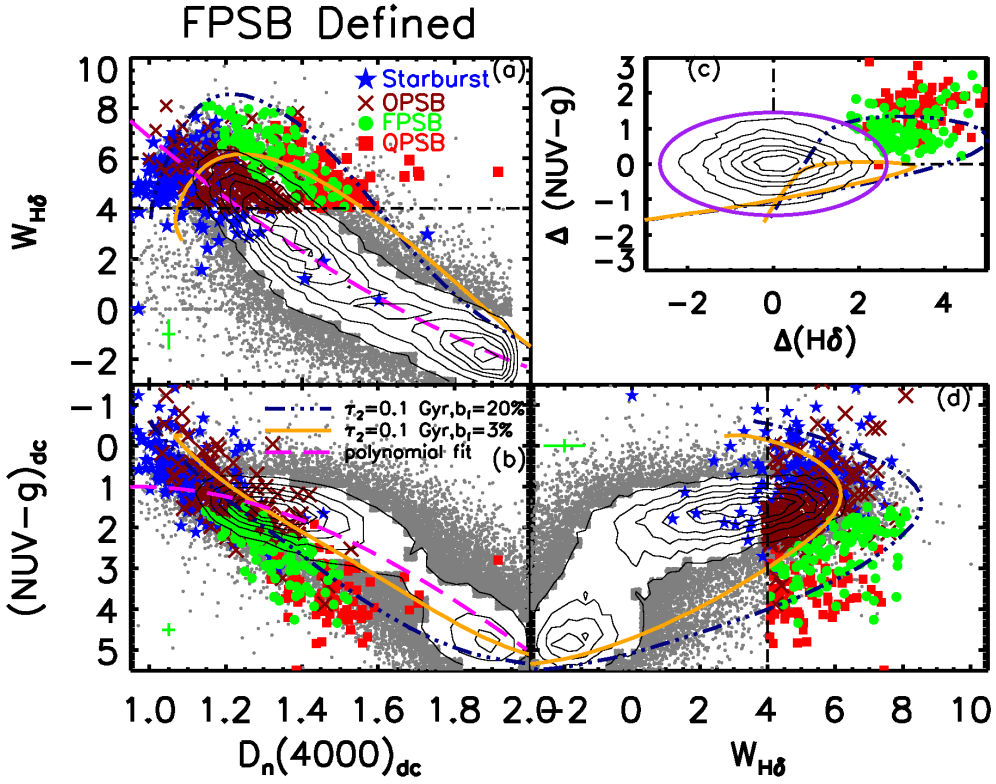

Figure 2.4:. The co-joined plots show the relation among dust-corrected $D_n(4000)$, $W_{H\delta}$ and dust-corrected NUV-g color for galaxies in the parent sample (grey), starbursts (blue stars), obscured post-starburst (OPSB; brown Xs), fading post-starbursts (FPSB; green circles), and quenched post-starbursts (QPSB; red squares). The (magenta) dashed curves in panel a and panel b are the polynomial fits to the main galaxy sequence (these are fits to the data, not burst models). The (dark blue) dash-dotted curve and the solid (orange) curve are BC03 burst tracks with a star formation timescale, $\tau_2 = 0.1$ Gyr and a burst mass fraction (b_f) 3% or 20%. Panel c shows the difference in $W_{H\delta}$ and $(NUV-g)_{dc}$ from the polynomial fit at a given $D_n(4000)$. The FPSBs are selected if they are found in the upper right corner and outside the (purple) ellipse, which encloses normal galaxies at the $> 2\,\sigma$ level. The typical errors in each panel for transiting post-starbursts are shown as green crosses.

general star-forming population. The fact that $(\text{NUV-g})_{\text{dc}}$ color is an integrated galaxy-wide photometric quantity also makes it complementary to $D_n(4000)_{\text{dc}}$ and $\text{W}_{\text{H}\delta}$, which are spectroscopic quantities measured within a $3''$ aperture and therefore may not be representative values of the entire galaxy. We select the fading post-starbursts as galaxies that are outliers from normal galaxies in $(\text{NUV-g})_{\text{dc}}$ and $\text{W}_{\text{H}\delta}$ at a given $D_n(4000)_{\text{dc}}$.

As shown in Figure 2.4a, $D_n(4000)_{\text{dc}}$ and $\text{W}_{\text{H}\delta}$ are well-correlated for normal galaxies with smooth SFHs. Galaxies with bursty histories are found off the main relation, as shown by the (orange and navy) curved BC03 model tracks, which represent bursty SFHs. The (magenta) dashed curve across the main sequence denotes the fourth order polynomial fit to the normal data (see Appendix 5.1.3 for more information).

Figure 2.4b plots dust-corrected $(\text{NUV-g})_{\text{dc}}$ color versus $D_n(4000)_{\text{dc}}$. In this figure, two clouds of points are visible for normal galaxies, the blue cloud of young star-forming galaxies to the upper left, and the quenched old and red galaxies to the lower right. The (magenta) dashed curve across the two clouds again denotes the fourth order polynomial fit to the normal data (see Appendix 5.1.3). Galaxies with bursty star formation histories deviate off the main relation to the lower left.

In both Figures 2.4 a & b, the starbursts and the quenched post-starbursts are located at the extrema of the burst tracks. SBs are found at the tip of the blue cloud, with very blue $(\text{NUV-g})_{\text{dc}}$ color, low $D_n(4000)_{\text{dc}}$ and relatively high $\text{W}_{\text{H}\delta}$. Likewise, QPSBs are also located off the main relation for normal galaxies, with very red $(\text{NUV-g})_{\text{dc}}$ color, intermediate $D_n(4000)_{\text{dc}}$ and relatively high $\text{W}_{\text{H}\delta}$. The FPSBs are located in the intermediate region between starbursts and quenched

post-starbursts in both figures. Hence, both $(\text{NUV-g})_{\text{dc}}$ and $W_{\text{H}\delta}$ are useful to identify this population.

FPSBs are selected quantitatively as objects that are more than $2\,\sigma$ outliers from normal galaxies in $(\text{NUV-g})_{\text{dc}}$ and $W_{\text{H}\delta}$. This is illustrated in Figure 2.4c, which depicts the difference in $(\text{NUV-g})_{\text{dc}}$ color, Δ(NUV-g), and the difference in Hδ equivalent width, $\Delta(\text{H}\delta)$, from the polynomial fit values at a given $D_n(4000)$. The FPSBs are indicated by the (green) circles. The (purple) ellipse encloses most normal galaxies at the $2\,\sigma$ level. Thus, FPSBs are selected to be well outside the normal galaxy locus (defined by the purple ellipse) with well-measured Δ quantities ($\Delta(\text{H}\delta)/\sigma(\text{H}\delta) > 3$ and Δ(NUV-g)/σ(NUV-g)> 3, the σs denoting the measurement errors of Hδ and NUV-g). This method of selecting post-starbursts recovers almost all of the quenched post-starbursts from Figure 2.3 and identifies many FPSBs ($N \sim 105$). By using $(\text{NUV-g})_{\text{dc}}$ color as an additional selection criterion, specifically by requiring Δ(NUV-g)> 0, a large number of contaminants ($N \sim 50$) are removed. A significant number of these contaminant galaxies show color gradient (have red centers but blue outer parts) and are (edge-on) disk galaxies.

In Figure 2.4d we plot $(\text{NUV-g})_{\text{dc}}$ color versus $W_{\text{H}\delta}$, a variant of Figure 2.3 in which $W_{\text{H}\alpha,\text{dc}}$ is replaced by $(\text{NUV-g})_{\text{dc}}$ color. The overall trends of this figure and Figure 2.3 are similar. We previously used Δ(NUV-g) and $\Delta(\text{H}\delta)$ in our selection because a starburst will cause these deviations in this diagram. By construction, the FPSBs do not overlap with normal galaxies in this diagram. There is also minimum overlap in Figure 2.4a, and the overlap in Figure 2.4b is a projection effect. The selection in 3D space cleanly separates FPSBs because it

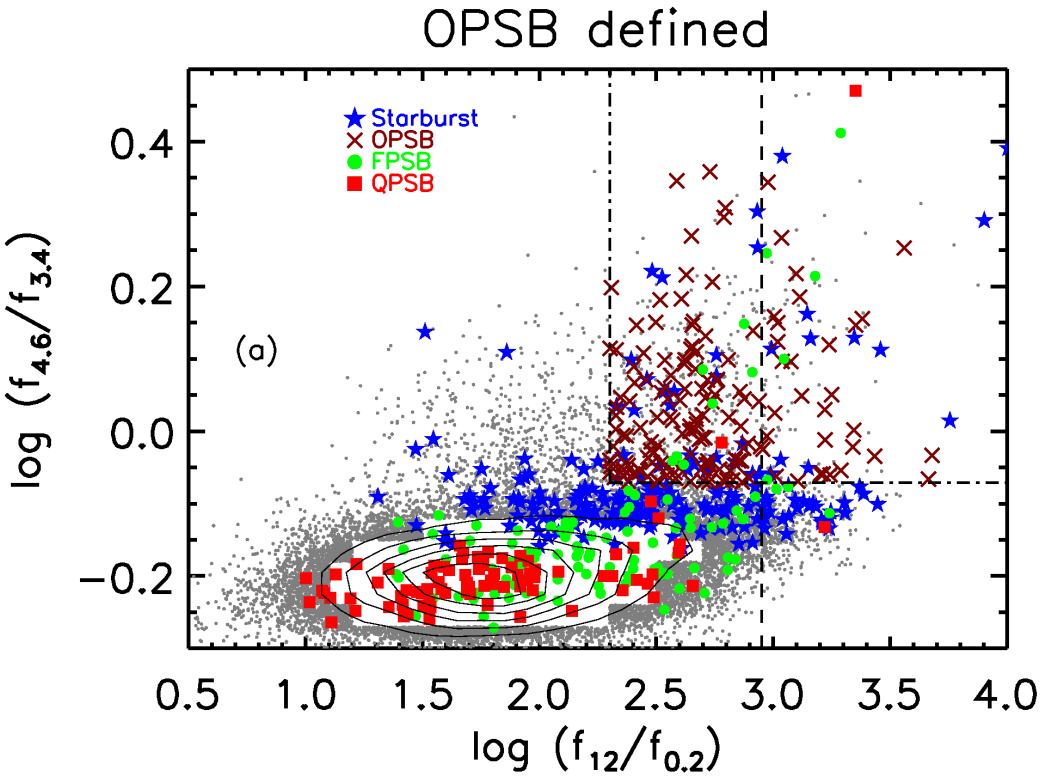

Figure 2.5:. The flux density ratio between WISE 12 μm and GALEX NUV, $f_{12\mu m}/f_{0.2\mu m}$, versus the ratio of WISE 4.6 μm to WISE 3.4 μm. The $f_{12\mu m}/f_{0.2\mu m}$ ratio quantifies the amount of obscured star formation versus unobscured star formation while the $f_{4.6\mu m}/f_{3.4\mu m}$ ratio quantifies hot dust emission from an AGN or a starburst. We define obscured post-starbursts (OPSBs) as galaxies in the upper right box and with $W_{H\delta} > 4$Å. Many of the previously-selected starbursts (69%) and fading post-starbursts (45%) are as obscured as OPSBs, even though this previous selection may be biased against obscured galaxies. We will later show these obscured post-starbursts galaxies have similar properties as the fading post-starbursts. The dashed vertical line denotes the boundary for local DOGs (Hwang & Geller, 2013).

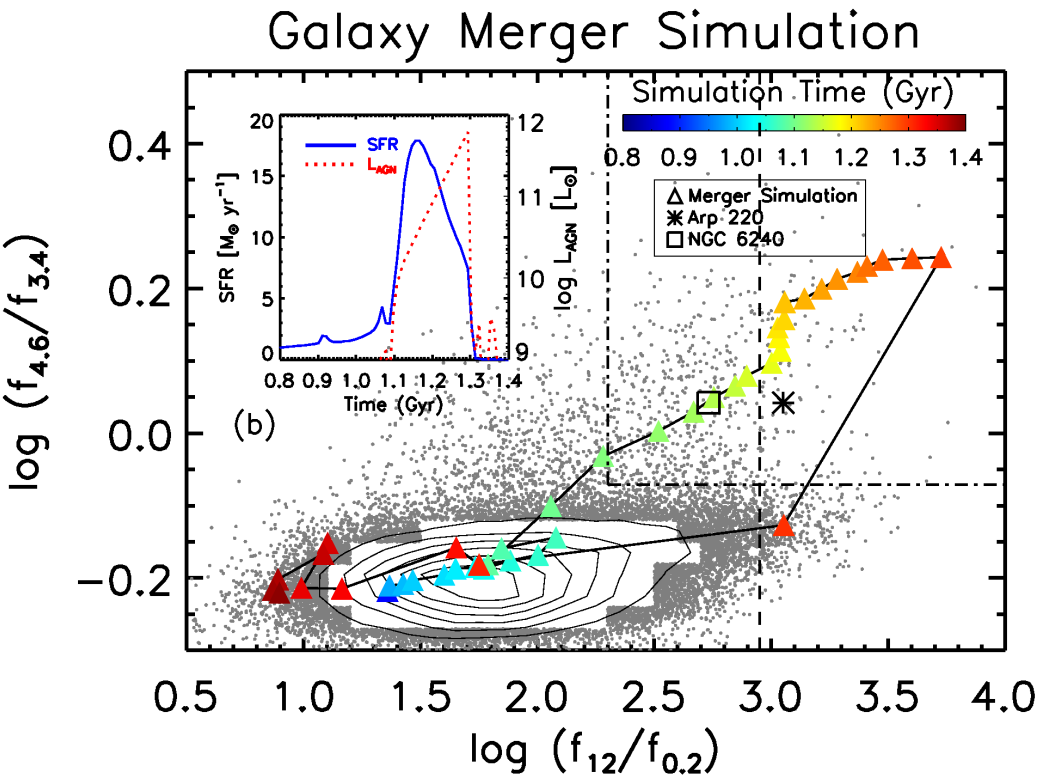

Figure 2.6:. The evolutionary path of a simulated merger-induced starburst. The merger model (triangles colored-coded by time since the start of simulation) shows that starbursts pass through the DOG phase which coincides with AGN activity. Two classic dust-obscured AGN, Arp 220 and NGC 6240, are shown for a reference. The inset plot shows that star formation declines before the peak of AGN activity.

removes contaminants that are offset from normal galaxy in Figure 2.4a but not Figure 2.4d. Perhaps the offset of these contaminants in Figure 2.4a is due to the fiber effect of SDSS spectra.

The selection of the TPSBs employed so far only identifies objects that are significantly offset from the normal galaxy locus and therefore misses a subset that overlaps with the normal galaxies (or those whose colors and spectral indices are not well-measured). This is evident from the small gaps between the SBs and the FPSBs in Figure 2.3 & 2.4. The next subsection will describe how some of these missing objects are identified.

2.3.4.2 Obscured Post-starbursts (OPSB)

As discussed in the introduction, we aim to test the merger-driven evolutionary framework for post-starbursts. Theoretically, it is thought that major mergers naturally result in highly dust-obscured galaxies (Hopkins et al., 2006; Jonsson et al., 2006; Chakrabarti et al., 2008; Narayanan et al., 2010; Hayward et al., 2012). Since PSBs are believed to be the results of such mergers (Hopkins et al., 2006, 2008; Bekki et al., 2001, 2005; Snyder et al., 2011), it is plausible that they exist in dust-obscured phase as they quench (Poggianti & Wu, 2000; Bekki et al., 2001; Shioya et al., 2001). Thus, we search for dust-obscured objects in our sample that likely bridge the gap between SBs and FPSBs. These objects have similar spectral indices and near UV colors as normal galaxies and therefore could not be identified in the previous section.

Figure 2.5 plots the flux density ratio between WISE 12 μm and GALEX NUV, $f_{12\mu m}/f_{0.2\mu m}$ versus the ratio of WISE 4.6 μm to WISE 3.4 μm. The $f_{12\mu m}/f_{0.2\mu m}$

ratio roughly quantifies the amount of obscured versus unobscured star formation (Narayanan et al., 2010; Hwang & Geller, 2013). We consider galaxies with $f_{12\mu m}/f_{0.2\mu m} > 200$ as significantly dust-obscured (cf. Narayanan et al., 2010). Local DOGs have $f_{12\mu m}/f_{0.2\mu m} > 892$ (Hwang & Geller, 2013). According to our definition, 69% of the starbursts, 45% the FPSBs and the 20% QPSBs are significantly dust-obscured. Likewise, 20% of the starbursts and 8% of the FPSBs are classified as DOGs. In comparison, only about 13% of galaxies in the parent sample are significantly dust-obscured and only 0.8% are DOGs.

The fact that starbursts and post-starbursts selected thus far are significantly more dust-obscured than normal galaxies provides further motivation to select the second class of transiting post-starbursts using Figure 2.5. We define the obscured post-starbursts (OPSBs) as galaxies with $W_{H\delta} > 4$Å, $f_{12\mu m}/f_{0.2\mu m} > 200$ and $f_{4.6\mu m}/f_{3.4\mu m} > 0.85$ (the median value for SB is 0.8). Note that 20% of the OPSBs are DOGs.

As further confirmation of the OPSB selection, Figure 2.6 shows how a simulated major merger evolves in the $f_{4.6\mu m}/f_{3.4\mu m}$ vs. $f_{12\mu m}/f_{0.2\mu m}$ plot. The inset in this figure shows the time evolution of the star formation rate and AGN luminosity near the time of coalescence of the galaxies (at $\sim$ 1.13 Gyr). As the galaxies coalesce, a strong starburst is induced. Simultaneously, the AGN luminosity increases rapidly as the black hole particles accrete gas. Because most of the gas in the galaxies is consumed or heated (by shocks and AGN feedback) during the starburst, the star formation rate rapidly decreases. The AGN continues to accrete for $\sim$ 100 Myr after star formation is terminated because the gas inflow rate needed to sustain the black hole accretion is $\leq 0.1 M_{\odot}$ yr^{-1}, which is orders

of magnitude less than the star formation rate during the starburst. Dynamical effects can also cause a delay between the maxima in the star formation rate and black hole accretion rate (Hopkins, 2012). Note that gas consumption, not AGN feedback, is the dominant cause for the termination of the simulated starburst. The effect of the AGN feedback in the simulation is to further reduce the post-starburst star formation rate and expel the remaining gas and dust in the nuclear region (Hayward et al., 2014a; Snyder et al., 2011).

2.4 AGN and Their Connection to PSBs

Having identified plausible candidate galaxies on the evolutionary pathway from starburst to quenched post-starbursts, we now explore the possible connection between AGN activity and quenching in these objects. The tight correlation between masses of galactic center super-massive black holes (SMBH) and properties of host galaxy bulges (e.g., Magorrian et al., 1998; Ferrarese & Merritt, 2000; Tremaine et al., 2002) imply that galaxy evolution and SMBH accretion occur in a long history of coupled growth and regulation (but see Kormendy & Ho (2013) for a contrarian perspective on co-evolution). Many semi-analytical models and theoretical simulations require AGN feedback to quench star formation and correctly predict the observed color bi-modality of galaxies and the shape of the galaxy luminosity function (e.g., Kauffmann & Haehnelt, 2000; Croton et al., 2006; Hopkins et al., 2006; Somerville et al., 2008; Gabor et al., 2011).

The rapid quenching of post-starburst galaxies makes them the ideal test-bed for AGN feedback models (e.g., Hopkins et al., 2006; Snyder et al., 2011; Cen, 2012). With our samples spanning the whole post-starburst evolutionary path,

we quantify the fraction of AGN hosts among post-starbursts and their properties (stellar population age, AGN strength, dust properties, etc). These quantities may help us infer whether AGN are primarily responsible for quenching starbursts or not.

2.4.1 Optical AGN diagnostics

In Figure 2.7a, we show the BPT diagnostic using the O III/Hβ and N II/Hα line ratios (Baldwin et al., 1981; Veilleux & Osterbrock, 1987). The position of an object in this diagram depends on its nebular metallicity and the hardness of its radiation field. Thus, the BPT diagram distinguishes between emission lines from H II regions and AGN. AGN-dominated galaxies have larger O III/Hβ and N II/Hα ratios and occupy the upper right part of the diagram, while the softer ionization of H II regions means star-forming galaxies occupy the lower left.

The dashed (magenta) curve demarcates the theoretical boundary for extreme starbursts, and galaxies above this curve probably host AGN (Kewley et al., 2001). The solid (orange) curve demarcates the empirical lower boundary for AGN (Kauffmann et al., 2003c). Objects below this curve are likely "pure" star-forming galaxies. Galaxies between the boundaries of extreme starbursts and "pure" star formation are thought to be mostly composites of star formation and AGN, although some have argued that unusual ionization in H II regions can lead to starbursts without AGN lying in the composite region (e.g., Brinchmann et al., 2008). Similarly, galaxies in the AGN region may also have some star formation contribution, but their ionization state is dominated by the AGN.

The starburst galaxies are distributed over the star-forming and composite

regions (25%) of the diagram and only 3% are AGN. On the other hand, almost all (93%) of the quenched post-starburst galaxies with well-measured emission lines lie in the AGN region of the BPT diagram (cf. Yan et al., 2006). This might indicate weak AGN, although there is some evidence that photo-ionization in weak emission-line galaxies such as QPSBs can also be produced by shocks or post-asymptotic giant branch stars (Ho, 2008; Cid Fernandes et al., 2011; Yan & Blanton, 2012; Singh et al., 2013). For instance, Cid Fernandes et al. (2011) have found that the ionization in galaxies with (dust-extincted) $W_{H\alpha} < 3$Å can be sufficiently accounted for by ionization from hot evolved stars without invoking AGN. The authors classified AGN into Seyferts or Low Ionization Narrow Emission Region (LINER) galaxies if they have $\log(\text{N II}/\text{H}\alpha) > -0.4$ and $W_{H\alpha} > 6$Å or $\log(\text{N II}/\text{H}\alpha) > -0.4$ and $3\text{Å} \leq W_{H\alpha} \leq 6\text{Å}$ respectively. QPSBs are defined as objects with $W_{H\alpha,dc} < 3\mathring{A}$ and accordingly they are not LINERs, but they are LINER-like (objects above the starburst boundary of (Kewley et al., 2001) and with $W_{H\alpha,dc} < 3\mathring{A}$).

The OPSBs and FPSBs bridge the starbursts and QPSBs. This is consistent with our evolutionary path from starburst to transiting to quenched post-starburst galaxies, with star formation decreasing along the sequence as AGN emerge. 53% of the FPSBs and 37% OPBSs are AGN while about 16% FPSBs and 49% of OPSBs are composite. Therefore, about 36% and 35% of transiting PSBs are AGN and composites respectively. In comparison, only 10% and 32% of normal galaxies in the parent sample with $W_{H\alpha,dc} > 3$Å are AGN and composites respectively.

Figure 2.7b presents the AGN fraction in transiting post-starbursts using a bar chart. It subdivides the (BPT) AGN into Seyferts and LINERs if they have

$W_{H\alpha,dc} > 6$Å or 3Å $\leq W_{H\alpha,dc} \leq 6$Å respectively. Seyferts are about 5 times more common in transiting post-starburst galaxies than in normal galaxies in our chosen mass range. LINER-like objects are shown in the figure for completeness, but our estimate of AGN fraction in PSBs does not include such objects.

2.4.2 A time delay between AGN and starbursts

In this subsection, we quantify the time delay between the starburst and AGN phase.

Figure 2.8 shows the distribution of $(\text{NUV-g})_{dc}$ color and $D_n(4000)_{dc}$ (i.e, observable proxy for age) of starbursts and AGN in transiting post-starbursts. The $(\text{NUV-g})_{dc}$ color and $D_n(4000)_{dc}$ of TPSBs are significantly offset to higher values (older age) compare to values of starburst. The Kolmogorov-Smirnov test (K-S test) indicates that the null hypothesis that the $(\text{NUV-g})_{dc}$ color and $D_n(4000)_{dc}$ of starbursts and TPSBs come from the same distribution (i.e, the two population are coeval) can be rejected at $\alpha < 0.001$ significance level.

Furthermore, Figure 2.9 shows the z band-normalized median and quartile SEDs of galaxies evolving from the starburst to quenched post-starburst phase. We overplot BC03 models with SFR timescale, τ_2, of 100 Myr and burst mass-fraction b_f of 20% at different ages in order to indicate the time after the second burst. This ballpark estimate shows that the median age of OPSBs is about 400-500 Myr and there is $\gtrsim 200$ Myr gap between the median age of starbursts and the AGN hosts among TPSB. Because of the burst mass-age degeneracy, the ages of the post-starbursts depends on the decay timescale (τ_2) assumed. As shown in Appendix 5.1.2, models tracks with $\tau_2 = 0.05 - 0.2$ can describe the

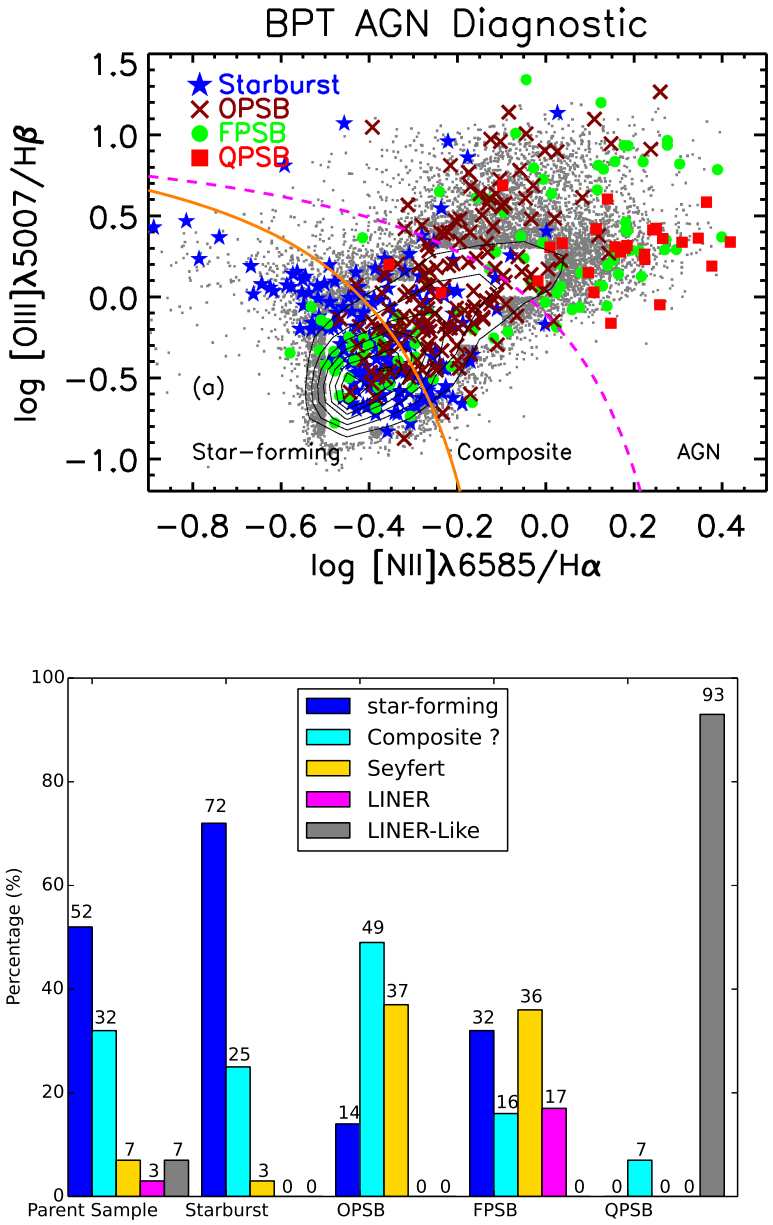

Figure 2.7:. Panel (a) shows the BPT emission-line ratio AGN diagnostic for the parent sample, starbursts and PSBs whose emission lines are detected with SNR > 3. The (magenta) dashed curve denotes the theoretical boundary for extreme starbursts (Kewley et al., 2001) while the solid (orange) curve denotes the empirical boundary of pure star-forming galaxies (Kauffmann et al., 2003c). The diagram shows that the QPSBs have LINER-like emission while TPSBs have both star formation and AGN-dominated emission line ratios. The latter smoothly bridge the starbursts and the QPSBs. Panel (b) shows the percentage of AGN in starbursts, post-starbursts and galaxies in the parent sample. LINERs are objects in AGN region of the BPT diagram with 3Å $\leq W_{H\alpha} \leq$ 6Å while LINER-like objects are the corresponding objects with $W_{H\alpha} <$ 3Å.

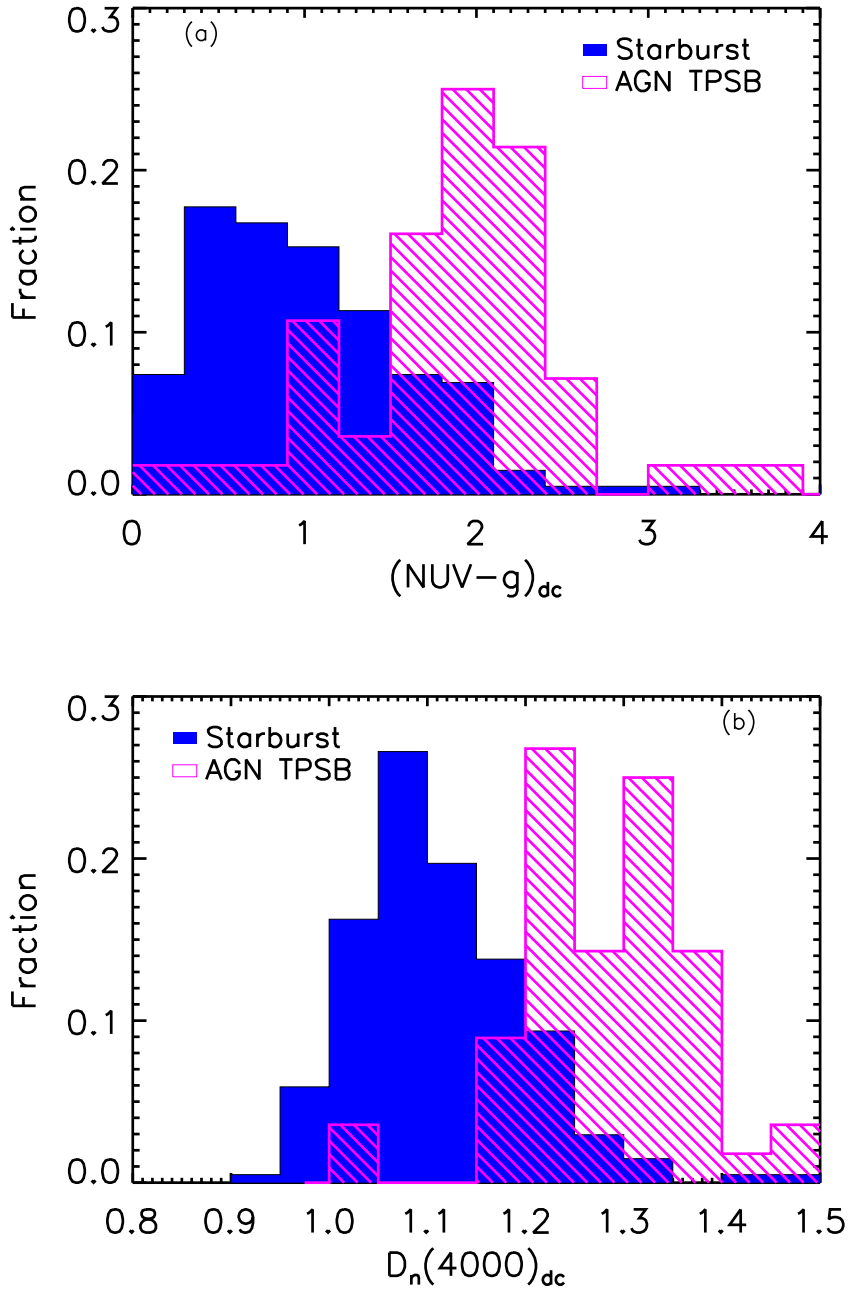

Figure 2.8:. The distributions of (NUV-g)$_{\rm dc}$ color and $D_n(4000)_{\rm dc}$ for starburst galaxies and transiting PSB with AGN. The offset between the peaks indicates that the two population are not coeval, with peak AGN activity appearing considerably after the peak star formation activity.

starburst to post-starburst evolution while models with τ_2 outside this range are excluded since they would not produce the observed population of post-starburst galaxies (cf. Wild et al., 2010). Therefore, in agreement with the findings of several recent observational works (e.g, Davies et al., 2007; Bennert et al., 2008; Schawinski et al., 2009a; Wild et al., 2010), the time delay might range between $100 - 400\,\mathrm{Myr}$ depending on the assumed τ_2.

The significance of this time delay is that it strongly suggests that AGN do not directly quench starbursts. Recent theoretical works are converging to a view that, in merger-fueled post-starburst evolution, AGN may play a secondary or limited role in quenching (Croton et al., 2006; Wild et al., 2009; Snyder et al., 2011; Cen, 2012; Hayward et al., 2014a). In other words, a post-starburst results from exhaustion of a bulk of its gas supply in a starburst and/or from its expulsion by stellar feedback; AGN feedback mainly reheats or ejects the remaining gas that would otherwise fuel low-level star formation over the next few billion years.

In particular, Cen (2012) proposed a new evolutionary model of galaxies and their SMBH. In this model, starbursts and AGN are not coeval and AGN do not quench starbursts. They argued that the main SMBH growth occurs in the post-starburst phase, fueled by recycled gas (cf. Scoville & Norman, 1988; Ciotti & Ostriker, 2007; Wild et al., 2010; Hopkins, 2012) from aging stars in a self-regulated fashion on a timescale that is substantially longer than 100 Myr. Our analysis supports the Cen (2012) model in that AGN are more frequent in post-starbursts and they appear significantly delayed from the starbursts phase. But as we will show later, we do not find observational support for the model's prediction that a substantial ($\times 10$) black hole growth occurs in the post-starburst phase

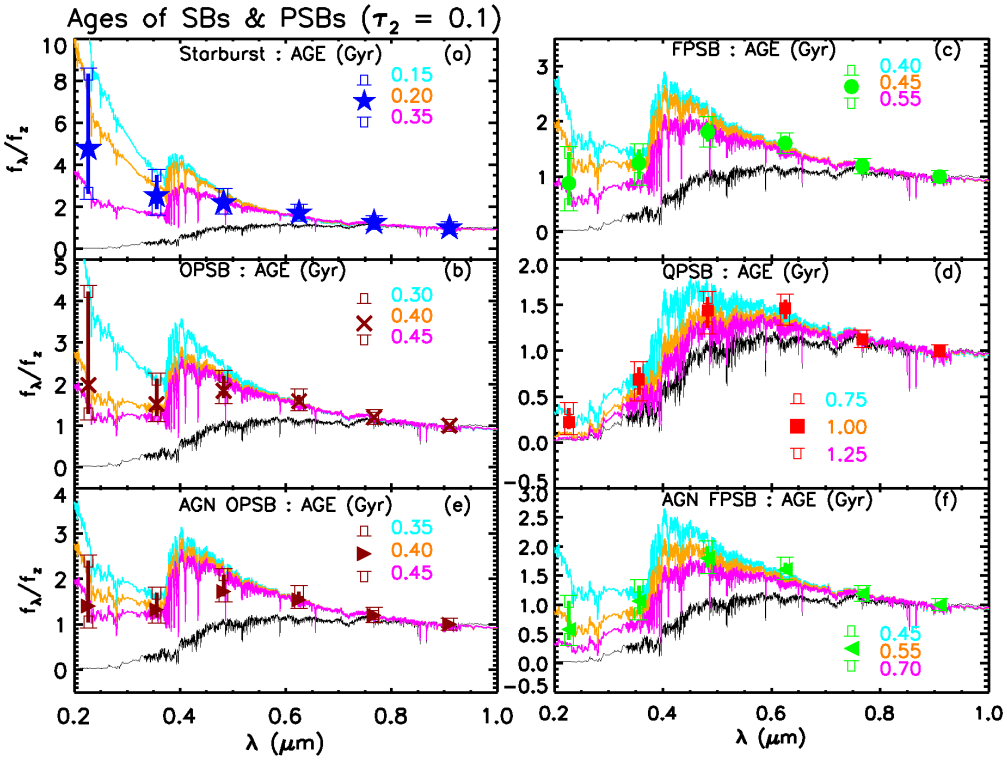

Figure 2.9:. The z band-normalized median and quartile fluxes at the effective wavelengths of the NUV, u, g, r, i, z bands (the flux ratios are dust-corrected). The (cyan, orange and magenta) overplotted spectra are Bruzual & Charlot (2003) burst models with SFR timescale $\tau_2 = 0.1$ Gyr and burst fraction $b_f = 20\%$ of different ages, as indicated on each panel. The lowest (black) spectrum in each panel is that of a 12.5 Gyr old galaxy (before the burst). The model spectra are not actual fits to the data but are chosen to be approximately consistent with the data. Galaxies follow an age sequence from starbursts (panel a) to obscured PSBs (panel b) to fading PSBs (panel c) to quiescent PSBs (panel d). It is also notable that the SEDs of transiting PSBs hosting AGN (panels e and f) are significantly older than the starbursts, indicating a ∼200 Myr delay between a starburst and the appearance of an AGN. This indicates that the AGN is not the primary source of quenching in starbursts.

compared to the starburst phase.

2.4.3 Dust properties of AGN host

In Figure 2.5, we showed that more than two-thirds of starbursts and more than a third of FPSBs are significantly more dust-obscured compared to normal star-forming galaxies. We also identified heavily dust-obscured PSBs that precede the FPSBs. Therefore, our finding that quenched post-starbursts were once heavily dust-obscured, and that some dust-obscured AGN are likely post-starbursts, is consistent with the later removal of obscuring gas and dust by AGN feedback. However, beyond this consistency, there is no clear observational evidence yet that AGN clear away the remaining gas and dust in post-starburst galaxies (e.g., Tremonti et al., 2007; Coil et al., 2011). Therefore, future study of post-starburst with strong AGN identified in this work, may provide further clues on the (secondary) role of AGN and its relationship with its host galaxy. As presented in Chapter 3, we have done a follow up of AGN identified in this chapter and we find a compelling evidence that AGN are responsible for the destruction molecular gas in later stage Seyfert post-starbursts.

Figure 2.10 shows the distribution of V-band nebular attenuation A_V for normal star-forming galaxies, starbursts and transiting post-starbursts. SBs and AGN in TPSB have higher dust attenuation ($A_V = 2.7 \pm 3.4$ and $A_V = 2.2 \pm 0.9$ respectively) than normal star-forming galaxies ($A_V = 1.6 \pm 0.7$). K-S test indicates that the null hypothesis that the A_V distribution of SBs or AGN TPSBs come from that of normal star-forming galaxies can be rejected at 3σ ($\alpha < 0.001$) significance while A_V distribution of SBs and AGN TPSBs are similar only at

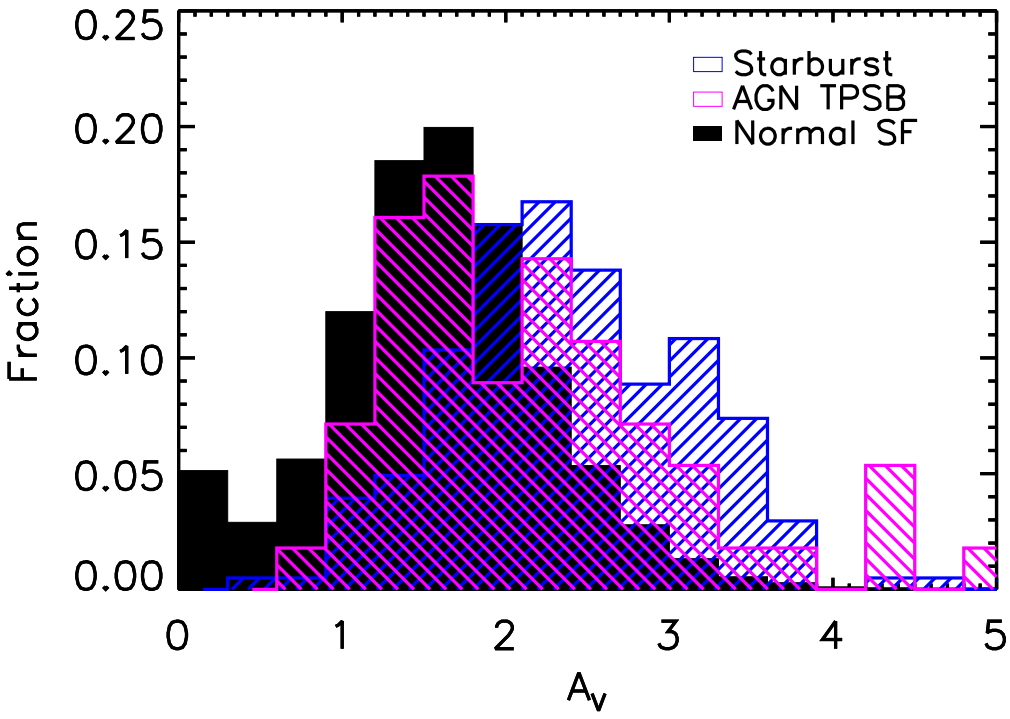

Figure 2.10:. The distribution of V-band nebular attenuation A_V for normal star-forming galaxies, starbursts and AGN in transiting post-starbursts.. The continuum attenuation are approximately half the nebular attenuation. The AGN hosted by TPSBs are significantly less dusty than the starbursts, consistent with the removal of dust by AGN feedback.

$\alpha \lesssim 0.05$. This observation is consistent with a removal of dust by AGN feedback.

So far we have shown: 1) Starbursts and post-starbursts are likely more dust-obscured than normal star-forming galaxies. The starburst to quenched post-starbursts evolutionary sequence is a decreasing dust sequence. 2) AGN are about three times more common in transiting post-starbursts than in normal galaxies. However, we found, similar to previous works, that there is a significant time delay between starburst and the peak of AGN activity in both obscured and fading post-starbursts.

2.4.4 Broad-Line AGN (BLAGN)

Special techniques are often required to disentangle AGN and galaxy emission in BLAGN host galaxies. Trump et al. (2013) have recently used SDSS aperture photometry and z band concentration index to disentangle the light of broad-line AGN and their host galaxies. By doing so, they have assembled a large sample of BLAGN with host galaxy colors and stellar mass measurements.

The selection criteria of post-starbursts discussed in previous subsections will not identify post-starbursts galaxies hosting BLAGN because their NUV fluxes and spectral indices are rendered immeasurable by the bright AGN. Nevertheless, to constrain how BLAGN fit in our starburst sequence, we select a subset of broad-line AGN from Trump et al. (2013) that have similar stellar mass and redshift range as the parent sample. The properties of these objects are discussed in Appendix 5.1.4 .

2.5 The bulge properties of PSBs and its necessity for quenching

The overall aim of this section is to provide a complimentary check on our sample selection by showing that the starbursts and post-starbursts are both bulge-dominated, unlike most normal star-forming galaxies. We show that their morphology is consistent with that of galaxies transitioning between blue and red galaxies. In a future work we will present other structural parameters that better discriminate between post-starbursts and the slowly quenching normal galaxies.

Figure 2.11a shows the relationship between the stellar mass surface density, μ_*, and the dust-corrected $(\text{NUV-g})_{\text{dc}}$ color. NUV-optical color and μ_* are known to trace gas consumption time and the change in SFH that takes place as galaxies transition from disc-dominated to bulge-dominated systems (Kauffmann et al., 2006; Catinella et al., 2010). Comparisons between stellar surface mass density and bulge-to-total ratio by Wild et al.(in preparation) shows that galaxies with $\mu_* > 3.0 \times 10^8\,\text{M}_\odot\,\text{kpc}^{-2}$ are classical bulge-dominated galaxies while ones with $1.0 \times 10^8\,\text{M}_\odot\,\text{kpc}^{-2} < \mu_* < 3.0 \times 10^8\,\text{M}_\odot\,\text{kpc}^{-2}$ are pseudo-bulges. About 67% (95%) of starbursts and 65% (91%) of post-starburst have $\mu_* > 6 \times 10^8\,(3 \times 10^8)\,\text{M}_\odot\,\text{kpc}^{-2}$. In comparison, only about 30% (68%) of normal star-forming galaxies have $\mu_* > 6 \times 10^8\,(3 \times 10^8)\text{M}_\odot\,\text{kpc}^{-2}$. K-S test also indicates that the distribution μ_* for starbursts and post-starbursts are significantly different from normal star-forming galaxies (they are drawn from same distribution at $\alpha \lesssim 0.001$). The compactness of large majority of starbursts and post-starbursts is consistent with the necessity of bulge build-up for quenching (Wuyts et al., 2011;

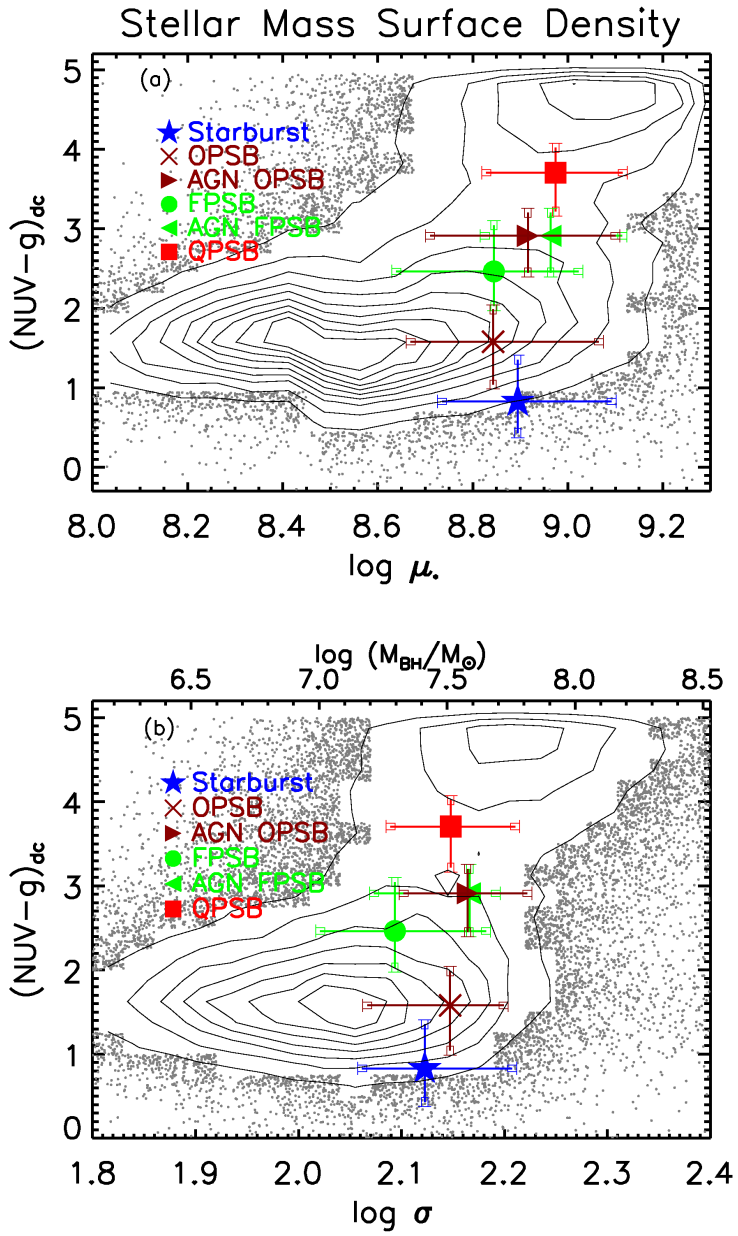

Figure 2.11:. The median and upper/lower quartile values of (NUV-g)$_{\rm dc}$ color versus stellar mass surface density in Panel (a) and (NUV-g)$_{\rm dc}$ color versus velocity dispersion in panel (b) are plotted. Starbursts and post-starbursts have similar morphology and they are offset from normal star-forming galaxies in mass surface density and velocity dispersion (i.e, have more prominent bulges). If we assume that velocity dispersion correlates with black hole mass following the $M_{BH} - \sigma$ relation from Tremaine et al. (2002), then there is little black hole growth from SBs to QPSBs, in contrast with the prediction of Cen (2012).

Bell et al., 2012; Cheung et al., 2012; Fang et al., 2013; Mendel et al., 2013).

Similarly, Figure 2.11b shows $(\text{NUV-g})_{\text{dc}}$ color as a function of the velocity dispersion, σ. The velocity dispersion is the best correlated parameter with galaxy color and star formation history (Wake et al., 2012; Fang et al., 2013). The $M_{\text{BH}}-\sigma$ relation (Magorrian et al., 1998) also means that velocity dispersion is a tracer of black hole mass: the upper x-axis in Figure 2.11b shows the inferred black hole mass using the Tremaine et al. (2002) relation.

The general galaxy population forms the blue cloud at lower velocity dispersions (median $\sigma = 108\,\text{km}\,\text{s}^{-1}$) and the red sequence at higher velocity dispersions (median $\sigma = 160\,\text{km}\,\text{s}^{-1}$). As expected for quenching/recently quenched galaxies, the starbursts and the three post-starbursts classes are located in the transition region between the blue cloud and the red sequence, at intermediate velocity dispersion ($\sigma \sim 125 - 140\,\text{km}\,\text{s}^{-1}$).

The SB to QPSB sequence is offset as a whole from the normal SFR galaxies by about a factor of two in black hole mass. However, from starburst to transiting to quenched post-starbursts, there is little or no black hole growth along the evolutionary sequence. This observation does not not support the prediction of substantial ($\times 10$) black hole growth in the post-starburst phase compared to the starburst phase (Cen, 2012).

In summary, we have shown that the three post-starburst classes are bulge-dominated unlike most normal star-forming galaxies. The fact both SBs and PSBs have similar morphology is independent evidence that these two populations are linked. Similarly, the fact FPSBs and OPSBs have structural properties that are fully consistent with each other supports that they are objects in the same

category despite their different selection criteria.

2.6 Discussion and Conclusion

2.6.1 Building the red sequence through post-starbursts

The quenching process happens in both slow and fast-mode (e.g., Cheung et al., 2012; Barro et al., 2013; Fang et al., 2013; Dekel & Burkert, 2014). We attempt to constrain the transit time and the fraction of galaxies evolving through the two modes of quenching using simple crude estimates. Assuming that the starbursts are triggered by mergers or by some other phenomenon that has a redshift dependence and using our thorough and fairly complete post-starbursts sample today, one can constrain how many of each kind of product evolved to the red sequence through the two quenching modes in the past 10 Gyr.

The number of galaxies in the parent sample is $\sim 67,000$ of which $\sim 40,400$ galaxies are located in the blue cloud, $\sim 14,700$ galaxies are in the red sequence and $\sim 11,900$ galaxies are in the green valley (see Figure 2.1b). If half of galaxies currently on the red sequence had under gone a dry major merger since $z \sim 2$ (Bell et al., 2006; Hopkins et al., 2010), accounting for galaxies that might have evolved out of the parent sample, a total of $\lesssim 22,000$ red sequence galaxies must have been in the parent sample since $z \sim 2$.

On the other hand, from Figure 2.3 the total number of post-starburst galaxies in the parent sample is 341. If we take the difference between the median age of SB and QPSB to be the quenching time or the transit time to the red sequence, this transit time is ~ 600 Myr for a star formation timescale of $\tau_2 = 0.1$ Gyr (as

shown Appendix 5.1.2, the transit time may range between 400-900 Myr). This suggests that about 570 galaxies per Gyr are currently moving to the red sequence through the post-starbursts path at the constant mass.

Theoretical models argue that post-starbursts are the end-products of galaxy mergers (Hopkins et al., 2006, 2008; Bekki et al., 2001, 2005; Snyder et al., 2011). Assuming a uniform merger (production) rate since $z \sim 2$ (last 10 Gyr), then the total production of post-starbursts in our adopted mass range would be about 5700 galaxies. This is about 40% of the galaxies on the red sequence in the parent sample today. The major-merger rate however is thought to increase with redshift roughly as $\propto (1+z)^{2-3}$ (Kartaltepe et al., 2007; Hopkins et al., 2010; Lotz et al., 2011). In this case, the transit rate through post-starbursts integrated to $z \sim 2$ gives $3-6$ times more post-starbursts than the estimate that assumes a uniform merger rate. Therefore, integrated over time post-starbursts are an important pathway to the red sequence. They can account for at least a quarter, and up to essentially all of the red sequence galaxies that are (were) in the parent sample.

At high redshifts, disk instability-induced starbursts may be more common than merger-induced starbursts (Bournaud et al., 2008; Dekel et al., 2009). Our estimate of post-starburst fraction above does not include post-starbursts that might have resulted from this mechanism. In addition, we also have not accounted for post-starbursts that host broad-line AGN (which we do not have a way of identifying). For these and other reasons, the total contribution of the post-starburst path over time to the build-up of the red sequence is certainly above 25%. Similarly, Wild et al. (2009) found that about 40% of the mass growth of the red sequence at $z \sim 1$ is likely due to galaxies passing through the post-starbursts

phase while Barro et al. (2013) found that almost all quiescent galaxies at $z \gtrsim 2$ are descendants of rapidly quenching compact star-forming galaxies.

If we conservatively assume that $\gtrsim 25\%$ of the red sequence galaxies in the parent sample (over the past 10 Gyr) descended from post-starbursts, we can constrain the transit time across green valley for slowly quenching galaxies. Excluding the ~ 5700 galaxies that might have descended from PSBs, about 16,300 out of the total of $\lesssim 22,000$ red sequence galaxies must have gone through the slow mode of quenching over the past 10 billion years. Assuming a constant transit time across the green valley (Faber et al., 2007), the fact that we currently observe $\sim 11,900$ slowly fading normal galaxies in green valley implies that the transit time through GV for the slow track is $\gtrsim 7\,\mathrm{Gyr}$. This lower limit is a factor of two higher than the transit time found by Martin et al. (2007). They estimated that slow fading blue galaxies take $\sim 3\,\mathrm{Gyr}$ to arrive in green valley, plus additional $\sim 3\,\mathrm{Gyr}$ to reach the red sequence. However, the $\sim 3\,\mathrm{Gyr}$ estimate of Martin et al. (2007) is strictly speaking a lower limit because it includes bursting and dust-extincted galaxies among green valley galaxies.

Moreover, even though PSBs may account for essentially all of the red sequence, the evidence for evolution via both the slow and fast track is indisputable. Previous studies suggest that nearly half of the red sequence galaxies have disk-like morphologies (e.g., Bundy et al., 2010; Cheng et al., 2011; van der Wel et al., 2011), indicating that the two modes of quenching are about equally important. Similarly, Fang et al. (2012) find that a non-negligible fraction of green valley galaxies have disk-like morphologies (Salim et al., 2012) and can remain in the GV for several Gyr, which both point to the slow mode.

Likewise, disks in quenched galaxies are not rare at high redshift despite the expected dominance of mergers then. Bundy et al. (2010) studied quiescent galaxies at $1 < z < 2$ and found that passive disks with typically Sa-Sb morphological types represent nearly one-half of all red sequence galaxies. Similarly, van der Wel et al. (2011) investigated morphology of massive, quiescent galaxies at $z \sim 2$. They estimate that more than 65% of these galaxies are disk dominated. At a similar redshift, Kocevski et al. (2012) found that moderate luminosity, X-ray-selected AGN do not exhibit a significant excess of distorted morphologies relative to a mass-matched control sample. About half of the AGN reside in galaxies with discernible disks. The observed high disk fraction in AGN hosts is hard to reconcile with the merger picture of AGN fueling discussed in § 2.1.

Despite its theoretical appeal, compelling observational evidence linking mergers with AGN activity has been elusive, with results in favor of (Silverman et al., 2011; Ellison et al., 2011; Liu et al., 2012) and against (Jahnke & Macciò, 2011; Cisternas et al., 2011; Kocevski et al., 2012; Schawinski et al., 2012; Villforth et al., 2014) this picture. There are several effects that make it difficult to identify the connection between AGN activity and mergers. One is the extreme dust obscuration that can be expected in such systems (Hopkins et al., 2006), making AGN detection challenging. The second is the significant time delay between the onset of the merger and the peak of the AGN activity. Because of this delay, the most obvious merger signatures may have faded by the time the merger remnant is identified as a bright AGN.

We have looked at mergers fraction in starbursts and post-starbursts in our sample. We entatively find that starbursts are more disturbed than normal star-

forming galaxies (the disturbance could be due to major or minor mergers). We visually classified about 30% the starbursts as merging or disturbed galaxies (they show either tidal tails or strong asymmetries or have close companions). In contrast, only about 3 % of 200 randomly selected normal star-forming galaxies show merger signatures. Likewise, according to the Galaxy Zoo classification (Lintott et al., 2011), which rather tend to be conservative in calling something a merger, about 10% of the starbursts have a weighted merger fraction $f_{\rm m} > 0.4$ while only 1% of normal star-forming galaxies have a weighted merger fraction above this value. The $f_{\rm m}$ is calculated by taking the ratio of the number of merger classifications for a given galaxy to the total number of classifications for that galaxy multiplied by a weighting factor that measures the quality of the classifiers that have classified the galaxy. Darg et al. (2010) have shown that almost all galaxies with $f_{\rm m} > 0.4$ are robust major mergers. However, we also find that merger signatures disappear after the starburst phase, and the transiting and quenched post-starburst galaxies in general are much smoother than the starbursts. We classify about 15% of TPSBs as as merging or disturbed galaxies and 6% have $f_{\rm m} > 0.4$. Perhaps the merger signature are washed out because of the substantial time lag between the starburst and the PSB (AGN) phases. Galaxy merger simulations estimate that major merger signatures have a timescale of 200–400 Myr (Lotz et al., 2010). Our estimated age of the transiting post-starburst phase ($\gtrsim 300\,$Myr) or the time delay between starbursts and AGN ($\gtrsim 200 \pm 100\,$Myr) is in accord with the timescale for the disappearance of merger signatures. The color gradient and metallicity of starbursts and PSB are also consistent with the merger origin of these galaxies (see Appendix 5.1.5 & 5.1.6).

The above tentative result supports that the fast-track, in local universe, is triggered by merger starbursts, whose signatures are washed out in the post-starbursts phase. We have also shown that velocity dispersion and global mass surface density are high, presumably from mergers, leaving post-starburst remnants which are smaller, more compact, and with high stellar surface mass density than non-bursty star-forming galaxies. However, despite their high velocity dispersion and global mass surface density, the post-starbursts still overlap in morphology with many slowly quenching galaxies. Future work will explore better morphological discriminants between the fast and slow mode (Yesuf et al., in preparation).

Deep high resolution studies of handful of K+A galaxies and post-starburst quasars however find significant morphological disturbances in these objects (e.g., Canalizo & Stockton, 2001; Bennert et al., 2008; Yang et al., 2008; Cales et al., 2011). Galaxies we classified as undisturbed using the SDSS images may have faint tidal features visible in deeper images. Therefore, deep high resolution studies with more robust measurements of merger signatures in transiting post-starburst galaxies will be useful to test merger origin of post-starbursts and to understand the AGN triggering mechanism in post-starbursts.

2.6.2 Conclusion and summary

The unique spectral properties of quenched post-starburst galaxies hint that these objects are recently quenched starbursts. We investigated this inferred relationship in detail by directly tracing them back to the starbursts through a newly identified population of "transiting" post-starbursts in the midst of quenching. We

showed that dust-obscured post-starbursts comprise the majority of the transiting post-starburst population.

With our new sample of post-starbursts, we studied the connection between quenching and AGN in post-starbursts. We found that AGN are more commonly hosted by post-starbursts than by normal galaxies. Post-starburst AGN hosts make up $\gtrsim 36 \pm 8\%$ of transiting post-starbursts. Despite the high frequency of AGN in post-starbursts, we found that the clear presence of AGN is significantly delayed from the peak of starbursts by $\gtrsim 200 \pm 100\,\mathrm{Myr}$.

As long as the AGN appearance is delayed, our results are generally consistent with "merger hypothesis" of post-starbursts (Hopkins et al., 2006; Snyder et al., 2011; Cen, 2012), where mergers between gas-rich galaxies drive nuclear inflows of gas thereby leading to nuclear starbursts, bulge formation, AGN activity, and eventually to quenched post-starbursts. In support of the merger hypothesis, we *tentatively* find that the starbursts are relatively metal-poor at earlier stages, exhibit clear merger signatures, and have shallower color gradients and prominent young bulges. On the other hand, consistent with the time delay, merger signatures disappear after the starburst phase and that our three post-starburst classes also have shallower color gradients and prominent young bulges.

We also showed that starbursts and transiting post-starbursts are significantly more dust-obscured than normal galaxies and quenched post-starbursts. The fact that starbursts and post-starbursts evolve through a heavily dust-obscured phase which also seems to coincide with AGN activity, is consistent with later removal of dust by AGN feedback. We therefore conclude that AGN may not *primarily* quench starbursts but may play an important role in quenching or

preventing low-level star formation in post-starbursts. We acknowledge that the large extent of the SDSS fiber beyond the nuclear region of a galaxy could be a major concern since the line ratios of an AGN may be diluted by on-going star formation inside the fiber. Future works with spatially resolved line ratios or with other AGN selection criteria unbiased by the host properties will hopefully provide a more definitive test on the time delay between the AGN phase and the starburst phase, and they will also help estimate the AGN fraction in post-starbursts more accurately than we have attempted in this work. Similarly, a more direct evidence on the role of AGN in removing a leftover gas and dust during the post-starburst phase may come to light from observations of TPSBs using new facilities such as ALMA.

Chapter 3

From Starburst to Quiescence: Rapid Evolution of Molecular Gas fraction in Local Seyfert, Post-starburst Galaxies, a compelling evidence for a delayed AGN feedback

3.1 Introduction

Despite extensive observational and theoretical studies, the physical mechanisms that regulate the star formation rates of galaxies are still poorly understood.

Star formation quenching, by yet unknown mechanisms, causes star-forming galaxies to migrate to the "red sequence" (Gladders et al., 1998; Faber et al., 2007). One likely such formation of mechanism of the red-sequence is the transformation of star forming, disk-dominated, gas-rich galaxies into early types via mergers and their associated feedback (Toomre & Toomre, 1972; Hopkins et al., 2006).

Post-starburst (PSB) galaxies are candidate post-merger objects, rapidly transitioning from the blue-cloud to the red-sequence (e.g., Dressler & Gunn, 1983; Couch & Sharples, 1987; Zabludoff et al., 1996; Wild et al., 2009; Snyder et al., 2011; Yesuf et al., 2014; Pawlik et al., 2016). In their quiescent phase, their spectra reveal little-to-no current star formation, but a substantial burst of star formation before an abrupt cessation $\sim$1 Gyr ago, long enough for the ionizing O&B stars to evolve away, but recent enough for A-stars to dominate the stellar light. Recent observational efforts have enlarged the traditional definition of post-starburst to include a more complete and less biased sample of galaxies with ongoing star formation or/and AGN activity (Wild et al., 2010; Yesuf et al., 2014; Alatalo et al., 2014). With the identification of this sample, which spans the entire starburst to quenched post-starburst evolutionary sequence, better constraints on theoretical models of galaxy evolution have started to emerge. One of the the firm constraints is the observed time delay between the starburst phase and the AGN activity by about 200 Myr (Wild et al., 2010; Yesuf et al., 2014). This time delay suggests that AGN are not primarily responsible in the original quenching of starbursts but may be responsible for keeping star formation at a low level by removing gas and dust during the post-starburst phase. The other emerging but contested constraint is the molecular evolution along starburst-AGN-quenched post-starburst

sequence (Schawinski et al., 2009b; Rowlands et al., 2015). This chapter aims to further examine the molecular gas evolution along this sequence using both new and existing data, and presents a unifying picture on this important constraint on galaxy evolution models.

In gas-rich model mergers, gas is funneled to galaxy centers, powering intense nuclear starbursts and obscured nuclear AGN activity. At the end of the starburst, the leftover gas and dust are cleared out due to feedback from the AGN (e.g., Sanders et al., 1988; Barnes & Hernquist, 1991; Silk & Rees, 1998; Di Matteo et al., 2005; Springel et al., 2005b; Kaviraj et al., 2007; Hopkins et al., 2006, 2008; Wild et al., 2009; Snyder et al., 2011; Cen, 2012). For instance, Narayanan et al. (2008) found that galactic winds are a natural consequence of merger-induced star formation and black hole growth. In their simulated galaxies, the galactic winds can entrain molecular gas of $\sim 10^8 - 10^9 \mathrm{M}_\odot$, which, the authors showed, should be observable in CO emission. The molecular gas entrained in the winds driven by AGN are predicted to be longer-lived than the gas entrained solely in starburst-driven winds. The wind velocities in the simulated galaxies with AGN-feedback can reach close to 2.5 times the circular velocity. Thus, making AGN-feedback a viable mechanism to get rid off a residual gas and dust at the end of a starburst.

Despite its theoretical appeal, the evidence that connects AGN activity with removal or destruction of gas and dust in galaxies has been elusive, with evidence both for (Schawinski et al., 2009b; Alatalo et al., 2011; Cicone et al., 2014; García-Burillo et al., 2014) and against (Fabello et al., 2011; French et al., 2015; Geréb et al., 2015; Rowlands et al., 2015; Alatalo et al., 2016).

Now we review previous works. Using IRAM CO observations, Rowlands

et al. (2015) investigated the evolution of molecular gas and dust properties in 11 PSBs on the starburst to quenched post-starburst sequence at $z \sim 0.03$. Two of these PSBs are Seyfert galaxies while the rest are either star-forming or composite galaxies of star formation and AGN activity. 10/11 of the PSBs were detected in the CO (1–0) transition and 9/11 of the PSBs were detected in CO (2–1) transition. The gas and dust contents, the star-formation efficiency, the gas depletion time of majority of these PSBs are similar to those of local star-forming spiral galaxies (Saintonge et al., 2011; Boselli et al., 2014) and gas-rich elliptical galaxies (Young et al., 2011; Davis et al., 2014). In addition, the authors found a decrease in dust temperature with the starburst age but they did not find evidence for dust heating by AGN at late times.

Similarly, Alatalo et al. (2016) studied 52 transition PSBs with shock signatures at $z = 0.02 - 0.2$ using IRAM and CARMA. About of half of these PSBs are at $z > 0.1$, 14/52 are Seyferts, and 90% have CO (1–0) detections. The molecular gas properties of these PSBs are also similar to those of normal star-forming galaxies. More than 80% of the PSBs in Alatalo et al. (2016) and Rowlands et al. (2015) samples are located in the blue-cloud.

French et al. (2015) studied 32 "quenched" PSBs in the green valley at $z = 0.01 - 0.12$ using IRAM and the Submillimeter Telescope (SMT). Almost all of these PSBs have signatures mimicking low-ionisation nuclear emission line regions (LINERs), and 53% of them have CO detections. Those detected in CO have gas masses and gas to stellar mass fractions comparable to those of star-forming galaxies while the non-detected PSBs have gas fractions more consistent with those observed in quiescent galaxies.

The three aforementioned studies on the molecular gas contents of PSBs suggested that the end of starburst in these galaxies cannot be ascribed to a complete exhaustion or removal or destruction of molecular gas. The studies also suggested that multiple episodes of starburst or/and AGN activities may be needed for the eventual migration of these galaxies to the red-sequence and that a transition time longer than 1 Gyr may be needed for this migration to take place.

Saintonge et al. (2012) found that, among the gas-rich, disk-dominated galaxy population, those which are ongoing mergers or are morphologically disturbed have the shortest molecular gas depletion times. They found no link between the presence of AGN and the long depletion times observed in bulge-dominated galaxies. Even though their AGN sample has lower molecular gas fractions than the control sample matched in NUV-r color and stellar mass surface density, the depletion times of the two populations are similar. More than 90% of the AGN studied by Saintonge et al. (2012) are not Seyferts, and instead are LINERs.

In contrast, Schawinski et al. (2009b) presented evidence that AGN are responsible for the destruction of molecular gas in morphologically early-type galaxies at $z \sim 0.05$. Their sample included 10 star-forming galaxies, 10 star-formation and AGN composite galaxies and 4 Seyfert galaxies. The galaxies studied by Schawinski et al. (2009b) are not post-starbursts but might have experienced mild recent star-formation (see Schawinski et al., 2007). The authors found that the gas mass drops significantly 200 Myr after a recent star formation in the composite galaxies, and none of their Seyferts have CO detections. The authors interpreted their observations as evidence for a destruction of molecular gas and for a suppression of residual star formation by low-luminosity AGN. Likewise, many studies have

reported molecular outflows with high mass-outflow rates as evidence for AGN feedback in non-PSB AGN host galaxies (e.g., Fischer et al., 2010; Feruglio et al., 2010; Sturm et al., 2011; Spoon et al., 2013; Veilleux et al., 2013; Cicone et al., 2014; García-Burillo et al., 2014; Sun et al., 2014).

In this work, we study molecular gas in 24 green-valley, Seyfert PSBs using SMT CO (2–1) observations, in combination with an existing sample of $\sim$ 100 PSBs from the literature. Our observations were motivated by French et al. (2015) and Rowlands et al. (2015) and were designed to be complementary to the samples in these two works. Our original aim was to increase the number of Seyfert PSBs, which are only three in the two works, by more than a factor five, and firmly test the effect of AGN in the molecular gas evolution of PSB galaxies. Fortunately, our sample is also complementary to the recently published 14 randomly selected Seyferts in Alatalo et al. (2016) sample. These Seyferts are mainly located in the blue-cloud. Our sample is comparable in number to the existing sample of Seyfert PSBs but represents the ones in the later stage of evolution. When combined with other samples, our sample is indispensable in sampling the entire starburst-AGN-quenched post-starburst evolutionary sequence.

The rest of this chapter is organized as follows: section 3.2 presents the sample selection. Section 3.3 presents overview of statistical methods used in the chapter. Section 3.4 presents the main results of the chapter. A hasty reader can skip section 3.3 and may read it later if necessary. Section 3.5 discusses our sample in comparison with other samples of PSBs, LIRGs, AGN and QSOs. Section 3.6 summarizes the main findings of this work. Section 5 provides ancillary information on how our sample relates to existing samples of PSBs with molecular gas

measurements. We assume $(\Omega_m, \Omega_\Lambda, h) = (0.3, 0.7, 0.7)$ cosmology.

3.2 Sample Selection & Observations

3.2.1 Sample selection

Using the cross-matched catalog of SDSS, GALEX and WISE (Martin et al., 2005; Wright et al., 2010; Aihara et al., 2011; Yesuf et al., 2014), we select a sample of 24 transition post-starburst Seyferts based on the evolutionary path that starbursts and post-starbursts follow in the dust-corrected NUV-g color and the 4000Å break (Yesuf et al., 2014), and based on the BPT line ratio AGN diagnostic (Baldwin et al., 1981; Kewley et al., 2001; Kauffmann et al., 2003c). $D_n(4000)$ probes the average temperature of the stars responsible for the continuum emission and is a good indicator of the mean stellar age (Bruzual A., 1983; Balogh et al., 1999). It is less sensitive to dust effects (MacArthur, 2005). As discussed in Yesuf et al. (2014), we acquired the measurements for physical parameters such as stellar masses and spectral indices from the publicly available catalogs. We did not measure them ourselves. Our sample is restricted to galaxies with redshift, $z < 0.06$, stellar mass, M $> 10^{10}$ M$_\odot$, NUV-g > 2.5 and $D_n(4000) < 1.6$.

Figure 3.1 shows the $D_n(4000)$ index versus the dust-corrected NUV-g color on top panel and the Hδ equivalent width against dust-corrected NUV-g color on bottom panel. The contours represent the number densities of SDSS galaxies at $z = 0.02 - 0.06$ and M$= 10^{10} - 10^{11}$ M$_\odot$. The density clouds are the blue-cloud of young star-forming galaxies in the upper left, and the quiescent old and red galaxies in the lower right. As shown by the two blue curves, which are Bruzual

& Charlot (2003) starburst tracks, with a star formation timescale, $\tau = 0.1$ Gyr, and a burst mass fraction (b_f) 3% or 20%, starbursts evolve differently in this diagram compared to non-starburst galaxies. As detailed in Yesuf et al. (2014), this diagram is useful in identifying late stage post-starburst galaxies, which are outliers at intermediate age from the main relation to the lower left. The red diamonds are the new sample of green valley Seyfert PSBs selected in this work. They are selected quantitatively as objects that are more than 2σ outliers from normal galaxies, at a given $D_n(4000)$, in their dust-corrected NUV - g colors and Hδ absorption equivalent widths (See Figure 4 of Yesuf et al., 2014).

As shown in Figure 3.2, the Seyfert activity is identified using the BPT diagram and it is used as an additional constraint in the sample selection (Baldwin et al., 1981; Kewley et al., 2001; Kauffmann et al., 2003c). Similar to the previous figure, the red diamonds are the Seyfert PSBs selected in this work. The magenta open squares are "quiescent" PSB studied by French et al. (2015). They were selected because they lack significant Hα emission but have enhanced Hδ absorption. The blue triangles are PSBs studied by Rowlands et al. (2015). They were identified using the principal component analysis (PCA) of the 4000Å break strength and the Balmer absorption lines (Wild et al., 2009). We showed in the previous chapter that about 35% of transiting PSBs host Seyferts AGN. However, only 3 of the 43 combined samples of Rowlands et al. (2015) and French et al. (2015) are Seyferts. Since Seyferts were under-represented in these two works, and because the previous works did not find evidence for AGN feedback, this work was initiated as a follow-up to increase sample of Seyferts PSBs with molecular gas measurements. The data on the 14 Seyfert PSBs by Alatalo et al. (2016) were

published after we have completed our observations. Fortuitously, this new sample is complementary to our sample as a large majority of these galaxies, including the Seyfert PSBs, are located in the blue-cloud. These galaxies are likely to be the precursors to our Seyfert PSBs.

Figure 3.3a shows the $D_n(4000)$ index versus NUV-g color without the dust correction. The symbols have the same meaning as the figure with the dust correction. It is clear that the Seyfert PSBs selection does not primarily depend on the dust correction. They would be still be selected as outliers from normal galaxies without the dust correction. The purpose of the dust correction is to remove normal dusty galaxies that masquerade as late stage post-starbursts. A visual inspection of their SDSS images (Figure fig:cutouts) also reveal that they are less dusty than most of the PSBs studied by Alatalo et al. (2016). Note that the Seyfert PSBs have similar colors and ages as the quiescent PSBs of French et al. (2015) according to Figure 3.3.

Figure 3.3b plots the time since the starburst versus $D_n(4000)$ for the Bruzual & Charlot (2003) starburst tracks with a star formation timescale, $\tau = 0.1$ Gyr, and a burst mass fraction (b_f) of 3% or 20%. Based on their $D_n(4000)$, the Seyfert PSBs have average stellar age of $\sim 0.5 - 0.7$ Gyr.

In the sample selection, the redshift cut, $z < 0.06$, was imposed due to the sensitivity of the SMT to achieve the desired signal-to-noise ratio in 6–8 hours. This severely limited the number of Seyferts available for the observation. In addition, in the second year of the observation, the sample was restricted to be above a declination of 35°(away from the sun avoidance zone for the SMT), further limiting the observable sample. Therefore, we did not impose the Hδ >

4Å absorption cut that was done in the original sample selection of Yesuf et al. (2014). Most of the galaxies in our sample have, within the measurement errors, Hδ absorptions above 3Å, which is expected in young post-starbursts or rapidly truncated star-forming galaxies (e.g., Poggianti et al., 1999). Our sample on average has lower Hδ than do the aforementioned previous samples. Note that the Hδ equivalent width is $\sim$ 2Å at 1 Gyr after a starburst with $\tau = 0.1$ Gyr and $b_f = 20\%$. For starburst with $\tau = 0.1$ Gyr and $b_f = 3\%$, H$\delta \sim 0$ at 1 Gyr (see Figure 5.9 in Appendix). Thus, not imposing H$\delta > 4$Å cut helps select old PSBs. In the Appendix section, we present series of plots that show our post-starburst sample relative to other post-starburst samples (French et al., 2015; Rowlands et al., 2015; Alatalo et al., 2016). The plots show that our PSBs are consistent with being later stage PSBs compared to more than 70% the previously studied PSBs.

It should be noted that at $z < 0.06$, the SDSS fiber covers only $\sim$ 3.5 kpc of the central region of a galaxy, and the spectroscopic measurements may not reflect the galaxy-wide values. On the other hand, the NUV-g color is an integrated galaxy-wide quantity. By combining the spectroscopic measurements with NUV-g color , we select only (PSB) galaxies that are fading galaxy-wide.

3.2.2 SMT CO observations

The observations were carried out using the Submillimeter Telescope (SMT) in Mount Graham, Arizona. The observing runs were in February 25 – March 10, 2015 and in March 4 – 25, 2016. We follow the same instrument set up and observing strategy as French et al. (2015). Namely, we used the 1 mm ALMA Band 6 dual

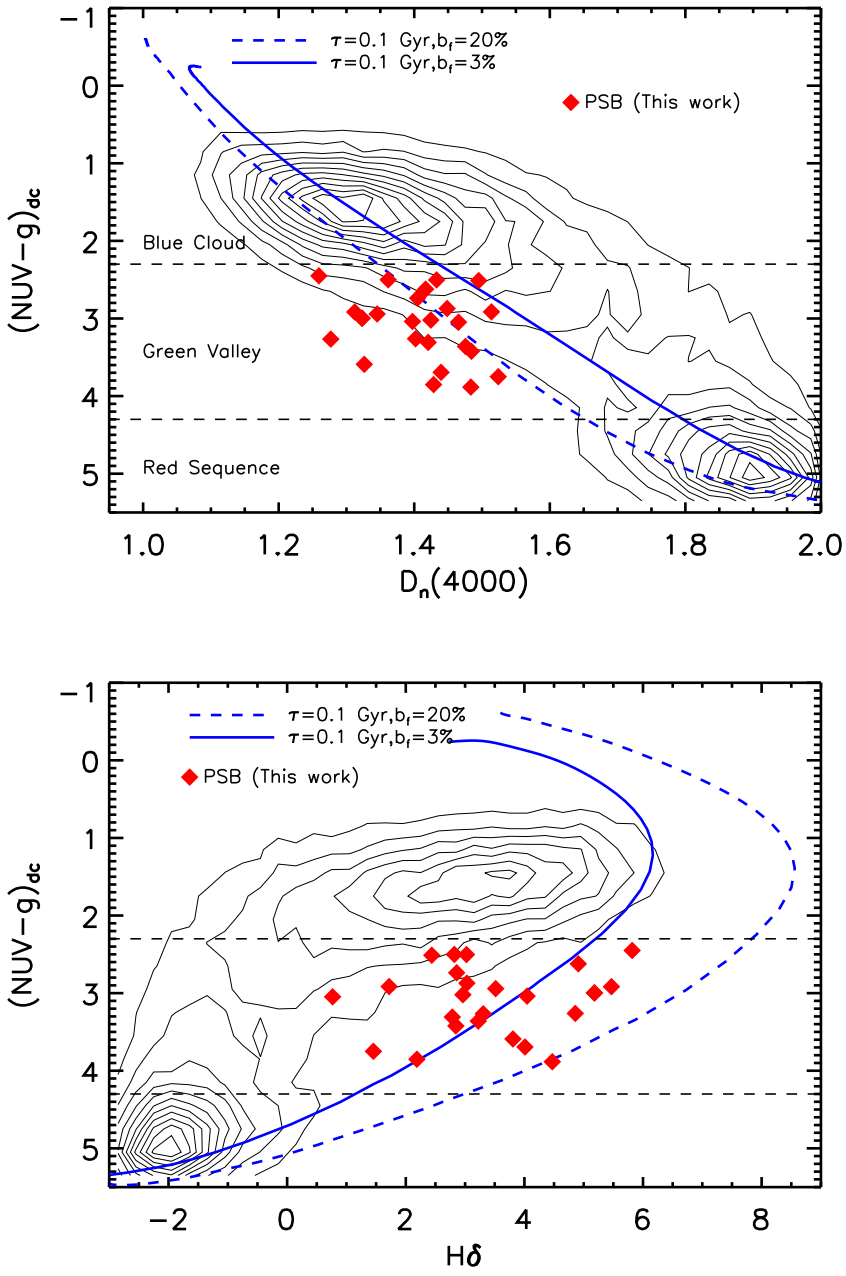

Figure 3.1:. Sample selection: The 4000Å break against dust-corrected NUV-g color (top panel). Hδ absorption equivalent width against dust-corrected NUV-g color (bottom panel). The contours denote the distribution of bi-model massive galaxy population at redshift z =0.02–0.06 and log M ($M_{\odot}$) =10–11 observed by SDSS and GALEX. The blue dashed and solid curves are the Bruzual & Charlot (2003) burst model tracks with a star formation timescale, τ = 0.1 Gyr and a burst mass fraction (b_f) 3% or 20%.

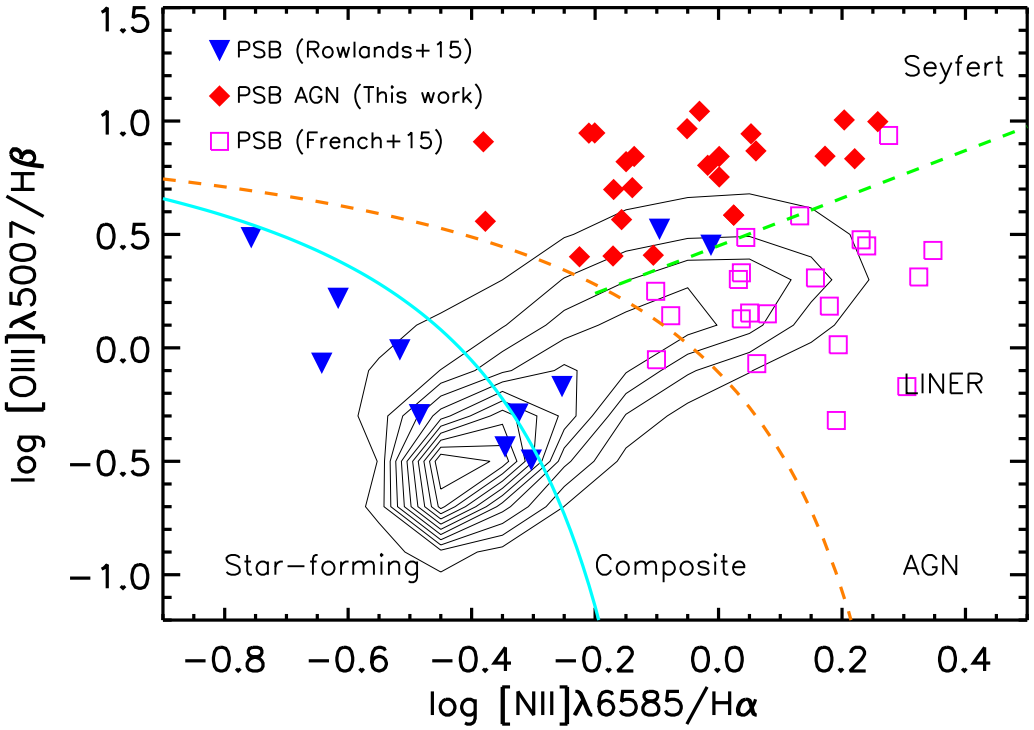

Figure 3.2:. Sample selection: The BPT emission-line ratio AGN diagnostic. Seyferts are located in the upper corner of the AGN region, above the dashed green line (Schawinski et al., 2007) and the orange dashed curve, which demarcates the maximum starburst boundary (Kewley et al., 2001). About 35% of PSBs are Seyferts (Yesuf et al., 2014). The previous two PSBs studies (French et al., 2015; Rowlands et al., 2015) only studied 3/43 Seyferts. This work was designed to be complementary to these two works.

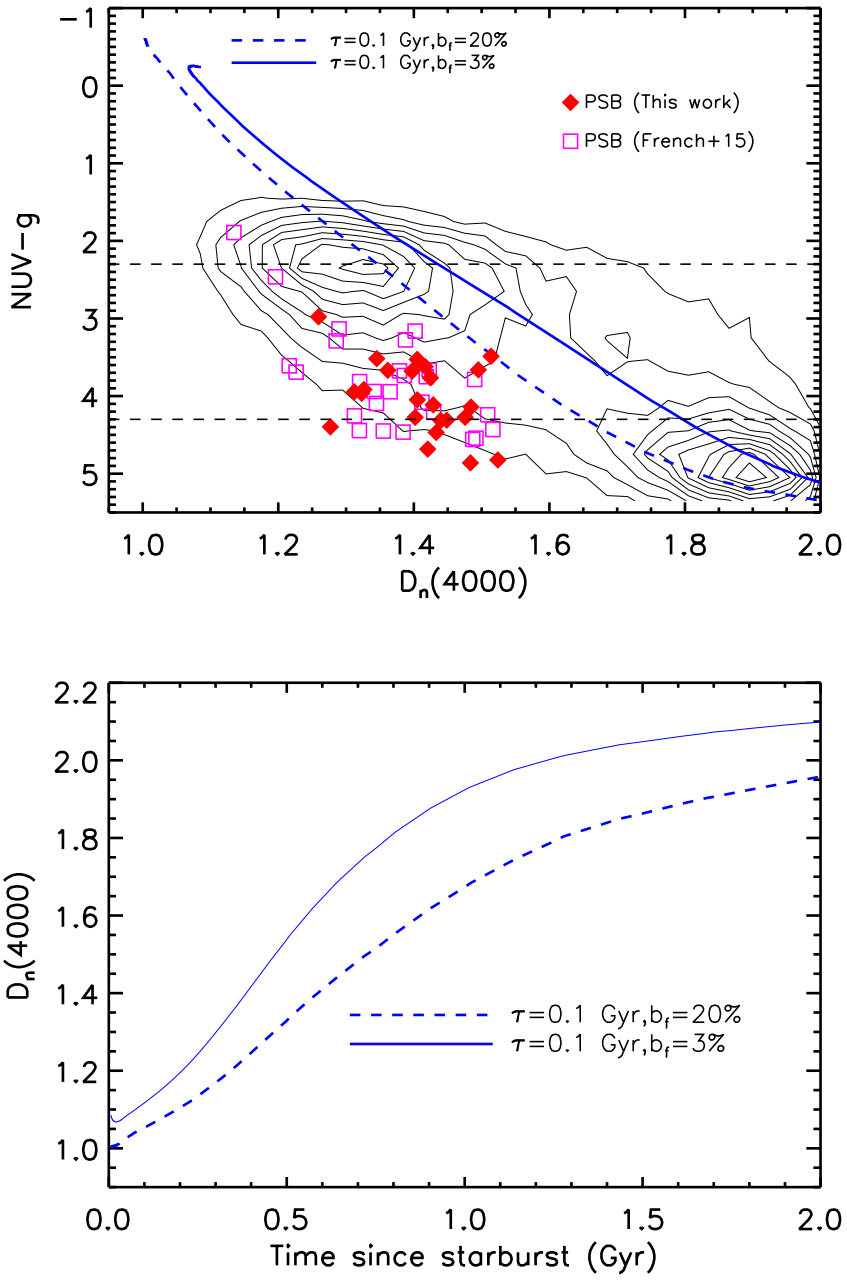

Figure 3.3:. Top: $D_n(4000)$ vs. NUV-g color (not dust-corrected). The symbols in this figure are the same as Figure 3.2. The magenta open squares denote the PSBs in French et al. (2015). Our PSB selection does not depend on the dust correction. Our Seyfert PSBs are outliers regardless of the dust correction. **Bottom** the relationship between $D_n(4000)$ and time since starburst for the Bruzual & Charlot (2003) burst model tracks with a star formation timescale, $\tau = 0.1$ Gyr, and a burst mass fraction (b_f) 3% or 20%.

polarization sideband separating SIS (superconductor-insulator-superconductor) receiver and 1 mHz filterbank to measure the CO (2–1) 230.5 GHz emission line. The beam size of the SMT for this line is about 33″. Beam switching was done with the secondary at 2.5 Hz switching rate and a throw of 120″, in the BSP (beam switching plus position switching) mode. Calibration using a hot load and the standard chopper wheel method was performed every 6 minutes. Calibration using a cold load was performed at every tuning. The observing times range between 4 – 9 hours. French et al. (2015) observed a subset of 13 PSBs using both SMT and IRAM have demonstrated that SMT can have comparable sensitivity and data quality as IRAM with a longer integration time, which was 3 – 9 hours for their sample.

The data reduction is done using CLASS, a program within the GILDAS software package[1]. The main beam efficiency is calculated using Jupiter/Saturn in each polarization. A first-order polynomial baseline is subtracted from the spectra using data between [-600, 600] km s^{-1}, excluding the central regions of [-300, 300] km s^{-1}. The spectra are scaled using the main beam efficiency, and are coadded by weighting with the root-mean square (RMS) noise. The spectra are rebinned to 14 km s^{-1} velocity bins. The typical RMS error per bin is 1–2 mK. Thus, we achieve similar sensitivity as previous works (Saintonge et al., 2011; French et al., 2015; Rowlands et al., 2015; Alatalo et al., 2016).

To calculate the integrated CO line intensity, $I_{\rm CO}$, we fit a Gaussian profile to each line, allowing the peak velocity to differ from the optical systemic velocity by up to 200 km s^{-1}. The statistical uncertainty in the line intensity is calculated

[1]http://www.iram.fr/IRAMFR/GILDAS/

following Young et al. (2011) as $\sigma_I = (\Delta v)^2 \sigma^2 N_I \left(1 + \frac{N_I}{N_b}\right)$, where Δv is the channel velocity width, σ is the channel RMS noise, N_I is the number of channels used to integrate over the line, and N_b is the number of channels used to fit the baseline. When the line is not detected, the upper limits of the line intensity is calculated as three times the statistical uncertainty. Following Solomon et al. (1997), the CO line luminosity in K km s^{-1} pc^2 is $L'_{\rm CO} = 23.5\,\Omega_{s*b} D_{\rm L}^2 I_{\rm CO} (1+z)^{-3}$ where Ω_{s*b} is the solid angle of the source convolved with the beam, z is the redshift from the SDSS optical spectrum, and $D_{\rm L}$ is the luminosity distance in Mpc. If the source is much smaller than the beam, then $\Omega_{s*b} \approx \Omega_b$. We do not know the CO emitting sizes of our galaxies. We adopt this approximation as a simplifying assumption. We do not expect this to affect our conclusion. Previous works also adopt the same approximation. The fact that SMT has larger beam-size than IRAM, and CO (2–1) is known to be more centrally concentrated than CO (1–0), make the effect of this approximation less significant in this work compared to previous works. French et al. (2015) estimated for their sample that the $L'_{\rm CO}$ may be underestimated by about 1.5× because of this effect.

The molecular gas mass can be calculated from $L'_{\rm CO}$ by assuming a CO conversion factor (mass-to-light ratio) $\alpha_{\rm CO}$, $\mathrm{M(H_2)} = \alpha_{\rm CO} L'_{\rm CO}$. We assume an $\alpha_{\rm CO} = 4.3\,\mathrm{M_\odot (K\,km\,s^{-1} pc^2)^{-1}}$ in Milky Way disk (Bolatto et al., 2013) and $R_{21} = L'_{\rm CO(2-1)}/L'_{\rm CO(1-0)} = 1$. As discussed in section 3.5.7, choosing a lower value of $\alpha_{\rm CO}$ strengthens our main conclusion. The ratio R_{21} is uncertain (Leroy et al., 2013; Sandstrom et al., 2013). Leroy et al. (2013) found $R_{21} \sim 0.7 \pm 0.3$ in nearby disk galaxies. We adopt the Galactic α_{CO} value throughout the paper unless explicitly stated. The observation are summarized in Table 1, the coadded spectra

are given in Figure 3.4–3.7 and the SDSS cutout images of the Seyfert PSBs are shown in Figure 3.8.

Table 3.1. Summary of the new Seyfert PSBs CO observations

Target	RA	Dec	z	$D_n(4000)$	$(\mathrm{NUV-g})_{\mathrm{dc}}$	Hδ	log $\mathrm{f_{12}/f_{4.6}}$	log $\mathrm{M_\star/M_\odot}$	log $\mathrm{M_{H_2}/M_\odot}$	Flag [a]
TPSB1	212.01668	7.32762	0.0238	1.26	2.5	5.8	0.62	10.04	8.79	1
TPSB2	134.61915	0.02347	0.0285	1.32	3.0	5.2	0.59	10.40	8.64	1
TPSB4	182.01943	55.40766	0.0513	1.40	3.0	4.0	0.66	10.30	9.19	0
TPSB5	173.41286	52.67458	0.0490	1.40	3.3	4.9	0.22	10.19	9.10	0
TPSB6	170.94591	35.44231	0.0341	1.42	2.6	4.9	0.52	10.29	8.97	0
TPSB7	203.56173	34.19415	0.0236	1.31	2.9	5.5	0.44	10.15	8.62	1
TPSB8	189.51736	48.34506	0.0306	1.44	3.7	4.0	0.04	10.21	8.81	0
TPSB9	180.51923	35.32168	0.0341	1.48	3.9	4.5	0.31	10.54	8.90	0
TPSB10	117.96618	49.81432	0.0244	1.40	2.7	2.9	0.41	10.45	9.29	1
TPSB10b	126.01534	51.90432	0.0315	1.36	2.5	2.8	0.72	10.12	9.12	0
TPSB11	137.87485	45.46828	0.0268	1.43	2.5	3.0	0.64	10.70	8.93	1
TPSB12	139.49938	50.00218	0.0342	1.41	3.1	0.8	0.53	10.33	8.94	0
TPSB13	173.16774	52.95040	0.0266	1.50	2.5	2.4	0.48	10.54	8.68	0
TPSB14	178.62255	42.98021	0.0235	1.51	2.9	1.7	0.57	10.05	8.71	0
TPSB15	179.02851	59.42492	0.0320	1.52	3.7	1.5	0.41	10.49	8.85	0

Table 3.1 (cont'd)

Target	RA	Dec	z	$D_n(4000)$	$(\mathrm{NUV\text{-}g})_{\mathrm{dc}}$	Hδ	log $f_{12}/f_{4.6}$	log $M_\star/M_\odot$	log $M_{H_2}/M_\odot$	Flag [a]
TPSB16	190.45029	47.70888	0.0308	1.48	3.4	3.2	0.45	10.25	8.81	0
TPSB17	198.74928	51.27259	0.0249	1.48	3.4	2.8	0.34	10.02	8.66	0
TPSB18	200.95187	43.30118	0.0273	1.28	3.3	3.3	0.74	10.68	9.21	1
TPSB19	236.93394	41.40230	0.0327	1.35	2.9	3.5	0.69	10.47	9.00	0
TPSB20	240.65806	41.29344	0.0348	1.45	2.9	3.0	0.08	10.59	8.97	0
TPSB21	247.63604	39.38420	0.0305	1.42	3.0	3.0	0.55	10.54	8.82	0
TPSB24	145.18542	21.23427	0.0244	1.43	3.9	2.2	0.71	10.33	8.60	0
TPSB26	172.08298	27.62209	0.0321	1.42	3.3	2.8	0.18	10.31	8.89	0
TPSB28	222.65772	22.73433	0.0210	1.33	3.6	3.8	0.60	10.09	8.47	0

[a]Flag =1 indicates CO detection in the galaxy and Flag = 0 indicates non-detection and the given molecular mass is a 3σ upper limit.

3.3 Overview of Statistical Methods

In this section, we briefly review the statistical methods and tests used in the next section with two aims in mind: 1) to give just enough information to make our results more understandable 2) to facilitate replicability of our work. Readers interested in more details of the methods should refer to the references provided. A hasty reader only interested in our results should skip to the next section.

In this section, we are concerned with how to analyze data that include both CO detections and CO upper limits, and make inference that is consistent with the incomplete information at hand. In statistics, a data set is called censored when the value of a measurement is only partially known to be above or below a threshold. Left-censoring occurs when a measurement is below a certain value but it is unknown by how much. Left-censoring is what is often encountered in astronomical data. However, right-censoring is what is common in other areas of study. Survival analysis is an area of statistics that mostly deals with modeling right-censored data such as time to an event (e.g., Klein & Moeschberger, 2005). An event could be a death of an individual or a failure of a machine. Methods developed for right-censored data can be used to analyze the left-censored astronomical data by "running the scale of measurement backward" (Feigelson & Nelson, 1985; Halsel, 2012). What is meant by this will be clear soon. We use existing survival analysis methods to properly extract information from our censored CO observations.

Let T denote a positive random variable representing time to an event of interest, say death. The survival function is the probability that an individual survives beyond time t, $S(t) = Pr(T \geq t) = 1 - F(t)$, where $F(t)$ is the cumulative

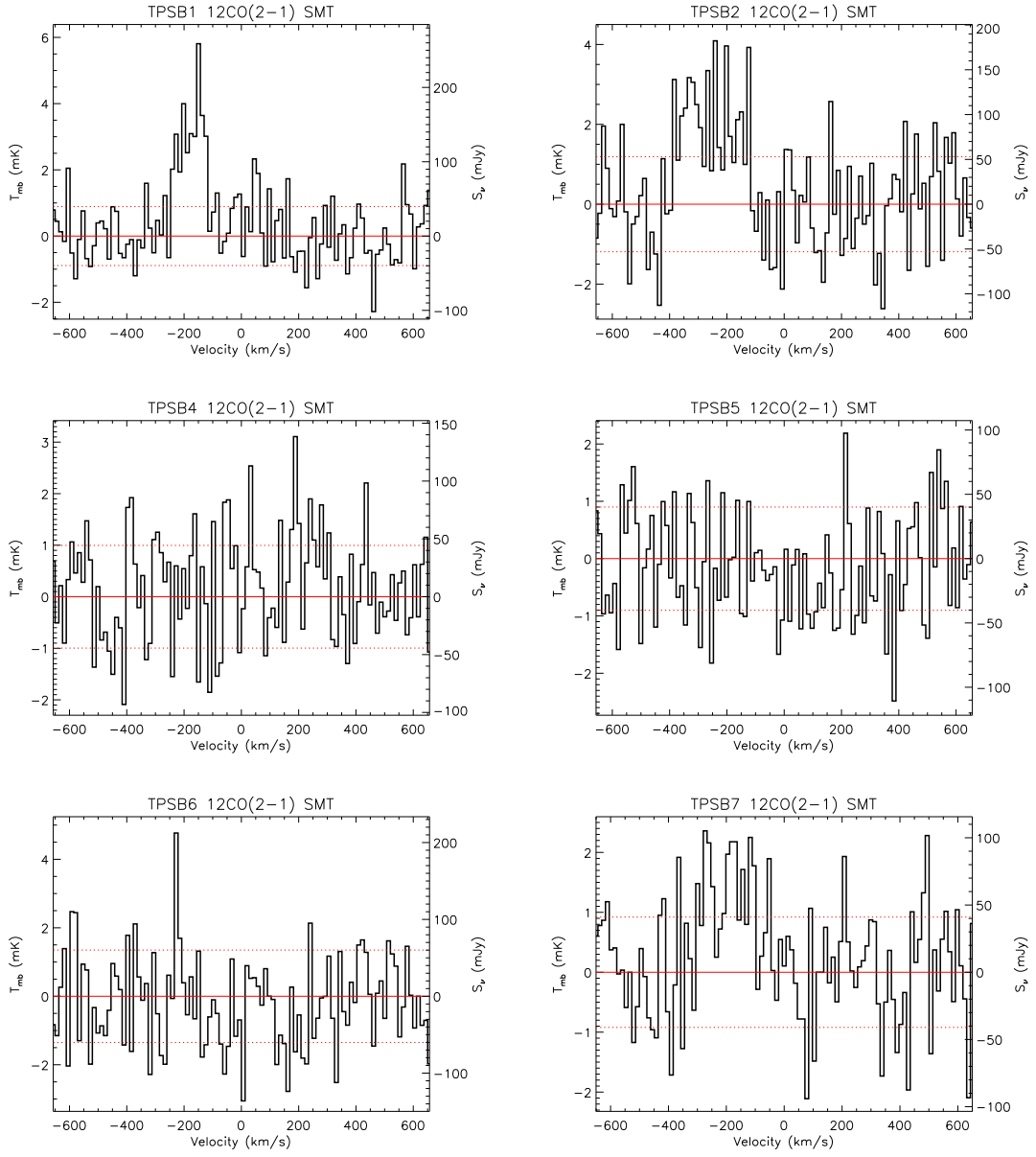

Figure 3.4:. CO (2–1) spectra for Seyfert PSBs. Spectra are shown in units of both main beam temperature $T_{\rm mb}$ (mK) and S_ν (Jy). The dashed red lines represent the RMS of the binned data. The data are binned by $14\,{\rm km\,s^{-1}}$.

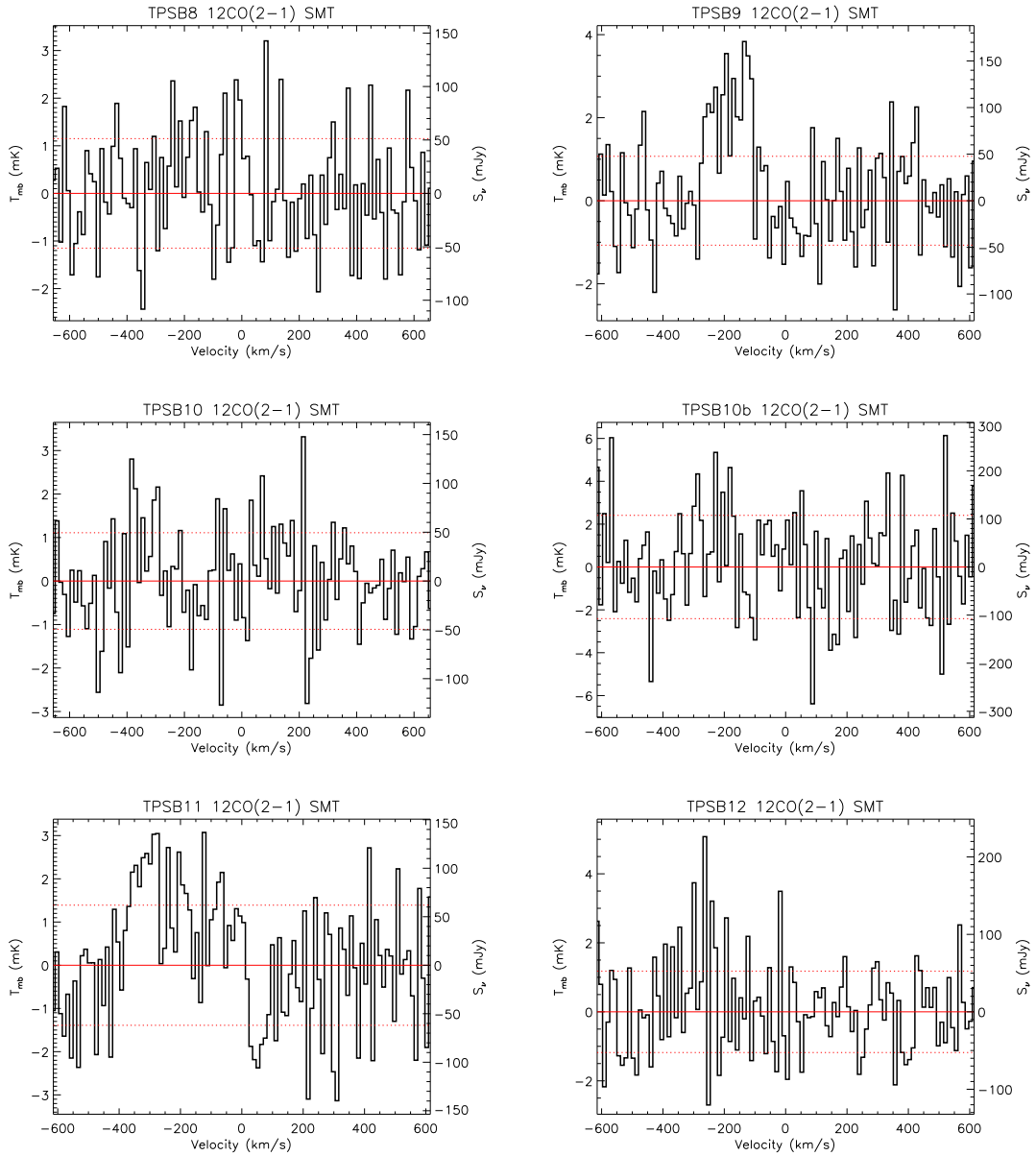

Figure 3.5:. CO (2–1) spectra (continued)

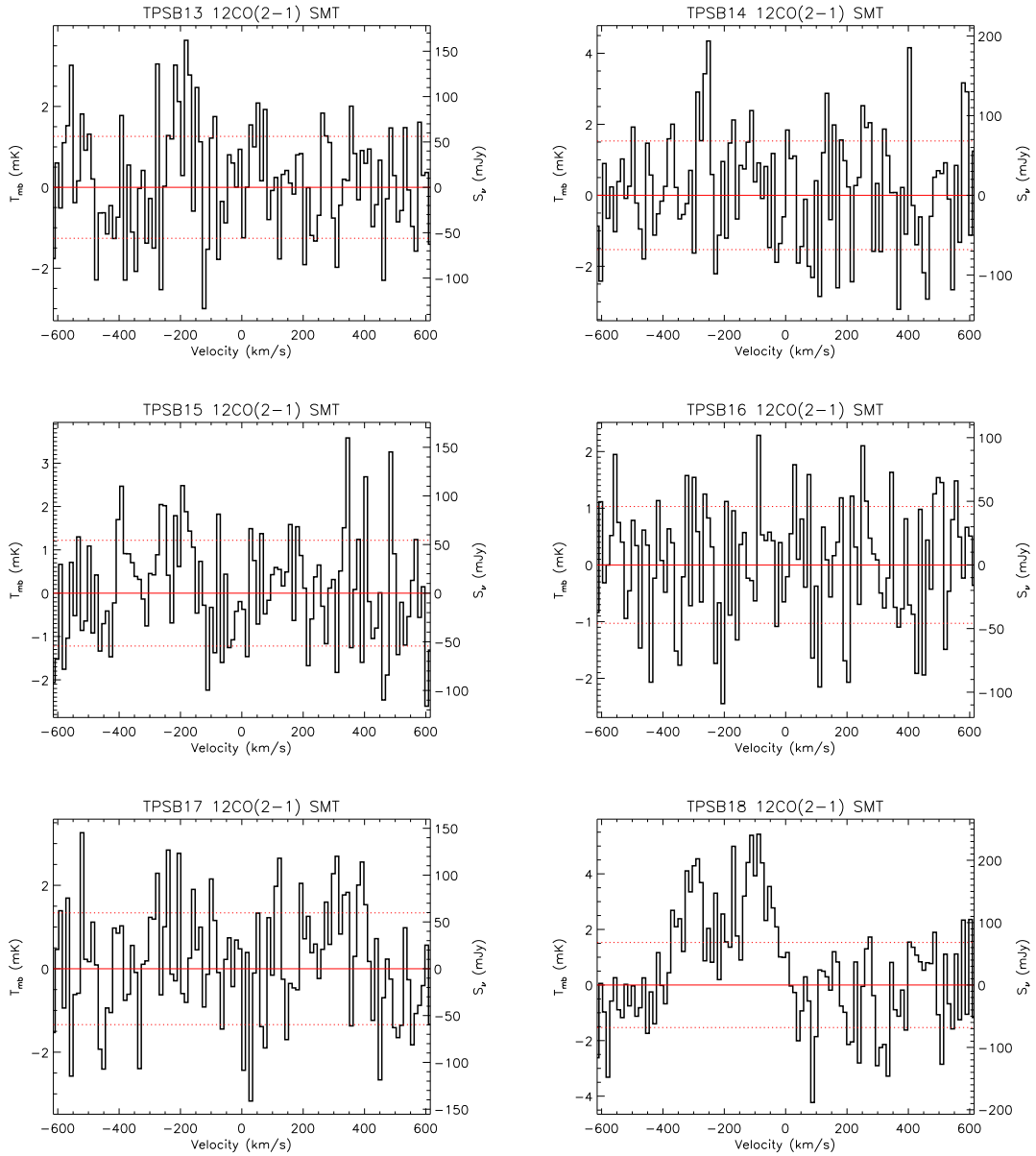

Figure 3.6:. CO (2–1) spectra (continued)

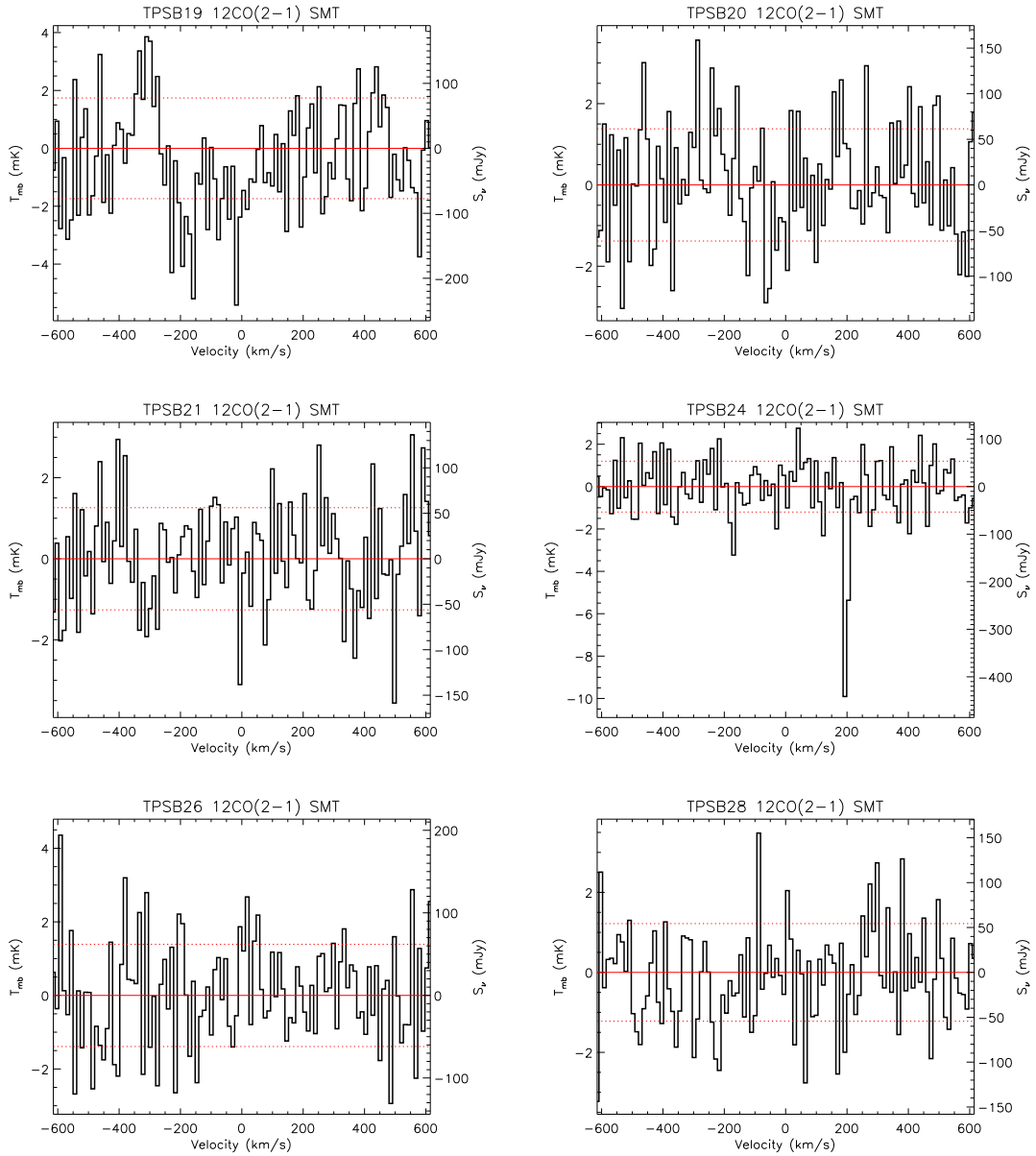

Figure 3.7:. CO (2–1) spectra (continued)

Figure 3.8:. SDSS cutout images of Seyfert PSBs. They show prominent bulges. But they do not show strong merger signatures and dust extinctions, unlike some of the previously studied PSBs.

distribution function (CDF). For example, a clinical trial may be conducted to test the longevity of patients after receiving a new treatment. Some patients may still be alive at the end of the study. The researcher only knows their survival time is longer than the period of the study but how much longer they live thereafter is unknown. Similarly, some patients may dropout before the completion period of the study. The researcher only knows they are alive when they dropout but does not know how much longer they live thereafter. Thus, in these two cases the survival times are right-censored because the death occurs to the right of the censoring time. To estimate the true survival function from the censored data, the researcher needs to take into account that the study has finite period and patients dropout.

The Kaplan-Meier estimator (Kaplan & Meier, 1958), also known as the Product-Limit estimator, is a non-parametric maximum likelihood estimator of the survival function, even in the presence of censoring. A non-parametric method does not require an assumption that the data follow a specific probability distribution. Instead, the data are ranked from smallest to largest, providing information on the relative positions of each observation. In the case of ties, Kaplan-Meier method assigns the smallest rank to each observation. The censored observations are also used in calculating the ranks. Let there be a set of $\{t_k\}_{k=1}^{n}$ data points and of these let $t'_1 < t'_2 < t'_3, \ldots, t'_r$ be ranked, distinct uncensored values. At each time point t'_j, we observe d_j, the number of deaths, c_j, the number of censored observations between the time t'_j and t'_{j-1} and, n_j, the number of individuals at risk just prior to the time t'_j. In other words, n_j is the total sample size minus those who are censored or have died before t'_j, $n_j = n - c_j - d_j = \sum_{l \geq j}(c_l + d_l)$. The

Kaplan-Meier estimator has a form : $\hat{S}(t) = \prod_{j:t'_j<t} \left(1 - d_j/n_j\right)$. It is a step function with jumps at times t'_j.

To compute the empirical cumulative distribution function (ECDF), using the Kaplan-Meier method for left-censored data, one needs to transform the measurements to a right-censored sample by subtracting from the largest observation, t_{max}, each t_k. This is what was meant by "running the scale of measurement backward". In our case, t_k is the kth gas fraction value. The ECDF is the survival function for the transformed data, $\hat{S}(t_{max} - t)$. The NADA package in R programing language implements parametric and nonparametric methods for left-censored data (Halsel, 2012; Lee & Lee, 2015). The package is built on existing software for right-censored survival analysis. We use the function *cenfit* in the NADA package to compute the Kaplan-Meier estimator for the CO data (Halsel, 2012; Lee & Lee, 2015).

The survival curves or ECDF of two groups can be compared using the log-rank test, which tests the null hypothesis that two groups have the same distribution against the alternative hypothesis that two groups have different distributions (Mantel, 1966; Cox, 1972; Harrington & Fleming, 1982; Martinez, 2007). Let $t'_1, t'_2, t'_3, \ldots, t'_r$ be r distinct, rank-ordered uncensored times for either group. For $j = 1, 2, \ldots, r$, let there be d_{1j} deaths in group 1, d_{2j} be deaths in group 2 and d_j be the total number of deaths in the two groups. Similarly, let n_{1j}, n_{2j} and n_j be the number of individuals at risk prior to time t'_j in group 1, in group 2 and in both groups respectively. The underlying distribution of d_{1j} has a hypergeometric distribution. This is because, if we consider death as a "success" for the sake of statistics, the probability of d_{1j} success in n_{1j} trials without replacement from a

sample size of n_j that has a total of d_j success is described by a hypergeometric distribution. The mean of the hypergeometric distribution is given by $\mu_{1j} = \frac{n_{1j}d_j}{n_j}$ and the variance is given by $\sigma_{1j}^2 = \frac{n_{1j}n_{2j}d_j(n_j-d_j)}{n_j^2(n_j-1)}$. The log-rank test statistics compares each d_{1j} with μ_{1j} under the null-hypothesis and it is defined by z^2, where $z = \frac{\sum_{j=1}^{J}(d_{1j}-\mu_{1j})}{\sqrt{\sum_{j=1}^{J}\sigma_{1j}^2}}$. The test statistic quantifies by how much the observed survival times in the two groups deviate from the expected values under the null hypothesis. Asymptotically, for large sample size, z^2 will have approximately the χ^2 distribution with one degree of freedom (Cox, 1972). So in testing the group difference, for instance at $\alpha = 0.05$ level, the null-hypothesis will be rejected if the p-value is less α. In general, a p-value is the probability of obtaining a test statistic at least as extreme as the one that was actually observed. In this case, the probability is computed from the χ^2 distribution. If the data are uncensored, the log-rank test gives similar result to the Mann-Whitney test. We use the routine *cendiff* in the NADA package to do the the log-rank test.

A correlation coefficient quantifies the strength of the association or dependence between two variables. The Kendall's τ is a non-parametric correlation coefficient that can be used for testing trends in both censored and uncensored data (e.g., Halsel, 2012). Let $(x_1, y_1), (x_2, y_2), \ldots (x_n, y_n)$ be n pairs of observations for the covariate variable, X, the response variable, Y, respectively. For the ease of explanation, let us assume that all pairs are unique and there are no ties. Let $r(x_1), r(x_2), \ldots r(x_n)$ and $r(y_1), r(y_2), \ldots, r(y_n)$ be the ranks of of the observations when the elements in X and Y are separately rank-ordered. Any pair of observations (x_i, y_i) and (x_j, y_j), where $i \neq j$, are said to be concordant if $\big(r(x_i) - r(x_j)\big) \times \big(r(y_i) - r(y_j)\big) > 0$. They are called discordant if

$\big(r(x_i) - r(x_j)\big) \times \big(r(y_i) - r(y_j)\big) < 0$. The Kendall's τ is defined, in the case of no ties, as the number of concordant pairs of observations (n_c) minus the number of discordant pairs (n_d), divided by the total number of pairs, $\tau = \frac{n_c - n_d}{n(n-1)/2}$. τ ranges between -1 and 1. $\tau = 0$ is no correlation, $\tau = 1$ is a perfect correlation, and $\tau = -1$ is a perfect anti-correlation. Tie corrections are made for the variance of the test statistic when computing p-values.

In the uncensored case, the slope a linear regression can be estimated using the Theil-Sen slope (Sen, 1968), which is the median of all pairwise slopes between two data points. This slope results in the Kendall's τ of 0 for the correlation between the residuals and the covariate, X. For censored data, the slope can be estimated using the extended version called Akritas - Theil - Sen estimator (Akritas et al., 1995). Let $(x_1^t, y_1^t), (x_2^t, y_2^t), \ldots (x_n^t, y_n^t)$ be n pairs of true observations that would have been observed in the absence of censoring for the covariate X^t and the response Y^t. Let also $(x_1, y_1), (x_2, y_2), \ldots (x_n, y_n)$ be the actual observed values with censoring, $\delta_i^x = I(x_i = x_i^t)$ and $\delta_i^y = I(y_i = y_i^t)$. $I(.)$ is an indictor function which is 0 if an observation is censored and 1 otherwise. To estimate the true slope, β, of the simple linear regression, $Y^t = \alpha + \beta X^t + \epsilon^t$, Akritas et al. (1995) proposed a concordant statistic between the covariate and the residuals, $T_n(b) = \sum_{i<j} \delta_i^x \delta_i^x \big(I(x_i < x_i^t) - I(x_j < x_j^t)\big) \times \big(\delta_i^y I(r_i(b) < r_j(b)) - \delta_j^y I(r_j(b) < r_i(b))\big)$, where $r(b) = Y - bX$ and b is a guessed slope at each iteration of an iterative search. The estimated slope is $\hat{\beta} = (\hat{b}_1 + \hat{b}_2)/2$, where $\hat{b}_1$ is the least upper bound of a set of b such that $T_n(b) > 0$, $\hat{b}_1 = \sup\{b : T_n(b) > 0\}$ and b_2 is the greatest upper bound of a set of b such that $T_n(b) < 0$, $\hat{b}_2 = \inf\{b : T_n(b) < 0\}$. Akritas et al. (1995) have shown that, if $b = \beta$, the mean of $T_n(\beta)$ is zero. The intercept of the

linear regression is the median of the residual, and the median for censored data is estimated using the Turnbull estimator (Turnbull, 1976). We use the *cenken* routine in NADA package to compute the Kendall's τ correlation coefficient and fit the ATS regression line to our censored CO data (Halsel, 2012; Lee & Lee, 2015).

3.4 Results

Figure 3.9 plots the 4000Å break against the logarithm of gas-to-stellar mass fraction, $\log f_{\rm gas} = \log \frac{M_{gas}}{M_*}$, for non-PSB galaxies in the COLD GASS survey (Saintonge et al., 2011). The measurements for CO-detected galaxies in this survey are shown as black points while the upper limits for the non-detected galaxies are shown as open circles and vertical dashed lines. The solid black line is the best linear fit to the data. The upper limits are also included in the fit (see §3.3). As expected, a strong anti-correlation is observed between the 4000Å break and the $\log f_{\rm gas}$. The slope of the best fit line is -1.657 and its intercept is 1.2±0.1. The null hypothesis that there is no correlation between the 4000Å break and $\log f_{\rm gas}$ can be rejected at 5σ significance level. The quiescent galaxies have $D_n(4000)$ between $\sim 1.7 - 2.1$. The fitted relation between $D_n(4000)$ and $\log f_{\rm gas}$ implies that the quiescent galaxies have gas fractions of $-2.28 \lesssim \log f_{\rm gas} \lesssim -1.62$. The important question we will attempt to answer in the rest of this section is : do PSBs achieve similar gas fraction at the end of their rapid evolution ? The answer is affirmative, and the rest of this section will demonstrate why this is the case.

Figure 3.10 plots $D_n(4000)$ against $\log f_{\rm gas}$ for PSB galaxies. The plot uses the molecular gas data of 126 PSBs observed by us and others to date (French

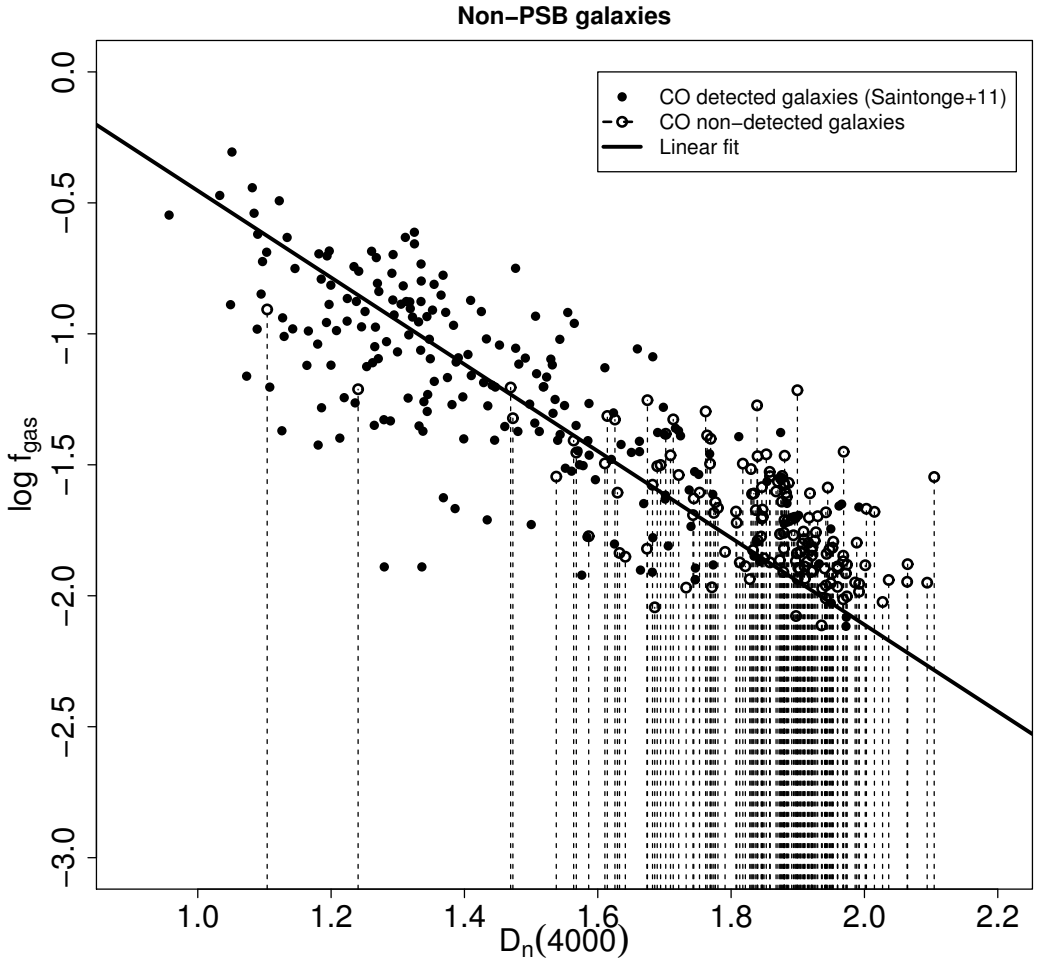

Figure 3.9:. The 4000Å break versus molecular gas fraction for galaxies in COLD GASS survey (Saintonge et al., 2011). The filled circles denote galaxies with CO detections while the open circles and the dashed lines denote non-detected galaxies and their upper-limits. The black line is the linear fit to the data including the upper-limits. As expected, young star-forming galaxies have higher gas fractions than do old quiescent galaxies.

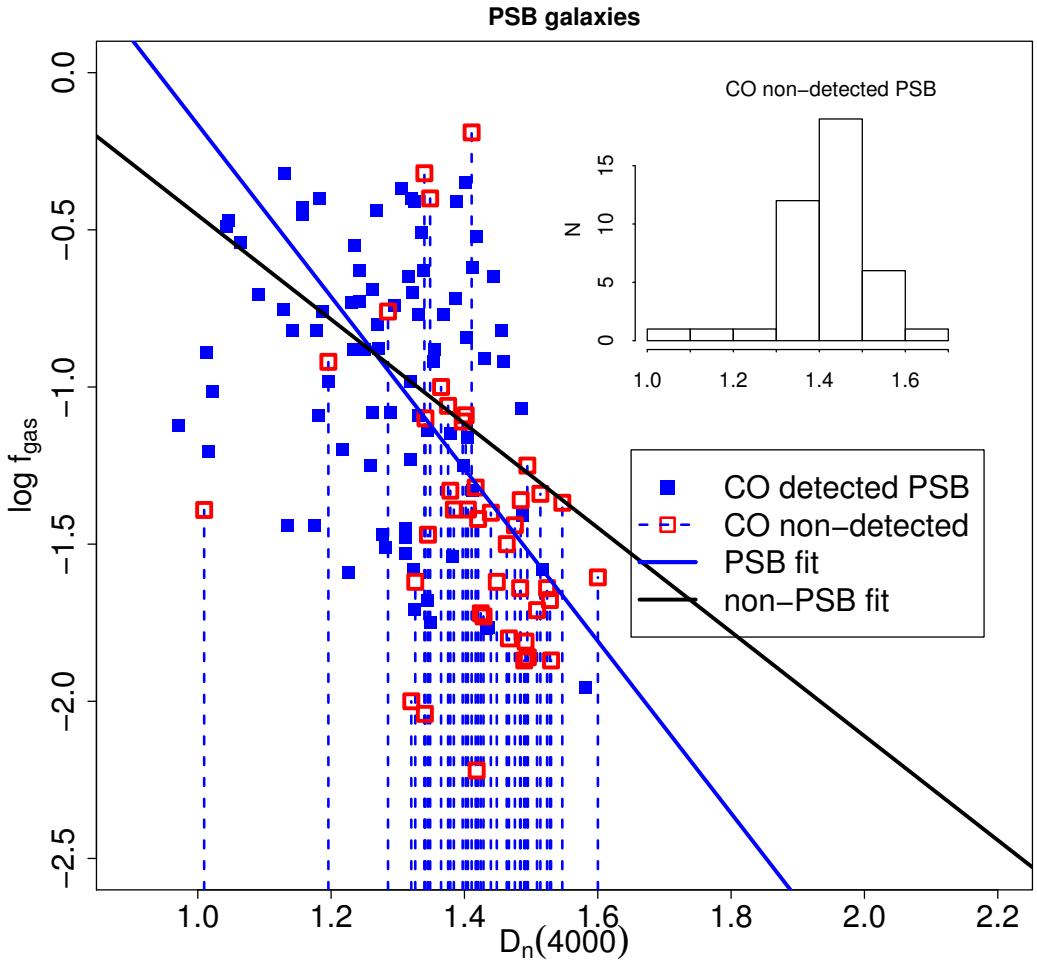

Figure 3.10:. The 4000Å break versus molecular gas fraction for PSBs (in this work, French et al., 2015; Rowlands et al., 2015; Alatalo et al., 2016). The filled blue squares denote PSBs with CO detections while the open red squares and the dashed lines denote non-detected PSBs and their upper-limits. The blue line is the linear fit to the PSB data including the upper-limits while the black line is the fit for non-PSBs in Figure 3.9. At later times, $D_n(4000) \sim 1.4$, PSBs have significantly lower gas fractions compared to non-PSB galaxies. This late dramatic drop in gas fraction signals AGN feedback. The inset histogram shows the distribution of the number of non-detected PSBs.

et al., 2015; Rowlands et al., 2015; Alatalo et al., 2016), including 8 PSB galaxies in Saintonge et al. (2011). The blue squares denote CO detections, and the open red squares with vertical dashed lines denote the upper limits. PSBs are proportionally detected less (i.e., have lower gas fractions) at a later stage of their evolution, at $1.3 < D_n(4000) < 1.6$, in comparison to non-PSB galaxies with $D_n(4000) < 1.6$. The mode of $D_n(4000)$ for the non-detected PSBs is ~ 1.4, which corresponds to an age of ~ 0.6 Gyr after the starburst. The solid blue line denotes the best fit line to the data including the upper limits. This linear trend is not statistically significant and is not well-constrained. The black line is the fit for non-PSB galaxies in Figure 3.9. At higher $D_n(4000)$, PSBs have more negative residuals, $\Delta \log f_{\rm gas}$, from the non-PBS $D_n(4000)-\log f_{\rm gas}$ relation. We interpret this late rapid decline in $\log f_{\rm gas}$, long after the starburst, as a smoking gun evidence for the AGN feedback. Next, we perform non-parametric tests to confirm that the $\log f_{\rm gas}$ distribution of the Seyfert PSBs is different from that of non-PSB galaxies of similar age.

Figure 3.11 compares the empirical cumulative distribution functions (ECDF) of $\log f_{\rm gas}$ of young non-PSBs ($D_n(4000) < 1.6$) with that of PSBs while Figure 3.12 compares the ECDF of non-PSBs ($1.3 < D_n(4000) < 1.6$) with Seyfert PSBs. The vertical probability axis in both plots tracks the estimated Kaplan-Meier percentiles for each group with gas fraction less than a given threshold (Kaplan & Meier, 1958; Halsel, 2012). The $\log f_{\rm gas}$ curves for the PSBs and non-PSBs are similar at high gas fractions but are different at lower gas fractions. The log-rank test indicates that ECDF of all PSBs or Seyfert only PSBs are significantly different from that of the young non-PSBs. When the ECDF for Seyfert

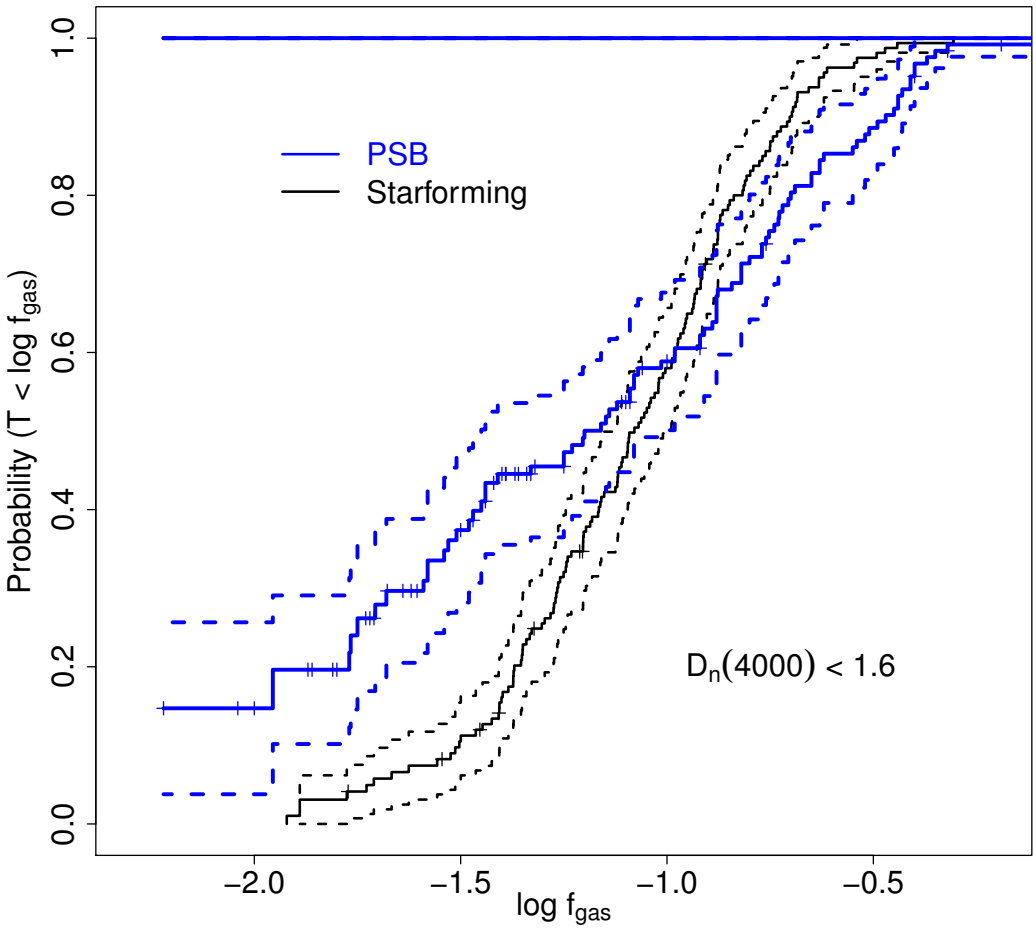

Figure 3.11:. Compares the empirical cumulative distribution function (ECDF) of molecular gas fraction, log $f_{\rm gas}$, of PSBs and of star forming non-PSBs. The ECDF is estimated using the Kaplan & Meier (1958) estimator and takes into account the upper limits, which are shown as +s. 95% confidence curves are shown as dashed lines.The gas fractions in PSBs are significantly different from those in non-PSBs. See text in section in 3.4 for a quantitative test that compare the two curves.

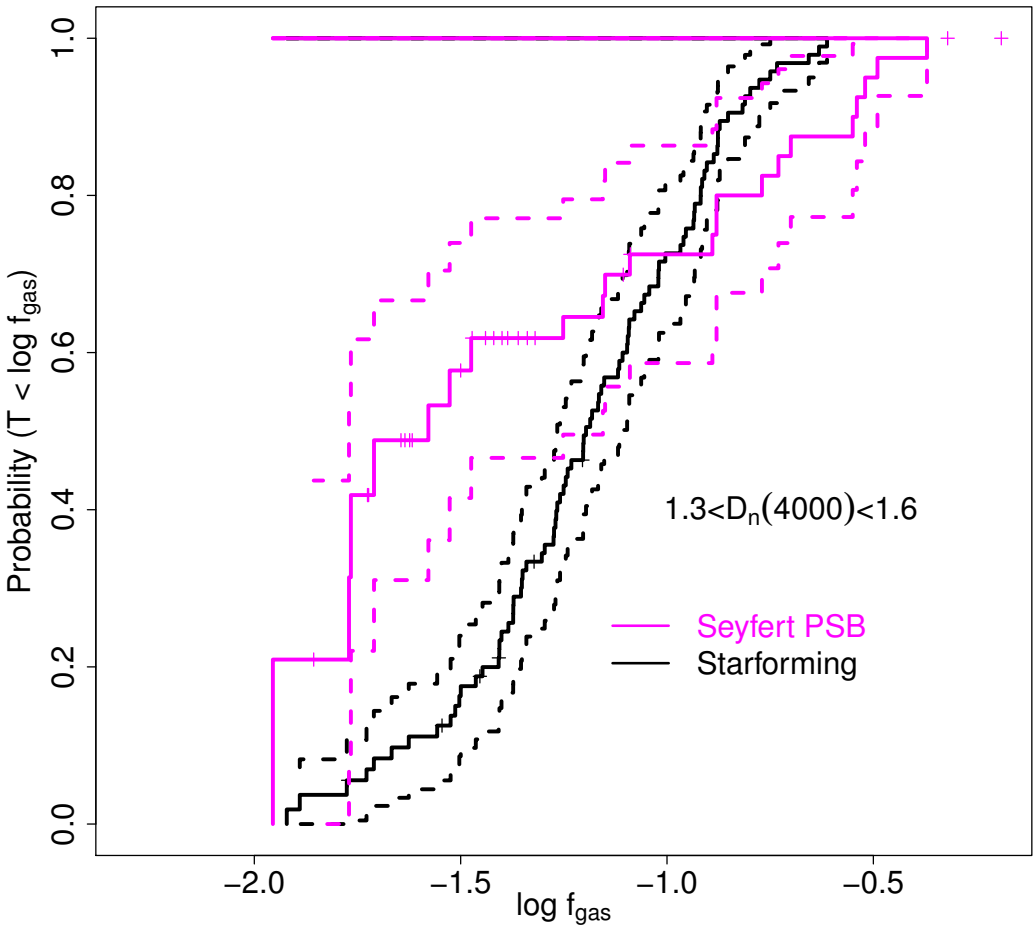

Figure 3.12:. Compares the ECDF of molecular gas fraction, $\log f_{\rm gas}$, of Seyfert PSBs and of star forming non-PSBs, both with $1.3 < D_n(4000) < 1.6$. The ECDF is estimated using the Kaplan & Meier (1958) estimator and takes into account the upper limits, which are shown as +s. 95% confidence curves are shown as dashed lines. The gas fractions in Seyfert PSBs is significantly different from those in non-PSBs of similar age.

PSBs is compared to that of the young non-PSBs, the test gives a χ^2 of 23.5 on one degrees of freedom corresponding to a p-value of 1.2×10^{-6}. Therefore, the null-hypothesis that the EDCFs for these two populations are the same can be rejected at a 4σ significance level. Similarly, the test gives a χ^2 of 15.7 on one degrees of freedom, corresponding to a p-value of 7.5×10^{-5}, when EDCFs of all-PSBs and non-PSBs with $D_n(4000) < 1.6$ are compared. The difference is even more significant if we compares late stage PSBs with non-PSBs, both groups having $1.3 < D_n(4000) < 1.6$.

Having established that there is a statistically significant difference between the gas fraction of young non-PSBs and of PSBs in general, and of Seyfert PSBs in particular, in the rest of this section we quantify the gas fractions of the PSBs at the end of their evolution ($\lesssim$ 1Gyr) and show that they are similar to those of quiescent galaxies, $-2.28 \lesssim \log f_{\rm gas} \lesssim -1.62$. For this purpose, we first demonstrate that the WISE flux ratio between 12μm and 4.6μm is an excellent proxy for $\log f_{\rm gas}$ using the COLD GASS sample of non-PSBs (Saintonge et al., 2011) and then use it as a tool to constrain the gas fraction in PSBs. Stellar populations younger than 0.6 Gyr dominate the 12μm emission and, this ratio is known to correlate well with the specific star formation rate (sSFR, Donoso et al., 2012). The AGN hot dust emission is mostly between $\sim 3-5$ and this ratio is not appreciably affected by AGN emission and it also probes sSFR well in AGN (Donley et al., 2012; Donoso et al., 2012). Yesuf et al. (2014) have shown that starbursts and post-starbursts form a sequence in this ratio, with starbursts having the highest ratios and quiescent PSBs having ratios similar to those of green-valley and red-sequence galaxies.

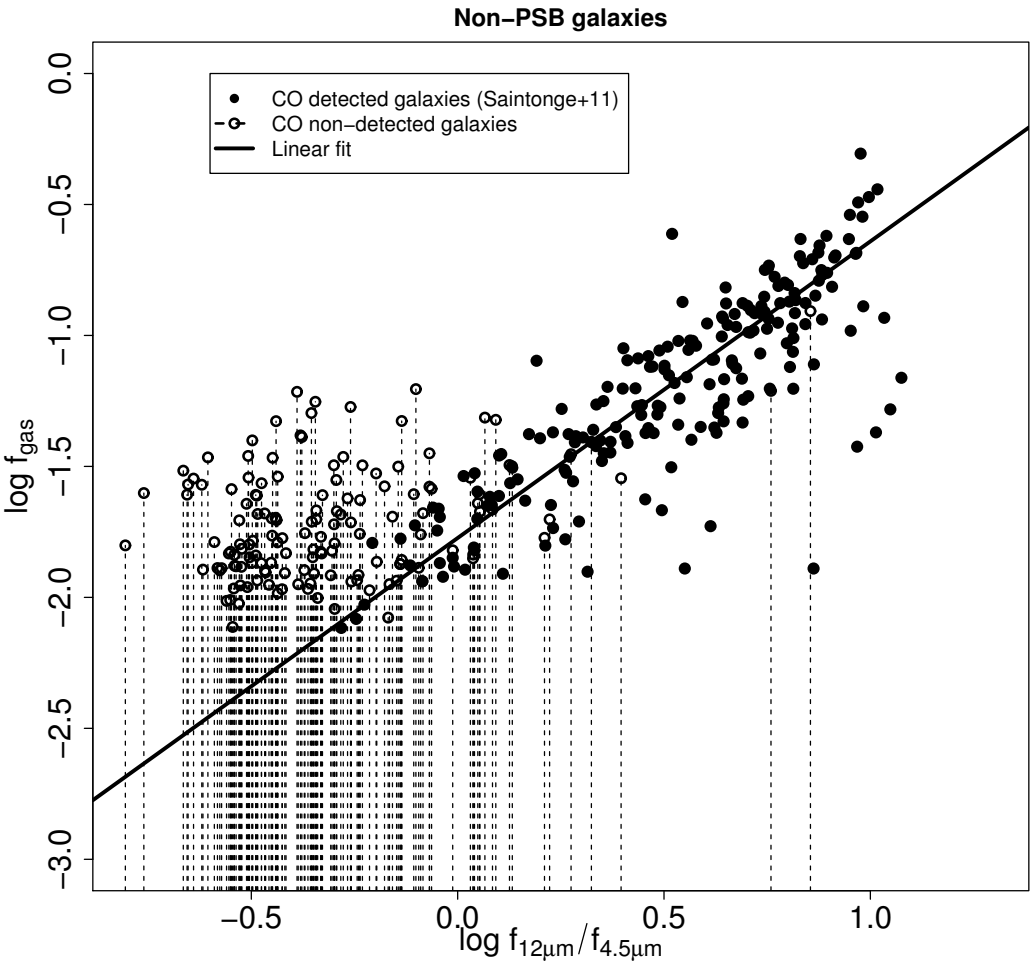

Figure 3.13:. WISE flux ratio $\log f_{12}/f_{4.6}$ versus molecular gas fraction for galaxies in COLD GASS survey (Saintonge et al., 2011). The filled circles denote galaxies with CO detections while the open circles and the dashed lines denote non-detected galaxies and their upper-limits. The black line is the linear fit to the data and it includes the upper-limits. The $\log f_{12}/f_{4.6}$ is an excellent proxy for the molecular gas fraction.

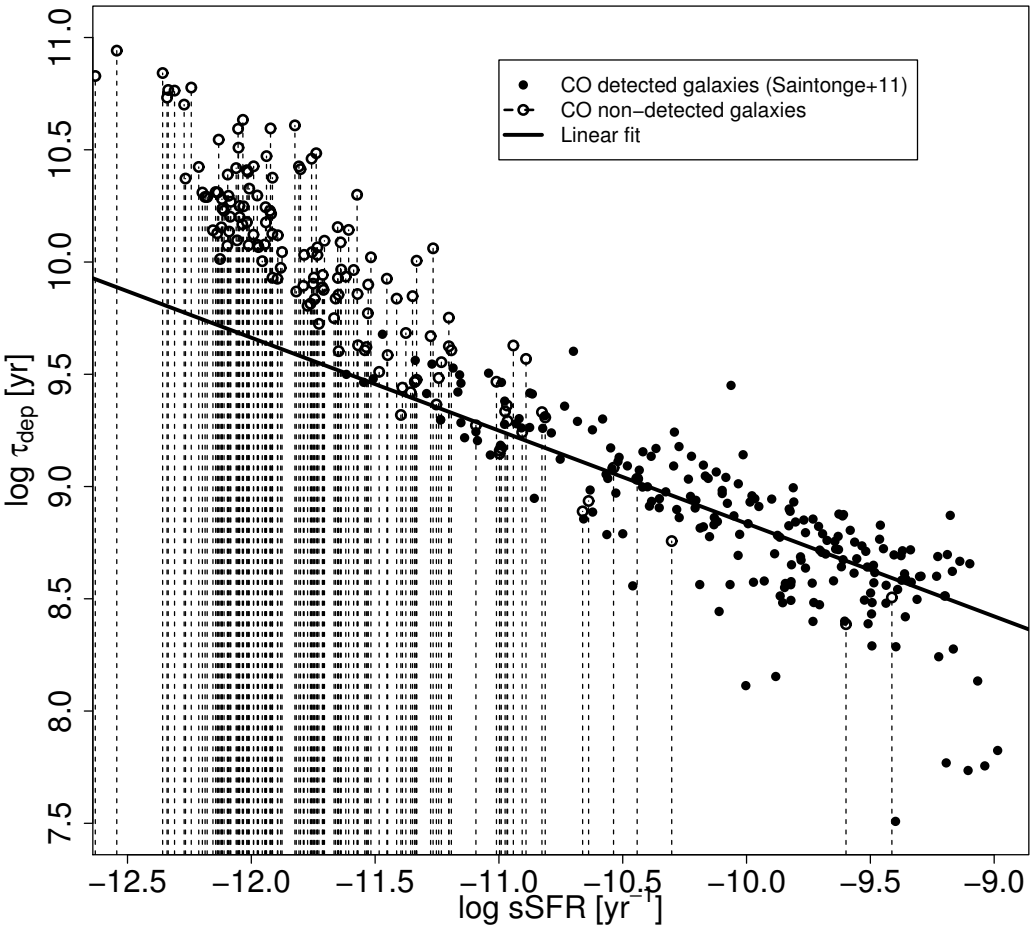

Figure 3.14:. Specific star formation rate versus molecular depletion time for galaxies COLD GASS survey. The filled circles denote galaxies with CO detections while the open circles and the dashed lines denote non-detected galaxies and their upper-limits. The black line is the linear fit to the data and it includes the upper-limits. We use the WISE flux ratio $\log f_{12}/f_{4.6}$ to estimate the sSFR following Donoso et al. (2012).

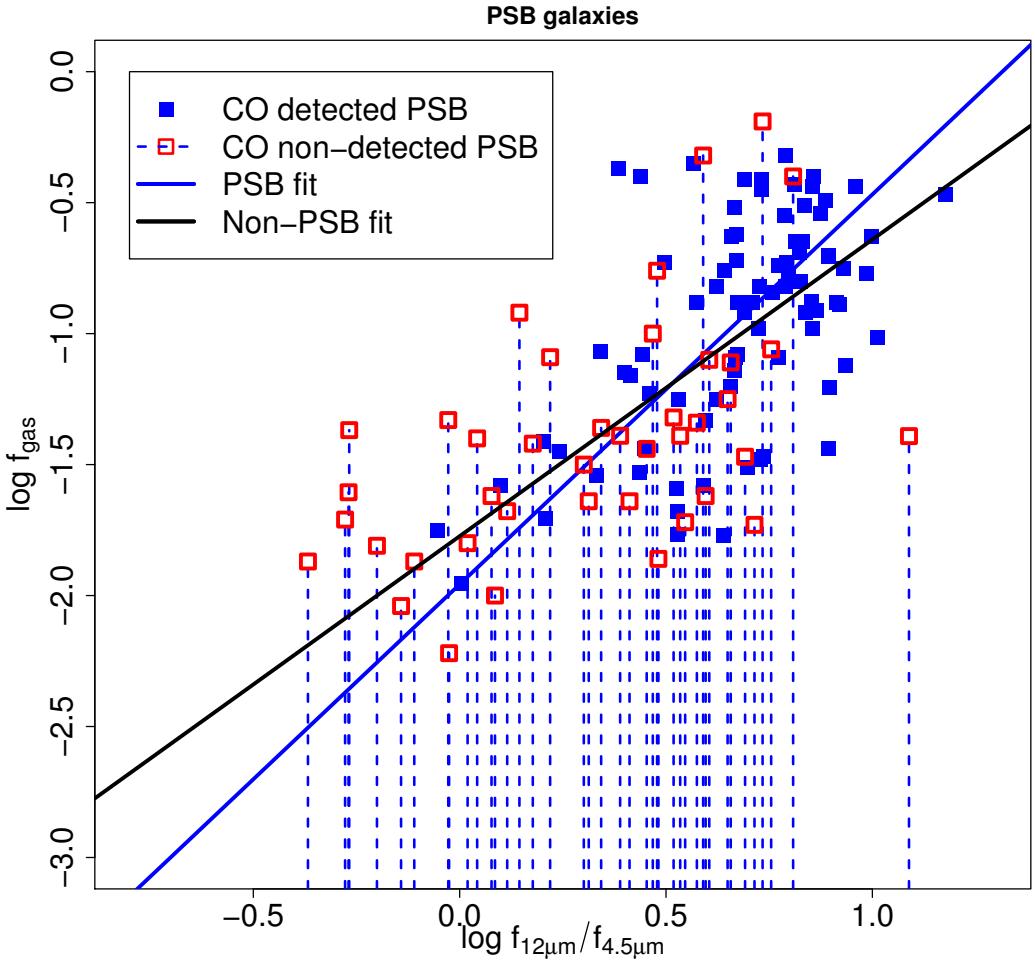

Figure 3.15:. WISE flux ratio log $f_{12}/f_{4.6}$ versus molecular gas fraction for PSBs (in this work, French et al., 2015; Rowlands et al., 2015; Alatalo et al., 2016). The filled blue squares denote PSBs with CO detections while the open red squares and the dashed lines denote non-detected PSBs and their upper-limits. The blue line is a linear fit to the PSB data ncluding the upper-limits while the black line is the fit for non-PSBs in Figure 3.13. The slope of the best fit line (the correlation) for PSBs is statistically significant. The fit indicates that PSBs reach the gas fraction observed in normal quiescent galaxies at end of their evolution, $\sim$ 1 Gyr. Therefore, both the star formation rate and molecular gas evolution in PSBs are rapid.

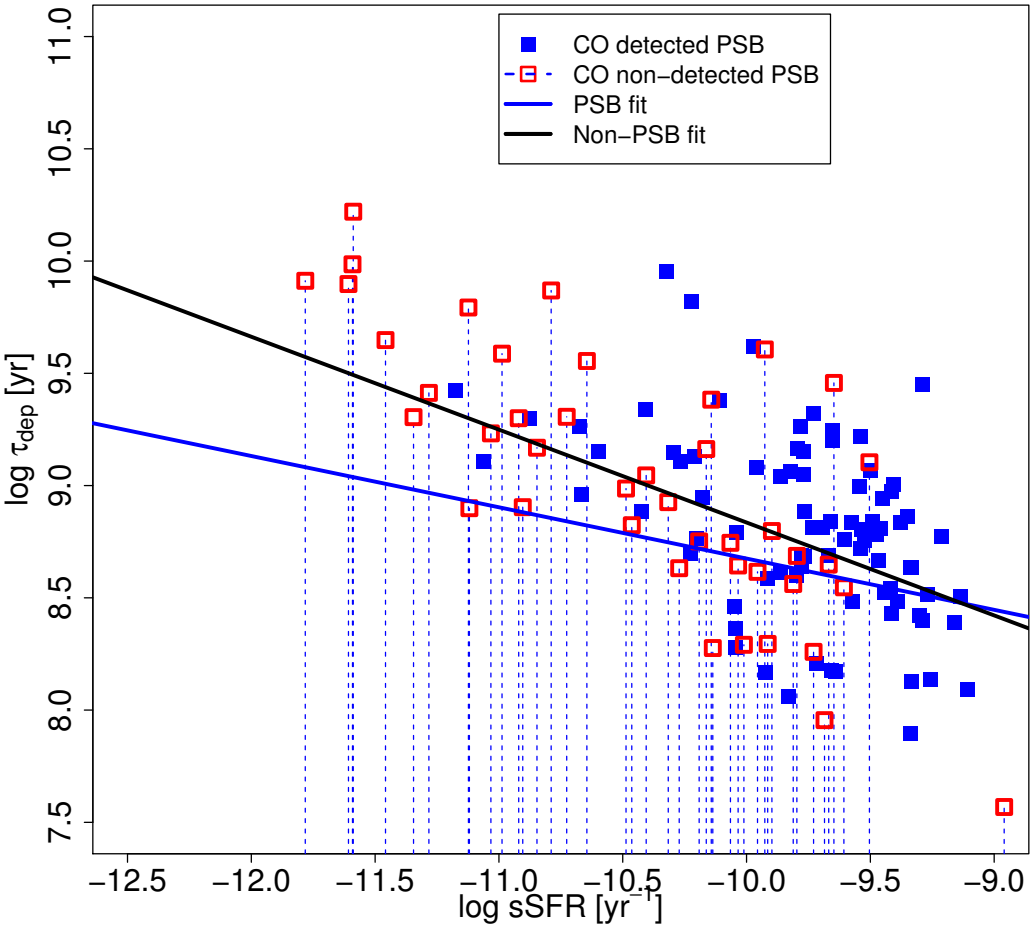

Figure 3.16:. The Specific star formation rate versus molecular depletion time for PSBs. We use the WISE flux ratio $\log f_{12}/f_{4.6}$ to estimate the sSFR following Donoso et al. (2012). The blue line is our fit for the PSB data shown as squares (this work, French et al., 2015; Rowlands et al., 2015; Alatalo et al., 2016). This fit is not statistically significant. The data is consistent with no dependence of depletion time on sSFR for PSBs. The black line is the fit to the data for non-PSBs from Figure 3.14. Despite the large scatter, there is a hint in the data that the depletion times of PSBs may be on average lower than that of non-PSBs provided that both samples follow similar relation between $\log f_{12}/f_{4.6}$ and sSFR. This relation is quite uncertain for PSBs. Here we assume $\alpha_{CO} = 4.3\,M_{\odot}(K\,km\,s^{-1}pc^{2})^{-1}$ and lower α_{CO} will shift the PSB depletion times further down.

Figure 3.13 shows the WISE flux ratio $\log f_{12}/f_{4.6}$ versus $\log f_{\rm gas}$ for non-PSB galaxies in the COLD GASS survey. As shown in the Appendix, the general population of SDSS galaxies show bimodal $\log f_{12}/f_{4.6}$ distribution. Star-forming galaxies have ratios between $\log f_{12}/f_{4.6} \sim$ 0.2–1 while quiescent galaxies have ratios between $\log f_{12}/f_{4.6} \sim$ -0.8–0.0. A tight correlation is observed between $\log f_{12}/f_{4.6}$ and $\log f_{\rm gas}$ in the COLD GASS sample. The slope of the best fit line is $\beta = 1.132$ and its intercept is $\beta_0 = -1.8 \pm 0.1$. The Kendall's τ correlation coefficient for the fit is 0.643. The statistical significance of the correlation is more than 5σ. One can easily show that β and β_0 are related to the logarithm of the molecular gas depletion time at a given sSFR by the relation: $\log \tau_{\rm dep} = \hat{\beta} \log {\rm sSFR} + \hat{\beta}_0$, where $\hat{\beta} = (\beta/\alpha - 1)$, $\hat{\beta}_0 = -\beta(\alpha_0/\alpha + 0.769) + \beta_0$, where α and α_0 define the relation: $\log {\rm sSFR} = \alpha(\log f_{12}/f_{4.6} + 0.769) + \alpha_0$. Donoso et al. (2012) computed the relation between sSFR and 4.6 - 12μm color in Vega magnitude and 0.769 is subtracted to change the color to AB magnitude. They found $\alpha = 2.5 \times 0.775 = 1.938$ and $\alpha_0 = -12.56$ for the SDSS star-forming galaxies. Using these values with our fitted values of β and β_0 gives $\hat{\beta} = -0.416$ and $\hat{\beta}_0 = 4.7$. In comparison, Huang & Kauffmann (2014) found $\hat{\beta} = -0.37 \pm 0.04$ and $\hat{\beta} = 5.45 \pm 0.42$ for the COLD GASS sample. The authors used the GALEX FUV and WISE 22μm to estimate the sSFR. Our inferred depletion times are consistent with Huang & Kauffmann (2014) but there is likely a systematic offset in the two SFR estimates. Regardless, we would like to stress that β and β_0 can be related to the depletion time by using the relation between $\log f_{12}/f_{4.6}$ and sSFR found by Donoso et al. (2012) and assuming this relation is the same for PSBs and non-PSBs, one can compare the depletion times of the two populations in a

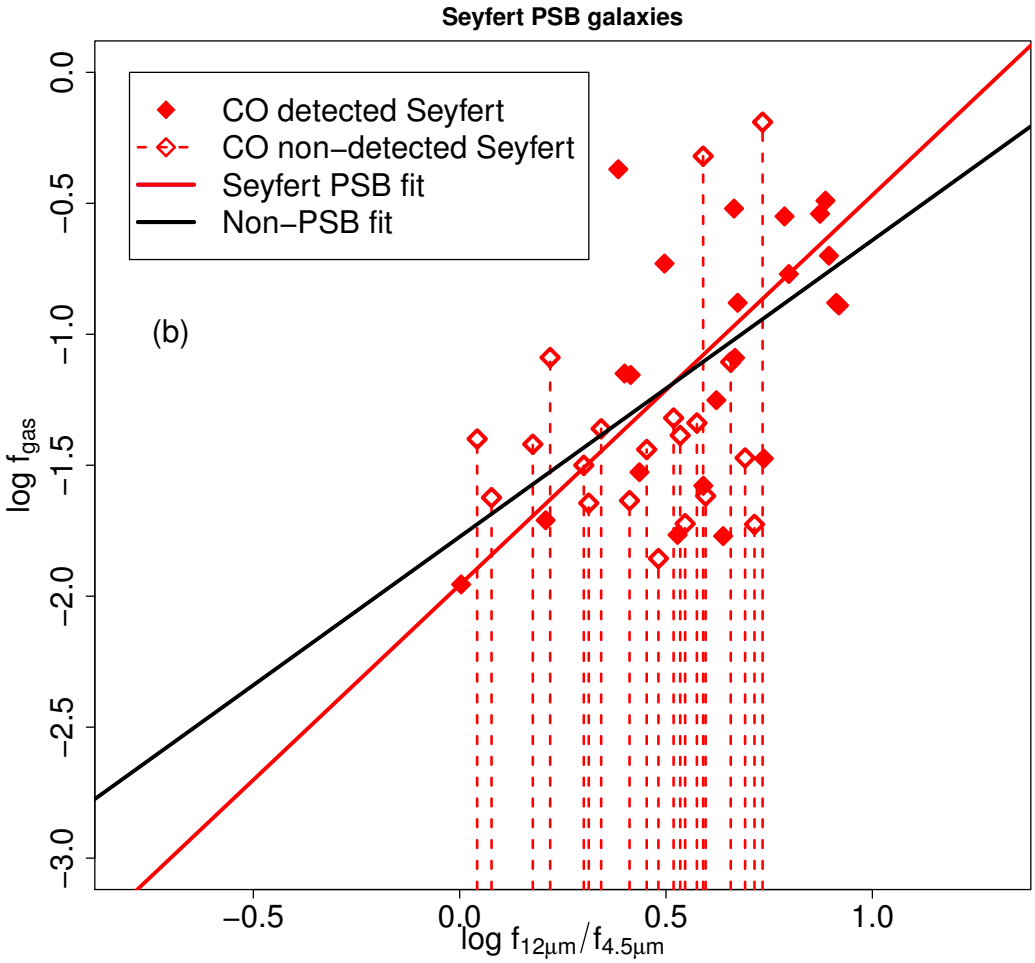

Figure 3.17:. Similar to Figure 3.15 but shows only Seyfert PSBs. The slope of the linear fit to Seyfert PSBs data is statistically significant. At later times, Seyfert PSBs have lower $\log f_{\rm gas}$ than the normal star-forming galaxies do.

relative sense. Figure 3.14 explicitly shows relationship between sSFR, inferred from the $\log f_{12}/f_{4.6}$, and the depletion times for non-PSB galaxies in the COLD GASS survey. As expected, the fitted line has more than 5σ significance, similar slope and intercept as given above. The main purpose of this figure is to show the scatter in this relation for later comparison with the depletion times of PSBs.

Figure 3.15 shows the relationship between $\log f_{12}/f_{4.6}$ and $\log f_{\rm gas}$ for PSBs. They also show statistically significant (5σ) correlation between these two quanti-

ties. The slope of the best fit line is $\beta = 1.489$ and its intercept is -1.957. Our analysis of the correlation between the gas fraction and D(4000) or the $\log f_{12}/f_{4.6}$ for non-PSB galaxies in COLD GASS survey suggests that a galaxy with gas fraction below $\sim$0.5–1% is consistent with being a red sequence galaxy (see also, Boselli et al., 2014). The $\log f_{12}/f_{4.6}$ is a rough age indictor, and the best fitting line for the relationship between $\log f_{12}/f_{4.6}$ and $\log f_{\rm gas}$ for PSBs, indicates that the old PSBs with low $\log f_{12}/f_{4.6}$ achieve gas fractions below 1%. The typical lifetime of a PSB is believed to be $\sim$ 1 Gyr (e.g., Wild et al., 2010; Snyder et al., 2011; Yesuf et al., 2014). As can be seen from Figure 3.3, the PSBs analyzed in this work have mean stellar ages less than one Gyr. The evolutionary time through the green valley for typical local galaxies is $\gtrsim 3$ Gyr (Martin et al., 2005). Therefore, the current data, albeit incomplete, suggests that the gas evolution in PSBs is rapid, and they reach the gas fractions observed in quiescent galaxies within $\sim$ 1 Gyr after the starburst.

It should be noted that the gas fractions in very nearby early type galaxies are found to be $\lesssim 0.1\%$ (e.g., Young et al., 2011). We think these galaxies are not a good comparison sample for our galaxies. Because of the redshift difference, there is huge difference in sensitivity of detecting molecular gas, and difference in the areas of the galaxies probed (i.e., aperture effects) between the two samples. It is possible that if the early type galaxies in COLD GASS are observed for longer integration times, their measured upper limits on their gas fractions may move significantly down and change the inferred slopes of our fits. But the same may also happen for the upper limits of the undetected PSBs, if they too are observed for longer times. So in a relative sense, using the incomplete data at hand, we

infer that the oldest PSBs in our sample achieve gas fractions similar to some of the red-sequence galaxies in the COLD GASS survey. It should be emphasized that this result is robust and is independent of the origins of the strong correlation between $\log f_{12}/f_{4.6}$ and $\log f_{\rm gas}$ for PSBs and non-PSBs. Future deeper and more complete observations of PSBs and a comparison sample will be necessary to unequivocally affirm or refute this result.

To further interpret the observed strong correlation between $\log f_{12}/f_{4.6}$ and $\log f_{\rm gas}$ in PSBs, Figure 3.16 shows the sSFR versus the depletion time for PSBs. To calculate these two quantities, we assume the relationship between $\log f_{12}/f_{4.6}$ and sSFR found by Donoso et al. (2012) holds for PSBs. Therefore, here we are ascribing the origin $\log f_{12}/f_{4.6}$ in PSBs to be ongoing star formation. However, it should be noted that the relationship between the ongoing star formation rate and mid-IR emission is complicated for PSBs. These galaxies may simply be luminous in the mid-IR because of their TP-AGB stars long after the cessation of their ongoing star formation activity (Kelson & Holden, 2010). Therefore, the calibration we adopt and its implication are very uncertain for PSBs. Regardless, with the above caveat, we explore the implication of adopting this same calibration for the depletion times of PSB galaxies. The blue line in Figure 3.15 shows the best fit line for sSFR versus the depletion time for PSBs. For a comparison, the fit for non-PSBs in Figure 3.14 is shown by the black line. The blue line has a slope of $\hat{\beta} = -0.23$ and an intercept $\hat{\beta}_0 = 6.4$. The fit to the data is not statistically significant and the data is consistent with no trend between sSFR and depletion time for PSBs. Thus, the figure suggests that the depletion times for PSB may be on average around ~ 1 Gyr regardless of sSFR, and they may also be lower

than the depletion times of non-PSBs at lower sSFR. If the adopted calibration is correct, it implies that a mechanism other than star-formation must be depleting gas when the star-formation is low.

Similarly, Figure 3.17 shows the relationship between $\log f_{12}/f_{4.6}$ and $\log f_{\rm gas}$ for only Seyfert PSBs. They also show statistically significant (3σ) correlation between these two quantities. The Kendall's τ correlation coefficient is 0.36 with p-value of 0.0006. The slope of the best fit line is $\beta = 1.626$ and its intercept is -2.067. Similarly, Figure 3.18 shows sSFR versus the depletion time for Seyfert PSBs, again assuming the $\log f_{12}/f_{4.6}$ traces sSFR in these galaxies. The best fit red line has a slope of $\hat{\beta} = -0.15$ and an intercept $\hat{\beta}_0 = 7.0$. The fit to the data is not statistically significant and the data is consistent with no trend between sSFR and depletion time for Seyfert PSBs. If our calibration is correct, perhaps AGN feedback may be the mechanism for depleting gas at later times when the star-formation is low. Donoso et al. (2012) have shown that the relationship between $\log f_{12}/f_{4.6}$ and $\log f_{\rm gas}$ for strong AGN, with O III luminosity above $10^7 L_{\odot}$, is is similar to that of normal star-forming galaxies. The Seyfert PSBs studied in this work satisfy this criterion of strong AGN.

3.5 Discussion

3.5.1 Comparison of our sample with the previous samples of PSBs

We study the molecular gas evolution of 126 post-starburst galaxies, of which 24 have new observations undertaken by us while the rest are compiled from

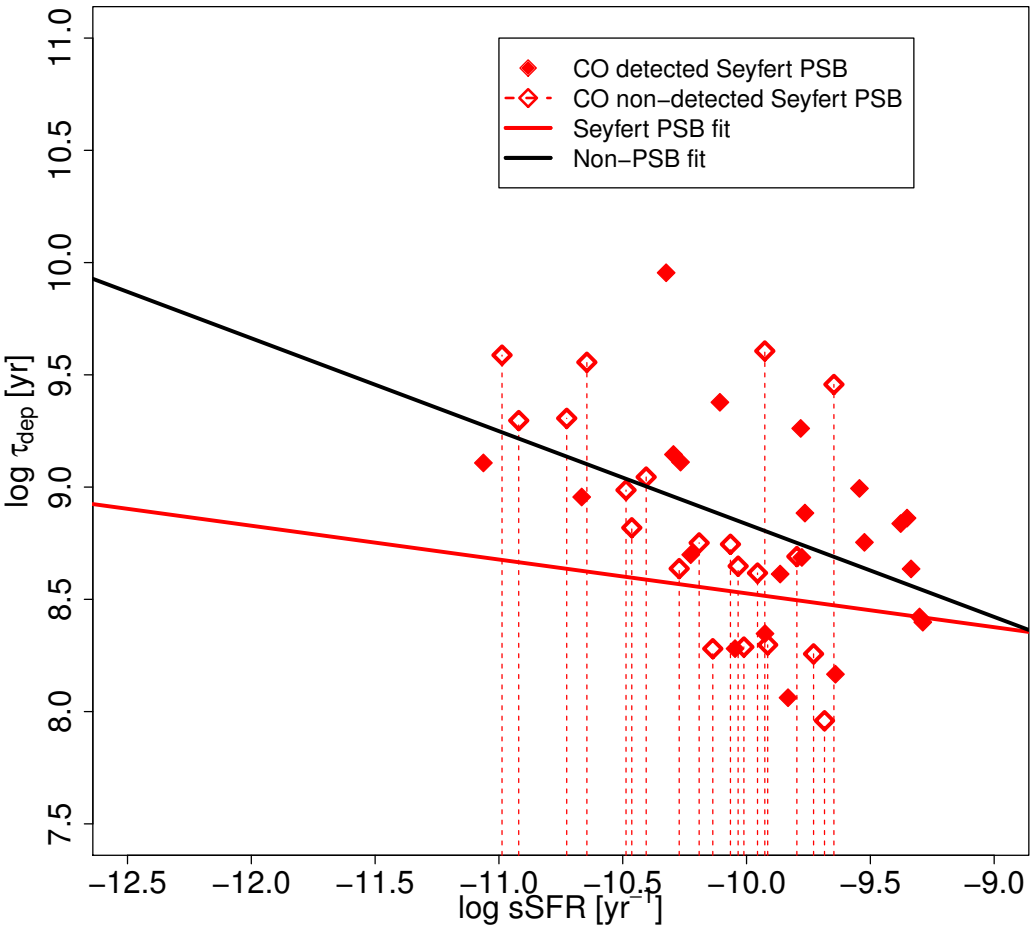

Figure 3.18:. The specific star formation rate versus molecular depletion time for Seyfert PSBs. We use the WISE flux ratio $\log f_{12}/f_{4.6}$ to estimate the sSFR following Donoso et al. (2012). The red line is our fit for the Seyfert PSB data shown as diamonds (this work, French et al., 2015; Rowlands et al., 2015; Alatalo et al., 2016). This fit is not statistically significant. The data is consistent with no dependence of depletion times on sSFR for Seyfert PSBs. The black line is the fit to the data for non-PSBs from Figure 3.14. There is a hint in the data that the depletion times of Seyfert PSBs may be on average lower than that of non-PSBs. Here we assume $\alpha_{\rm CO} = 4.3\,{\rm M}_\odot({\rm K\,km\,s^{-1}pc^2})^{-1}$ and lower $\alpha_{\rm CO}$ will shift the Seyfert PSB depletion times further down.

the literature (Saintonge et al., 2011; Rowlands et al., 2015; French et al., 2015; Alatalo et al., 2016). The galaxies in the new sample are selected using their spectral indices and NUV-g colors, to identify them as green valley PSBs, and their emission line ratios, to identify them as Seyferts. Our sample represents half of the Seyferts PSBs in the combined sample. The Seyfert PSBs from the previous works were "randomly" selected and are mostly younger than our PSBs. Analyzing our sample together with the existing samples, we find that as the starburst ages, both the star formation rate and molecular gas fraction decrease with time, and PSBs attain gas fractions observed in quiescent galaxies within one billion years. Therefore, the evolution of molecular gas in PSBs is rapid compared to normal galaxies. We observe a sharp decline of $\log f_{\rm gas}$ in PSBs at ~ 0.6 Gyr after the starburst. We interpret this as evidence for the AGN feedback. We show that $\log f_{\rm gas}$ distribution of the Seyfert PSBs is significantly different from that of non-PSB galaxies of similar age. The previous works reached different conclusions than ours because 1) they individually did not sample well the whole starburst-AGN-quenched PSB evolutionary sequence and 2) the quenched PSBs sample was contaminated by dust-reddened PSBs in Hα, giving a false impression that PSBs have a large amount of gas at the end of their evolution. We use the significant correlation between $\log f_{12}/f_{4.6}$ and $\log f_{\rm gas}$, observed in both PSBs and non-PSBs, to show that some of the Hα-weak PSBs are not yet quenched. This section explicitly shows the previous samples and our samples in the $\log f_{12}/f_{4.6}$ vs. $\log f_{\rm gas}$ diagrams and discusses their plausible relationships.

Figure 3.19 plots the the WISE flux ratio $\log f_{12}/f_{4.6}$ versus $\log f_{\rm gas}$ and compares our Seyfert PSBs with the "quenched" PSBs studied by French et al. (2015).

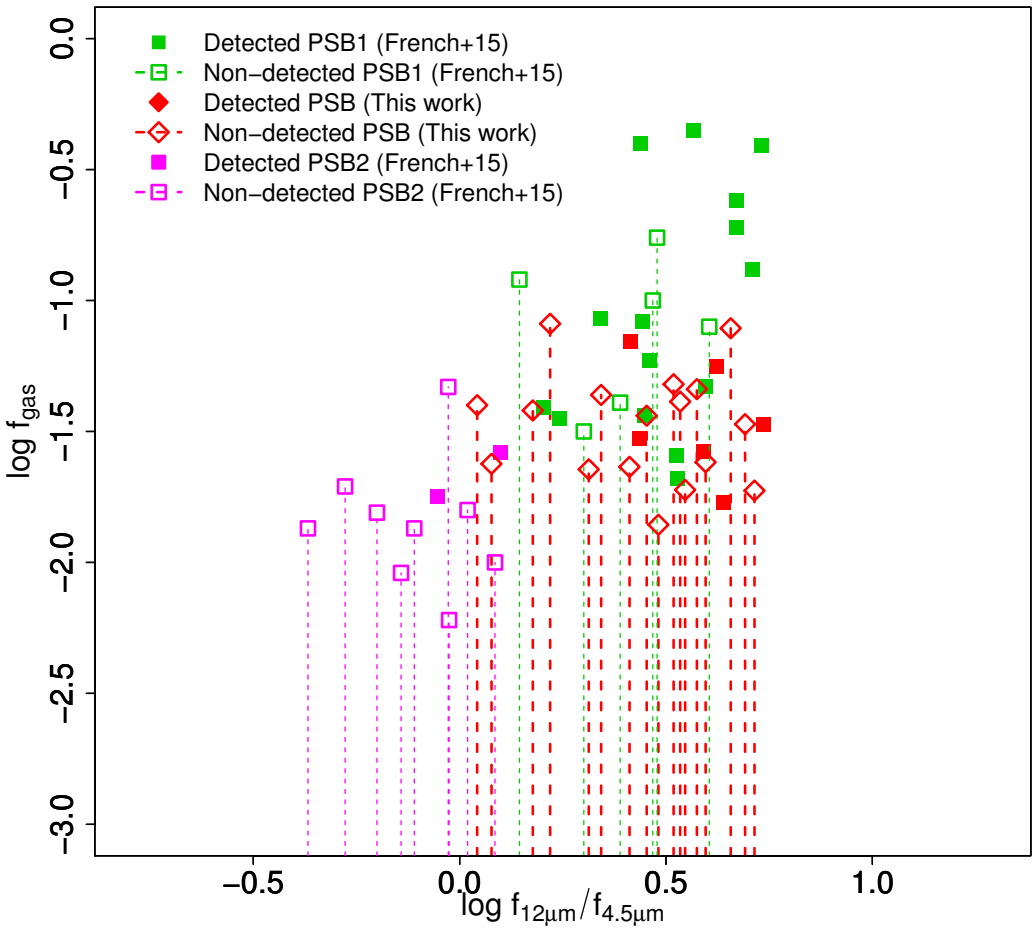

Figure 3.19:. compares WISE flux ratio $\log f_{12}/f_{4.6}$ and molecular gas fraction $\log f_{\rm gas}$ of our Seyfert PSBs with those of PSBs studied by French et al. (2015). The latter PSBs were selected because they lack significant Hα emission but show strong $H\delta$ absorption. A significant number of them have obscured star formation and high gas fractions. Therefore, they are not fully quenched yet. Some of them may be descendants of our sample while others are likely precursors to our sample.

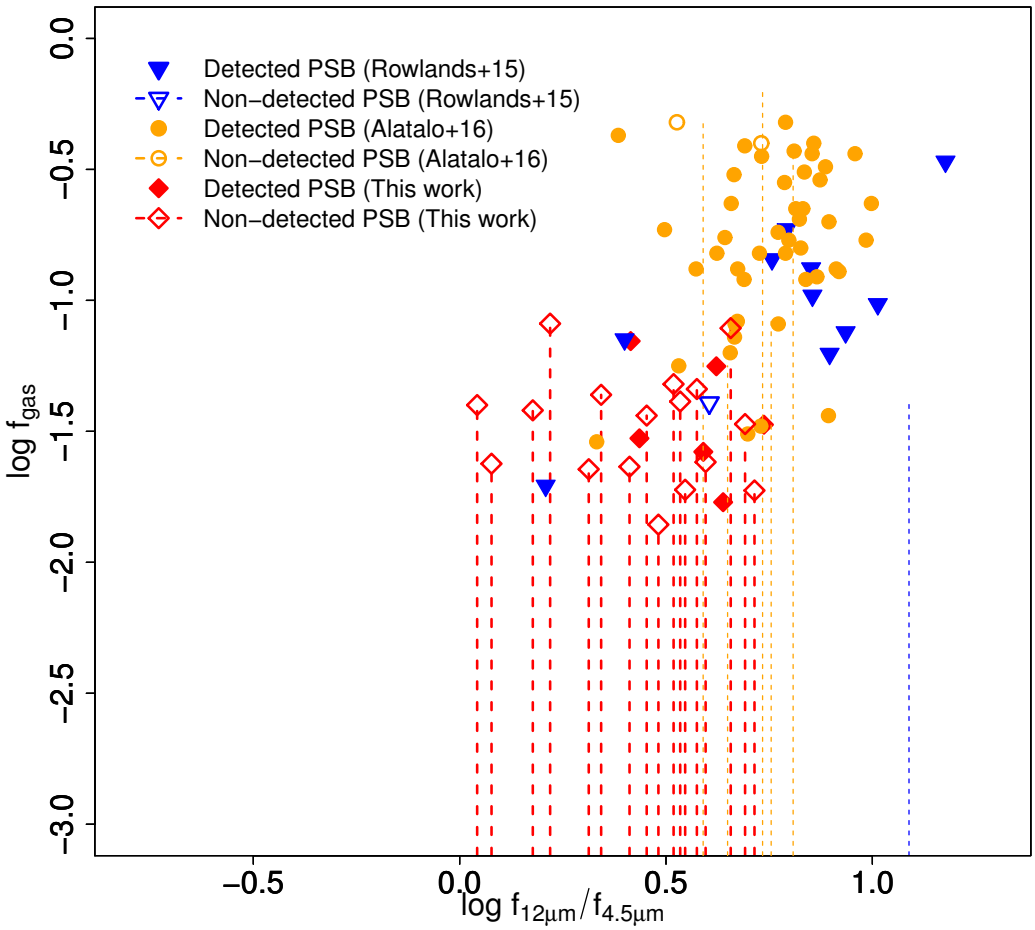

Figure 3.20:. compares WISE flux ratio $\log f_{12}/f_{4.6}$ and molecular gas fraction $\log f_{\rm gas}$ of our Seyfert PSBs with those of PSBs studied by Rowlands et al. (2015) and Alatalo et al. (2016). The PSBs in the two works generally have higher star formation and gas fraction than our Seyfert PSBs. Their stellar population age indicates that they are likely precursors to our sample.

The authors selected their sample using the traditional definition of PSB which requires lack of a significant Hα emission (ongoing star-formation) and a strong $H\delta$ absorption (recent star-formation). A large amount of gas ($\log f_{\rm gas} \gtrsim 0.1$) was reported in half of this sample. It was quite surprising that about half of these seemingly quiescent PSBs have similar gas fractions as normal star-forming galaxies. The authors argued that the large amount of molecular gas in these galaxies rules out complete gas consumption, expulsion, or starvation as the primary mechanism that ends the starburst in these galaxies. However, Figure 3.19 shows that about two-thirds of the French et al. (2015) PSBs have obscured star formation unseen in Hα, which explains the observed high molecular gas contents of these galaxies. In other words, these obscured PSBs have $\log f_{12}/f_{4.6}$ and $\log f_{\rm gas}$ similar to those of star-forming galaxies. The French et al. (2015) sample as whole shows a significant correlation between $\log f_{12}/f_{4.6}$ and $\log f_{\rm gas}$; the PSBs with high obscured star formation rates have high gas fractions. For an illustrative purpose, we split the sample into two populations using $\log f_{12}/f_{4.6} = 0.1$ as approximate boundary between the green-valley and the blue-cloud. We refer to the split samples as PSB1 and PSB2. The PSB2 sample has $\log f_{12}/f_{4.6} < 0.1$. As it can be inferred from the series of plots in the Appendix, the population with $\log f_{12}/f_{4.6} > 0.1$ have stellar ages younger or comparable to the ages of our Seyfert PSBs. These Hα obscured PSBs span similar $\log f_{12}/f_{4.6}$ range as our Seyferts PSBs but have significantly higher gas fractions than the PSBs in our sample do. Therefore, if this population is evolutionarily linked to our Seyfert PSBs, the dramatic drop in gas fraction at similar $\log f_{12}/f_{4.6}$ is could be a signature of AGN feedback.

The existence of the evolutionary link also implies that the PSB1 sample might

harbor heavily obscured AGN (undetected in both the BPT line-ratio AGN diagnostic and the WISE two color diagram), or their black holes are dormant now but will be reactivated as they evolve to become like our Seyfert PSBs. The second implication seems more likely. The episodic lifetime of an individual AGN event is currently not well-constrained and it may range between $\sim 0.3 - 1$ times the effective AGN lifetime (Hopkins & Hernquist, 2009). The effective AGN lifetime for the Seyfert PSBs is likely to be $\sim$ 2 Gyr. This estimate uses the median $\sigma = 110\,\mathrm{km\,s^{-1}}$ to estimate the median black hole mass, $10^{7.4}\mathrm{M}_{\odot}$, from the $\mathrm{M_{BH}} - \sigma$ relation (Kormendy & Ho, 2013), the median dust-corrected O III luminosity, $10^{7.3}\mathrm{L}_{\odot}$, to estimate the Eddington ratio, $\lambda = 0.003$, (Lamastra et al., 2009), and Figure 9 of Hopkins & Hernquist (2009) to estimate the effective AGN lifetime from $\mathrm{M_{BH}}$ & λ. The effective AGN lifetime for the Seyfert PSBs is longer than the quenched PSB lifetime of $\sim$ 1 Gyr, which suggests than the quenched PSBs may experience another episode of AGN activity. Canalizo & Stockton (2013) have also observed intermediate age (0.7–2.4 Gyr) stellar populations in elliptical galaxies hosting QSOs. Therefore, a second episode of AGN activity is not unlikely within or beyond the typical lifetime of PSBs.

On the other hand, the French et al. (2015) PSB2 sample, with $\log f_{12}/f_{4.6} < 0.1$, have both lower sSFR and lower molecular gas contents than do our Seyfert PSBs. It is not clear how they are evolutionary linked to our sample. As shown in the Appendix, the $D_n(4000)$ vs. Hδ plots indicates that our sample has $\sim$1–2Å lower Hδ absorption equivalent width, but similar $D_n(4000)$. Thus, they seem to have overall older ages. If this is the case, the immediate precursors of the genuinely quiescent PSBs of French et al. (2015) sample may be missing in the

current data. But we note that there are some Seyferts with higher Hδ in the previous PSB samples which may evolve to be PSB2s.

Alternatively, if we insist that the PSB2s are linked to our sample, the difference in Hδ absorption may be due to a selective dust-extinction prior to the dust removal by AGN feedback, not mainly due to an age difference. Snyder et al. (2011) found that the AGN feedback can disperse the remaining diffuse gas and dust from the central few kilo-parsec region. As a result, the observed Balmer absorption strength can be enhanced after the feedback. The authors found a difference of $\sim$ 1Å between their simulations with and without AGN feedback. This might explain why the PSB2 sample has lower sSFR and $\log f_{\rm gas}$ but higher Hδ than our sample does. Future more sensitive observations can distinguish between these two scenarios by studying green valley Seyfert PSBs with Hδ >5Å by surveying larger volume than we did in this work.

Fig 3.20 replots $\log f_{12}/f_{4.6}$ versus $\log f_{\rm gas}$ compares our sample with the PSBs studied by Rowlands et al. (2015) and Alatalo et al. (2016). Even though there is some overlap, the majority of PSBs from these two studies have both high sSFR and high molecular gas fractions in comparison to our sample. The stellar properties of the PSBs in these two works indicate that most of them are likely precursors to the PSBs in our sample and to those in the French et al. (2015) sample.

In summary, although the previous samples of PSBs may relate to our sample in a complicated way, analyzing them as whole, we have uncovered a relatively simple evolutionary picture of molecular gas and star formation in post-starburst galaxies. In this picture, the molecular gas and star-formation rates decrease

rapidly in tandem; Within $\sim$ 1 Gyr, molecular gas fraction in PSBs change from several tens of percents, seen in normal star-forming galaxies and starbursts, to less than one percent, seen in elliptical galaxies.

3.5.2 Comparison of our sample with the previous samples of infrared luminous galaxies and quasars

In this section we will investigate whether or not the gas contents our Seyfert PSBs are consistent with their being remnants of gas-rich, merger-induced starbursts and quasars (Hopkins et al., 2008; Wild et al., 2009; Snyder et al., 2011).

Luminous Infrared luminous galaxies (LIRGs, Sanders & Mirabel, 1996) are galaxies with intense infrared emission ($> 10^{11}$ $L_{\odot}$) as a result of merger-induced starburst or/and AGN activities. Larson et al. (2016) studied the relationship between molecular gas fraction and merger morphology as a function of infrared luminosity and merger stages. The study used a sample of 65 local LIRGs from the Great Observatories All-Sky LIRG Survey (GOALS, Armus et al., 2009). Less than a third of the sample are Seyferts.

Fig 3.21 replots $\log f_{12}/f_{4.6}$ versus $\log f_{\rm gas}$ with the 42 LIRGs detected in the WISE survey to compare them with our sample. The LIRGs are denoted by the purple filled circles. In comparison to our Seyfert PSBs, the LIRGs have higher gas fractions and $\log f_{12}/f_{4.6}$. But there is a significant overlap in gas fraction and $\log f_{12}/f_{4.6}$ between the LIRGs and the PSBs studied by Alatalo et al. (2016). A large fraction (37–46%) of the Alatalo et al. (2016) sample was visually classified as morphologically disturbed.

Figure 3.21 also overplots some of the nearby QSOs with molecular gas mass

measurements (Evans et al., 2001; Scoville et al., 2003; Xia et al., 2012). Xia et al. (2012) studied a sample of 19 ultra-luminous infrared QSO (IR QSO) at $z \sim 0.1 - 0.3$. They found that the molecular gas properties of the IR QSOs are similar to those observed in LIRGs. Their result suggested that large amount of molecular gas exists to sustain massive starbursts even in the ultra-luminous IR QSO phase. Direct comparison between this sample and the PSB samples is difficult to make because accurate stellar mass estimates for IR QSO do not exist. Using the black hole mass and the total stellar mass scaling relation found by Reines & Volonteri (2015), we make rough estimates of the stellar masses of the IR QSOs and calculate their gas-to-stellar mass fractions. We use the black hole mass estimates by Hao et al. (2005). According to our estimate, the IR QSOs have similar gas fraction as LIRGs but have significantly higher gas fraction than our Seyfert PSBs. The sSFR of the IR QSOs, inferred from the $\log f_{12}/f_{4.6}$, is more similar to our Seyfert PSBs than to the LIRGs.

In comparison to our sample, the Palomar-Green quasi-stellar objects (PG QSOs) with molecular gas observations, WISE observations, and black hole mass estimates (Evans et al., 2001; Scoville et al., 2003; Hao et al., 2005) at $z \sim 0.1$, have similar or lower gas fractions than which is observed in our Seyfert PSBs. Several molecular studies have found more gas-rich quasars than PG QSOs (e.g., Bertram et al., 2007; Villar-Martín et al., 2013; Rodríguez et al., 2014). PG QSOs seem to reside in the lower end of the correlation between molecular gas and infrared luminosity seen in the local QSOs studied to date.

In summary, AGN/QSOs span a wide range of molecular gas fraction ($\sim 0.3 - 30\%$) at similar $\log f_{12}/f_{4.6}$. Our Seyfert PSBs have lower $\log f_{\rm gas}$ than LIRGs

and IR QSOs but similar $\log f_{\rm gas}$ as in PG QSOs. Thus, their gas content is consistent with their being remnants of gas-rich, merger-induced starbursts and quasars (Hopkins et al., 2008; Wild et al., 2009; Snyder et al., 2011). Some QSOs have high molecular gas contents, which indicates that most of the gas is consumed by the starbursts and is not expelled immediately by the quasar.

3.5.3 Comparison with quenching early types

Schawinski et al. (2009b) studied a sample 24 early-type galaxies with minor episodes of starburst. These galaxies are in the process of moving from the blue-cloud to the red-sequence via a low-luminosity AGN. 10 of their galaxies were composites of AGN and star formation activity and 4 were Seyferts. An abrupt drop of gas mass in the composite galaxies, and non-detections in the four Seyferts were reported. The authors interpreted their observations as evidence for the destruction of molecular gas by AGN feedback. Rowlands et al. (2015) stressed that their result disagrees with that of Schawinski et al. (2009b). Figure 3.22 compares $\log f_{\rm gas}$ of our sample with that of the Schawinski et al. (2009b). We find excellent agreement between the gas fractions of our Seyfert PSBs and those of the Seyferts and composite galaxies studied by Schawinski et al. (2009b).

3.5.4 Velocity offsets and Molecular outflows

Cicone et al. (2014) reported high velocity molecular outflows driven by AGN. 10 of their sample are Seyferts. The $\log f_{12}/f_{4.6}$ of their Seyfert sample is similar to ours and has a median, mean and standard deviation of 0.67, 0.63, and 0.24 respectively. Two of their Seyferts are among the PG QSOs discussed above.

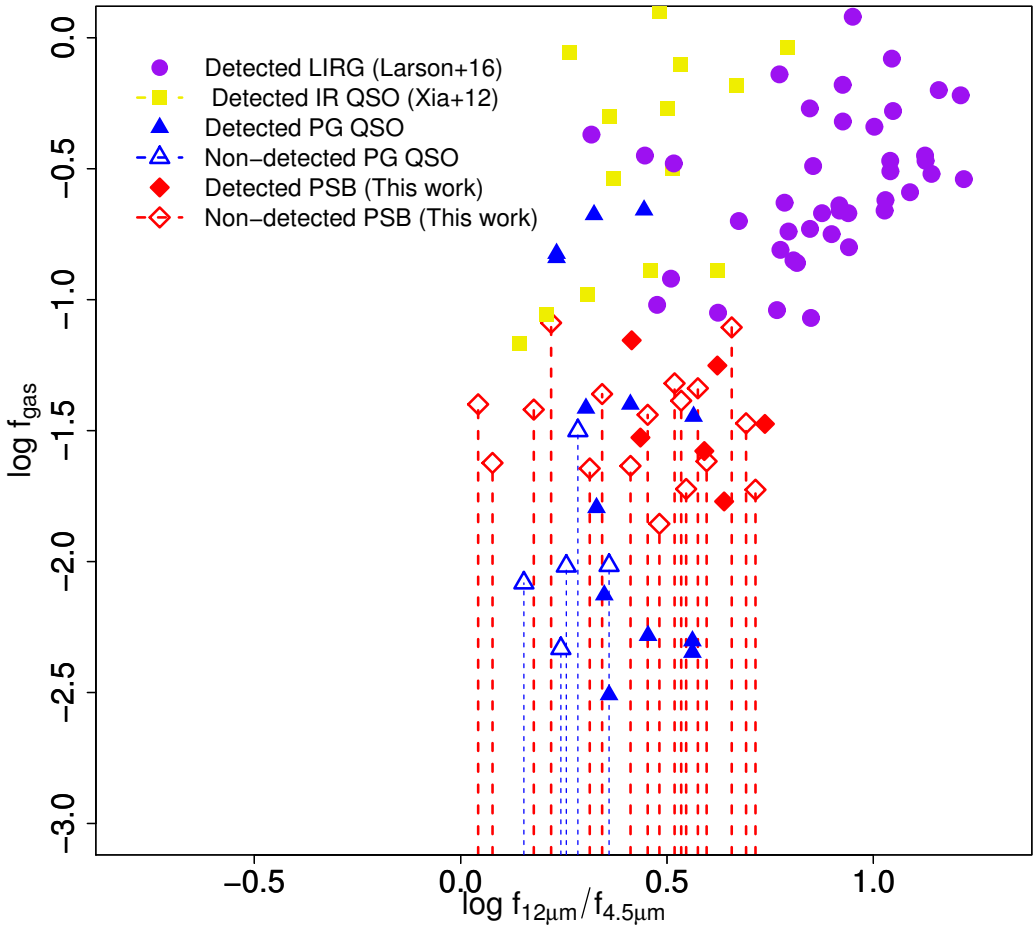

Figure 3.21:. compares WISE flux ratios, log $f_{12}/f_{4.6}$, and molecular gas fractions, log $f_{\rm gas}$, of our Seyfert PSBs with those of local LIRGs (Larson et al., 2016) and QSOs (Evans et al., 2001; Scoville et al., 2003; Xia et al., 2012). As expected, LIRGs have higher sSFR and gas fractions than those of our Seyfert PSBs. On the other hand, QSOs span a wide range in gas fraction and some have similar gas fractions as in our sample. The stellar masses of QSOs were estimated from their black hole masses (Reines & Volonteri, 2015) and the gas fraction in QSOs may be very uncertain. The gas fractions of our Seyfert PSBs are consistent with these galaxies being remnants of gas-rich, merger-induced starbursts and quasars.

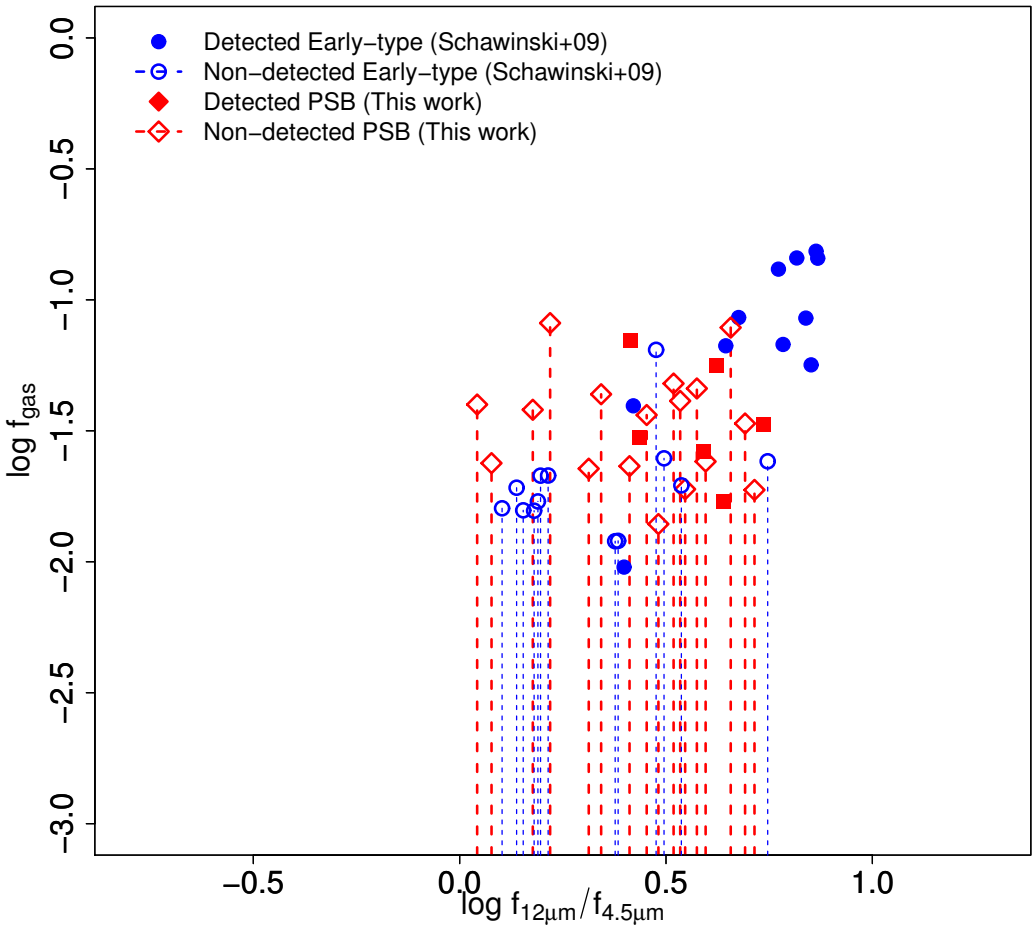

Figure 3.22:. compares WISE flux ratios, $\log f_{12}/f_{4.6}$, and molecular gas fractions, $\log f_{\rm gas}$, of our Seyfert PSBs with those of early-type galaxies studied by Schawinski et al. (2009b), which includes 4/24 Seyferts and 10/24 composite galaxies of AGN and star formation. These early-type galaxies are not PSBs but some might have mild recent star formation. The authors reported evidence for the destruction of molecular gas by AGN. There is a good agreement between the gas fractions of our Seyfert PSBs and those of the Seyferts and composite galaxies studied by Schawinski et al. (2009b).

PG 1613+658 has $\log f_{\rm gas} = -2.13$ while PG 0050+124 $\log f_{\rm gas} = -0.658$. For an additional four Seyferts, we could find stellar mass measurements in the literature and estimate their gas fractions. Mrk 231 and Mrk 273 have $\log f_{\rm gas} \sim -1.4$, similar to our Seyfert PSBs, while F08572+3915 and NGC 6240 have $\log f_{\rm gas}$ of -0.6 and -1.0 respectively. Therefore, the low molecular gas fraction in the our Seyfert PSBs could be due to gas removal by AGN-driven outflows. Alatalo et al. (2016) also find enhanced NaD absorptions in their PSBs which exhibit radio emissions. Six of the Seyfert with CO detections in our sample show blue-shifted CO emission peaks of order 200 km s^{-1}, and so do the two Seyferts in Rowlands et al. (2015) sample. About a third of the Alatalo et al. (2016) PSBs also show either significantly blue-shifted or red-shifted CO emission centers from the the systemic velocity. Some of them are AGN. These velocity shifts may be due to outflows.

3.5.5 Comparison with PSBs detected in H I

Zwaan et al. (2013) studied H I gas in 11 "quiescent" PSBs $z \sim 0.03$. Combining their sample with 11 previously studied PSBs, the authors found that at least half of the PSBs have an H I detectable gas reservoir (Chang et al., 2001; Buyle et al., 2006). The H I-detected PSBs have gas fractions similar to those observed in the most gas-rich early-type galaxies and the most gas-poor late-type galaxies (Catinella et al., 2012). As the authors pointed out, this observation is consistent with the idea that PSBs are in transition between gas-rich actively star-forming galaxies and quiescent early-type galaxies.

The PSBs in the combined sample do not have molecular gas measurements.

We use their WISE flux ratios, $\log f_{12}/f_{4.6}$, to predict their molecular gas fractions. 19 of the PSBs are found in the WISE survey. Ten of them have $\log f_{12}/f_{4.6} > 0.1$ and thus have obscured star formation. Based on the relationship between the molecular gas fraction and the WISE flux ratio, we predict significantly high gas fractions ($\log f_{\rm gas} > -1.7$) in these galaxies. The median, mean and the standard deviation of $\log f_{12}/f_{4.6}$ for this sample are 0.18, 0.21 and 0.49 respectively. The sample is expected to have $\log f_{\rm gas} \sim -1.5 \pm 0.2$. A gas fraction of this magnitude is observed in a green valley galaxy, and is consistent with the finding of Zwaan et al. (2013). Six of the eleven galaxies with H I detections have $\log f_{12}/f_{4.6} > 0.1$. This analysis also reveals how the traditional definition of PSB fails to exclusively select truly quiescent PSBs. Some of these galaxies have obscured star formation, and, not surprisingly, a large amount of gas.

3.5.6 Implication for galaxy evolution

It is thought that star formation quenching happens in both slow and fast modes (e.g., Faber et al., 2007; Cheung et al., 2012; Barro et al., 2013; Fang et al., 2012; Dekel & Burkert, 2014; Schawinski et al., 2014; Yesuf et al., 2014; Woo et al., 2015). The existence of these modes, their relative importance and the physical mechanisms that drive them are still open questions in galaxy evolution. Some works have indicated that PSBs quench rapidly and may exemplify an important mode quenching for the build-up of the red sequence (Kaviraj et al., 2007; Wild et al., 2009; Wong et al., 2012; Yesuf et al., 2014), while others have questioned their importance (De Lucia et al., 2009; Dressler et al., 2013).

Recent studies found a large gas fraction in PSBs further questioning their

importance. They suggested that PSBs do not evolve fast and they remain in the green valley for extended period of time to get rid of their gas (Rowlands et al., 2015; French et al., 2015; Alatalo et al., 2016). These works have not individually sampled the evolutionary sequence of gas and SFR in PSBs well. We have observed a new sample of aged Seyfert PSBs, and, together, have re-analyzed the previous samples. We reach a different conclusion that the molecular gas evolution in the PSB galaxies is rapid compared to normal galaxies. We find that PSBs span a wide range in molecular gas fraction ($\sim 0.3-30\%$), and their molecular gas fraction correlates significantly with their specific star formation rates. The older PSBs in the green valley, with lower SFRs, have gas fractions similar to those in red-sequence galaxies. Therefore, we advocate for a rapid evolution of gas and star-formation in PSBs. The existing data are consistent with a removal or destruction of molecular gas at later stages by AGN feedback. Better and deeper observations, especially at a later stage of PSB evolution, are need to firmly and more directly test the merger-induced AGN feedback hypothesis. In the theoretical front, developments in cosmological simulations with AGN feedback are needed to be compared to these future observations. For a preliminary comparison, see §3.5.8.

3.5.7 The effect of CO conversion factor

The CO luminosity to the molecular hydrogen conversion factor is a widely acknowledged source of uncertainty in studies that use CO as a tracer of molecular hydrogen (Bolatto et al., 2013). Up to this point, we have assumed that all objects including PSBs have a conversion factor similar to the factor observed

in the Milky Way disk. There is no study to date that measured the conversion factor in PSBs. As discussed in detail in Bolatto et al. (2013), departure from the Galactic conversion factor are both observed and expected in starburst galaxies. It has been shown that adopting the Galactic conversion factor would cause the inferred molecular gas mass to exceed the dynamical mass for the central region of a starburst galaxy (Solomon et al., 1997; Downes & Solomon, 1998). Using galaxy merger hydrodynamic simulations, which incorporate dust and molecular line radiative transfer calculations, Narayanan et al. (2011) have shown that in merger-induced starbursts, the combined effect of increased velocity dispersion and kinetic temperature increases the velocity-integrated CO intensity, and lowers the CO conversion factor from the Galactic value by a factor of $\sim 2-10$. The authors also note that in the PSB phase, it is less trivial to simply relate the conversion factor to the gas velocity dispersion and temperature owing to varying physical conditions in the PSB galaxy. Some of their merger simulations returned to a Galactic conversion factor value quickly after the peak of the starburst, while others remained low. Furthermore, if AGN heat the bulk of molecular gas, the conversion factor could be lower from the Galactic value in PSBs with AGN. Figure 3.23 shows the dependence of depletion times on sSFR for the combined data of LIRGs and PSBs. In this figure a conversion factor $\alpha_{\rm CO} = 0.8\,{\rm M}_{\odot}({\rm K\,km\,s^{-1}pc^2})^{-1}$ is assumed for the LIRGs and PSBs. The fit to combined data gives weaker but statically significant dependence ($\sim 3\sigma$) between of depletion times on sSFR. The slope of the fit is $\hat{\beta} = -0.26$, which is similar to the slope we got without including LIRG data, and the intercept $\hat{\beta}_0 = 5.4$. Thus, a lower CO conversion factors than the assumed Galactic value will strengthen

our main conclusion that the molecular gas evolution in PSBs is rapid compared normal galaxies.

3.5.8 Comparison with a merger simulation with AGN feedback

For an illustrative purpose, Figure 3.24 compares the molecular gas fraction of our compiled data of LIRGs, QSO,PSBs with an isolated merger simulation that includes AGN feedback (Lanz et al., 2014; Hayward et al., 2014a). Black hole accretion and AGN feedback are included using the model of Springel et al. (2005b). Each merging disk galaxy is composed of a dark matter halo, gaseous and stellar exponential disks, and a bulge. The progenitor galaxies each have a stellar mass of 1.1×10^{10} $M_{\odot}$ and initial gas mass of 3.3×10^{9} $M_{\odot}$. Note that same simulation was used by Yesuf et al. (2014) to justify their PSB selection method (see their Figure 5)

The agreement between data and the simulation is better if the gas fractions in the data of LIRGs, QSO, PSBs are computed assuming a lower CO conversion factor than the Galactic value. In the figure we adopted $\alpha_{\rm CO} = 0.8\,{\rm M}_{\odot}({\rm K\,km\,s^{-1}pc^{2}})^{-1}$, observed in LIRGs. If the simulation is correct, and the CO conversion factor is indeed lower, it implies that the molecular gas in PSBs is lower than our previous estimate in 3.4, further strengthening our conclusion. With better observations, and more realistic cosmological simulations with large number of galaxies, the comparison between data and theory using simple diagnostics such as Figure 3.24 will likely be useful in our understanding of galaxy quenching and AGN feedback. There is a reasonable consistency between the

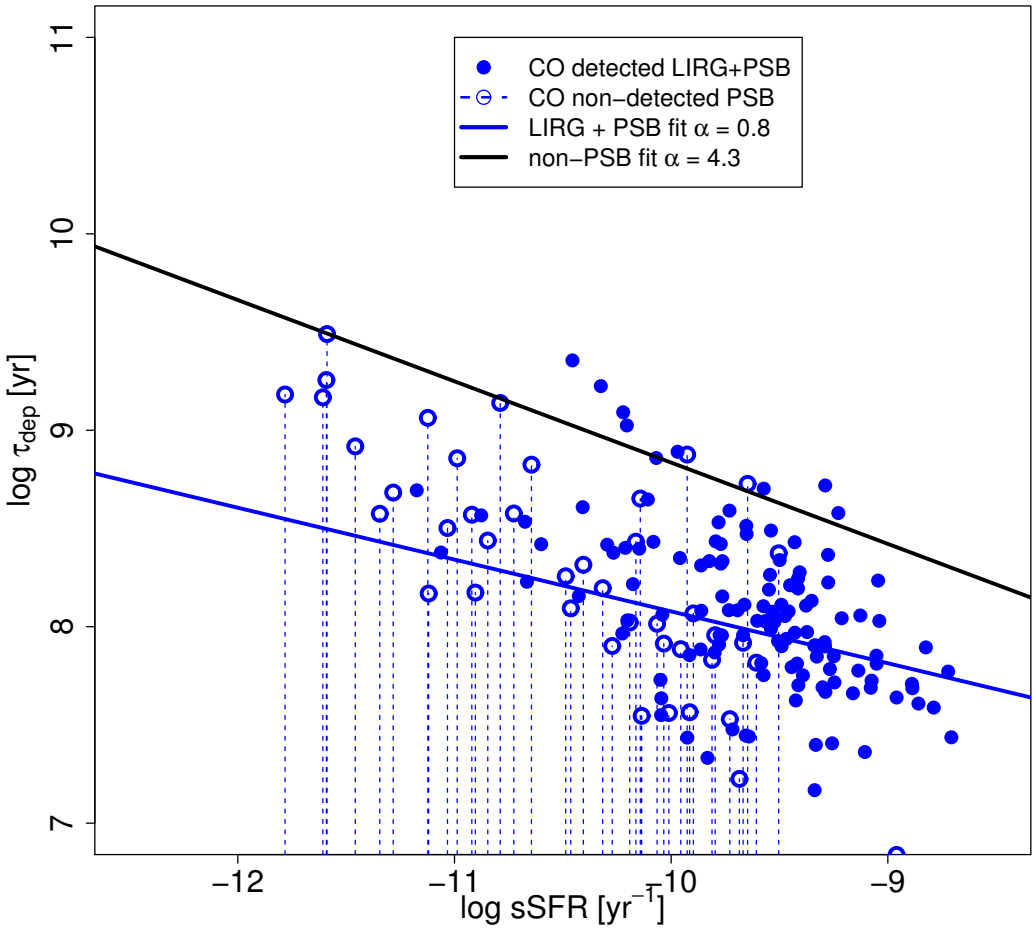

Figure 3.23:. The effect of changing the CO conversion factor for PSBs and LIRGs. The black line is our fit for the non-PSB galaxies in COLD GASS survey. This fit assume $\alpha_{\rm CO} = 4.3\,{\rm M}_{\odot}({\rm K\,km\,s^{-1}pc^{2}})^{-1}$. The blue line fits the data of LIRGs (Larson et al., 2016) and PSBs (in this work, French et al., 2015; Rowlands et al., 2015; Alatalo et al., 2016) assuming $\alpha_{\rm CO} = 0.8\,{\rm M}_{\odot}({\rm K\,km\,s^{-1}pc^{2}})^{-1}$, observed in LIRGs and starbursts. When we combined with LIRGs data, we get similar slope as the slope we got when we analyzed the PSB data alone but the combined fit gives a statistically trend, with weaker slope than that of non-PSBs.

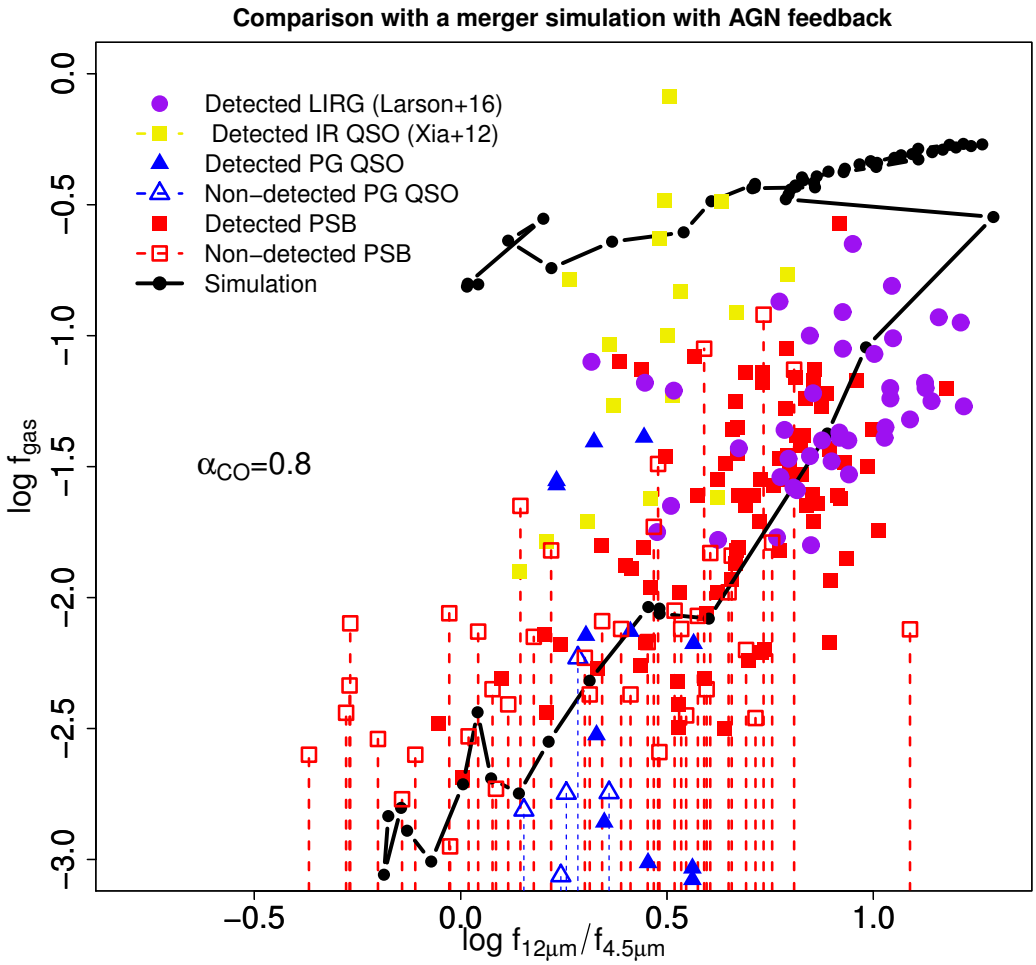

Figure 3.24:. compares WISE flux ratios, log $f_{12}/f_{4.6}$, and molecular gas fractions, log $f_{\rm gas}$, of PSBs (This work, French et al., 2015; Rowlands et al., 2015; Alatalo et al., 2016), LIRGs (Larson et al., 2016) and QSOs (Evans et al., 2001; Scoville et al., 2003; Xia et al., 2012) and QSOs and with that predicted by a merger simulation with AGN feedback (Hayward et al., 2014a; Lanz et al., 2014). Unlike in the rest of the chapter, we adopt here $\alpha_{\rm CO} = 0.8\,{\rm M}_{\odot}({\rm K\,km\,s^{-1}pc^2})^{-1}$, observed in LIRGs, instead of the Galactic conversion factor. If the simulation is correct and the CO conversion factor is indeed lower, the molecular gas in PSBs is lower than our previous estimate in § 3.4, further strengthening our conclusion.

molecular gas fractions in galaxies in the Illustris cosmological simulation (Genel et al., 2014) and in real galaxies at $z \sim 0$ but more still remain to be done on the theoretical front as well (e.g., Weinberger et al., 2016).

3.6 Summary & Conclusions

Using the SMT, we undertook new CO (2–1) observations of 24 Seyfert post-starburst galaxies at redshift $z = 0.02 - 0.05$. The sample was selected using the dust-corrected NUV-g color and 4000Å break to indicate a PSB signature, and the emission line ratios to indicate a Seyfert activity. We analyzed our sample with previous samples of ~ 100 PSBs. In comparison, our sample probes the later stage of PSB evolution. When combined with the other samples, it is indispensable in sampling the entire starburst-AGN-quenched post-starburst evolutionary sequence. Our main results are:

- We detect molecular gas in 6/24 Seyfert PSB galaxies.We find a significantly lower molecular gas detection rate (25%) in our sample than do previous PSBs studies (50-90%, Rowlands et al., 2015; Alatalo et al., 2016).

- The distribution of gas fraction in PSBs is significantly different from young star-forming galaxies (Saintonge et al., 2011). We observe a rapid decline in $\log f_{\rm gas}$ around 0.6 Gyr after the starburst. We interpret this far removed event from the peak of the starburst as evidence for a delayed AGN feedback. The Seyfert PSBs have a distribution of $\log f_{\rm gas}$ which is even more significantly different from that of normal galaxies of similar age.

- The WISE flux ratio, $\log f_{12}/f_{4.6}$, is an excellent proxy for gas fraction

for both PSBs and non-PSBs. We find a statistically significant relationship between $\log f_{12}/f_{4.6}$ and $\log f_{\rm gas}$. This relationship indicates that PSBs reach the gas fractions observed in quiescent galaxies by ~ 1 Gyr. Therefore, both star-formation and molecular gas evolutions in PSBs are rapid and these galaxies do not need to linger in the green valley for more a longer period of time as previous studies suggested.

Previous works reached different conclusions than ours because they individually did not sample well the whole starburst-AGN-quenched PSB evolutionary sequence and because the traditional definition of PSB fails to exclusively select truly quiescent PSBs, giving a false impression that half of classical PSBs have large amounts of gas at the end of their evolution. We show that these galaxies have obscured star formation undetected in Hα. We also discuss a similar possibility in classical PSBs studied in H I (Chang et al., 2001; Buyle et al., 2006; Zwaan et al., 2013). We found half of these PSBs have significantly obscured star formation. Our result is in agreement with Schawinski et al. (2009b) who also found AGN are responsible for the destruction of molecular gas in morphologically early-type galaxies with mild starbursts.

Furthermore, we discuss the $\log f_{\rm gas}$ of LIRGs and QSOs in comparison with those of PSBs. PSBs and QSOs show a wide range of gas fractions ($\sim 0.3-30\%$) at $\log f_{12}/f_{4.6}$ corresponding to the lower blue-cloud and the green-valley. LIRGs have similar $\log f_{\rm gas}$ as the most gas rich PSBs in Rowlands et al. (2015) and Alatalo et al. (2016). We found that the 10 Seyferts with large molecular mass outflows studied by Cicone et al. (2014) have similar $\log f_{12}/f_{4.6}$ as our Seyferts PSBs, and a significant number of PSBs also show shifted CO peaks from the

systemic velocities, suggesting that AGN outflows may be important mechanisms to explain the observed molecular evolution. Future deep CO observations might constrain better both the mass outflow rate and the total amount of gas inside PSB galaxies. These observations will also be in vital testing future cosmological simulations. Our compiled data on PSBs, LIRGs and QSOs are in good agreement with the predicted $\log f_{\rm gas}$ and $\log f_{12}/f_{4.6}$ values by an idealized merger simulation with AGN feedback (Hayward et al., 2014a; Lanz et al., 2014), provided that the $\alpha_{\rm CO} = 0.8\,{\rm M}_{\odot}({\rm K\,km\,s^{-1}pc^2})^{-1}$ is assumed to convert the CO luminosities in all the data. This is value of the conversion factor is observed in starbursts and LIRGs (Solomon et al., 1997; Downes & Solomon, 1998) but its reasonableness in PSBs has yet to be shown.

Chapter 4

No evidence for feedback: Unexceptional Low-ionization winds in Host galaxies of Low Luminosity Active Galactic Nuclei at Redshift $z \sim 1$

4.1 Introduction

Galactic scale winds are one of the most fundamental, yet least understood, facets of galaxy evolution. They are recognized to be fundamental in shaping the baryonic growth, dark matter density profile, star formation and metallicity of galaxies as well as the enrichment of the intergalactic medium (e.g., Aguirre

et al., 2001; Veilleux et al., 2005; Oppenheimer et al., 2010; Davé et al., 2011; Pontzen & Governato, 2012). Galaxy formation models that do not include feedback processes form stars too efficiently and fail to reproduce even basic observed galaxy properties.

High velocity winds are predicted manifestations of the AGN feedback process invoked to reproduce observed properties of massive galaxies (Silk & Rees, 1998; Fabian, 1999; Granato et al., 2004; Di Matteo et al., 2005; Springel et al., 2005b; Hopkins et al., 2008; Debuhr et al., 2012). In AGN feedback process, a tremendous energy output from accretion onto a black hole, if somehow harnessed, removes or heats gas in the host galaxy and shuts down subsequent star formation. The consequence of the black hole's action in turn limits gas accretion onto the black hole and stunts its growth. AGN feedback is an essential ingredient in current theoretical models of massive galaxy evolution (for recent reviews, see Alexander & Hickox, 2012; Fabian, 2012; Kormendy & Ho, 2013; Heckman & Best, 2014). Many semi-analytical models and theoretical simulations require AGN feedback to correctly predict the observed color bi-modality of galaxies and the lack of extremely luminous galaxies (e.g., Benson et al., 2003; Croton et al., 2006; Hopkins et al., 2006; Cattaneo et al., 2007; Somerville et al., 2008; Gabor et al., 2011).

It is predicted that outflows driven by stellar feedback alone are less likely to reach typical velocities higher than $500\,\mathrm{km\,s^{-1}}$ (Thacker et al., 2006; Bower et al., 2012; Hopkins et al., 2013). In their simulations of stellar feedback (without AGN feedback) in major mergers, Hopkins et al. (2013) found that in all cases the winds have a broad velocity distribution extending up to $\sim 1000\,\mathrm{km\,s^{-1}}$, but most of the wind mass is near the circular velocity ($\sim 100 - 200\,\mathrm{km\,s^{-1}}$), with

relatively little ($\ll 1\%$ of the wind mass) at $v \geq 500\,\mathrm{km\,s^{-1}}$. Muratov et al. (2015) also found winds with similar properties in their analysis of galaxy-scale outflows from the Feedback in Realistic Environments (FIRE) cosmological simulations. In contrast, considerably higher bulk outflow velocities $v \sim 1000 - 3000\,\mathrm{km\,s^{-1}}$ are predicted from AGN feedback (e.g., King et al., 2011; Zubovas & King, 2012; Choi et al., 2012; Debuhr et al., 2012; Gabor & Bournaud, 2014). In observations, in particular in those that indirectly infer the bulk velocity, the high velocity tail of the star formation-driven wind could be confused for a wind powered by AGN.

However, other models predict that AGN feedback affects a galaxy very little, despite the large outflow velocities (Gabor & Bournaud, 2014; Roos et al., 2015) or it could even enhance star formation (Silk & Nusser, 2010; Ishibashi & Fabian, 2012; Bourne et al., 2015). Bourne et al. (2015) claim that the mass resolution of a simulation significantly affects the inferred AGN feedback. At resolutions typical of cosmological simulations, they found that simulated AGN are artificially more efficient in gas removal. Yet at a higher resolution, the authors found that simulated AGN expel only diffuse gas, and a denser gas falls in towards the black hole and forms stars. Thus, it is not clear whether AGN have negative or positive feedback or both happening simultaneously (Cresci et al., 2015) or on different timescales. A consistent and unified theoretical picture on the role of AGN outflows in galaxy evolution is still lacking and observations need to inform and aid the theoretical developments.

Recent observational studies at $z \sim 0.5 - 2.5$, using the background light of star forming galaxies in self-absorption, have observed ubiquitous velocity offsets from the the systemic zero velocities of the galaxies, indicative of galactic winds

(Weiner et al., 2009; Erb et al., 2012; Law et al., 2012; Tang et al., 2014; Martin et al., 2012; Bordoloi et al., 2014; Rubin et al., 2014; Zhu et al., 2015). Using the background light of galaxies gives a clearer indication of inflow or outflow unlike using bright background QSOs to probe gas associated with the foreground galaxies (e.g., Churchill et al., 2000). Since galaxies are much fainter, the analysis is performed on stacks of hundreds of short exposure galaxy spectra or on very deep spectra of a modest sample of individual galaxies ($3-8$ hr integration on Keck for instance). The outflows studied in both ways show asymmetric absorption profiles with a typical velocity offset of $\sim 200\,\mathrm{km\,s^{-1}}$ and a high velocity tail which may reach up to $\sim 1000\,\mathrm{km\,s^{-1}}$ (e.g., Weiner et al., 2009; Martin et al., 2012). Note that this high velocity tail in star-forming non-AGN galaxies is observed more prominently in Mg II λ2796 and it is consistent with the theoretical expectation (e.g., Hopkins et al., 2013; Muratov et al., 2015).

In the latest works that used deep spectroscopic data of individual galaxies, the wind speed is best correlated with SFR surface density but it is not significantly correlated with either galaxy stellar mass or inclination (Martin et al., 2012; Kornei et al., 2012; Rubin et al., 2014). The wind detection rate on the other hand is highly dependent on inclination (Rubin et al., 2014). While the recent works have made important advances in characterizing such outflows and in establishing their relationships to host galaxy properties, many basic properties of these winds and their driving physics remain uncertain. One such uncertainty is the wind velocity of AGN host galaxies.

The evidence for AGN hosts having ubiquitous high mean galaxy-wide velocity outflows with the potential to impact star formation is sparse (more detailed

discussion in §4.4). Ionized outflows have been studied in emission using large samples both at low-redshift (e.g., Zakamska & Greene, 2014) and high-redshift (e.g., Harrison et al., 2016). Even though, convincing evidence for ubiquitous, ionized outflows exists, details on the interpretation of the observed wind properties are debatable. Most of the emission-line studies have found high-velocity, extended outflows on several kpc scale, resulting in very large inferred mass outflow rates and kinetic power, in support of AGN feedback models (e.g., Liu et al., 2013; Harrison et al., 2014; McElroy et al., 2015). However, recent studies have questioned these results and have argued that the apparently very extended emission is a consequence of seeing smearing (Husemann et al., 2015; Karouzos et al., 2016; Villar-Martín et al., 2016). Accounting for the seeing effect, these later works found much smaller and weaker winds, which may not significantly impact the star formation in their host galaxies.

On the other hand, absorption line wind studies are hard to undertake in distant galaxies but are relatively easy to interpret. Existing absorption line studies of winds in AGN host galaxies have small sample sizes $\sim 10-30$ at $z \sim 0.5-2.5$ (Coil et al., 2011; Hainline et al., 2011) and the aforementioned deep spectroscopic wind absorption studies did not primarly target AGN. This may be because AGN hosts are rare and are generally fainter than the targeted star-forming galaxies. Coil et al. (2011) studied a sample of 10 low-luminosity, narrow line AGN ($L_{\rm X} \sim 10^{41-42}\,{\rm erg\,s^{-1}}$) at $0.2 < z < 0.6$. Five of the ten X-ray AGN host galaxies show a wind in Fe II λ2586 absorption, with a typical mean outflow velocity signatures of only ~ 200 to $300\,{\rm km\,s^{-1}}$. The velocity widths are generally unresolved but are, $\sim 100-300\,{\rm km\,s^{-1}}$. On the other hand, Hainline et al. (2011)

qualitatively studied a stacked spectrum of 33 UV-selected narrow AGN at $z \sim 2.5$ and reported a detection of a highly blue-shifted ($v \sim -850\,\mathrm{km\,s^{-1}}$) and weak Si IV$\lambda$1393, 1402 absorption line, which is different from the Si IV absorption in the composite spectrum of non-AGN Lyman break galaxies at a similar redshift.

It should be noted that Prochaska et al. (2011) have found that atomic transitions that are only coupled to the ground state (e.g., Si IV, Mg II, Na I) have line emission preferentially at the systemic velocity and their observed absorption profiles are significantly reduced in depth as well as are significantly offset in velocity from the intrinsic profile. On the hand, they also found that resonance transitions that are strongly coupled to fine-structure transitions (e.g., Fe II and Si II) dominantly produce florescent emissions at longer wavelength which do not affect the absorption profiles. These resonance absorption lines offer the best characterization of the opacity of the wind as well as the opacity of the gas near the systemic velocity. Therefore, the discrepancy between the two previous works on AGN winds may be due to this effect. The AGN sample in Hainline et al. (2011) show stronger Si IV λ1393, 1402 emission near the systemic and have much weaker absorption than do their non-AGN star-forming counterparts. In the follow up work, the same authors showed that the stellar population properties of their AGN sample are consistent with those of the mass-matched control sample of star-forming galaxies. They inferred that the presence of an AGN is not connected with the cessation of star formation activity in star-forming galaxies at $z \sim 2-3$ (Hainline et al., 2012). In other words, the observed high winds in these AGN have not yet affected star formation even if the measured mean velocity is reliable.

The work in this chapter bridges the gap in redshift between the two major previous studies of AGN winds in absorption and aims to independently confirm the previously reported wind velocities in AGN. We examine winds in a composite spectrum of 12 X-ray selected AGN at $z = 0.9 - 1.5$ or that of a comparison sample of star-forming galaxies using Fe II λ2586, a preferred wind diagnostic. Our AGN sample has a comparable X-ray luminosity to that of Coil et al. (2011). Our spectral resolution is two times higher than theirs and we have three times more wavelength sampling. Our sample also has more extensive multi-wavelength deep HST photometry and other ancillary data to better characterize the host galaxy properties. This has enabled a first attempt to have a control sample for star-forming galaxies matched both in stellar mass and galaxy inclination. Furthermore, we use similar wind model and methods that have been adopted in the most recent wind studies (Martin et al., 2012; Rubin et al., 2014). These methods were not used in the two previous studies of AGN. Thus, for a fair comparison, we present a reanalysis of the Coil et al. (2011) data using the new approach, which also has better quantified model uncertainties.

The rest of the chapter is organized as follows: Section 4.2 presents the data and sample selection. Section 4.3 presents the analysis and results on winds in AGN at $z \sim 1$, AGN at $z \sim 0.5$ and the comparison sample. Section 4.4 extensively discusses previous work to put the result of this work in a larger context. A brief summary and conclusion is given in section 4.5 . $(\Omega_m, \Omega_\Lambda, h) = (0.3, 0.7, 0.7)$ cosmology is assumed and a wavelength measured in air is given throughout the paper. AB magnitude is adopted. We use words "wind" and "outflow" interchangeably to mean outward movement of gas without making

subtle distinctions in some previous works.

4.2 Data

4.2.1 Observation & data reduction

The spectroscopic data are taken from our on going deep (8–24 hr) Keck/DEIMOS (Faber et al., 2003) spectroscopic survey in CANDELS fields (Grogin et al., 2011; Koekemoer et al., 2011; Guo et al., 2013) called HALO7D. This multi-semester program will survey faint halo stars with HST-measured proper motions, to measure their line-of-sight velocities and chemical abundances, giving 6D phase-space information and chemical abundances for hundreds of Milky Way halo stars. The deep exposures necessary to reach the faintest stars in the distant halo is an opportunity for a novel synergy of extragalactic and Galactic science. In addition to the primary halo star targets, which only occupy about a quarter of slitlets on a given DEIMOS mask, we are conducting a survey of galactic winds in star-forming galaxies at $z \sim 1$, and stellar populations of quiescent galaxies at redshifts $0.4 < z < 0.8$. A total of about ~ 1500 deep spectra of galaxies are expected with survey completion in a year.

The HALO7D survey uses the 600 line/mm grating on DEIMOS centered around 7200Å with the GG455 order-blocking filter. This setup gives a nominal wavelength coverage of 4600-9500Å at a resolution (FWHM) of ~ 3.5Å for a $1''$ slit width and 0.65Å/pixel dispersion. The slit position angles are set to within $\pm 30^\circ$ of the parallactic angle to minimize light loss in the blue due to atmospheric dispersion. The exposure times for AGN studied in this work range between

$5 - 12$ hr and the observations were taken over the course of two years under variable seeing ($0.8 - 1.2''$) and fair to good transparency conditions. Despite the long integration times, poor seeing has significantly lowered the signal-to-noise for almost half of the AGN sample in the current work. Additional make-up observations of these AGN are scheduled.

The observations were reduced using the automated DEEP2/DEIMOS *spec2d* pipeline developed by DEEP2 team (Newman et al., 2013). Calibrations were done using a quartz lamp for flat fielding and both red NeKrArXe lamps and blue CdHgZn lamps for wavelength calibration. The spectroscopic redshifts were measured from the reduced spectra using the *spec1d* pipeline. All spectra were visually inspected using the interactive *zspec* tool to access the quality of the redshift estimated by *spec1d* (for software details, see Newman et al., 2013). Almost all galaxies studied in this work have previous spectroscopic measurements and the new spectroscopic redshifts imply minor changes if any.

Based on the available redshifts, stellar masses and other stellar population properties (age, extinction A_V, etc.) were computed using FAST (Kriek et al., 2009). The modeling is based on a Bruzual & Charlot (2003) stellar population synthesis model and assumes a Chabrier (2003) IMF, exponentially declining star formation histories, solar metallicity, and a Calzetti et al. (2000) dust extinction law. The star-formation rates (SFR) are the sum of the SFR_{UV}, derived from the rest-frame near-UV luminosity at 2800Å, and the SFR_{IR}, derived from the total infrared luminosity. If a galaxy is not detected in infrared, its dust-corrected UV-based star formation rate is used (Barro et al., 2011; Wuyts et al., 2011). The axis-ratio measurements were done on HST/WFC3 F160W (H) band imaging

using GALFIT (Peng et al., 2002).

For comparison, we also used data of 6 previously studied low-luminosity AGN at $0.3 < z < 0.6$ with Fe II coverage (Coil et al., 2011). These AGN were observed using Keck LRIS (Oke et al., 1995) for roughly one half hour to one hour. The average apparent brightness for this sample is $B \sim 20.9$ and our AGN sample has about 9 times fainter average apparent brightness. Coil et al. (2011) have stellar mass and star-formation rate measurements for four of the six AGN. We adopted their measurements. In comparison plots that use the stellar mass and star-formation rate measurements, we only show their four AGN with such measurements, but we reanalyzed the spectra for all six AGN.

4.2.2 Sample selection

For the wind study, we primarily targeted sources that are brighter in the V band ($V < 23.5$) and above $z > 0.7$, such that we would detect near-UV continuum levels in the individual spectra in eight hours at a signal-to-noise ratio per Angstrom (SNR/Å) of 5 in good observing conditions. We gave higher priority to sources that are brighter and are above $z > 0.9$, which likely have both Fe II and Mg II coverage. Galaxies with $V > 23.5$ were targeted at lower priority as fillers. AGN are a small fraction ($< 10\%$) of all galaxies in our survey. In some cases, we targeted bright X-ray sources (Alexander et al., 2003; Laird et al., 2009; Xue et al., 2011) and gave them highest weights in the mask design process. In other cases, the AGN were selected by chance (i.e., were selected for other reasons). So far, there are about one hundred X-ray sources in the observed sample. Only about a third of them are above $z > 0.9$ and, therefore, have coverage of Fe II

λ2586.

Out of the $\sim$ 100 targeted X-ray sources, we selected 12 AGN candidates at $z > 0.9$ with X-ray luminosity $L_{\rm X} \gtrsim 5 \times 10^{41}$ erg s^{-1} with SNR/Å > 2.7 around Fe II λ2586 and and with uncontaminated Fe II λ2586 by skylines. We also require that they have HST WFC3 imaging for axis-ratio measurements and have highly reliable redshift measurements (show clear O II emission and/or Ca II H & K absorption lines).

Figure 4.1a plots star formation rate against X-ray luminosity. Nine of the selected AGN candidates are 2σ outliers from the relationship between X-ray luminosity and star formation rates for normal star-forming galaxies (Mineo et al., 2014). Of these, 3 show broad Mg II emission. When we have previous spectroscopic data, we targeted objects with broad Mg II emission at lower priority. Quasars have hard X-ray luminosities $\gtrsim 10^{44}\,{\rm erg\,s^{-1}}$ (e.g., Ku et al., 1980; Piconcelli et al., 2005). Except for the 3 AGN with broad Mg II, the AGN studied in this work have significantly lower X-ray luminosities compared to quasars. We thus refer to them as low-luminosity AGN to differentiate them from quasars.

Furthermore, 3 of the 12 X-ray sources lie within 2σ of the mean relation between X-ray luminosity and star formation rate. One of them has strong Ne V λ3426 emission, a strong signature of AGN. Therefore, 10 of the AGN sample have robust AGN identifications. Excluding the two X-ray sources which may not be AGN does not change the main results of this work. We have excluded from our sample some AGN candidates which satisfy the SNR cut but their spectra around Fe II are contaminated by a skyline or possible absorption from a foreground galaxy.

The three broad-line AGN in our sample show no or very weak and narrow Fe II and/or Mg II absorption but have higher X-ray luminosity $L_{\rm X} > 10^{43}$ erg s^{-1}. Coil et al. (2011) did not target objects with broad Mg II emission in their spectra, as strong broad emission may affect one's ability to detect or interpret blue-shifted absorption features because of emission infill or ionization to a higher state. We present analyses both with and without the inclusion of the three broad-line AGN. The current estimates of stellar masses and star-formation rates of these AGN do not properly account for the presence of the luminous AGN and thus they may be biased compared to the measurements for the star-forming comparison sample.

Figure 4.1b−d show the stellar mass, star formation rate and axis-ratio of the AGN and the comparison sample of star-forming non-AGN galaxies at $z \sim 1$. Due to the limited sample size from which the comparison sample of non-AGN were drawn, our matching is crude but sufficient since winds are expected to depend weakly on galaxy properties (Coil et al., 2011; Martin et al., 2012; Rubin et al., 2014; Balmaverde et al., 2016).

The galaxy properties of the AGN and the star-forming non-AGN sample are summarized in Tables 4.1 & 4.2. The rest-fame RGB images of the two samples are shown in Fig. 4.2 and Fig. 4.3.

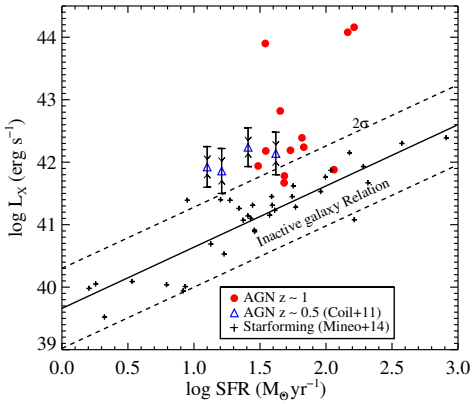

(a) Star formation rate vs. Full X-ray luminosity

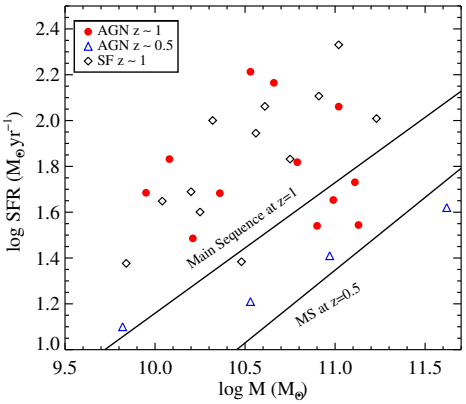

(b) Stellar mass vs. Star formation rate

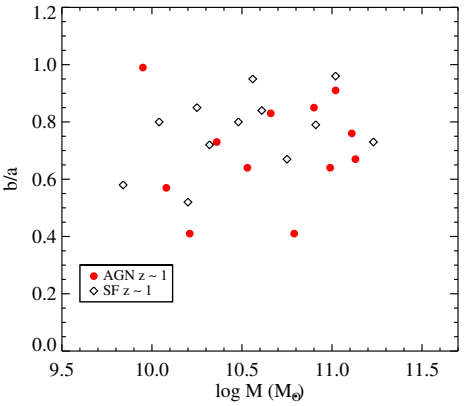

(c) Stellar mass vs. observed H-band axis-ratio

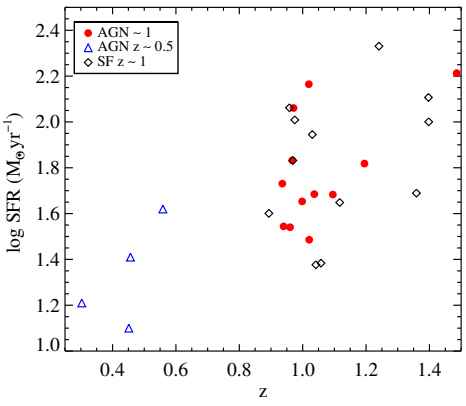

(d) Redshift vs. Star formation rate

Figure 4.1:. In all panels the red dots are the low-luminosity AGN at $z \sim 1$, the diamonds are the comparison star-forming sample at $z \sim 1$ and the blue triangles are AGN at $z \sim 0.5$ from Coil et al. (2011). In panel (a) the blue triangles are shown with arrows to indicate upper and lower limits of their X-ray luminosities. The + signs denote X-ray detected star forming galaxies in Chandra Deep Field South (CDFS) from Mineo et al. (2014). The solid and dashed lines indicate best fit line and its 2σ scatter for the correlation between star formation rate and X-ray luminosity in the star forming non-AGN galaxies. In panel (b) the black lines indicate the main sequence of galaxies at $z = 1$ and $z = 0.5$ (Whitaker et al., 2014)

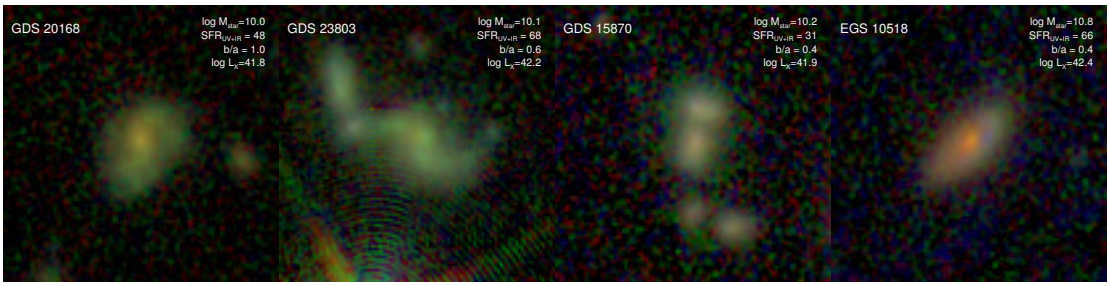

(a) GDS 20168 (b) GDS 23803 (c) GDS 15870 (d) EGS 10518

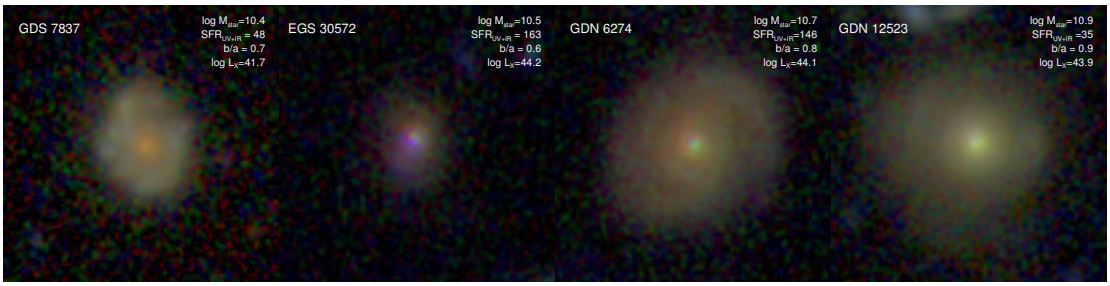

(e) GDS 7837 (f) EGS 30572 (g) GDN 6274 (h) GDN 12523

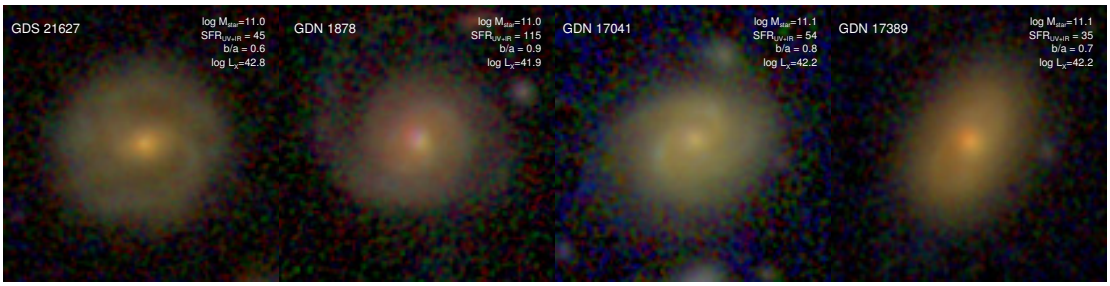

(i) GDS 21627 (j) GDS 21627 (k) GDN 17041 (l) GDN 17389

Figure 4.2:. Rest-frame RGB composite images of the AGN at $z \sim 1$. The number at the top of the image indicates galaxy id, stellar mass, total star formation rate, the axis-ratio and X-ray luminosity of the host galaxy. Each image is 50×50 kpc. North is to the top and East is to the left.

Table 4.1. $z \sim 1$ AGN sample

Field	ID	RA (degree)	Dec. (degree)	z	log L_X (erg s^{-1})	log M ($M_\odot$)	SFR ($M_\odot yr^{-1}$)	b/a	B mag	V mag	SNR (per Å)	t_{obs} (hr)
EGS	10518	214.877075	52.819477	1.19500	42.4	10.8	66	0.4	24.6	24.1	3	6
EGS	30572	214.671600	52.773415	1.48599	44.2	10.5	163	0.6[a]	23.9	23.1	8	9
GDN	17041	189.282730	62.268250	0.93573	42.2	11.1	54	0.8	23.8	22.6	3	9
GDN	17389	189.282242	62.271099	0.93971	42.2	11.1	35	0.7	23.1	23.0	3	9
GDN	1878[b]	189.194458	62.142590	0.97115	41.9	11.0	115	0.9	22.9	22.1	12	9
GDN	12523	189.193115	62.234634	0.96023	43.9	10.9	35	0.9	23.8	22.6	10	11
GDN	6274	189.077515	62.187534	1.01933	44.1	10.7	146	0.8	22.1	21.5	16	0
GDS	21627	53.045460	-27.728624	0.99829	42.8	11.0	45	0.6[a]	23.1	22.6	3	9
GDS	7837	53.107758	-27.838812	1.09525	41.7	10.4	48	0.7	23.2	22.7	9	12
GDS	15870	53.065838	-27.775131	1.02060	41.9	10.2	31	0.4	23.7	23.4	10	9
GDS	23803	53.150719	-27.716194	0.96708	42.2	10.1	68	0.6	22.3	22.1	7	5
GDS	20168	53.150126	-27.739926	1.03670	41.8	10.0	48	1.0	23.2	22.9	3	5

[a]has a bad or suspicious GALFIT flag

[b]has a strong Ne V emission

Table 4.2. $z \sim 1$ inactive star-forming comparison sample

Field	ID	RA (degree)	Dec. (degree)	z	log M ($M_\odot$)	SFR ($M_\odot$ yr^{-1})	b/a
EGS	9240	215.054153	52.937103	1.03030	10.6	88	1.0
EGS	13622	214.953293	52.890411	1.39770	10.3	100	0.7
EGS	31460	214.708572	52.791351	0.95830	10.6	115	0.8
EGS	25589	214.655823	52.738495	1.39700	10.9	128	0.8
EGS	15131	215.095734	52.999435	1.11690	10.0	45	0.8
EGS	27292	214.931488	52.945190	0.89330	10.3	40	0.9
EGS	12671	215.110123	52.994293	1.24070	11.0	214	1.0
GDN	17481	189.379868	62.272289	0.97500	11.2	102	0.7
GDN	11799	189.219743	62.231889	1.35896	10.2	49	0.5
GDS	25246	53.046933	-27.690841	1.05765	10.5	24	0.8
GDS	26255	53.144206	-27.700337	1.04180	9.8	24	0.6
GDS	19443	53.086326	-27.748261	0.96900	10.8	68	0.7

4.3 Analysis & Results

4.3.1 Coadding spectra

First, multiple exposures of the same object were averaged with inverse-variance weighting per pixel, which minimizes the variance of the weighted average spectrum. Then to coadd the spectra of AGN or their comparison sample, each spectrum was shifted to its rest frame wavelength. The rest-frame spectra were then interpolated on a linear wavelength grid with $\Delta\lambda = 0.3$Å bin, which is close to the pixel size of the DEIMOS spectrograph at $z \sim 1$ for our setup. We co-added the observed photon counts at a given wavelength bin for each rest-frame spectrum with inverse-variance weighting.

The individual near-UV spectra of the redshift $z \sim 1$ AGN sample are plotted in Figure 4.4. The Fe II and Mg II absorption lines are observed in most of the spectra. Figure 4.5 shows the normalized near UV composite spectra of all AGN

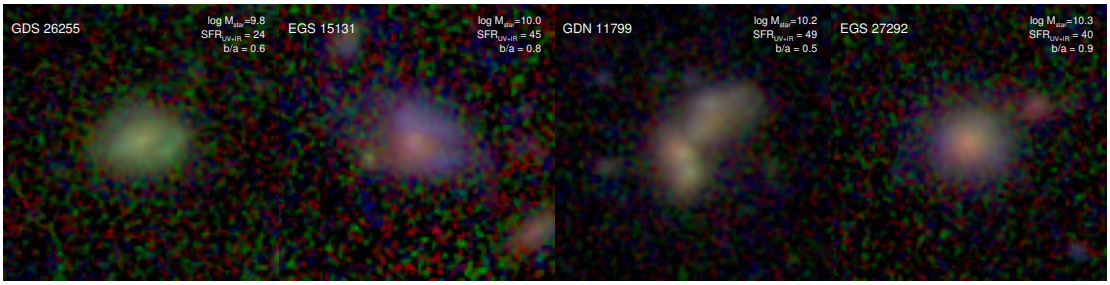

(a) GDS 26255 (b) EGS 15131 (c) GDS 11799 (d) EGS 27292

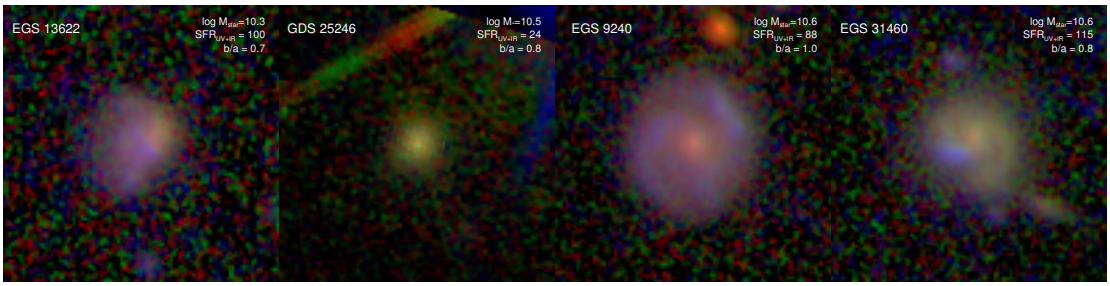

(e) EGS 13622 (f) GDS 25246 (g) EGS 9240 (h) EGS 31460

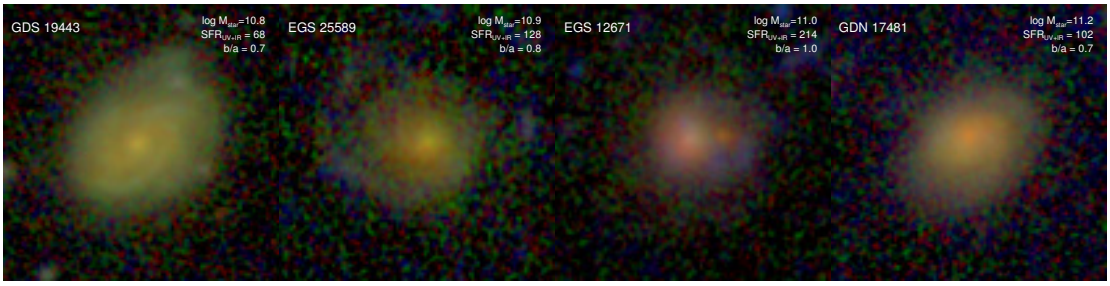

(i) GDS 19443 (j) EGS 25589 (k) EGS 12671 (l) GDN 17481

Figure 4.3:. Similar to Figure 4.2 but showing the RGB composite images of the comparison sample of non-AGN star-forming galaxies at $z \sim 1$.

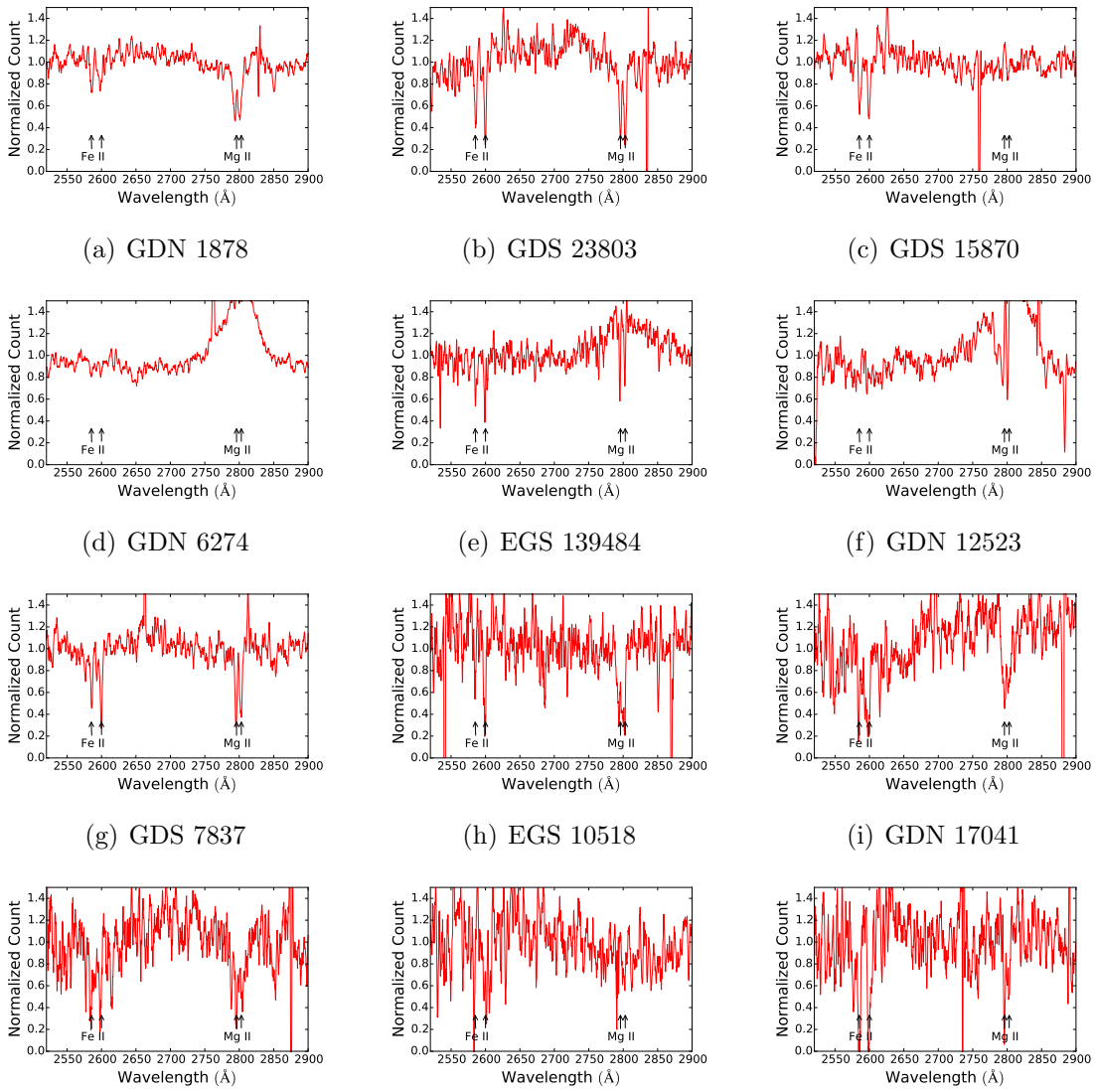

(a) GDN 1878 (b) GDS 23803 (c) GDS 15870

(d) GDN 6274 (e) EGS 139484 (f) GDN 12523

(g) GDS 7837 (h) EGS 10518 (i) GDN 17041

(j) GDN 17389 (k) GDS 21627 (l) GDS 20168

Figure 4.4:. Near UV spectra of the AGN sample at $z \sim 1$. The spectra are boxcar smoothed by 7 pixels (2 Å). Absorption lines of Fe II and Mg II are evident in most AGN. Spectra in the second row are for the three broad-line AGN. The Fe II absorption are very weak in two of the AGN with broad Mg II emission. These galaxies have high X-ray luminosities in Figure 4.1.

and subsets of the AGN sample separated into narrow and broad-line AGN. The normalization was determined by a linear fit to the continuum around both sides of the Fe II absorption doublet. We used the wavelength ranges $2520 - 2578$Å, $2640 - 2770$Å, and $2900 - 2970$Å to fit the continuum level. Figure 4.6a shows the normalized composite spectrum near the Fe II absorption line of the 7 narrow-line AGN at $z \sim 1$ with robust AGN identifications. The composite spectrum of the comparison sample of non-AGN, star-forming galaxies is overplotted on the same figure. It is clear from this figure that both AGN and normal star-forming galaxies have asymmetrically blue-shifted Fe II absorption lines. The absorption profiles of AGN and the comparison sample have very similar width and depth. Therefore, without detailed modeling, one can infer that they have similar wind velocity and strength. The wind velocities, in both samples, are in the order of $100 - 200$ km s^{-1} and extend to ~ 500 km s^{-1} A variant of this figure for all 12 AGN candidates can be found in the Appendix Figure 5.17. Figure 4.6b plots the O II emission lines of AGN and the comparison sample. O II is vital in determining the redshift and the systemic zero velocity of the galaxies.

Figure 4.6c & d are similar to Figure 4.6a & b. In these later figures the comparison is made between the composite spectrum of our AGN at $z \sim 1$ and that of the 6 AGN studied by Coil et al. (2011) at $z < 0.6$. We note that these authors studied winds in their AGN using individual spectra. Since we coadd the spectra of our AGN for improved signal-to-noise average spectrum, we also coadd the AGN at $z < 0.6$. We interpolate the individual AGN spectra onto a linear wavelength grid with $\Delta\lambda = 1.3$Å, which is about the pixel size of the LRIS spectrograph at $z \sim 0.6$ for their setup. We convolve our composite spectrum

to the instrumental resolution of LRIS and rebin it to match the resolution and bin size of the composite spectrum of their data. There is a very good agreement between the Fe II absorption profiles of AGN at $z \sim 1$ and that of the AGN at $z \sim 0.5$. However, the strength and the shapes of O II emission lines of the two AGN sample are somewhat different. This may be partly to differences in star formation rates or dust-contents of the two sample. This O II profile difference is likely not important for our wind comparison, so we do not investigate it further.

We reanalyze the Coil et al. (2011) data both separately and jointly with our data. For the joint analysis, we linearly interpolate the composite spectrum of their data to a wavelength grid with $\Delta\lambda = 1.2$Å bin, convolve our AGN composite spectrum to the LRIS resolution, and average the normalized counts in the bins where the two datasets coincide (i.e., every fourth bin in our spectrum). The averaging uses inverse-variance weighting per pixel. In the bins where the two datasets do not overlap, we use values of our composite spectrum. The joint analysis is done using the composite spectrum of our 7 narrow line AGN with robust AGN identification, which are more similar to the Coil et al. (2011) sample, as well as with the composite spectrum of all AGN in our sample.

To give a quantitative gauge of the significance of the average variation between our AGN sample and the comparison sample, and to account for the effects caused by the outlier galaxies within a sample, which may not be good representatives of the average population, we present alternative analyses in the Appendix section 5.3.2 using the errors estimated by a bootstrapping scheme on the average composite spectrum. In the bootstrapping scheme, we randomly resample, with replacement, the ID of galaxies of a sample size equal to the size of the original

sample size at each iteration. This resampling was done 1000 times. At each iteration, we averaged the spectra of the selected galaxies using inverse-variance weighting at each pixel. We used the standard deviation of the average counts in a given wavelength bin of all 1000 composite spectra as the error of the original averaged spectrum at that given bin. Table 5.3 and Fig. 5.18 summarize the bootstrapping analysis. The errors from the bootstrapping scheme are about twice as large as errors of the original inverse-variance weighted average. This scheme reinforces our main result that the average absorption profiles of AGN and the comparison sample are not significantly different. In the next section, we quantitatively show that the winds in the two samples are similar using a standard wind model.

4.3.2 The simple wind model

We adopt the partial covering wind model of Rupke et al. (2005b) to model the observed Fe II λ2586 absorption profile, similar to recent works that studied galactic winds in star-forming galaxies (Kornei et al., 2012; Martin et al., 2012; Rubin et al., 2014; Tang et al., 2014). Due to signal-to-noise and spectral resolution limitations of observational data to fully constrain the wind model, the following simplifying assumptions were customarily made in the previous works and are also adopted in this work: 1) the covering factor of the wind is independent of velocity. Some studies suggest that this may not be a good assumption (Martin & Bouché, 2009); 2) the stellar continuum emission is fully covered by a uniform screen of ISM absorption. If this assumption is not valid, the inferred ISM column density is lower than the actual column density since the covering fraction

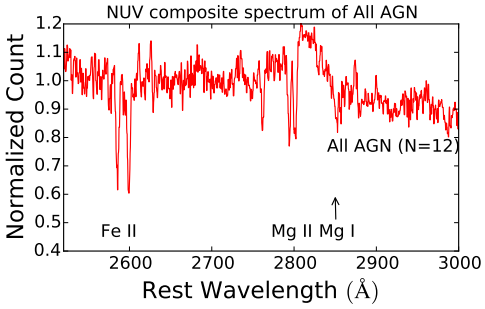

(a) All AGN

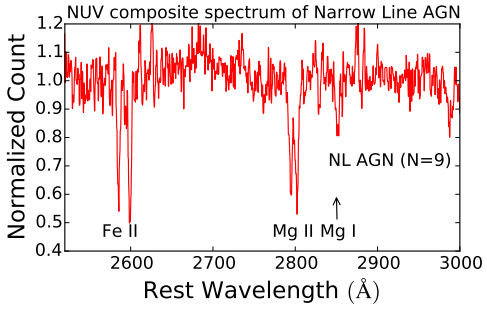

(b) All Narrow line AGN candidates

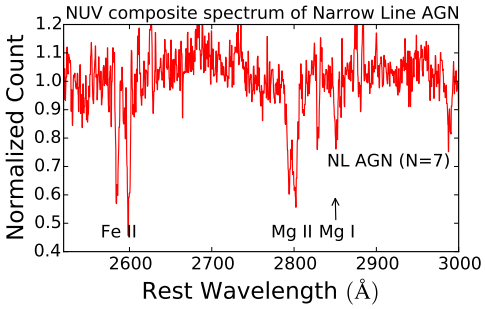

(c) Narrow line AGN with robust AGN identification

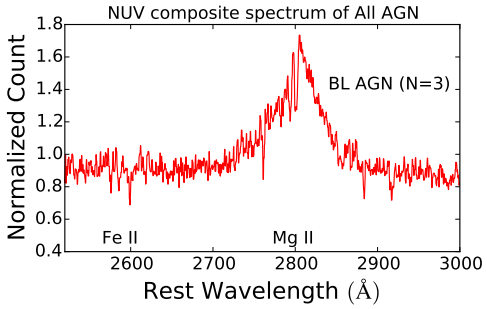

(d) Broad-line AGN

Figure 4.5:. Near UV composite spectra of the AGN sample and subsamples.

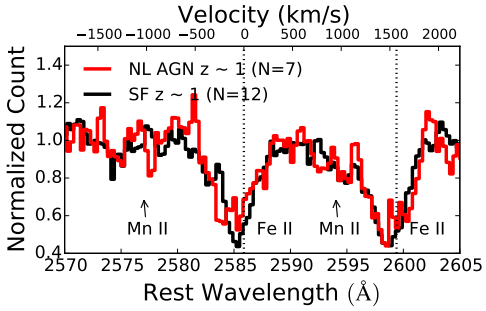

(a) Narrow-line AGN compared to inactive star-forming galaxies

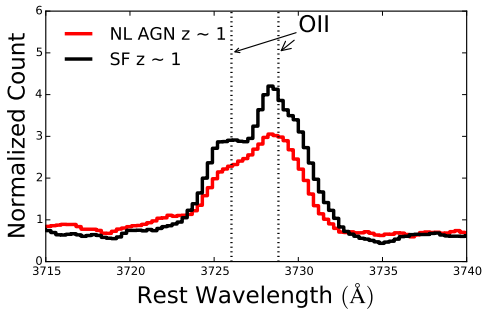

(b) Narrow-line AGN compared to inactive star-forming galaxies

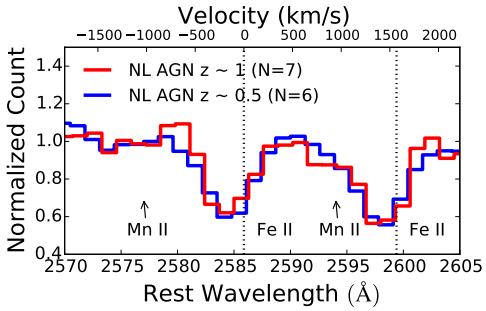

(c) Narrow-line AGN at $z \sim 1$ and $z \sim 0.5$ compared

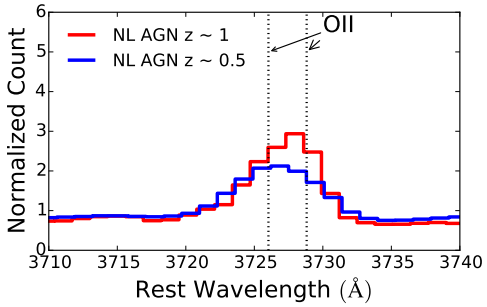

(d) [Narrow-line AGN at $z \sim 1$ and $z \sim 0.5$ compared

Figure 4.6:. Panel (a) The near UV composite spectrum around Fe IIλ2586 of the 7 bona fide narrow AGN at $z \sim 1$ compared to composite spectrum of non-AGN star-forming sample at a similar redshift. A variant of this figure for other subsamples of AGN can be found in the Appendix. Panel (b) A comparison between O II emission of AGN at $z \sim 1$ with the O II emission of the inactive star-forming sample. The O II line is vital in determining the redshift and the systemic zero velocity of the galaxies. Panel (c) A comparison between the composite spectra around Fe IIλ2586 of AGN at $z \sim 1$ and $z \sim 0.5$. The composite spectrum of $z \sim 1$ AGN is rebinned and convolved to match the spectrum of $z \sim 0.5$ AGN. Panel (d) A comparison between O II emission of AGN at $z \sim 1$ and of AGN at $z \sim 0.5$. The main point that the data shows is that there are robust systematic blue shifts in the Fe IIλ2586 absorption profiles of AGN at the two redshifts and of the comparison sample. The blueshift are less than 500 km $^{-1}$. Interpreting the blueshifts as wind signatures, one can conclude that winds with average velocity above 500 km $^{-1}$ are not observed in AGN as well as the comparison sample. Therefore, the winds in the low-luminosity AGN are most likely driven by star formation activity.

anti-correlates with column density. In this work, we do not aim to constrain these two values independently. We show in the Appendix Table 5.3.4 that the wind velocities are not affected by this assumption when using a covering fraction of 50% for the ISM; 3) The line profile shape is due entirely to the absorption of the stellar continuum. However, scattered emission infill may also affect the absorption profile. This effect is expected to be less significant for Fe II λ2586 compared to resonant lines without florescent emission lines such as Mg II (see Prochaska et al., 2011). Zhu et al. (2015) estimated that the equivalent width of the Fe II λ2586 absorption profile is affected by only 10% due to emission infill; 4) Two absorption components, an ISM component centered at zero systemic velocity and a wind component, are sufficient to characterize the observed absorption line profiles. This assumption may result in inaccurate column densities and line widths, if the profiles are composed of multi-components from multiple clouds. Higher-resolution galaxy spectra are required to test the effects of this assumption. Studies using high resolution spectra of background quasars find the absorption lines are composed of multiple clouds with more complex kinematics (e.g., Churchill et al., 2000); 5) the velocity distribution of absorbing atoms within a component is Maxwellian such that each absorption optical depth is modeled as a Gaussian, $\tau(\lambda) = \tau_c \exp\, -(\lambda - \lambda_c)^2/(\lambda_c\, b/c)^2$ where τ_c is a central optical depth at the line center, λ_c, c is the speed of light, and $b = \sqrt{2}\,\sigma$ is the Doppler parameter. This assumption is likely to be an over-simplification but it is reasonable given that the observed shape of the absorption trough is strongly influenced by the instrumental resolution.

According to this simple model, the normalized continuum can be described as

a product of the line intensity of the galaxy component and of the wind component. Each component has the form $1-C(1-\exp\ -\tau(\lambda))$. C is the covering fraction and it is set to 1 for the galaxy ISM component. We can express λ_c in terms of centroid velocity $v = c(\lambda_c - \lambda_0)/\lambda_0$, where λ_0 is the rest wavelength of the transition. For the galaxy component, $\lambda_c = \lambda_0$ (i.e., no velocity shift). The central optical depth is expressed in term of the column density, N, oscillator strength, f_0, and b using the relation $\tau_c = 1.45 \times 10^{-15} \lambda_0 f_0 N/b$ for N in unit of cm^{-2}, λ in Å and b in $\mathrm{km\,s}^{-1}$.

To summarize, the 6 free parameters of this two component model are: the covering fraction of the wind, C_w, the velocity centroid shifts of the wind, v_w, the Doppler broadening parameter of the wind, b_w, the Doppler parameter of the ISM in the galaxy, b_g, column density of the wind, N_w, and the column density of the gas in the galaxy, N_g. The model is convolved with the instrumental resolution and rebinned to match the observed data before comparing the two.

The model is fit to the data using a Bayesian method with custom Python code. Only the Fe II λ2586 absorption line is fitted. Regions that are covered by Fe II λ2600 absorption or the Fe II emission or Mn II absorption lines were masked out (i.e, $\lambda = (2591, 2632)$, or $\lambda = (2572, 2578)$). The posterior probability densities (PDFs) of the model parameters were computed using the affine-invariant ensemble Metropolis-Hastings sampling algorithm (Foreman-Mackey et al., 2013) assuming uniform priors: $v_w = (-450, 450)$, $b_w = (20, 450)$, $b_g = (20, 450)$, $\log N_w = (14, 17.5)$ and $\log N_g = (14, 17.5)$. A centroid velocity shift greater than $500\,\mathrm{km\,s}^{-1}$ is rule out by the data without the model, so we have restricted the velocity prior to estimate the velocity shift which is supported by the data. To

compute the likelihood of the data given the model parameters, we assumed that each data point is drawn from independent Gaussians centered around the model profile with a dispersion given by the measurement errors. This is equivalent to assuming a χ^2 distribution for the sum of squares of flux differences between the model and the data, with degrees of freedom equal to the number of observed data points.

We have checked our implementation of the simple model with simulated data. Results of this exercise are summarized in Table 5.5 and Fig. 5.5.

4.3.3 The wind velocities of AGN at $z \sim 1$ are similar to those of star-forming non-AGN galaxies at similar redshifts

Table 4.3 summarizes the marginalized PDFs of the six model parameters fitted to Fe II λ2586 absorption lines for both the AGN and the comparison samples . We used the median, 16th and 84th percentiles as summary statistics for the marginalized PDFs. Thus, the errors given in the table indicate the percentile deviation from the median. Detailed information on the PDFs for all six parameters can be found in the Appendix .

Figure 4.7 shows, for both AGN and the comparison sample at $z \sim 1$, the observed Fe II λ2586 absorption profiles and the fitted model profiles. In the top row, we show the fit to the composite spectrum of all 12 AGN candidates (Figure 4.7 a) or of only the 9 AGN without broad line AGN (Figure 4.7 b) or only the 7 narrow-line AGN with robust AGN identifications (Figure 4.7 c). In the second row, Figure 4.7d-f show the corresponding velocity centroid and

Doppler parameter PDFs for the three AGN subsamples. Figure 4.7g & h show similar figure for Coil et al. (2011) $z \sim 0.5$ AGN sample analyzed separately or jointly with our data. Figure 4.7i shows observed Fe II λ2586 absorption profiles and the model profiles for the comparison sample non-AGN star-forming galaxies at $z \sim 1$. In last row, Figure 4.7j & l show the velocity centroid and Doppler parameter PDFs of two reanalyses of the Coil et al. (2011) data and of the non-AGN sample. In each plot of the Fe II profile, the black points with error bars are the observed data points. The blue curve is the wind component while the orange curve is the galaxy absorption component. Both the blue and orange curves are shown before the convolution with the instrumental line-spread-function and thus represent the true components. The red curve is the product of the two components after convolution. All three curves are constructed from medians of the six marginalized model parameters. The marginalized median model fits the data well. The randomly drawn 500 model profiles from the PDFs of the model parameters are shown in pink. They also characterize the flux uncertainties very well. Cutting the histograms depicting PDFs of the centroid velocities and Doppler parameters, the dashed vertical lines mark the 16th, 50th (median), and 84th percentiles of the PDFs.

To summarize results presented in Table 4.3 and Figure 4.7, the wind centroid-velocity in $z \sim 1$ AGN, as derived using Fe II λ2586, is about $-140^{+72}_{-83}\,\mathrm{km\,s^{-1}}$ and its Doppler dispersion parameter is about $120^{+75}_{-64}\,\mathrm{km\,s^{-1}}$. These two parameters anti-correlate and their joint PDF is bi-modal or heavy-tailed (asymmetric). Even so, the marginalized, centroid-velocity PDF is fairly constrained (to 2σ significance). The maximum, centroid, velocity-shift ($v_w - 2\sigma_{v_w}$) in AGN is likely less

than $300\,\mathrm{km\,s^{-1}}$, while the maximum wind velocity ($v_w - 2\,b_w/\sqrt{2}$) is less than $600\,\mathrm{km\,s^{-1}}$. Similarly, the star-forming comparison sample has a wind centroid velocity of $-148^{+76}_{-125}\,\mathrm{km\,s^{-1}}$ and a Doppler parameter of $237^{+76}_{-83}\,\mathrm{km\,s^{-1}}$. Therefore, the velocity profiles of winds in AGN at $z \sim 1$ overlap those of the comparison sample similar redshifts.

Even though the comparison sample has higher SFRs than typical galaxies at a similar redshift, its wind properties are similar to what was found in typical galaxies at $z \sim 1$. For instance, Martin et al. (2012) found an Fe II centroid velocity of $-119 \pm 6\,\mathrm{km\,s^{-1}}$ in several tens of star-forming galaxies at at $z \sim 1$.

The escape velocity from a galaxy is approximately $5-6\times$ its O II emission line velocity dispersion (Weiner et al., 2009), which is about $120\,\mathrm{km\,s^{-1}}$ for the AGN sample and the comparison sample (see Figure 5.19 in the Appendix). Therefore, most of the outflowing gas does not escape from the host galaxies. Incidentally, the galaxy velocity dispersion inferred from fitting the Fe II λ2586 absorption profile is consistent with the O II emission-line, velocity-dispersion in both AGN and non-AGN samples.

The observed total equivalent width, without decomposing into the ISM and the wind components, is about 1.8Å for AGN and 1.9Å for the star-forming sample. Only half of the total equivalent width is due to the wind component in both samples. The presence of strong ISM component implies that substantial amount cold gas is present in the host galaxies and it has not been affected by AGN feedback. Large samples are need to firmly establish if the wind equivalent width is differently distributed in velocity in AGN and non-AGN, even though this is hinted by the current data.

We also find weak winds in AGN at $z \sim 0.5$ upon reanalysis of (Coil et al., 2011) data. The wind centroid velocity for this sample is $-151^{+67}_{-100}\,\mathrm{km\,s^{-1}}$ and its Doppler dispersion parameter is $112^{+74}_{-54}\,\mathrm{km\,s^{-1}}$. Coil et al. (2011) have measured the Fe II λ2586 centroid velocities and velocity widths for four of their AGN. Their measurements for both these two quantities range roughly between -130 to $-330\,\mathrm{km\,s^{-1}}$. Averaging their four measurements with inverse-variance weighting gives, a centroid velocity shift of $-180 \pm 9\,\mathrm{km\,s^{-1}}$ and a Doppler parameter of $274 \pm 13\,\mathrm{km\,s^{-1}}$. The total equivalent width of Fe II in this sample is 2.0Å and half of it is due to the wind component. The average wind equivalent width measured by Coil et al. (2011) is 1.2Å.

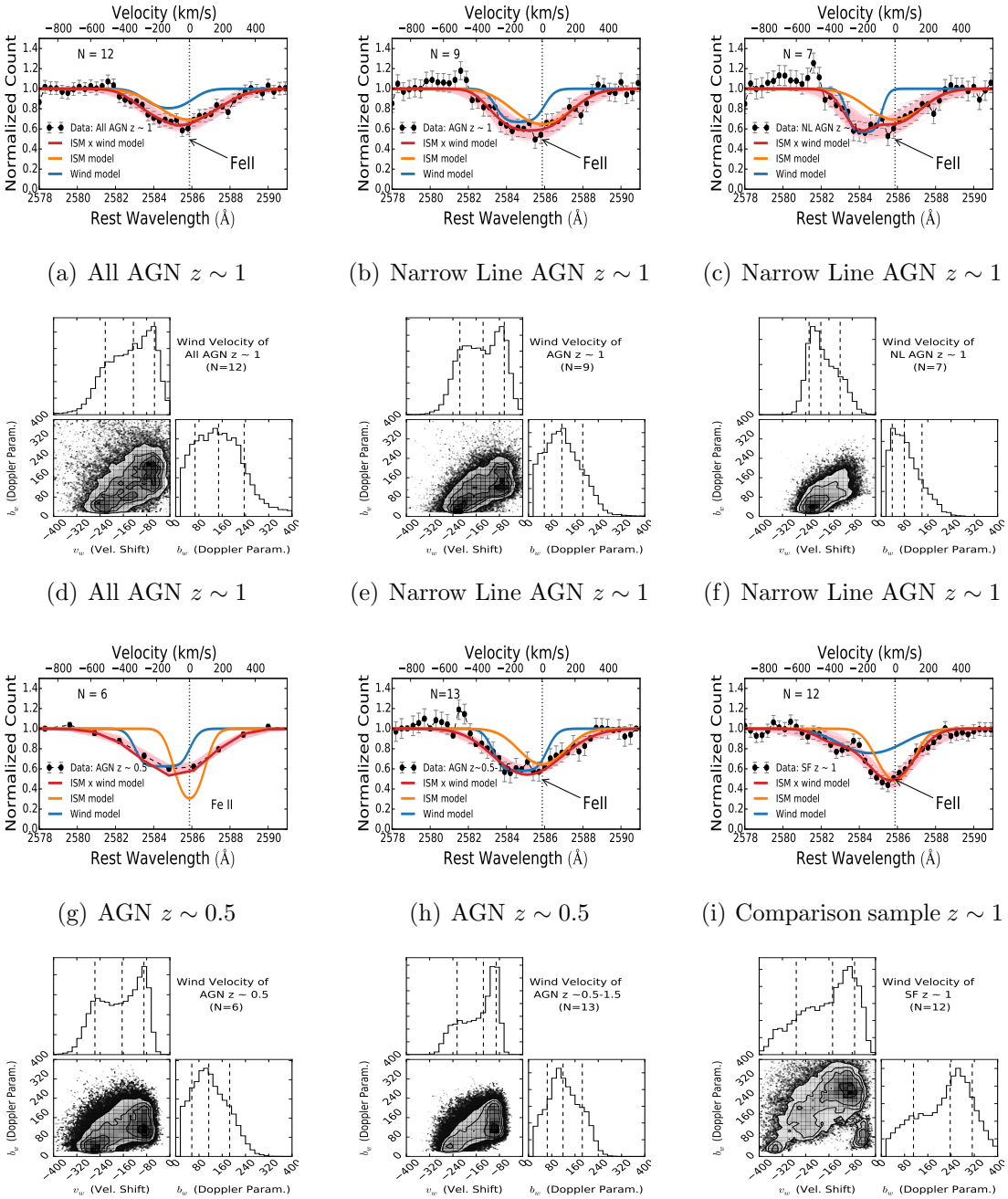

(a) All AGN $z \sim 1$ (b) Narrow Line AGN $z \sim 1$ (c) Narrow Line AGN $z \sim 1$

(d) All AGN $z \sim 1$ (e) Narrow Line AGN $z \sim 1$ (f) Narrow Line AGN $z \sim 1$

(g) AGN $z \sim 0.5$ (h) AGN $z \sim 0.5$ (i) Comparison sample $z \sim 1$

(j) AGN $z \sim 0.5$ (k) AGN $z \sim 1$ (l) Comparison sample $z \sim 1$

Figure 4.7:. Fitting the wind model to Fe II λ2586 absorption lines of AGN and a comparison sample of non-AGN galaxies. The red curves are convolved wind models constructed from the medians of marginalized posterior PDFs of the model parameters. The orange curves are the unconvolved ISM components of the models while blue curves are the unconvolved wind components. The histograms show the posterior PDFs of wind velocities and wind Doppler dispersion parameters. AGN have a wind centroid velocity of $\sim 150\,\mathrm{km\,s^{-1}}$ which extends only to $\sim 300\,\mathrm{km\,s^{-1}}$. Similar wind velocities are observed in star-forming non-AGN galaxies.

Table 4.3. Model parameter fits to Fe II λ2586 profiles.

Model Param.	AGN $z\sim1$ (N = 12)	NLAGN $z\sim1$ (N = 9)	NLAGN $z\sim1$ (N = 7)	SF $z\sim1$ (N = 12)	AGN $z\sim0.5$[a] (N = 6)	AGN $z\sim0.5-1.5$[b] (N = 13)	AGN $z\sim0.5-1.5$[c] (N=18)[d]
v_w	-124^{+69}_{-92}	-140^{+72}_{-83}	-192^{+70}_{-40}	-148^{+76}_{-125}	-161^{+72}_{-100}	-132^{+42}_{-88}	-128^{+47}_{-70}
b_w	150^{+91}_{-79}	120^{+75}_{-64}	77^{+61}_{-40}	237^{+76}_{-126}	112^{+74}_{-54}	121^{+65}_{-53}	136^{+74}_{-70}
C_w	$0.3^{+0.4}_{-0.1}$	$0.4^{+0.4}_{-0.1}$	$0.4^{+0.3}_{-0.1}$	$0.5^{+0.3}_{-0.3}$	$0.3^{+0.4}_{-0.1}$	$0.3^{+0.3}_{-0.1}$	$0.4^{+0.3}_{-0.1}$
N_w	$14.8^{+1.3}_{-0.5}$	$15.0^{+1.3}_{-0.7}$	$15.1^{+1.3}_{-0.7}$	$14.8^{+0.7}_{-0.3}$	$15.3^{+1.3}_{-0.7}$	$15.4^{+1.2}_{-0.8}$	$15.3^{+1.3}_{-0.6}$
b_g	245^{+45}_{-35}	228^{+48}_{-34}	214^{+51}_{-44}	134^{+37}_{-44}	130^{+65}_{-67}	181^{+69}_{-50}	179^{+60}_{-44}
N_g	$14.5^{+0.1}_{-0.2}$	$14.5^{+0.1}_{-0.2}$	$14.5^{+0.1}_{-0.2}$	$14.5^{+0.1}_{-0.2}$	$14.6^{+0.3}_{-0.3}$	$14.5^{+0.2}_{-0.3}$	$14.5^{+0.1}_{-0.1}$

[a]Renalysis of Coil et al. (2011) data

[b]A joint renalysis of Coil et al. (2011) data with our 7 narrow line AGN with highly reliable AGN identification.

[c]A joint renalysis of Coil et al. (2011) data with all AGN including 3 broad-line AGN and 2 with less reliable AGN identification.

[d]N denotes the number of galaxies in the stacked spectra.

Note. — The median, the 84th and 16th percentile deviations of the PDFs of parameters the are given in the table.

4.4 Discussion

We study winds using the Fe II λ2586 absorption line in 12 low-luminosity AGN host galaxies at $z \sim 1$. We find that the centroid velocity shift in the composite spectrum of these AGN host galaxies is -124^{+69}_{-92} km s^{-1} and its velocity dispersion is 106^{+64}_{-56} km s^{-1}. The wind velocities in these AGN are significantly lower than their escape velocities, and they are similar to those observed in star-forming non-AGN galaxies at a similar redshift. There is also strong ISM component in Fe II λ2586 absorption, implying substantial amount cold gas is present in the host galaxies. Thus, we do not find evidence for wind-mode AGN feedback in low-luminosity AGN host galaxies.

Prior observations have shown that black hole masses correlate tightly with bulge masses and velocity dispersions of classical bulges and ellipticals but correlate weakly or not all with pseudo-bulge and disk properties (e.g., Kormendy & Ho, 2013; Graham & Scott, 2013; McConnell & Ma, 2013, and references therein). It is not evident whether the tight correlation is due to merger-induced AGN feedback or non-causal connections by the hierarchical build-up of black holes and stellar masses through galaxy merging (Peng, 2007; Jahnke & Macciò, 2011). In particular, at $z \sim 1-2$ redshift, where both AGN and star-formation activities are at their peak (Aird et al., 2010; Madau & Dickinson, 2014), observations suggest that most AGN are not preferentially fueled by mergers or by violent disk instabilities (e.g., Cisternas et al., 2011; Kocevski et al., 2012; Schawinski et al., 2012; Böhm et al., 2013; Trump et al., 2014). On the other hand, the highest luminosity AGN with $L_{\rm X} > 10^{44}$ erg s^{-1} may be triggered by merger-induced starbursts (Treister et al., 2012; Villforth et al., 2014; Kocevski et al., 2015; Del

Moro et al., 2016). A consensus is emerging on two major modes of AGN feedback, depending on the fueling mechanism of black holes (Hopkins & Hernquist, 2006; Kauffmann & Heckman, 2009; Sijacki et al., 2007; Hopkins et al., 2014). A major merger-induced high accretion rate "quasar mode" feedback, which quenches star-formation by radiatively driven powerful (dusty) winds (Silk & Rees, 1998; Di Matteo et al., 2005; Murray et al., 2005; Hopkins et al., 2006), and a stochastic low accretion rate "radio-mode" feedback which maintains low star formation by radio jet mechanical gas heating (Fabian et al., 2003; Croton et al., 2006; McNamara & Nulsen, 2007; Blanton et al., 2011; Gabor et al., 2011; Hlavacek-Larrondo et al., 2012).

Despite theoretical appeal, confirming evidence of quasar mode feedback from AGN remains elusive. Here, we discuss some of the evidence reported in the literature, with emphasis on those with larger samples when multiple, similar studies exist. Our aim is to show that most wind studies using cold, warm or molecular gas are either in agreement or consistent with our finding that low luminosity AGN ($L_{\rm X} \sim 10^{42}$ erg s^{-1}) have similar winds as those from star-forming galaxies of similar galaxy properties, especially if the comparison is made at similar AGN luminosities as those of our sample.

4.4.1 Most previous cold gas absorption studies also found low wind velocities

Neutral gas outflows in low redshift $z \sim 0.1$ AGN have been extensively studied using Na I (e.g., Rupke et al., 2005a; Krug et al., 2010). The clearest result from these studies is that the wind velocities of narrow-line (type 2) AGN are similar

to the wind velocities of starburst and star-forming galaxies. Krug et al. (2010) studied outflows in 35 infrared-faint (i.e., low star-forming) Seyferts in an effort to disentangle the starburst effects on the winds from the AGN effects. The authors compared the outflow properties of these Seyferts with that of infrared-bright composite Seyferts in which both starbursts and AGN co-exist. The wind detection rates for the infrared-faint Seyfert 1s (6%) and Seyfert 2s (18%) are lower than previously reported for infrared-luminous Seyfert 1s (50%) and Seyfert 2s (45%). In addition, the outflow velocities of both high and low SFR Seyfert 2s are similar to those of starburst galaxies, while the outflow velocity in only one out of eighteen Seyfert1s is significantly higher. The measured average wind velocity for infrared-faint Seyferts 2 galaxies ($v = -137 \pm 8$ km s^{-1}, $b = 250 \pm 214\,\mathrm{km\,s^{-1}}$) and the authors' conclusion that AGN do not play a significant role in driving the outflows in most local infrared-faint and infrared-bright Seyferts 2s is consistent with our result. The particular Seyfert1 with the strong wind has an average wind velocity -600 $\mathrm{km\,s^{-1}}$ and very small velocity dispersion ($b = 21 \pm 6\,\mathrm{km\,s^{-1}}$). It is likely that this object's high velocity measurement is affected by emission infill at systemic velocity.

Likewise, Rupke et al. (2005a) studied a sample of 26 Seyfert ULIRGs using Na I. They found no significant differences between the velocities of Seyfert 2s which are ultra-Infrared galaxies (ULIRGs) ($v = -456^{+330}_{-191}\,\mathrm{km\,s^{-1}}$, $b = 232^{+244}_{-119}\,\mathrm{km\,s^{-1}}$) and starbursts of comparable infrared luminosity ($v = -408^{+224}_{-191}\,\mathrm{km\,s^{-1}}$, $b = 232^{+244}_{-119}\,\mathrm{km\,s^{-1}}$). They also found very high velocities ($\sim 5000\,\mathrm{km\,s^{-1}}$) in two Seyfert 1 AGN and argued that they are likely small-scale ($\sim 10\,\mathrm{pc}$) disk winds. They stressed that large-scale, lower velocity outflows certainly exist in Seyfert 1

ULIRGs, but their signature are wiped out by the bright light of the nucleus.

Recently, Sarzi et al. (2016) studied a sample of 456 nearby galaxies of which 103 exhibit compact radio emission indicating radio AGN activity. They found that only 23 objects (5%) out of their entire sample exhibited outflow signatures in Na I. Not even a single object showed evidence of AGN activity in radio and of cold-gas outflow simultaneously. Radio-AGN activity was found predominantly in early-type galaxies, while cold-gas outflows were mainly observed in late-type galaxies with central star formation or with composite galaxies of star formation and AGN activities. The authors emphasized that their work supports a picture in which the onset of AGN activity appears to lag behind the peak of starburst activity (e.g., Wild et al., 2010; Yesuf et al., 2014), and in which the gas reservoir has been significantly depleted by star-formation or stellar feedback before the AGN had a chance to couple to it.

Similarly, Sato et al. (2009) found Na I outflow velocities of $\sim 100\,\mathrm{km\,s^{-1}}$ in fading post-starburst galaxies with low-level nuclear activity at $0.1 < z < 0.5$. Within a similar redshift range, Coil et al. (2011) also found low velocity winds ($\sim 200\,\mathrm{km\,s^{-1}}$) in 13 post-starbursts galaxies by using Mg II and Fe II absorption lines. This result is in addition to the low-velocity outflows they found in low-luminosity AGN.

In contrast, Tremonti et al. (2007) observed high-velocity winds (with median $v \sim 1100\,\mathrm{km\,s^{-1}}$) in massive transitional post-starburst galaxies and concluded that AGN likely played a major role in the abrupt truncation of star-formation in these systems. But, in subsequent works, they argued that these fast outflows are most likely driven by feedback from extremely-compact, obscured, star for-

mation rather than AGN (Diamond-Stanic et al., 2012; Geach et al., 2014; Sell et al., 2014). But, it remains possible that the outflows were driven by AGN activity that has been recently switched off or are driven by extremely obscured AGN. Sell et al. (2014) found low-luminosity AGN in half of their post-starburst sample. Nevertheless, it should be noted that the authors concluded that the fast outflows are most likely driven by feedback from star formation rather than AGN. Generally, AGN are known to be common among post-starburst galaxies but are not directly linked to quenching starbursts (Yesuf et al., 2014).

To summarize the discussion so far, to our knowledge, all AGN-host galactic-wind studies using (near-)UV or optical absorption lines, with the exception of Hainline et al. (2011), mentioned in the introduction, found moderate wind velocities in AGN which are similar to those from star-forming galaxies. Attributing emission infill for the difference with Hainline et al. (2011)'s absorption profiles, Coil et al. (2011) concluded that their finding, namely, AGN host galaxies at $z \sim 0.2 - 0.5$ do not have significantly faster winds than star-forming galaxies at similar redshifts, was not strongly at odds with results from lower and higher redshifts. Our work and those discussed above affirm this conclusion.

Next, we discuss AGN winds detected in emission lines of ionized gas. Emission lines as wind diagnostics are much more difficult to interpret compared to absorption lines. For instance, to infer the mean velocity of the wind from emission lines, detailed understanding of the geometry of the wind, velocity distribution of the gas, and dust extinction in the host galaxy is needed. In a spherically-symmetric optically-thin outflow, the emission-line profile is symmetric and peaks at the systemic velocity of the galaxy (i.e, zero velocity). In contrast, in absorp-

tion lines which are minimally affected by resonant emission, the wind velocity profile is significantly offset from the systemic velocity. Regardless of how the emission line observations are interpreted, the result that low luminosity AGN at redshifts $z \sim 0.2 - 1$ do not have significantly faster winds (in absorption) than star-forming galaxies is consistent with the wind speeds inferred from emission lines in AGN of comparable luminosities.

4.4.2 Some previous ionized gas emission-line studies found high wind velocities and some did not

Rupke & Veilleux (2013) have explored the multiphase structure of galactic winds in six local ULIRGs using deep integral-field spectroscopy. Three of the ULIRGs host obscured quasars. Despite its small sample size, this work is unique by studying winds in the same objects in both emission and absorption, and it serves as a benchmark for interpreting myriads of emission-line only wind studies. Both the neutral and ionized gas of the six ULIRGs were studied by fitting the Na I absorption line and multiple Gaussian components to strong, nebular, emission lines ([O I], Hα and [N II]). In all systems, high-velocity, collimated, multiphase kiloparsec-scale outflows were reported and the neutral phase dominates the mass outflow rate. The spatially-averaged, mean, wind velocities were found to be similar ($v \sim 200 - 400$ km s^{-1}) in AGN and non-AGN, both for cold, neutral and warm, ionized gas. While the maximum wind velocities reach ~ 1000 km s^{-1} in neutral gas for both AGN and non-AGN, the highest gas velocities ($2000 - 3000$ km s^{-1}) were only observed in ionized gas in the obscured quasars.

Several spatially-resolved, spectroscopic studies at both low and high redshifts

have shown that broad, ionized emissions are common in luminous AGN (Liu et al., 2013; Förster Schreiber et al., 2014; Genzel et al., 2014; Liu et al., 2014; McElroy et al., 2015; Harrison et al., 2016; Zakamska & Greene, 2014). For example, Harrison et al. (2016) studied ionized gas kinematics in a representative sample of 89 X-ray AGN using [O III] at $z = 1.1 - 1.7$ or Hα emission at $z = 0.6 - 1.1$. The authors found high-velocity emission-line features in about half of the targets studied using [O III] . The velocity-width containing 80 % (W_{80}) of the [O III] line flux was found to mildly correlate with X-ray luminosity. For a Gaussian velocity distribution, $W_{80} = 2.56\,\sigma$, where σ is the velocity dispersion. Liu et al. (2013) found $W_{80} \sim 1.3 - 1.6\,v_0$ for their wind models, where v_0 is the initial velocity of the wind. Harrison et al. (2016) found that 70% of higher-luminosity AGN ($L_{\rm X} > 6 \times 10^{43}$ erg s^{-1}) have line widths of $W_{80} > 600$ km s^{-1}, while only 30% of the lower-luminosity AGN have velocity widths above 600 km s^{-1}. If we use the trend in Harrison et al. (2016), the 9 low-luminosity AGN studied in this work would have $W_{80} \sim 300$ km s^{-1} based on their X-ray luminosity. This value is roughly consistent with the velocity estimated using the Fe II absorption line.

AGN are known to exhibit jet-ISM interactions that accelerate gas to high velocities (Morganti et al., 2005; Nesvadba et al., 2006, 2008; Dasyra et al., 2015). Based on their current sample, Harrison et al. (2016) could not conclusively determine whether the radio luminosity or the X-ray luminosity is more fundamental in driving the highest-velocity outflows. They found marginal evidence that a higher fraction of the radio-luminous AGN have $W_{80} > 600$ km s^{-1} compared to the non-radio-luminous AGN. Thus, high-velocity outflows may be due to small-scale, compact radio jets instead of radiation from the quasar (Villar Martín et al., 2014;

Mullaney et al., 2013). Spatially-resolved studies have observed very-broadened [O III] emission-line that are co-spatial with kiloparsec scale jets (Holt et al., 2008; Müller-Sánchez et al., 2011; Husemann et al., 2013; Shih et al., 2013). At $z \sim 0.4$, using a large sample from SDSS, Mullaney et al. (2013) have shown that the highest velocity outflows are better linked to the mechanical radio luminosity of the AGN rather than to the radiative luminosity of the AGN. Alternatively, Zakamska & Greene (2014) have proposed that radio emission in radio-quiet quasars could be due to relativistic particles accelerated in the shocks initiated by the quasar-driven outflow.

Furthermore, Husemann et al. (2013) performed a detailed analysis of the extended ionized gas around 31 low-redshift QSOs and found only 3 QSOs have outflows with velocities greater than 400 km s^{-1}. In all three cases, they found a radio jet that is most likely driving the outflows, and they argued that jet-cloud interactions are the most likely cause of disturbances in the kinematics of the quasars. Husemann et al. (2015) have argued that disagreements between their work and the aforementioned previous works, that claimed high velocity outflows in luminous AGN, are likely due to the effects of beam smearing of unresolved emission lines caused by seeing (see also Karouzos et al., 2016; Villar-Martín et al., 2016). They reanalyzed the unobscured QSO sample of Liu et al. (2014) and found that the widths of [O III] lines on kiloparsec scales are significantly narrower after PSF deblending. The estimated kinetic power of the outflow is reduced by two orders of magnitude ($< 0.1\%$ of the quasar bolometric luminosity) after the correction. Thus, the feedback efficiency is smaller than required by some numerical simulations of AGN feedback. As the authors pointed out, the

majority of previous works have not carefully taken into account the effects of beam smearing. The incidence and energetics of large-scale AGN-driven outflows still remain an unsolved issue, especially in spatially unresolved observations of ionized gas outflows beyond the local universe.

4.4.3 Some previous molecular gas studies found high wind velocities

Molecular outflows have been reported in several AGN both in absorption and emission (Fischer et al., 2010; Feruglio et al., 2010; Sturm et al., 2011; Spoon et al., 2013; Veilleux et al., 2013; Cicone et al., 2014; García-Burillo et al., 2014; Sun et al., 2014). Veilleux et al. (2013) studied molecular OH 119μm outflows in a sample of 43, $z < 0.3$, galaxy mergers, which are mostly ULIRGs and QSOs. The OH 119μm feature is observed in emission, absorption, or both depending on the AGN strength. The OH emission is stronger relative to OH absorption in quasar-dominated systems and the feature is seen in pure emission in the most luminous quasars. The authors found that the median outflow velocities are typically ~ 200 km s^{-1} but the maximum velocities may reach ~ 1000 km s^{-1} in some objects. For even the most AGN-dominated systems with pure OH emissions, the emission line widths and shifts are ~ 200 km s^{-1}. The authors also reported that the absorption line centroids are distinctly more blue-shifted among systems with large AGN fractions and luminosities. It not clear how much this trend is due to emission infill of the absorption profile. Nevertheless, the velocity profiles of our AGN are in a good agreement with those of their AGN with comparable luminosity.

A recent X-ray observation of a mildly relativistic accretion disk wind in a local

Seyfet 1 ULIRG, which also shows high velocity molecular OH 119μm outflow have been hailed as providing direct connections between large-scale molecular outflows and the small-scale, AGN accretion wind in ULIRGs (Tombesi et al., 2015). A review of the powerful and highly ionized accretion winds observed in X-ray spectra of luminous AGN can be found in King & Pounds (2015).

Cicone et al. (2014) have studied CO emission in 19 local ULIRGS and quasars hosts. They found that starburst-dominated galaxies can have an outflow rate which are $\sim 2-4$ times their star formation rates and the presence of AGN may enhance the outflow rates by a large factor depending on its luminosity. The maximum velocities reach up to ~ 750 km s^{-1}. The authors estimated that the outflow kinetic power for galaxies with the most powerful AGN is about 5% of the AGN luminosity, as expected from some numerical models of AGN feedback.

In contrast, recent, local studies of molecular gas in recently quenched or quenching post-starbursts surprisingly found that these galaxies have large gas reservoirs comparable to star-forming galaxies (French et al., 2015; Rowlands et al., 2015). Therefore, they did not find evidence that the global gas reservoir is expelled by stellar winds or active galactic nuclei feedback. Similarly, at $z \sim 2$, quasar halos are observed to have abundant, cool gas which is sufficient to fuel the observed SFR for at least 1 Gyr (Prochaska et al., 2014). Current AGN feedback models remove too much gas from galactic halos and, therefore, under-predict the gas observed within quasar halos at $z \sim 2$.

To summarize, most absorption-line studies found that the wind velocities in AGN are moderate ($\sim 200-400$) km s^{-1} and are similar to velocities in star-formation-driven winds. Most high-velocity AGN winds reported to date are con-

troversial and can be attributed to observational complications such as emission infill and PSF smearing or they may not be due to radiation from luminous AGN, or they may just be spatially-unresolved, small-scale wind confined to the vicinity of black holes.

4.4.4 The feedback efficiency in the low-luminosity AGN at $z \sim 1$ and in most other AGN samples is less than 5%

The wind kinetic power can be parametrized in terms of the radiative luminosity of an AGN as $\dot{E} = \epsilon_f L_{\rm AGN}$, where ϵ_f is the fraction of the radiative luminosity transferred to the wind. Popular AGN feedback models invoke feedback efficiency, $\epsilon_f \sim 5\%$ to reproduce the properties of massive galaxies (e.g., Scannapieco & Oh, 2004; Di Matteo et al., 2005; Choi et al., 2012; Zubovas & King, 2012). Following Rupke et al. (2005b), we find $\epsilon_f \sim 0.1$ for our AGN sample, assuming a wind radius of 3 kpc and using the wind parameters estimated in Table 4.3. To convert our estimated Iron column density to Hydrogen column density, we adopt solar abundance ratio and a dust depletion factor of 10% and no ionization correction (Rubin et al., 2014). The sample bolometric luminosity of our AGN is estimated by multiplying the median X-ray luminosity of our sample with bolometric correction of 20 (Vasudevan & Fabian, 2007).

Figure 4.8 shows AGN bolometric luminosity against the wind kinetic power for our sample and other AGN wind samples in the literature, covering a wind range in redshift $z \sim 0.1 - 2$. Our compilation include AGN which are known to show wind signatures in cool gas absorption (Edmonds et al., 2011; Rupke et al.,

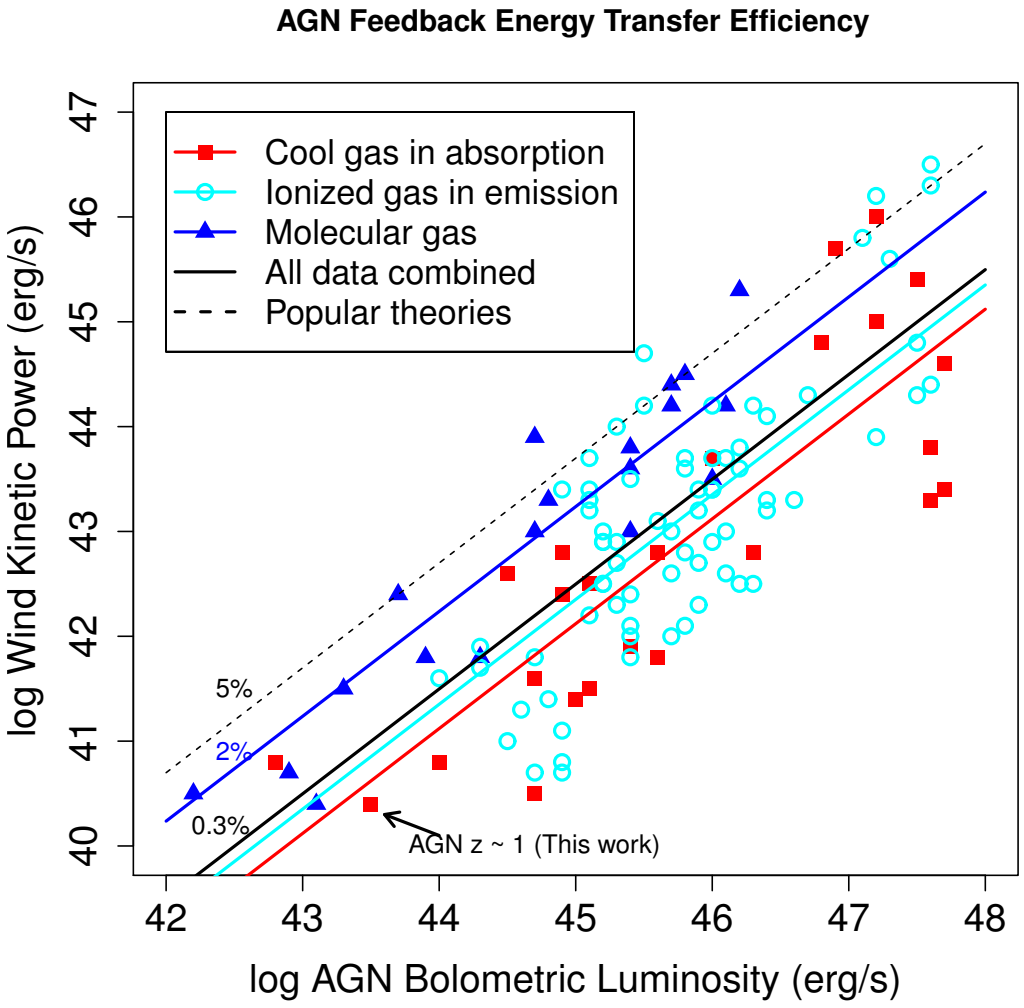

Figure 4.8:. AGN bolometric luminosity against the wind kinetic power for our sample and other AGN wind samples in the literature, covering a wind range in redshift $z \sim 0.1 - 2$. Our compilation include AGN which are known to show wind signatures in cool gas absorption (Edmonds et al., 2011; Rupke et al., 2005a; Krug et al., 2010; Borguet et al., 2012; Arav et al., 2013; Borguet et al., 2013; Rupke & Veilleux, 2013; Chamberlain & Arav, 2015), in ionized gas emission (Liu et al., 2013; Rupke & Veilleux, 2013; Harrison et al., 2014, 2016; McElroy et al., 2015; Carniani et al., 2015; Zakamska et al., 2016) and in molecular gas (Combes et al., 2013; Cicone et al., 2014; Sun et al., 2014; García-Burillo et al., 2015; Tombesi et al., 2015). The soild lines show linear model fits of the form $\log \dot{E} = \log L_{\rm AGN} + \log \epsilon_f$. The feedback efficiency, ϵ_f, is the only free parameter. The dashed line shows the 5% feedback efficency used in popular feedback models (e.g., Scannapieco & Oh, 2004; Di Matteo et al., 2005; Choi et al., 2012; Zubovas & King, 2012).

2005a; Krug et al., 2010; Borguet et al., 2012; Arav et al., 2013; Borguet et al., 2013; Rupke & Veilleux, 2013; Chamberlain & Arav, 2015), in ionized gas emission (Liu et al., 2013; Rupke & Veilleux, 2013; Harrison et al., 2014, 2016; McElroy et al., 2015; Carniani et al., 2015; Zakamska et al., 2016) and in molecular gas (Combes et al., 2013; Cicone et al., 2014; Sun et al., 2014; García-Burillo et al., 2015; Tombesi et al., 2015).

Where the wind power measurements for the ionized gas are not readily available, we estimate them following the standard methods and assumptions (e.g., Nesvadba et al., 2006; Zakamska et al., 2016). The wind power for all ionized gas measurements are estimated from nebular emission lines assuming a wind radius of 3 kpc, electron density of 100 cm^{-3} and the velocity-width is 1.3 times the the initial wind velocity, $W_{80} = 1.3v_0$. As discussed in (Zakamska et al., 2016), a standard method of estimating the wind power for the ionized gas is to use Hydrogen recombination lines to estimate the mass of the emitting Hydrogen, but [O III] emission-line may be a better probe of the extended emission. When they are available, O III velocity width and luminosity are used to estimate wind kinetic power, assuming [O III]/Hβ ratio of 10. Otherwise, Hydrogen lines are used. For the consistency, we adjust the literature wind power measurements for the cool gas to our assumed wind radius of 3 kpc when the wind radius were not previously measured. When the bolometric luminosities are not provided in the previous works, they are estimated from literature X-ray luminosities using bolometric correction of 20.

Fitting the data in Figure 4.8, with a model $\log \dot{E} = \log L_{\mathrm{AGN}} + \log \epsilon_f$, we find that ϵ_f is 0.3% for the combined multi-phase data. The ϵ_f estimated from

molecular wind data is 2% and is significantly different from ϵ_f estimated from outflowing ionized gas in emission or cool gas in absorption. Although the wind power and the bolometric luminosity estimates can be a very uncertain, provided that the assumptions above are correct, the current analysis suggests that most AGN have significantly lower feedback efficiency than what is assumed or predicted by some theoretical AGN feedback models.

4.5 Summary and Conclusion

We study winds using the Fe II λ2586 absorption line in 12 AGN host galaxies at $z \sim 1$. Nine of these galaxies significantly deviate from the relationship between star-formation and X-ray luminosity and one of them has strong Ne V emission. We find that the centroid velocity shift in the composite spectrum of these AGN host galaxies is -124^{+69}_{-92} km s^{-1} and its velocity dispersion is 106^{+64}_{-56} km s^{-1}. The wind velocities in these AGN are significantly lower than their escape velocities. Thus, the bulk of their gas likely remains bound. The winds in these AGN are consistent with those observed in star-forming non-AGN galaxies at a similar redshift roughly matched in mass and galaxy axis-ratio. The average spectrum of the comparison sample has a centroid velocity of -148^{+76}_{-125} km s^{-1} and a velocity dispersion of 168^{+54}_{-89} km s^{-1}. We have reanalyzed the sample of 6 low-luminosity AGN at $z \sim 0.5$ from Coil et al. (2011). Our result is consistent with the winds seen in these and other lower-redshift low-luminosity AGN. We conclude that the wind-mode AGN feedback is insignificant in low-luminosity AGN hosts. Qualitatively, the feedback efficiency in our low-luminosity AGN and most other AGN samples is $\sim 0.3\%$, which is the significantly smaller than required by

some numerical simulations of AGN feedback. Future, large-sample-size and high signal-to-noise studies of winds in AGN and in a well-matched control sample of non-AGN are needed to significantly advance our knowledge from existing small sample absorption line studies, and to enable detailed modeling of winds which will potentially uncover subtle differences between the winds in AGN and in their control sample.

Chapter 5

Appendix

5.1 Ancillary Material for Chapter 2

5.1.1 Details of Dust Correction

5.1.1.1 Methods of dust correction

We correct for dust effects on emission-line luminosities (O II, Hα, and etc), GALEX and SDSS colors, the Hα equivalent width, $W_{\mathrm{H}\alpha}$, and $D_n(4000)$. For emission line extinction curve, we use eqn. 5.1 and for the continuum extinction curve, we use eqn. 5.2 (Charlot & Fall, 2000; Wild et al., 2011a,b). In this section, continuum quantities will be denoted by '$*$' superscript.

$$Q_\lambda = (1-\mu)\,(\lambda/5500)^{-1.3} + \mu\,(\lambda/5500)^{-0.7} \text{ where } \mu = 0.4 \tag{5.1}$$

$$Q^*_\lambda = 1/N\,[(\lambda/\lambda_{b_1})^{n\,s_1} + (\lambda/\lambda_{b_1})^{n\,s_2} + (\lambda/\lambda_{b_2})^{n\,s_3} + (\lambda/\lambda_{b_3})^{n\,s_4}]^{-1/n} \tag{5.2}$$

Q^*_λ is composed of four power-law functions with exponents $s_{[1-4]}$ smoothly joined with a smoothness parameter $n = 20$. The power-law exponents vary with both axis ratio, b/a, and fiber specific star formation rate, ψ_s, according to linear functions given in Wild et al. (2011a) eqn. 22-25. The $\lambda_{b[1-3]}$ are related to the position of the three break points at $0.2175\,\mu$m, $0.3\,\mu$m and $0.8\,\mu$m and the power-law exponents according to eqn. 19-21 in Wild et al. (2011a). N is the normalization, defined such that Q^*_λ is unity at $5500\,\mathring{A}$.

The line optical depth is given by eqn. 5.3 and uses the expression of τ_V in eqn. 5.4

$$\tau_\lambda = \tau_V Q_\lambda \tag{5.3}$$

$$\tau_V = 0.921 \times 2.5/\left(Q_{4861} - Q_{6563}\right) \times \log\left(\mathrm{H}\alpha/\mathrm{H}\beta \times (\mathrm{H}\alpha/\mathrm{H}\beta)^{-1}_{\mathrm{int}}\right) \tag{5.4}$$

We require SNR $> 1\sigma$ on Hα and Hβ lines. We assume dust-free $(\mathrm{H}\alpha/\mathrm{H}\beta)_{\mathrm{df}} = 2.86$ for star-forming galaxies (Osterbrock, 1989) and $(\mathrm{H}\alpha/\mathrm{H}\beta)_{\mathrm{df}} = 3.1$ for AGN (Veilleux & Osterbrock, 1987). For example, using the above equations, the dust corrected O II flux is given by:

$$f_{\mathrm{OII,dc}} = f_{\mathrm{OII}} \times 10^{0.4 \times 1.086 \times \tau_{3727}} \tag{5.5}$$

To correct for galaxy fluxes (colors) we use the ratios of τ_V/τ^*_V in eqn. 13-16 Wild et al. (2011a), which are found to vary strongly with galaxy properties such as axis-ratio and specific SFR. We use the ratios that give maximal stellar ex-

tinction. In other words, $\min\{\tau_V/\tau_V^*(\psi_s), \tau_V/\tau_V^*(b/a)\}$. We prefer maximal stellar extinction because the optical depth ratios in Wild et al. (2011a) are generally smaller but asymptote to 2.08, the measured values in starbursts (Calzetti et al., 2000). In estimating the optical depth ratios, we use star formation rates calculated from dust-corrected Hα using the conversion factor of Kennicutt (1998). The SFRs will be overestimated if there is a significant contribution from AGN to the Hα emission line. We used the optical depth ratios estimated from axis-ratio (i.e, inclination) only as a check, and the possible over-estimation of SFR due to AGN does not significantly affect our results. It should be noted that we do not purposely use the star formation rate measurements provided in SDSS DR8 which are derived from photometry for AGN, because they may be systematically underestimated for dusty galaxies (including AGN, Wild et al., 2011a).

$$\tau_\lambda^* = Q_\lambda^* \times \tau_V^* = Q_\lambda^* \times (\tau_V^*/\tau_V) \times \tau_V \tag{5.6}$$

$$A_\lambda^* = 1.086\tau_\lambda^* \tag{5.7}$$

Because we are correcting for the global galaxy colors, while our estimate of τ is based on fiber quantities, we will approximately correct for gradient (aperture bias) in τ_V by dividing A_λ^* with a correction factor $f_\nabla = 1.0 - 1.25$ according to Figure 6 of Wild et al. (2011a): for bulge-dominated galaxies we use eqn. 5.8 while

for disk-dominated galaxies we use eqn. 5.9

$$f_{\nabla} = \begin{cases} 1.0 & \text{if } R_{fib}/R_{90} \geq 1 \text{ else} \\ 1.05 & \text{if } R_{fib}/R_{90} < 1 \ \ \& \ \ \log\psi \leq -9.9 \\ 1.1 & \text{if } R_{fib}/R_{50} \geq 1 \ \ \& \ \ -9.9 < \log\psi < -9.6 \\ 1.15 & \text{if } R_{fib}/R_{50} < 1 \ \ \& \ \ -9.9 < \log\psi < -9.6 \\ 1.2 & \text{if } R_{fib}/R_{50} \geq 1 \ \ \& \ \ \log\psi > -9.6 \\ 1.25 & \text{if } R_{fib}/R_{50} < 1 \ \ \& \ \ \log\psi > -9.6 \end{cases} \tag{5.8}$$

$$f_{\nabla} = \begin{cases} 1.0 & \text{if } R_{fib}/R_{90} \geq 1 \text{ else} \\ 1.05 & \text{if } R_{fib}/R_{90} < 1 \ \ \& \ \ \log\psi \leq -9.9 \\ 1.05 & \text{if } R_{fib}/R_{50} \geq 1 \ \ \& \ \ -9.9 < \log\psi < -9.6 \\ 1.1 & \text{if } R_{fib}/R_{50} \geq 1 \ \& \ \log\psi \geq -9.6 \\ 1.15 & \text{if } R_{fib}/R_{50} < 1 \ \ \& \ \ -9.9 < \log\psi < -9.6 \\ 1.2 & \text{if } R_{fib}/R_{50} < 1 \ \ \& \ \ \log\psi \geq -9.6 \end{cases} \tag{5.9}$$

For instance, $(\text{NUV-g})_{\text{dc}}$ is given by eqn. 5.10 below. We use the effective wavelengths of SDSS bands given in Fukugita et al. (1996).

$$(NUV - g)_{\text{dc}} = (NUV - g) - (A^*_{2267} - A^*_{4825})/f_{\nabla} \tag{5.10}$$

We correct the $W_{\text{H}\alpha}$ using the following equation:

$$W_{\text{H}\alpha,\text{dc}} = W_{\text{H}\alpha} \times \frac{10^{0.4\times1.086\times\tau_{6563}}}{10^{0.4\times1.086\times\tau^*_{6563}}} = W_{\text{H}\alpha} \times 10^{0.4\times1.086\times(\tau_{6563}-\tau^*_{6563})} \tag{5.11}$$

$D_n(4000)$ is defined as a flux ratio of a narrow continuum range red-ward of

4000 Å break $(4000-4100)$ to a narrow continuum range blue-ward of the break $(3850-3950$, Balogh et al., 2005).

Therefore, $D_n(4000)_{\rm dc} \approx D_n(4000) \times 10^{0.4\times(A^*_{\rm red}-A^*_{\rm blue})}$. where $A^*_{\rm red} = (A^*_{4000} + A^*_{4050} + A^*_{4100})/3.0$ and $A^*_{\rm blue} = (A^*_{3850} + A^*_{3900} + A^*_{3950})/3.0$

In the rest of this section we will show that our post-starburst selection does not significantly depend on the detail assumptions of the dust correction described above. To that end, Figure 5.1 replots the NUV-g color versus $\rm D_n(4000)$ diagram for different dust-correction assumptions. In Panel a and b, we show the version of the figure in which NUV-g color versus $\rm D_n(4000)$ are corrected using the Calzetti et al. (2000) extinction curve with the ratio of excess $B-V$ colors of gas to stars is, $E^*(B-V)/E(B-V) = 0.44$ and 1.0. Note that we adopted in the main text the empirical attenuation curve of (Wild et al., 2011a) and their prescription to estimate $E^*(B-V)/E(B-V)$ ratios. Since the selection of FPSBs explicitly depends on the dust correction, we show in panel a to b, the alternative selection of this class for the the given dust-correction prescription adopted in each panel. In panel a 136 FPSBs and in panel b 126 FPSBs are identified. About 15-25% of the FPSBs are previously (§ 2.3.4.1) unidentified but about 85% of the FPSBs identified in section three are also identified in panel a to b. The Calzetti et al. (2000) curve lacks the 2175 Å bump and Wild et al. (2011a) find typically $0.3-1.0$ magnitudes more attenuation in the NUV compared to the Calzetti extinction curve. Thus, the previously unidentified FPSBs may be dusty contaminants. Overall, the fact that each panel identified comparable number of FPSBs and recovered 85% of FPSBs defined in § 2.3.4.1, suggests that the details of dust-correction are not important for the selection of these objects. Furthermore, the

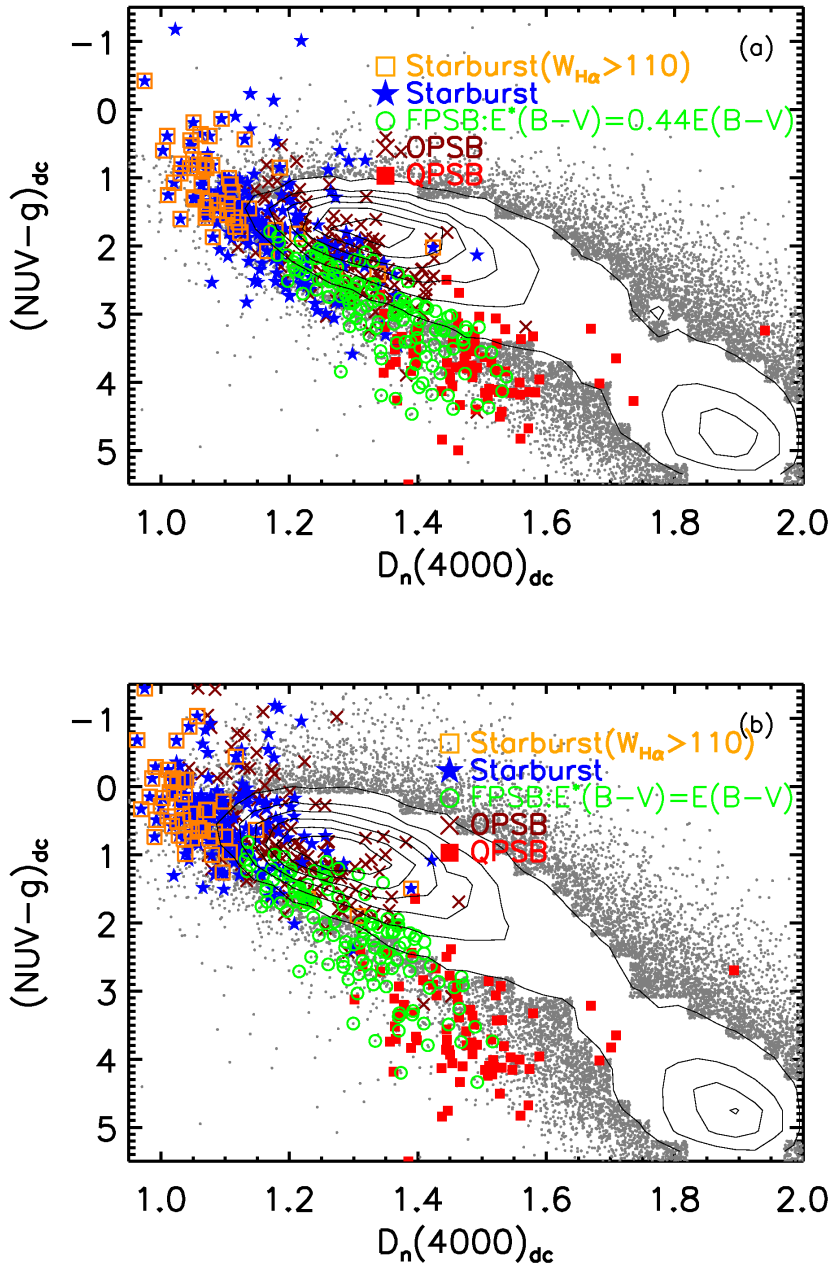

Figure 5.1:. Panel (a): Dust-corrected NUV-g color versus $D(4000)$. The FPSBs are selected assuming the Calzetti extinction curve with $E^*(B-V)/E(B-V) = 0.44$. In panel (b) the FPSB selection assumes the Calzetti extinction curve with $E^*(B-V)/E(B-V) = 1.0$ instead. The main point of the figure is that the details of the dust-correction are not important for the post-starburst selection as long as dust in all galaxies are similar. On the other hand, most starbursts would not have been identified if it were not for the dust correction.

figure also shows (in orange square) the subset starbursts with (dust-extincted) $W_{H\alpha} > 110$, that is to say, those that satisfying the Lee et al. (2009) definition of starbursts. This subset only account for 25% of all starbursts we have identified. Therefore, the dust correction of Hα is important to identify majority of dust-extincted starbursts.

The AGN fraction for FPSBs selected in panel a and pane b is 45% and 48% respectively. In comparison, the AGN fraction for FPSBs selected in the main text (§3.4) is 53%. Therefore, the error on AGN fraction of transiting post-starbursts may be as high as 8% (or even higher if BPT composite galaxies indeed host AGN). Even with 8% error, the AGN fraction in post-starbursts is still more than two times higher than that of normal galaxies.

5.1.1.2 The color-color diagram: the intrinsic colors of obscured post-starbursts

Moreover, in this subsection we aim to show that our dust-correction works and our starburst evolutionary path is plausible. Figure 5.2 shows the $UVgz$ diagram (NUV-g vs. g-z), a variant of the widely used UVJ diagram in galaxy evolution studies (e.g., Wuyts et al., 2007; Williams et al., 2009; Whitaker et al., 2012). In these diagrams dusty star-forming, non-dusty star-forming and quiescent galaxies are well separated. Star-forming galaxies form a diagonal track which extends from blue to red colors. The red end of this track is populated by dusty galaxies. The quiescent galaxies form a separate clump above the dusty star-forming galaxies. We show the $UVgz$ diagram before and after the dust correction.

After dust-correction, blue star-forming and red quiescent galaxies are cleanly

separated in the $UVgz$ diagram. The starbursts are significantly bluer after the dust correction and they lie well off the blue cloud to the lower left. The dust correction is difficult for the quenched post-starbursts because of their weak emission lines. However their location in the upper right corner of the $UVgz$ diagram is consistent with little or no dust extinction(cf. Balogh et al., 2005; Kaviraj et al., 2007; Brown et al., 2009; Chilingarian & Zolotukhin, 2012; Whitaker et al., 2012). We also showed in Figure 2.5 that about 80% of quenched post-starbursts do not show significantly dust-obscured star formation (have $f_{12\mu m}/f_{0.2\mu m} < 200$).

Transiting post-starbursts show more significant dust-reddening than do quenched post-starbursts: their observed colors are significantly redder but they are indeed intrinsically bluer. Despite the large overlap with normal galaxies, the OPSBs generally have intermediate intrinsic colors between that of QPSBs and FPSBs. Their overlap with normal galaxies is not a problem because the the overplotted model tracks also pass through normal galaxies. In contrast to the dust-unreddened colors, the observed g-z colors of PSBs get redder from OPSBs to FPSBs to QPSB, suggesting a decreasing dust sequence we have seen in previous diagrams. The plausible arrangement of SBs and PSBs in color-color space is also further evidence that the dust corrections work.

5.1.2 Details of Stellar Population Modeling

We modeled SFHs of a post-starburst as a superposition of an old stellar population initially formed at time $t = 0$ following a delayed exponential SFH of a form $\psi \propto t \exp(-t/\tau_1)$ with e-folding time, $\tau_1 = 1\,\mathrm{Gyr}$ (cf. Kriek et al., 2011) and a young stellar population formed in a recent burst at $t = 12.5\,\mathrm{Gyr}$ ($z \sim 0.1$)

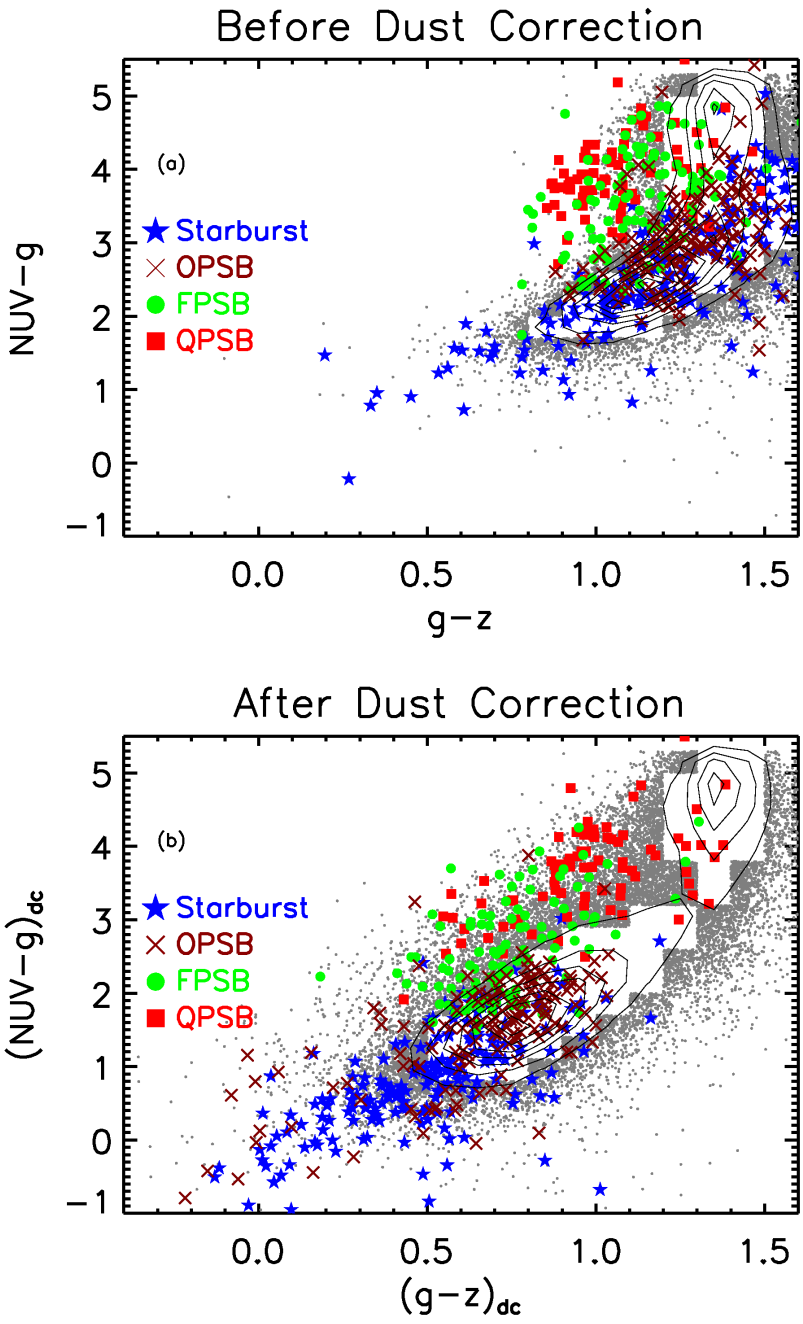

Figure 5.2:. Panel (a) : Rest-frame NUV-g vs. g-z color-color diagram, using observed (not dust-corrected) magnitudes. Panel (b) : Dust-corrected rest-frame NUV-g vs. g-z color-color diagram. The rapid quenching/strong burst model tracks nicely describe the sequence of starburst to transiting post-starburst to classical quenched post-starburst. The dust-obscured galaxies are also consistent with the transiting post-starbursts along this track. We use this with our other evidence (in Figures 2.4 and 2.9) to infer that, like the fading post-starburst population, the dust-obscured post-starbursts represent an intermediate phase from starbursts to post-starbursts.

with exponentially declining SFH, $\psi \propto \exp(-t/\tau_2)$, of $\tau_2 = 0.1\,\mathrm{Gyr}$ (cf. Kaviraj et al., 2007; Falkenberg et al., 2009). Because of the burst mass-age degeneracy, the ages of the post-starbursts depends on the decay timescale τ_2 we assumed. In this section, we quantify the effect of using different decay timescales ($\tau_2 = 0.05$ or $\tau_2 = 0.2$) instead of our fiducial value of $\tau_2 = 0.1\,\mathrm{Gyr}$ used in the main text .

Figure 5.3a replots the dust-corrected rest-frame NUV-g and g-z color-color diagram to show that the starbursts to quenched post-starbursts evolution can alternatively be modeled with $\tau_2 = 0.05\,\mathrm{Gyr}$ and burst fraction $b_f = 10\%$ or $\tau_2 = 0.2\,\mathrm{Gyr}$ and burst fraction $b_f = 30\%$. Likewise, Figure 5.3b plots fiber specific SFR against dust-corrected fiber g-z color to make a similar point. Thus, models with τ_2 outside the range 0.05-0.2 are excluded since they do not produce the observed population of post-starburst galaxies. The fiber specific star formation rates are estimated from dust-corrected Hα (§ 2.2.4) using the conversion factor of Kennicutt (1998) and the fiber stellar mass. Figure 5.4 estimates the age of starbursts and post-starbursts for these alternative burst models using the z band normalized median and quartile SEDs of these galaxies. Accordingly, the time lag between the starburst and AGN phase may be between 100 and 400 Myr.

5.1.3 Details of Post-starburst Selection

The following equations specify the fourth order polynomial fits to the data of main sequence galaxies in Figure 2.4.

$$\mathrm{W_{H\delta}} = 23.112 - 19.700 \times x + 3.355 \times x^2 + 0.0817 \times x^3 - 0.00871 \times x^4 \quad (5.12)$$

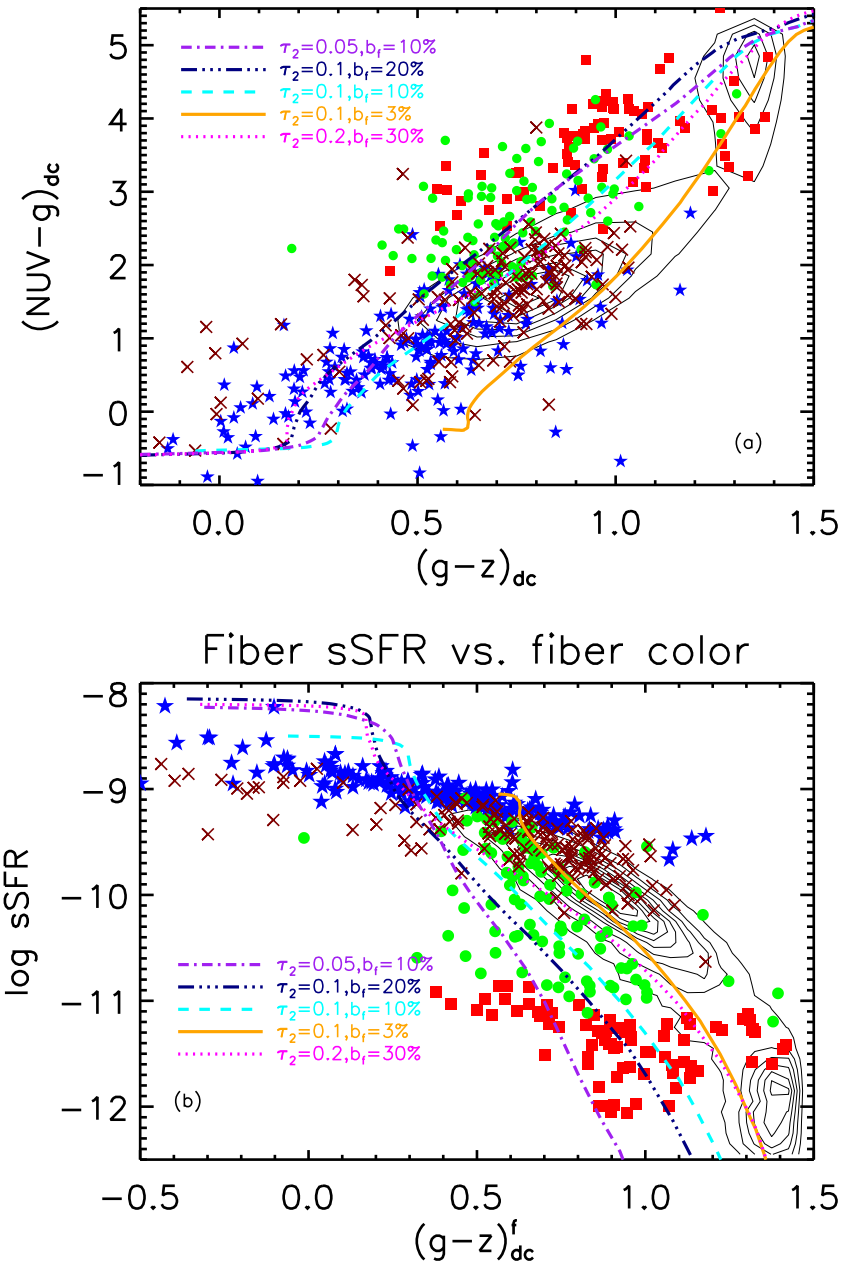

Figure 5.3:. Panel (a): dust-corrected rest-frame NUV-g and g-z color-color diagram. Overplotted are burst modeled tracks of $\tau_2 = 0.05, 0.1$ and 0.2 Gyr (Bruzual & Charlot, 2003). Panel (b): Specific fiber star formation rate versus dust-corrected fiber g-z color . These diagrams exclude burst models outside $\tau_2 = 0.05 - 0.2$ range.

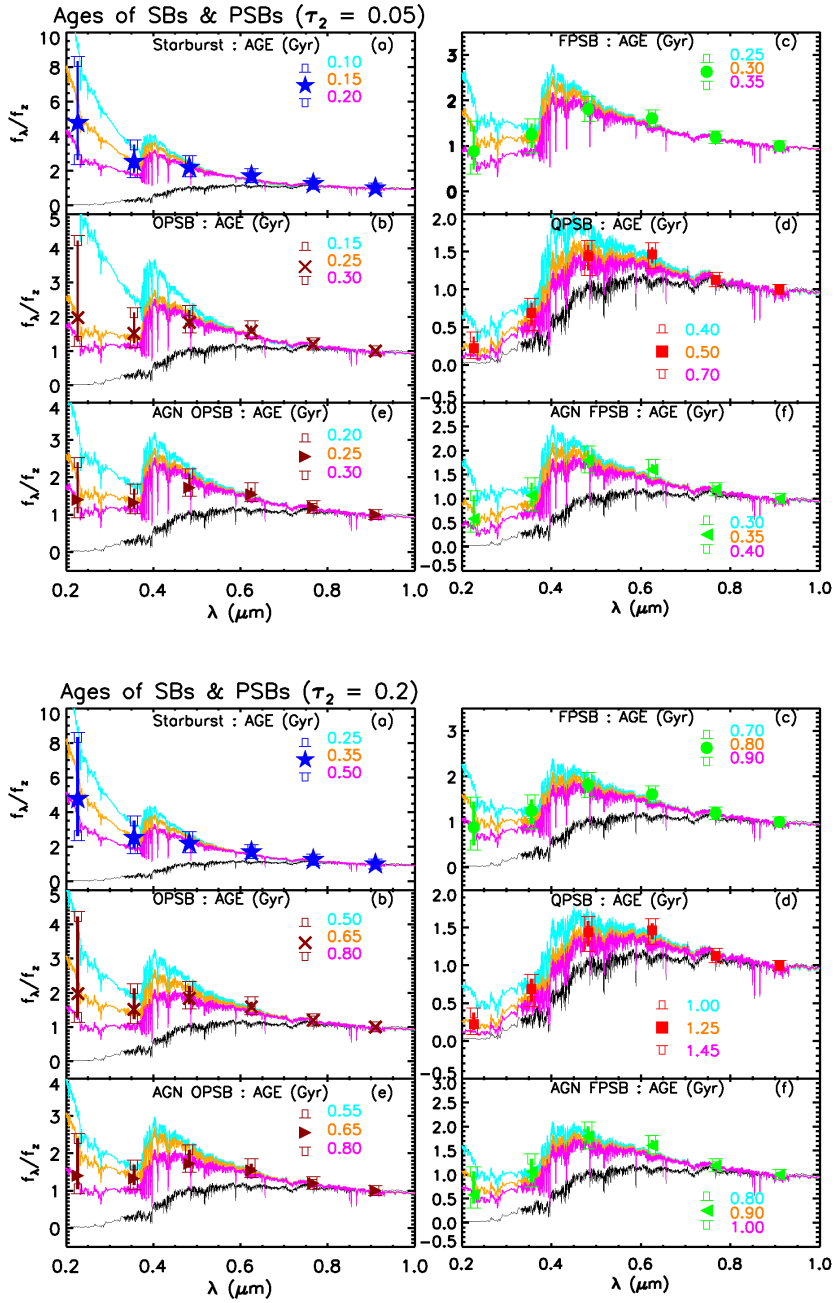

Figure 5.4:. The z band normalized median and quartile fluxes at the effective wavelengths of the NUV, u, g, r, i, z bands. This figure is the similar to Figure 2.9 but overplots Bruzual & Charlot (2003) burst models with different SFR timescale τ_2 and burst fraction b_f. Top figure: the overplotted spectra are $\tau_2 = 0.05\,\mathrm{Gyr}$ and $b_f = 10\%$ of different ages, as indicated on each panel. Bottom figure uses $\tau_2 = 0.2$ and $b_f = 30\%$ instead. The main point of the figure is that starbursts and AGN are not coeval, they are separated at least by about 100-400 Myr.

$$(NUV-g)_{\rm dc} = 7.010 - 13.547 \times x + 8.895 \times x^2 - 1.397 \times x^3 + 0.0462 \times x^4 \quad (5.13)$$

where $x = D_n(4000)_{\rm dc}$

5.1.4 More AGN Properties of Post-starbursts

5.1.4.1 WISE AGN diagnostic

An AGN has a spectral energy distribution (SED) that rises from $\sim 3-5\,\mu$m due to hot dust emission from its dusty torus (Nenkova et al., 2008), while a starburst has a composite stellar spectrum which peaks at $1.6\,\mu$m and declines over the range from $\sim 3-5\,\mu$m. Mid-IR color-color diagnostic diagrams use this idea to distinguish AGN dominated galaxies from starburst dominated ones (e.g., Lacy et al., 2004; Stern et al., 2005; Donley et al., 2012). The IR color-color diagrams select only luminous AGN, and do not detect weak AGN (Donley et al., 2012).

Figure 5.5 plots the WISE $\log(\mathrm{f}_{12\mu\mathrm{m}}/\mathrm{f}_{4.6\mu\mathrm{m}})$ vs. $\log(\mathrm{f}_{4.6\mu\mathrm{m}}/\mathrm{f}_{3.4\mu\mathrm{m}})$ diagram (Wright et al., 2010; Izotov et al., 2011; Assef et al., 2012; Lake et al., 2012; Stern et al., 2012). This figure is similar to Figure 2.5 and it is presented here for completeness. Stellar populations younger than 0.6 Gyr dominate $12\,\mu$m emission and, as a result, $[4.6\,\mu\mathrm{m}]-[12\,\mu\mathrm{m}]$ color is known to correlate well with SFR (Donoso et al., 2012). Normal galaxies in the parent sample form a tight and elongated bi-modal sequence with some vertical scatter at $\mathrm{f}_{12\mu\mathrm{m}}/\mathrm{f}_{4.6\mu\mathrm{m}} \gtrsim 1$. Generally, the starbursts are located at the right-most high-SFR end of the sequence,

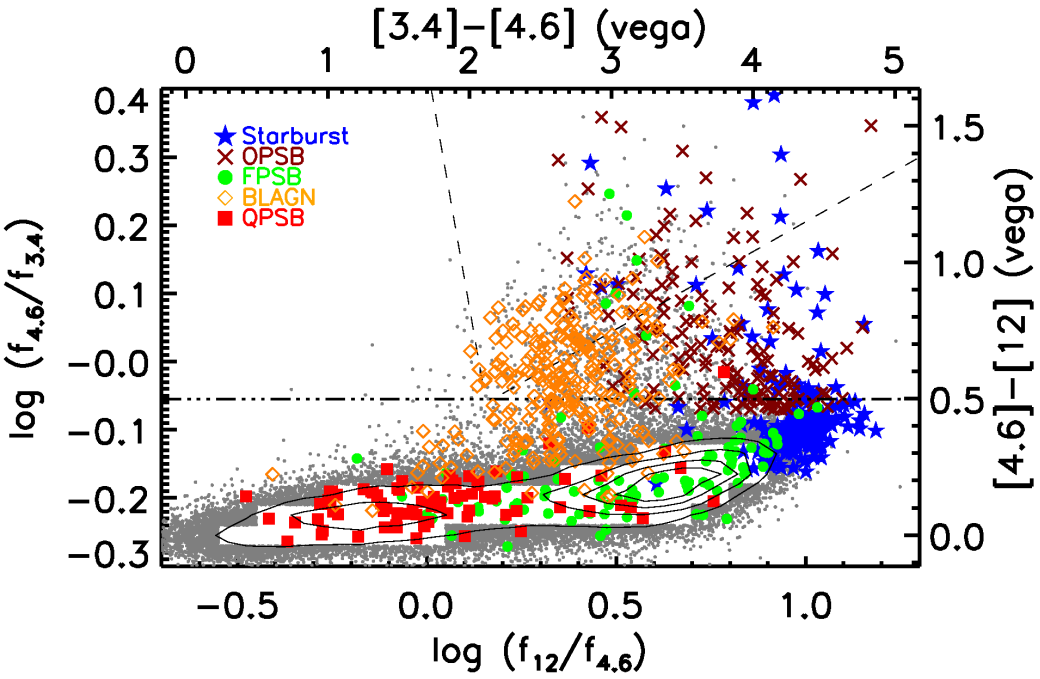

Figure 5.5:. The WISE color-color plot which can reliably identify luminous (obscured and unobscured) AGN. Starbursts (blue star), fading post-starbursts (green circles), obscured post-starbursts (brown Xs), quenched post-starbursts (red squares) and broad-line AGN (orange diamonds) are overplotted on the figure. The $f_{12\,\mu m}/f_{4.6\,\mu m}$ flux ratio is sensitive to PAH emission and is a first order star formation indicator while $f_{4.6\,\mu m}/f_{3.4\,\mu m}$ is sensitive to hot dust emission from AGN. The dashed wedge denotes the Mateos et al. (2012) AGN selection criteria while the horizontal dash-dotted line demarcates that of Ashby et al. (2009). The latter is more complete but less pure. For comparison, we overplot broad line AGN of comparable mass and redshift studied by Trump et al. (2013). The figure confirms that almost all starbursts and strongly star-forming transiting PSBs do not host strong or obscured AGN. Some transiting post-starbursts show hot dust emission from AGN. The BLAGN have lower $f_{12\mu m}/f_{4.6\mu m}$ ratios (less star-forming) than obscured post-starbursts but higher flux ratios than quenched post-starbursts, suggesting that they may come after the obscured AGN phase (Hopkins et al., 2006), if they are related to post-starbursts.

while quenched post-starbursts typically have lower $f_{12\mu m}/f_{4.6\mu m}$ ratios like quiescent galaxies. The transiting post-starbursts mostly have intermediate $f_{12\mu m}/f_{4.6\mu m}$ ratios between SBs and QPSBs. The arrangement of SBs, FPSBs and QPSBs in decreasing order of redness due to dust is another independent confirmation for the consistency of our evolutionary sequence. As expected from their selection, the obscured post-starbursts are found in between the FPSBs and SBs.

The $f_{4.6\mu m}/f_{3.4\mu m}$ ratio may indicate emission from hot dust, ionized gas or stars. The simple $f_{4.6\mu m}/f_{3.4\mu m} > 0.88$ criterion can identify hot dust emission from AGN but only with ∼50% reliability (Ashby et al., 2009; Stern et al., 2012). The dashed wedge, which is calibrated by X-ray-selected AGN, identifies a highly complete and reliable sample of luminous (hard X-ray luminosity, $L_{2-10\,\mathrm{kev}} > 10^{44}\,\mathrm{erg\,s^{-1}}$) AGN (Mateos et al., 2012). For a reference, we also overplot broad-line AGN in the similar mass and redshift range.

According to the Mateos et al. (2012) classification, only 7% of the FPSBs and 21% of the OPSBs show clear AGN signatures in WISE, and the majority of these galaxies are already classified as Seyferts by the optical emission line diagnostics. This indicates that most of AGN found in the transiting post-starbursts, including the ones in composite regions of the BPT diagram, must be weak ($L_{2-10\,\mathrm{kev}} < 10^{44}\,\mathrm{erg\,s^{-1}}$) if their presence is hidden by dilution from stellar emission.

5.1.4.2 The star formation rates of broad-line AGN

Note that our post-starburst selection does not apply to broad-line AGN (BLAGN) hosts because many of the indicators that we have used to characterize the main evolutionary PSB sequence are diluted or polluted by the strong

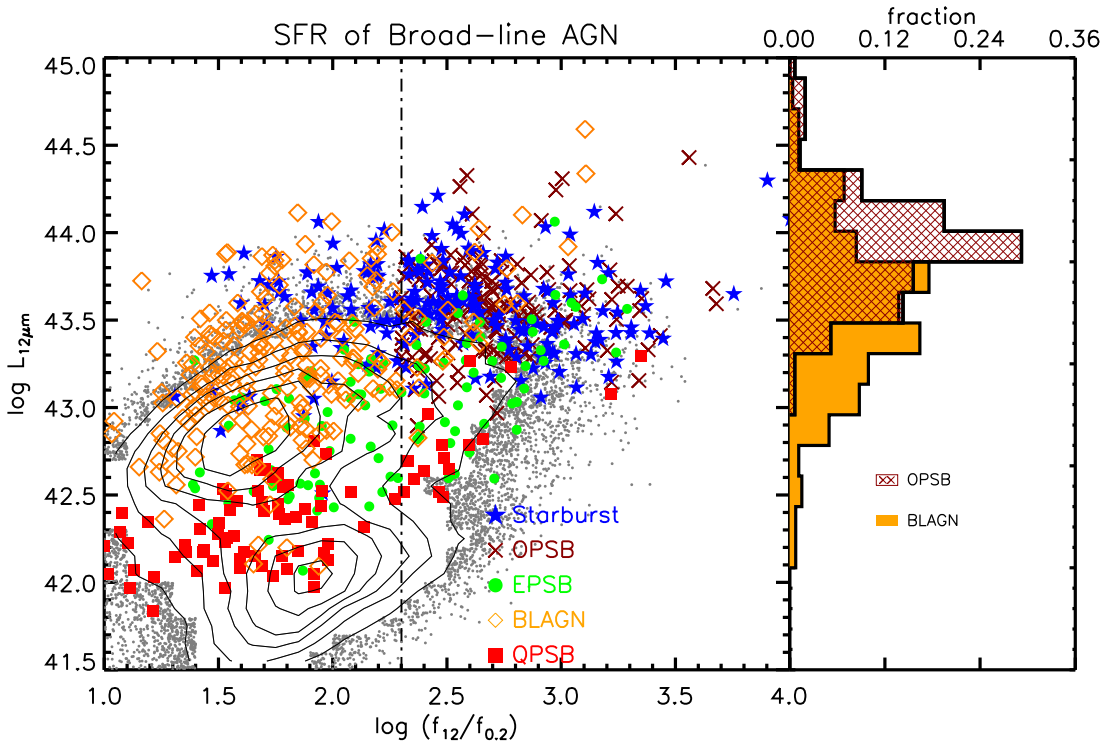

Figure 5.6:. The flux density ratio between WISE 12 μm and GALEX NUV, $f_{12\mu m}/f_{0.2\mu m}$, versus the WISE 12 μm luminosity. The 12 μm luminosity is used as a proxy for the (obscured) star formation rate (an upper limit in AGN, see Donoso et al., 2012). $f_{12\mu m}/f_{0.2\mu m}$ ratio may indicate the amount of dust-obscuration. The histograms on the right show the distribution of 12 μm luminosities for BLAGN and OPSBs respectively. Even with some contribution of AGN to the 12 μm luminosity, BLAGN are generally less star-forming than OPSBs (and majority of BLAGN are also likely less obscured). Therefore, BLAGN do not play a primary role quenching starbursts. Their properties in this diagram are consistent with the idea that BLAGN come after the obscured AGN phase (Hopkins et al., 2006).

AGN signature in BLAGN (e.g., optical-UV colors and optical spectral signatures). Therefore, we cannot directly constrain the role of broad-line AGN in our post-starburst evolutionary sequence. However, in the following analysis we use $12\,\mu$m luminosities of BLAGN hosts to infer upper limits on their star formation rates (Chary & Elbaz, 2001) and argue that their exclusion from the parent sample is not a problem. Their inferred star formation rates suggest that they either come after the obscured post-starburst AGN (e.g., Hopkins et al., 2006) or they are not part of our evolutionary sequence at all.

The fact that BLAGN seem older than SBs and OPSBs was already suggested by their intermediate $[4.6\,\mu\mathrm{m}]-[12\,\mu\mathrm{m}]$ color in Figure 5.5. However, some AGN are known to exhibit suppressed aromatic features short-ward of $11.3\,\mu$m (Smith et al., 2007; Diamond-Stanic & Rieke, 2010), suggesting that the $[4.6\,\mu\mathrm{m}]-[12\,\mu\mathrm{m}]$ color might underestimate the SFR.

Figure 5.6 shows $12\,\mu$m luminosity against the flux density ratio of WISE $12\,\mu$m to GALEX NUV, $\mathrm{f}_{12\mu\mathrm{m}}/\mathrm{f}_{0.2\mu\mathrm{m}}$. The $12\,\mu$m luminosity is dominated by stellar populations younger than 0.6 Gyr in star-forming galaxies and in type 2 AGN (Donoso et al., 2012). The $\mathrm{f}_{12\mu\mathrm{m}}/\mathrm{f}_{0.2\mu\mathrm{m}}$ ratio roughly quantifies the ratio of obscured to unobscured SFR in star-forming galaxies and in type 2 AGN. It is not clear what $\mathrm{f}_{12\mu\mathrm{m}}/\mathrm{f}_{0.2\mu\mathrm{m}}$ ratio exactly means for BLAGN because we do not know how much of their NUV and IR flux comes from stars and how much from the AGN. For this reason, we place more emphasis on the 12 μm luminosity as an upper limit on star formation.

The general galaxy population shows a bi-modality in $12\,\mu$m luminosity, reflecting the global bi-modality in star formation rates. As expected, the starbursts

have higher 12 μm luminosity than normal star-forming galaxies while quenched post-starbursts have intermediate 12 μm luminosity between quiescent and star-forming galaxies. Most obscured post-starbursts have comparable 12 μm luminosity to that of starbursts. This, at face value, is inconsistent with the fact their SFRs as indicated by their Hα and NUV-g colors are lower than those of starbursts (Figure 2.3 & 2.4). However the excess mid-IR emission in OPSBs may be due to additional dust heating from their intermediate age (~ 0.4 Gyr) stellar populations (Salim et al., 2009; Kelson & Holden, 2010).

The FPSBs have high to intermediate 12 μm luminosity but they are clearly offset to the right from normal star-forming galaxies, that is, they are more dust-obscured. On the other hand, the BLAGN have similar 12 μm luminosities to those of FPSBs but most of them coincide with normal blue star-forming galaxies, i.e, they are less obscured.

As the histograms of 12μm luminosities appended to the right of the plot shows, obscured post-starbursts are on average more luminous than BLAGN in 12 μm. K-S test indicates that distribution of 12 μm luminosities of OPSBs and BLAGN are significantly different ($D = 0.45, p_{\rm ks} = 5.0 \times 10^{-18}$, i.e, $\alpha < 0.001$). Therefore, BLAGN are likely less star-forming (older) than obscured post-starbursts. This indicates that our conclusion that AGN and starbursts are not coeval is not likely to be affected by the exclusion of BLAGN from our post-starburst sample. More work is needed to directly constrain the age (after the starburst phase) of the very luminous BLAGN. Other studies have shown that BLAGN hosts have comparable age ($0.7 - 2$ Gyr) to that of quenched post-starbursts but they are substantially older than starbursts (Jahnke et al., 2004; Canalizo & Stockton, 2013). At high

redshift, a recent far-infrared Herschel/PACS study by Rosario et al. (2013) found that the mean SFRs of BLAGN hosts are consistent with those of normal massive star-forming galaxies and do not show strong enhancement in their SFRs to suggest that they are starbursting systems.

The fact that BLAGN have intermediate $[4.6\,\mu\mathrm{m}] - [12\,\mu\mathrm{m}]$ color and $12\,\mu\mathrm{m}$ luminosity and are likely less dust-obscured is consistent with the expectation that AGN might quench or prevent low-level star formation in post-starburst galaxies by removing leftover gas and dust after the starburst events (Hopkins et al., 2006). Similarly, Zakamska et al. (2008) have shown that type 2 quasar hosts have increased star formation than type 1 quasar hosts, thereby supporting the suggestion that obscured quasars come before naked quasars.

We conclude that broad-line AGN are unlikely to play *a primary* role in the initial quenching of starbursts and their exclusion from our post-starburst sample does not affect our main conclusions. Future work to robustly constrain the instantaneous star formation rate of local BLAGN hosts would be very useful to understand whether BLAGN are associated with quenching of starbursts or low star-forming post-starburst galaxies.

5.1.5 Flat color gradients of starbursts & post-starbursts

Normal star-forming galaxies have red centers. A major merger likely alters or erases a color gradient of a pre-merger normal galaxy by inducing star formation at the center or throughout the galaxy. Since the truncation of the starburst is abrupt, post-starburst galaxies should still carry the imprint of their merger origin by having flatter or more positive color gradients than normal star-forming

galaxies.

Figure 5.7a shows the color gradient, $\nabla_{\rm color}$, versus (NUV-g)$_{\rm dc}$ color while Figure 5.7b plots dust-corrected NUV-g and g-z diagram color-coded by the color gradient. Starbursts and their descendants (transiting and quenched post-starbursts) have much shallower color gradients than the bulk of normal star-forming galaxies.

As expected, red quiescent galaxies have flat color gradients and are red throughout but blue galaxies show an interesting regularity in their color gradients: blue galaxies with bluer in (NUV-g)$_{\rm dc}$ color (or lower Hα) have negative color gradients (i.e, show large reddening in their centers) while blue galaxies with redder (NUV-g)$_{\rm dc}$ colors (or higher Hα) have flat color gradients. In other words, galaxies with red centers have most of their star formation in their outer blue disks and have small quiescent bulges. On the other hand, galaxies which are blue throughout are either experiencing nuclear bursts (have star formation rates above the average) or their nuclear bursts are abruptly terminated (have redder NUV-g colors). They have young bulges.

The fact that both starbursts and post-starbursts have flat color gradients (young blue bulges) suggests that star formation is uniformly distributed throughout these galaxies, remaining so even as the burst quenches throughout the galaxy. It also suggests that the centers of these galaxies must have been unreddened from the typical red centers of disk galaxies, perhaps by gas inflow during a merger. Likewise, the flat color gradients of obscured post-starbursts suggests that the dust-obscuration in these objects is likely a galaxy wide phenomenon. Previous studies have also shown that A stars in K+A galaxies are widespread and are not confined to their nuclear regions (Kauffmann et al., 2003c; Swinbank et al., 2005;

Goto et al., 2008; Pracy et al., 2009; Swinbank et al., 2012).

5.1.6 Metalicity of post-starbursts

Figure 5.8 depicts the distribution of dust-corrected (N II/O II)$_{\rm dc}$ ratios for normal star-forming galaxies, starbursts and post-starbursts. This ratio is a very reliable metallicity diagnostic and it is not very sensitive to the ionization level (Kewley & Dopita, 2002). Panel a compares the (N II/O II)$_{\rm dc}$ ratios of transiting PSBs with those of quenched PSBs and starbursts. The (N II/O II)$_{\rm dc}$ ratio increases as the starbursts progressively evolve to the transiting and quenched post-starbursts. The starbursts have (N II/O II)$_{\rm dc}$ ratios that correspond to $1-1.5\,Z_{\odot}$ solar metallicity range (Kewley & Dopita, 2002) while the QPSBs have ratios corresponding to $2-3\,Z_{\odot}$ solar metallicity, although their (N II/O II)$_{\rm dc}$ ratio might not be well measured because their emission lines are weak. The TPSBs have intermediate metallicity between starbursts and QPSBs. K-S test indicates that the distributions of metallicity of starbursts and TPSBs are significantly different ($D = 0.28, p_{\rm KS} = 2.2 \times 10^{-8}$, i.e, $\alpha < 0.001$) and so are the distributions of TPSBs and QPSBs ($D = 0.46, p_{\rm KS} = 2.3 \times 10^{-12}$, i.e, $\alpha < 0.001$).

Furthermore, panel b shows that starbursts which are younger than the median age ($D_n(4000)_{\rm dc} < 1.1$) have even lower metallicity than the AGN hosts in TPSBs (cf. Groves et al., 2006) and normal star-forming galaxies. K-S test also indicates that the distributions of metallicity of younger starbursts (or all SBs) are significantly different (at $\alpha < 0.001$ level) from AGN in TPSBs or normal star-forming galaxies. The transiently lower metallicity of younger starbursts is consistent with metal poor gas inflows during merger-induced starbursts (Barnes

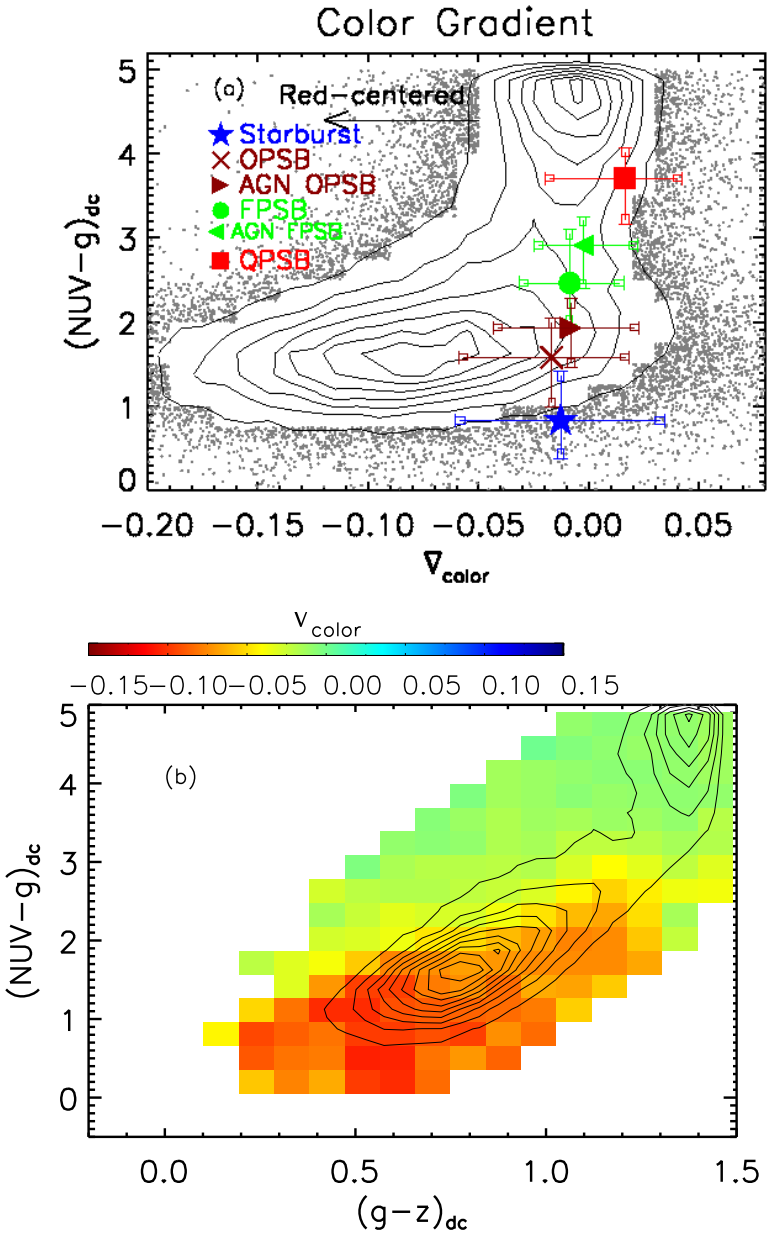

Figure 5.7:. Panel a: the median and upper/lower quartile values of $(NUV\text{-}g)_{dc}$ color versus color gradient, ∇_{color}. Panel b: NUVgz diagram color-coded by color gradient. The contours represent the number density of all galaxies in the parent sample. Where the number of galaxies within a bin is more than 15, we color code by the median values of the color gradient or the concentration index. Otherwise, the individual values for the galaxy is used.

& Hernquist, 1991, 1996) while the higher metallicity in post-starburst AGN is consistent with time delay between AGN and starbursts (e.g., Wild et al., 2010; Hopkins, 2012; Cen, 2012).

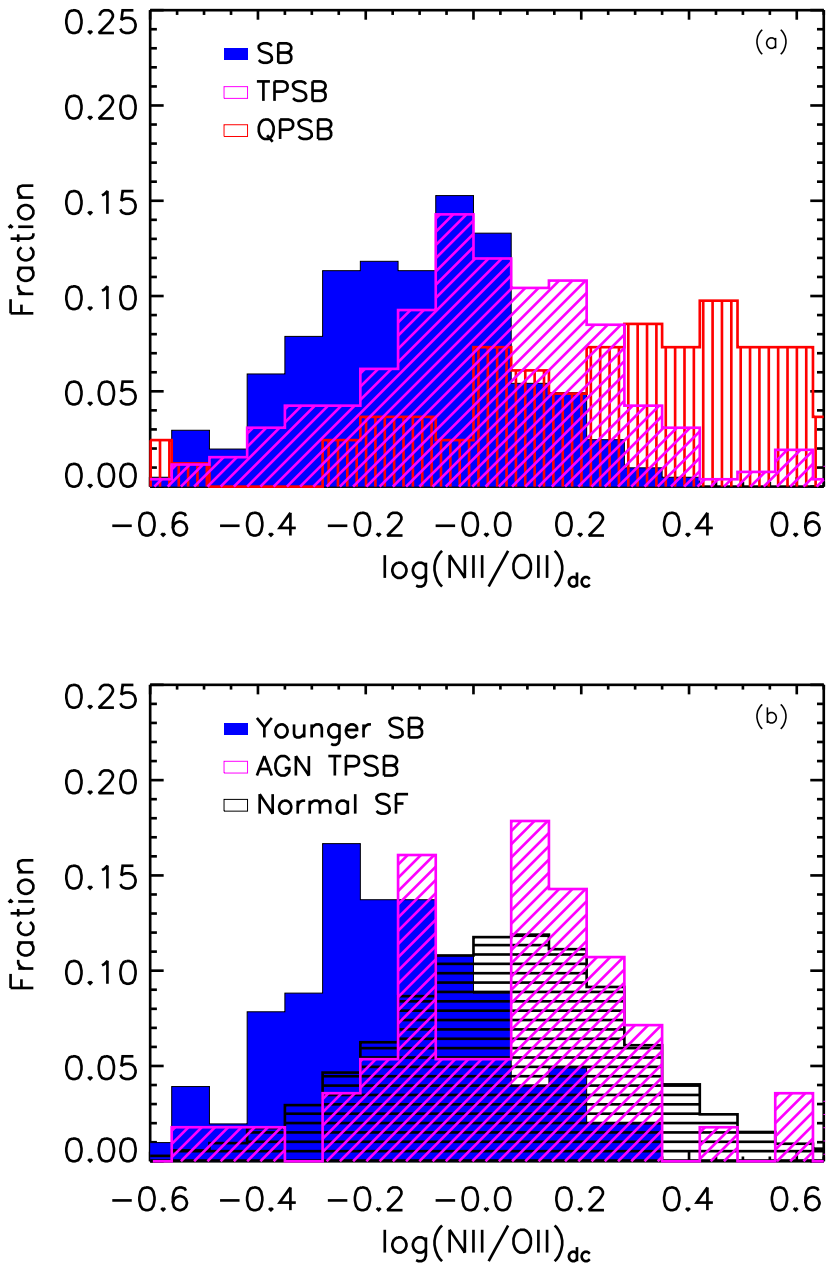

Figure 5.8:. Panel (a): The distribution dust-corrected N II/O II ratios for the starbursts, transiting post-starburst and quenched post-starbursts. The metallicity increases from the starbursts to the quenched post-starbursts. Panel (b):The distribution dust-corrected N II/O II ratios for the young starbursts ($D_n(4000) < 1.1$), normal star-forming galaxies and AGN in TPSBs. Starbursts are significantly metal poor especially at younger ages, consistent with gas inflow during merger-induced starbursts. The AGN is TPSBs have significantly higher metallicity than starbursts, suggesting a time delay between the starburst and AGN phase.

5.2 Ancillary Material for Chapter 3

This section presents materials that support the analysis in Chapter 3.

5.2.1 Evolution of Hδ equivalent width after a starburst

Fig. 5.9 shows the evolution of Hδ equivalent width for Bruzual & Charlot (2003) starburst models, with a star formation timescale, τ = 0.1 Gyr, and a burst mass fraction (b_f) 3% or 20%, starbursts evolve differently in this diagram compared to non-starburst galaxies. As detailed in Yesuf et al. (2014). The Hδ is dependent on the magnitude of the and a burst mass fraction, and there is generally a degeneracy between the mass fraction and the bust time scale. The figure demonstrates with particular models above that late stage PSBs can have H$\delta < 3$Å, which is lower than the threshold often used to define PSBs.

5.2.2 A comparison of our PSB sample with previous samples

Fig. 5.10 to Fig. 5.16 show the relationship among $\log f_{12}/f_{4.6}$, $D_n(4000)$, Hδ and Hα for our Seyfert PSB sample and the previous samples of PSBs (French et al., 2015; Rowlands et al., 2015; Alatalo et al., 2016). The points are: 1) The PSBs in Rowlands et al. (2015); Alatalo et al. (2016) have younger stellar populations and higher SSFRs ($\log f_{12}/f_{4.6}$) than do PSBs in our sample and in the French et al. (2015) sample. 2) The French et al. (2015) sample shows a wide range in $\log f_{12}/f_{4.6}$. We split this sample into two. The galaxies in the PSB2 category have have obscured SFR undetected in Hα. They are slightly older (have

lower Hδ EW and higher $D_n(4000)$ than the PSB1. 3) Both PSB1 and PSB2 do not show signs of strong AGN in WISE two color diagram. 4) Our Seyfert PSBs have comparable SSFRs ($\log f_{12}/f_{4.6}$) to those of PSB2s but higher SSFRs than those of PSB1s. 5) The $D_n(4000)$ of our Seyfert PSBs are similar to those of PSB1s and PSB2s. 6) PSB1s are consistent with being precursors to our Seyfet PSBs. They have yet to experience a Seyfert activity and be quenched. 7) PSB2s are already quenched. They have higher Hδ than our Seyfert PSBs. There are Seyferts with similar Hδ in Rowlands et al. (2015); Alatalo et al. (2016) that may be precursors to the PSB1s. Since these Seyferts are mostly in the blue-cloud. The immediate green-valley precursors may be missing from the current data. Alternatively, our Seyfert could be the immediate precursors if the Hδ is slightly enhance after dust is removed by AGN feedback. 7) A PSB selection which replaces Hα with $\log f_{12}/f_{4.6}$ is better in identifying quiescent PSBs, and is more useful in studying evolution of PSB galaxies. Hα is severely affected by dust extinction and also likely by AGN emission. $\log f_{12}/f_{4.6}$ may also be a better alternative to NUV-optical color since the dust correction using Balmer decrement is not possible for heavily obscured galaxies with weak emission lines.

5.2.3 CO luminosities of Seyfert PSBs

Target	RA (degree)	DEC (degree)	L'_{CO} (10^7 K km s^{-1} pc^2)	FWHM (km s^{-1})
TPSB1	212.01667	7.3276444	14.17 ± 2.74	109.8 ± 13.8
TPSB2	134.61917	0.02346944	21.5222 ± 4.95	234.8 ± 54.0
TPSB4	182.01942	55.407672	< 35.36	...
TPSB5	173.41283	52.674611	< 29.27	...
TPSB6	170.94588	35.442308	< 21.61	...
TPSB7	203.56175	34.194147	9.59 ± 2.55	201.7 ± 48.3
TPSB8	189.51733	48.345097	< 14.97	...
TPSB9	117.96617	49.814314	44.81 ± 11.92	137.8 ± 22.2
TPSB10	180.51921	35.321681	< 17.77	...
TPSB11	137.87483	45.468278	19.60 ± 4.72	370.2 ± 169.2
TPSB12	139.49937	50.002175	< 20.09	...
TPSB13	173.16771	52.950400	< 11.08	...
TPSB14	178.62254	42.980203	< 11.86	...
TPSB15	179.02850	59.424919	< 16.27	...
TPSB16	190.45025	47.708878	< 14.73	...
TPSB17	198.74925	51.272583	< 10.41	...
TPSB18	200.95183	43.301181	37.94 ± 5.70	436.3 ± 125.8
TPSB19	236.93392	41.402294	< 23.06	...
TPSB20	240.65804	41.293433	< 21.51	...
TPSB21	247.63600	39.384192	< 15.28	...
TPSB23	134.61913	0.02346944	15.20 ± 4.18	126.1 ± 24.0
TPSB24	145.18546	21.234358	< 9.23	...
TPSB26	172.08300	27.622097	< 17.80	...
TPSB28	222.65771	22.734336	< 6.82	...

Table 5.1. CO (2–1) line luminosities and FWHM from fitting a Gaussian to the lines.

RA	DEC	z
131.369195	14.573784	0.0360000
156.961772	2.6094376	0.0284900
204.050751	4.7400708	0.0343100
236.726389	5.8912124	0.0418800
162.570527	6.1225920	0.0422100
32.8898323	13.9171282	0.0265100
25.4299380	13.6757968	0.0453100
190.229018	8.0564412	0.0478300

Table 5.2. Coordinates of PSBs in the Saintonge et al. (2011). These galaxies were not analyzed as PSBs before and we have included them in our analysis.

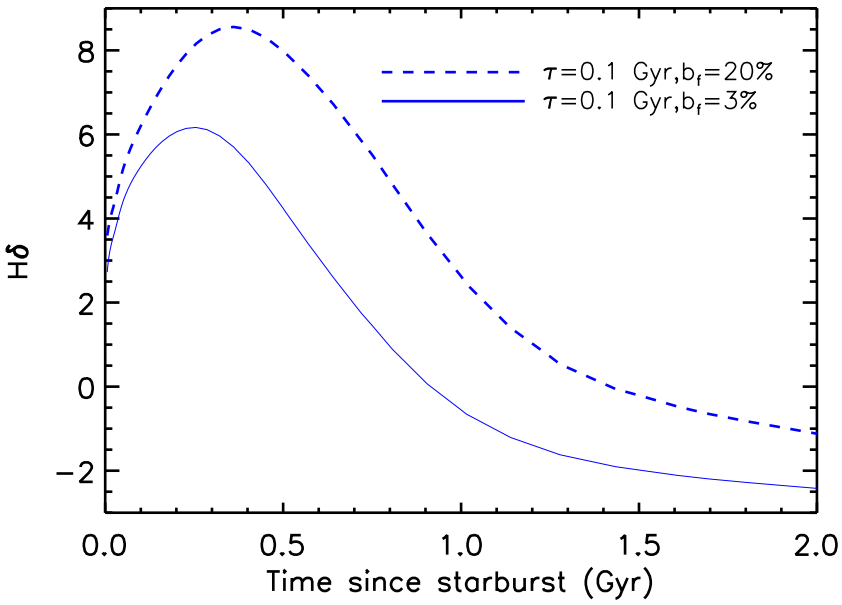

Figure 5.9:. Time since the starburst vs. Hδ EW

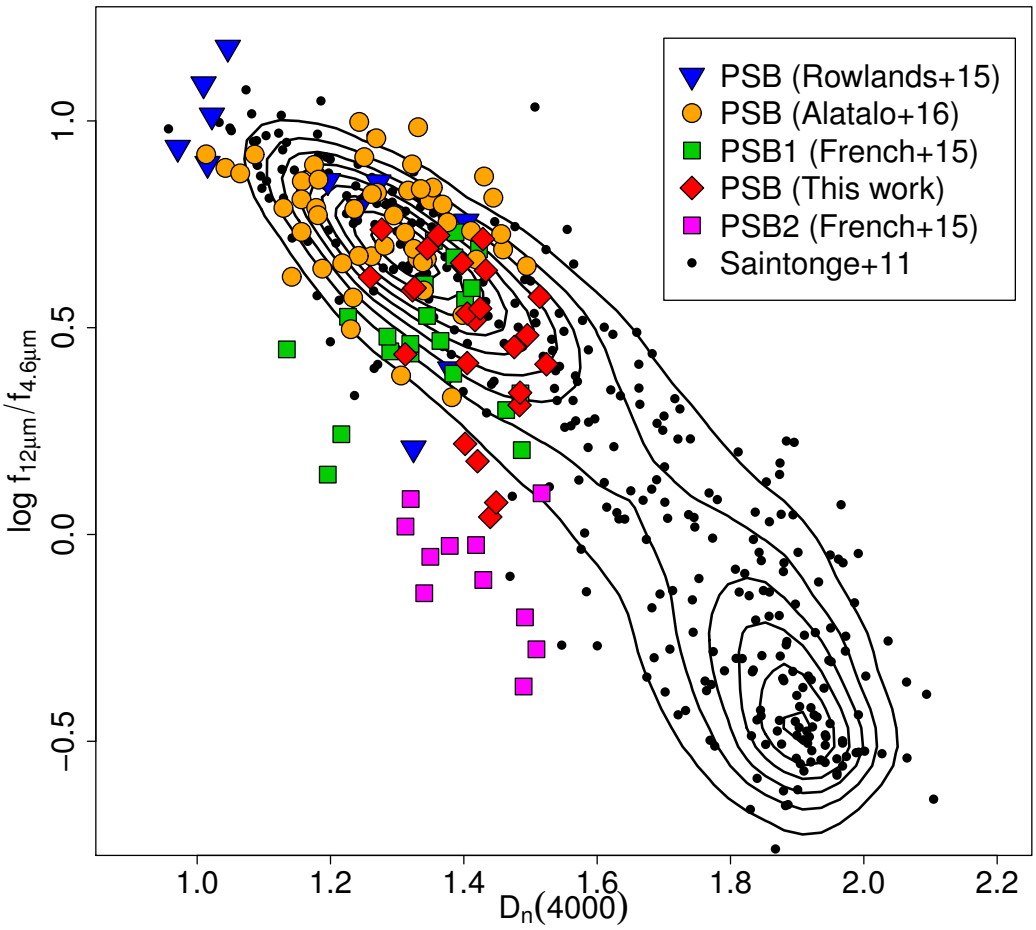

Figure 5.10:. shows the 4000Å against the WISE flux ratio $\log f_{12}/f_{4.6}$. The contours denote the distribution of bi-model galaxy population at $z = 0.02 - 0.06$ and $\log \mathrm{M}\ (\mathrm{M}_{\odot}) = 10 - 11$. On average, the figure supports the evolutionary sequence of PSBs in the order shown in the legend box, from PSB (Rowlands et al., 2015) to PSB2 (French et al., 2015). The $D_n(4000)$ of our sample and that of French et al. (2015) samples are very similar. PSB2 have obscured star formation rates similar to those of our galaxies. They seem on average slightly younger than our Seyfert PSBs. On the other hand, the PSB2s have lower sSFR than our Seyfert PSBs do. Therefore, in this diagram, PSB2s are consistent with being descendents of the Seyfert PSBs.The Rowlands et al. (2015) and Alatalo et al. (2016) samples have younger ages and higher sSFR than our sample does.

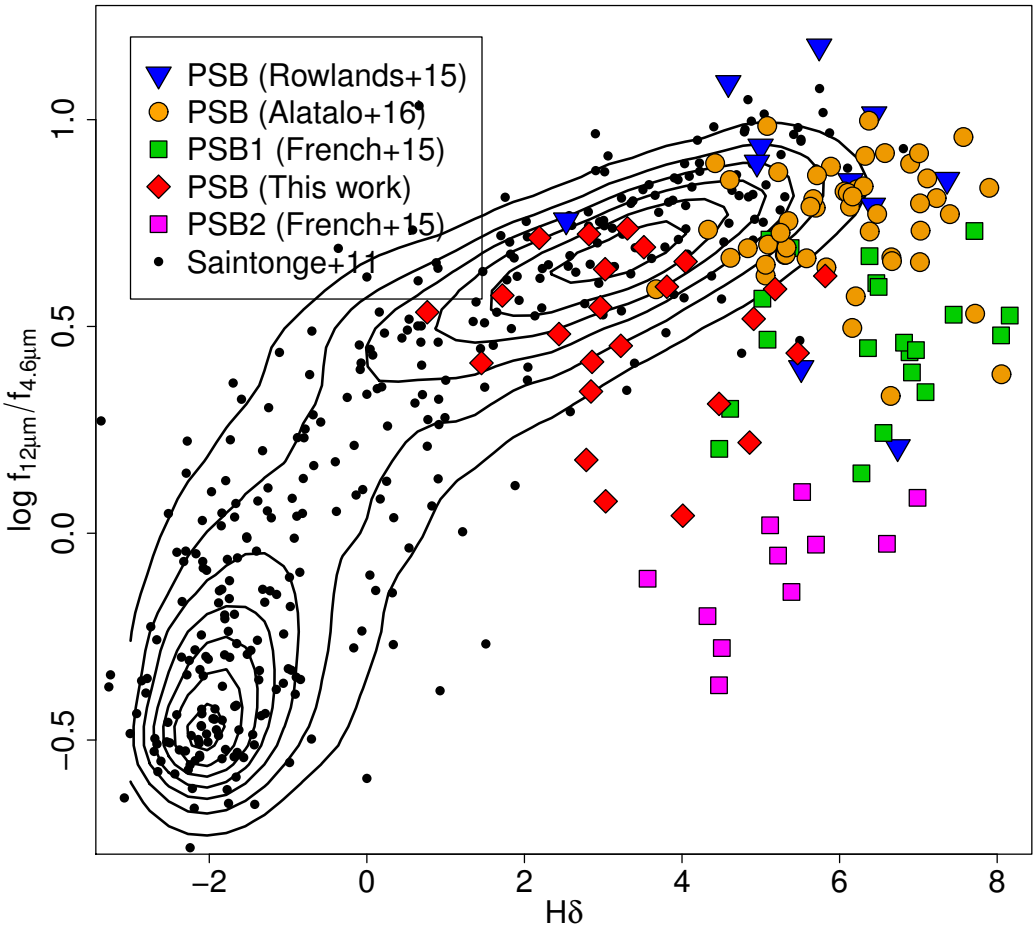

Figure 5.11:. shows the Hδ equivalent width (EW) against the WISE flux ratio $\log f_{12}/f_{4.6}$. The contours denote the distribution of bi-model galaxy population at $z = 0.02 - 0.06$ and log M ($M_{\odot}$) $= 10 - 11$. Our PSBs have on average lower Hδ equivalent width (EW) relative to the previous samples. But note that there is a considerable overlap between our PSBs and PSB2s. It is not implausible that the PSB1s evolve to become some of our Seyfert PSBs and they in turn evolve to become some of the PSB2s. Some of the PSB2s might also descend from the high Hδ EW Seyfert PSBs not in our sample but are in the Alatalo et al. (2016) & Rowlands et al. (2015) samples.

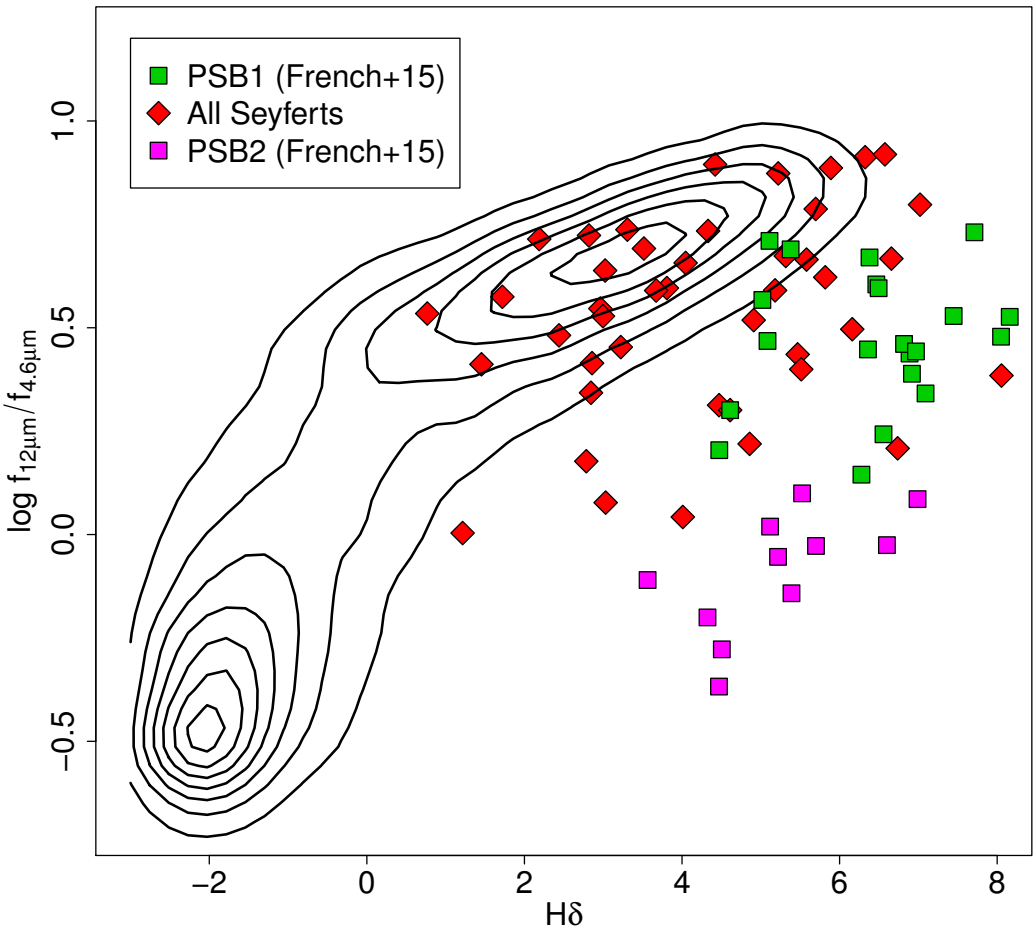

Figure 5.12:. Similar to the previous figure but here we show all Seyferts both in our sample and the other samples. Even though our sample might be slightly biased toward aged Seyferts with lower Hδ EW, the Seyferts in the combined sample are more representative of the PSBs with H$\delta > 4$ Å. It is plausible that the PSB2s descended from Seyferts above them, while PSB1s will likely evolve horizontally first to become like some of our Seyferts and then quench.

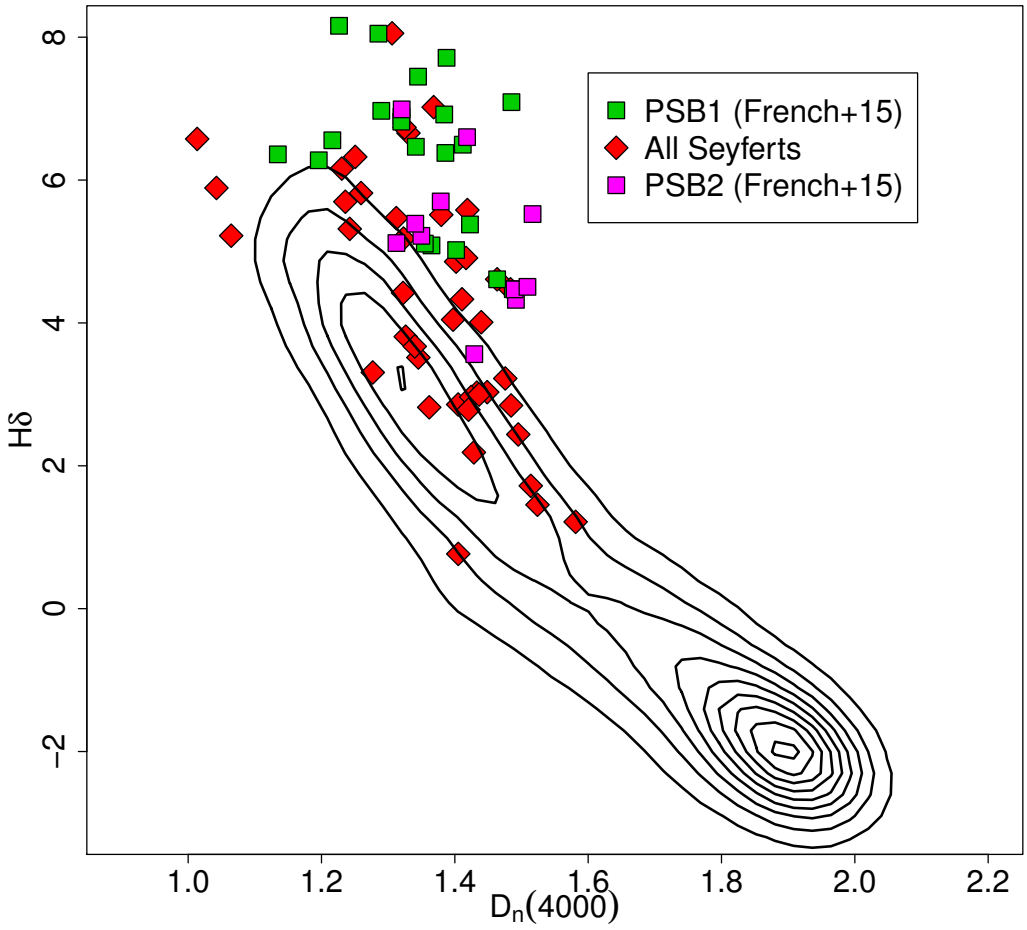

Figure 5.13:. The figure makes a similar point made earlier that the existing data is consistent with the fact that the quenched French et al. (2015) PSB2 galaxies likely descended from the younger Seyfert PSBs at comparable Hδ EW and $D_n(4000)$ while the PSB1s have yet to experience a Seyfert activity and evolve into the older Seyferts.

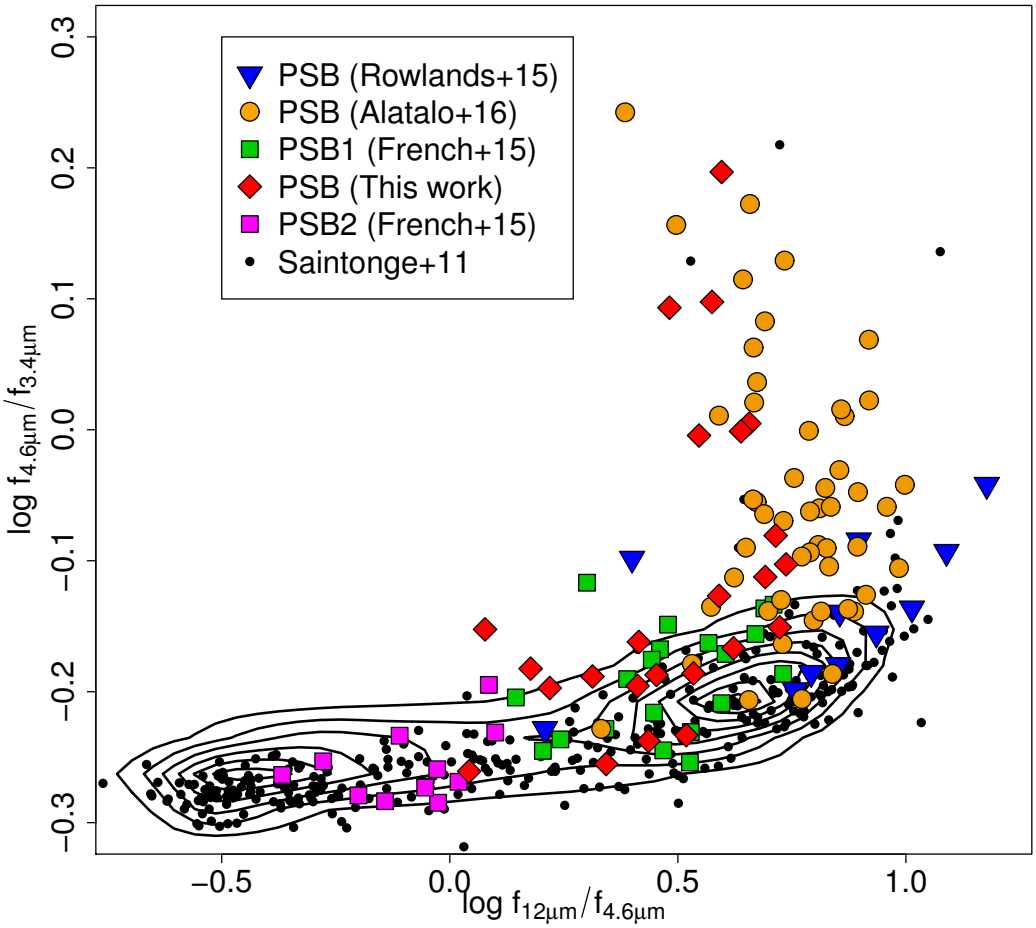

Figure 5.14:. The WISE two color diagram. $\log f_{12}/f_{4.6}$ is indicator of sSFR and while the $\log f_{4.6}/f_{3.4}$ is indictor hot dust emission by AGN or starburst or both. The contours denote the distribution of bi-model galaxy population at $z = 0.02 - 0.06$ and log M ($M_\odot$) $= 10 - 11$. The blue-cloud is the density cloud with peak at $\log f_{12}/f_{4.6} \sim 0.6$ while the red-sequence is the density cloud with peak at $\log f_{12}/f_{4.6} \sim -0.45$. PSBs show a wide range in $\log f_{12}/f_{4.6}$ and, on average, the figure supports the evolutionary sequence of PSBs in the order shown in the legend box. The PSB1s have obscured SFR similar to the blue-cloud galaxies while the PSB2s are like fading green-valley or upper red-sequence galaxies. Both PSB1s and PSB2s do not show signatures of dust heating by strong AGN. PSB2s likely underwent through a Seyfert activity while the PSB1s have yet to experience a Seyfert activity. This is supported by the fact that our Seyfert PSBs have lower gas fractions than PSB2 but higher gas fraction than PSB1s.

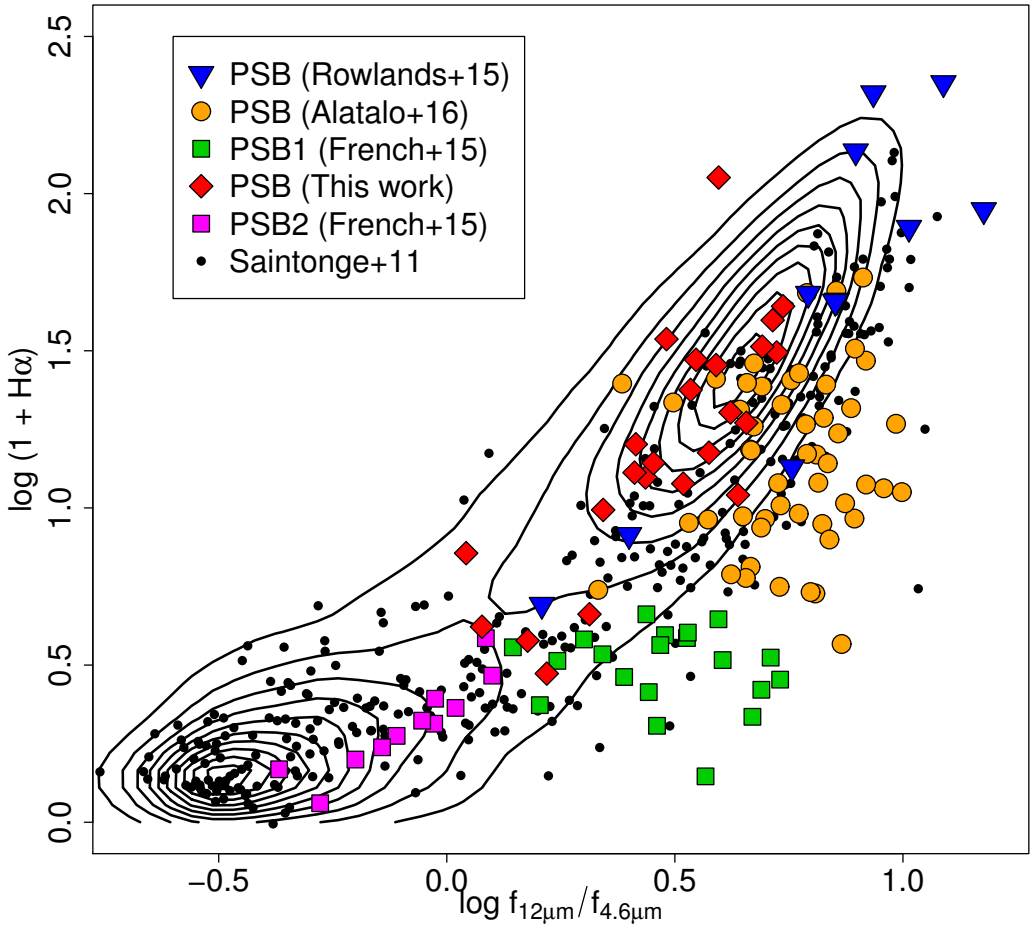

Figure 5.15:. $\log f_{12}/f_{4.6}$ versus Hα emission EW. The PSBs in the Alatalo et al. (2016) sample and (French et al., 2015) PSB1 sample deviate from the main sequence indicating their Hα is significantly obscured by dust. A PSB selection based on solely Hα will lead to a wrong conclusion that PSB1s are quenched.

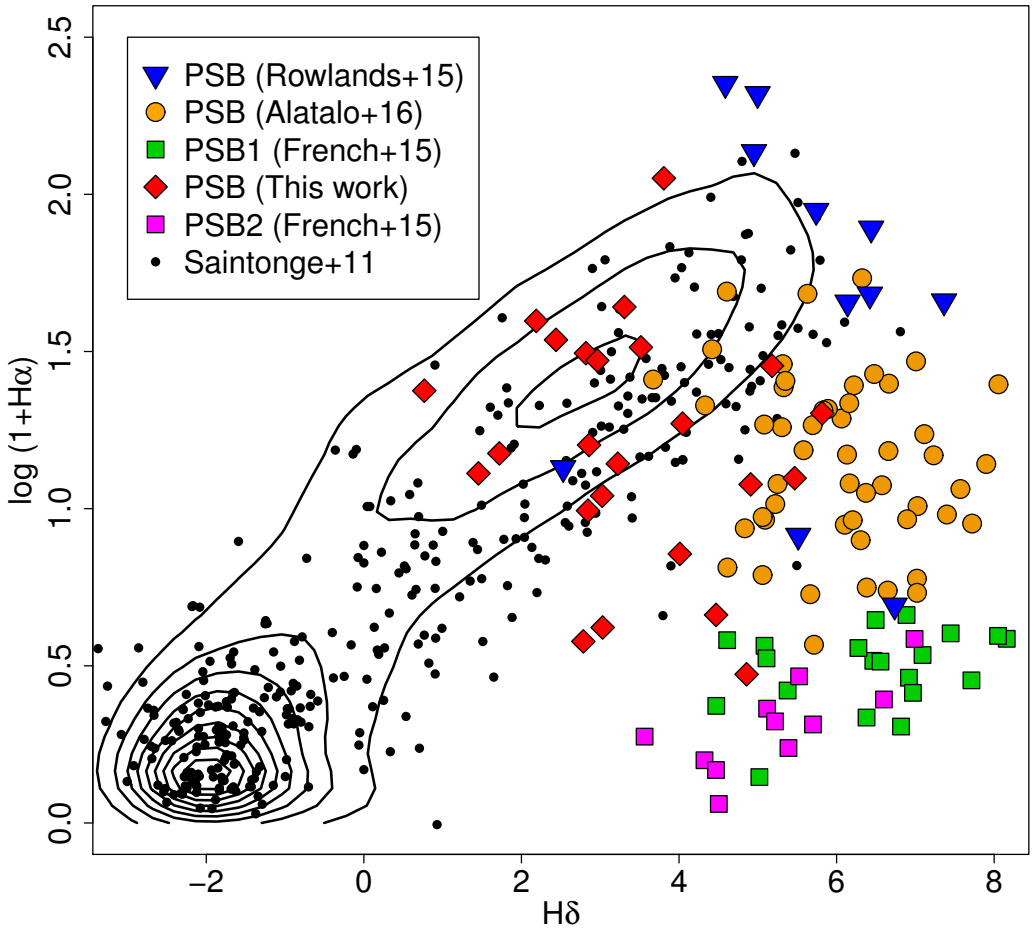

Figure 5.16:. Hδ absorption versus Hα emission EW. This plot is included for a completeness. We have argued that Hα is affected severely by dust extinction, and perhaps by AGN emission. A diagram in which Hα is replaced by $\log f_{12}/f_{4.6}$ is better in identifying quiescent PSBs, and is more useful in studying evolution of PSB galaxies.

5.3 Ancillary Material for Chapter 4

In this section we give ancillary information as figures and tables to support the result presented in Chapter 4.

5.3.1 NUV composite spectra of AGN and the comparison sample

Figure 5.17 shows the near UV composite spectra around Fe IIλ2586 or Mg II for AGN and non-AGN at $z \sim 1$.

5.3.2 Re-analysis with Bootstrap errors of the Fe II λ2586 profiles

Table 5.3 and Figure 5.18 present results of using bootstrapped errors of the average spectrum instead of the error calculated from inverse-variance of weighting scheme of the individual spectra and their errors output by the data reduction pipeline.

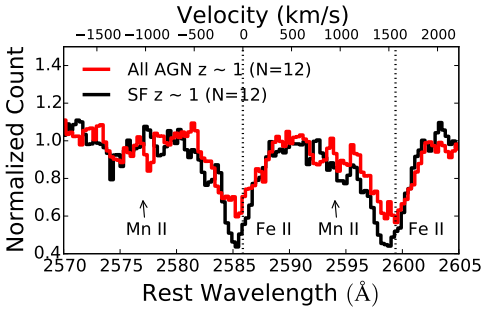

(a) Includes both narrow and broad line AGN

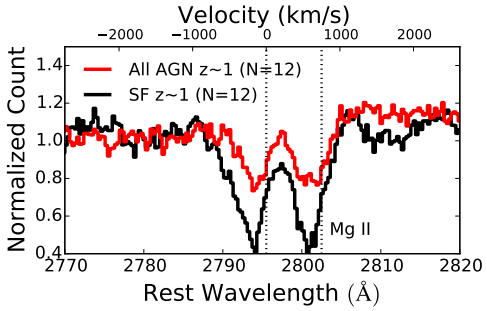

(b) Includes both narrow and broad line AGN

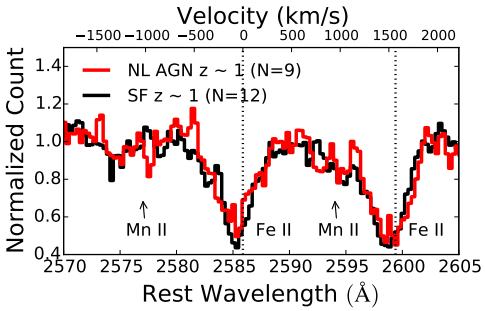

(c) Narrow-line AGN candidates

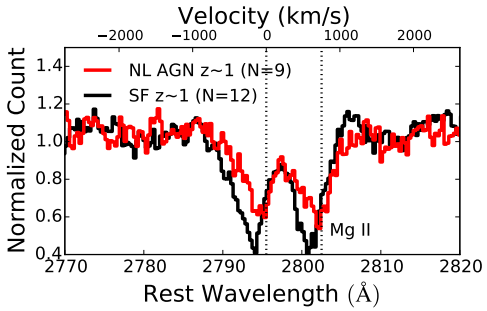

(d) Narrow-line AGN candidates

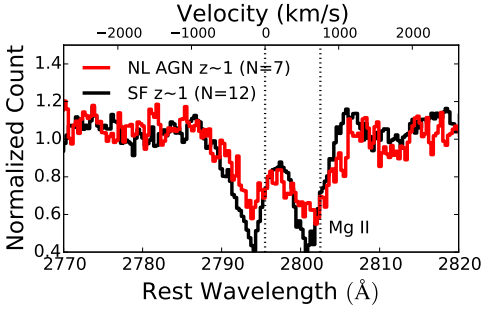

(e) Includes only high fidelity narrow-line AGN

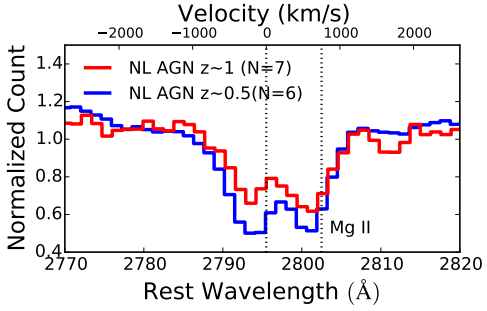

(f) Narrow-line AGN at $z \sim 1$ vs. at $z \sim 0.5$

Figure 5.17:. The near UV composite spectrum around Fe IIλ2586 or Mg II of AGN at $z \sim 1$ compared to the composite spectrum of non-AGN at $z \sim 1$ or to AGN at $z \sim 0.5$.

Table 5.3. Model parameter fits to Fe II λ2586 profiles using bootstrap errors.

Wind Model Parameters	All AGN at $z \sim 1$ (N = 12)	NL AGN at $z \sim 1$ (N = 9)	NL AGN at $z \sim 1$ (N = 7)	SF at $z \sim 1$ (N = 12)	AGN at $z \sim 0.5$[a] (N = 6)[b]
v_w	-110^{+94}_{-186}	-110^{+100}_{-123}	$-136-^{+120}_{-109}$	-110^{+114}_{-173}	-248^{+51}_{-17}
b_w	197^{+157}_{-131}	155^{+144}_{-96}	152^{+156}_{-93}	192^{+154}_{-115}	97^{+62}_{-40}
C_w	$0.3^{+0.4}_{-0.2}$	$0.3^{+0.4}_{-0.2}$	$0.4^{+0.4}_{-0.2}$	$0.3^{+0.4}_{-0.2}$	$0.6^{+0.3}_{-0.2}$
N_w	$15.0^{+1.4}_{-0.6}$	$14.8^{+1.5}_{-0.6}$	$14.8^{+1.4}_{-0.6}$	$14.9^{+1.4}_{-0.6}$	$14.5^{+0.3}_{-0.2}$
b_g	165^{+113}_{-71}	226^{+73}_{-62}	240^{+93}_{-87}	163^{+83}_{-70}	108^{+11}_{-12}
N_g	$14.6^{+0.1}_{-0.2}$	$14.6^{+0.1}_{-0.2}$	$14.5^{+0.1}_{-0.2}$	$14.6^{+0.1}_{-0.2}$	$14.68^{+0.03}_{-0.05}$

[a]Reanalysis of Coil et al. (2011) data

[b]N denotes the number of galaxies in the stacked spectra.

Note. — The median, the 84th and 16th percentile deviations of the PDFs of parameters from the median are given in the table.

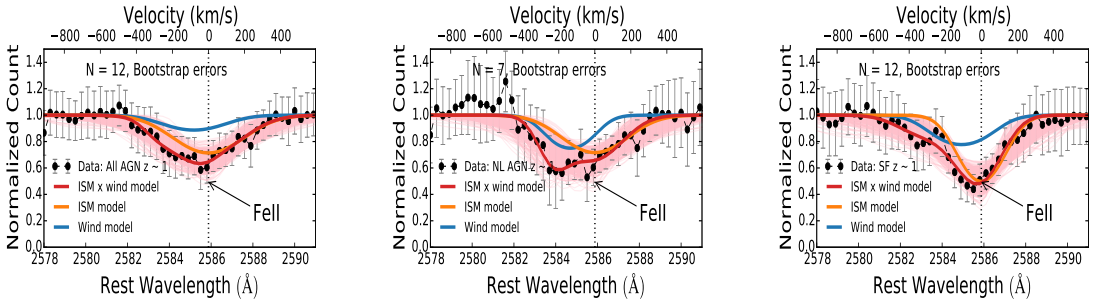

(a) AGN $z \sim 1$ (b) AGN $z \sim 1$ (c) SF $z \sim 1$

Figure 5.18:. The results of wind model fits of Fe II λ2586 profiles of AGN at $z \sim 1$ and a comparison sample star-forming galaxies at $z \sim 1$ using a bootstrapping scheme to estimate the normalized count errors. The data is shown as black points with the error bars. The red curves are median convolved wind models while the pink shades are 500 randomly drawn wind models from the posterior distributions of the model parameters. The orange curves are the unconvolved ISM components of the models while blue curves are the unconvolved wind components.

5.3.3 Fitting O II profile to estimate the escape velocity

Figure 5.19a shows the result of fitting two Gaussian with equal velocity dispersion to the O II doublet to the AGN spectra. The centroid of the Gaussian is fixed to the rest wavelengths of the doublet while the amplitudes of the doublet are free parameters of the fit. Figure 5.19b shows the corresponding fit for the star-forming comparison sample.

5.3.4 The effect of ISM covering fraction

In fiducial wind model in Chapter 4, we assumed that the ISM fully covers the stellar continuum emission. Table 5.4 shows that the results of the analysis using a covering fraction of 50%. Our main conclusion does not depend on the assumption of the covering fraction.

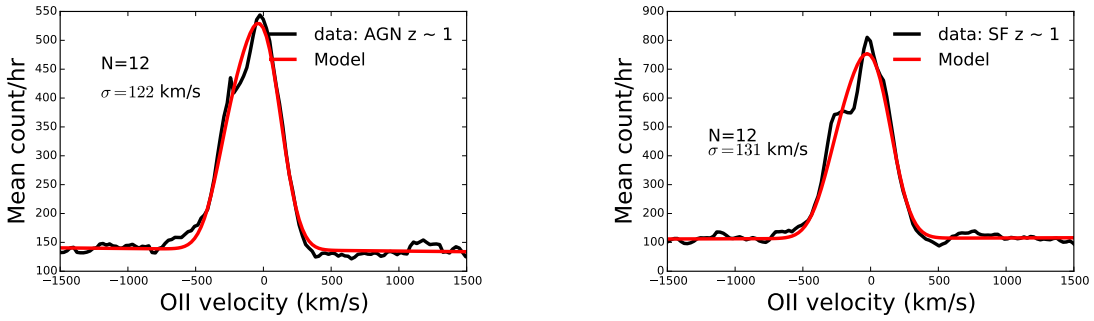

(a) AGN $z \sim 1$ (b) SF $z \sim 1$

Figure 5.19:. The result of fitting two Gaussian with equal width to the O II doublet. The velocity dispersions of the fits are shown on the figures. Compering the observed wind velocity to the O II width, we conclude that the winds, both in AGN and the comparison sample of non-AGN, are too weak to escape the gravitational potentials of their galaxies.

Table 5.4. Model parameter fits to Fe II λ2586 profiles after adopting a covering fraction of 50% for the ISM component of the wind model.

Wind Model Parameters	All AGN at $z \sim 1$ (N = 12)	NL AGN at $z \sim 1$ (N = 9)	NL AGN at $z \sim 1$ (N = 7)	SF at $z \sim 1$ (N = 12)	AGN at $z \sim 0.5$ (N = 6)
v_w	-121^{+74}_{-102}	-148^{+86}_{-86}	-190^{+80}_{-41}	-110^{+93}_{-185}	-169^{+78}_{-74}
b_w	153^{+84}_{-84}	114^{+74}_{-63}	79^{+62}_{-44}	197^{+157}_{-131}	120^{+72}_{-56}
C_w	$0.3^{+0.4}_{-0.2}$	$0.3^{+0.3}_{0.1}$	$0.4^{+0.3}_{-0.1}$	$0.3^{+0.4}_{-0.2}$	$0.4^{+0.3}_{-0.2}$
N_w	$14.8^{+1.2}_{-0.5}$	$15.2^{+1.3}_{-0.8}$	$15.2^{+1.4}_{-0.8}$	$15.0^{+1.4}_{-0.6}$	$15.2^{+1.4}_{-0.7}$
b_g	231^{+49}_{-66}	204^{+51}_{-42}	204^{+60}_{-47}	165^{+113}_{-71}	78^{+48}_{-23}
N_g	$14.9^{+0.1}_{-0.3}$	$15.0^{+0.1}_{-0.4}$	$14.9^{+0.1}_{-0.5}$	$14.6^{+0.1}_{-0.2}$	$15.7^{+1.1}_{-0.8}$

Note. — The median, the 84th and 16th percentile deviations of the PDFs of parameters from the median are given in the table.

Table 5.5. The wind model is fitted to simulated data.

Wind Model Parameters	S/N/Å = 24 (fitted values)	S/N/Å = 48 (fitted values)	S/N/Å = ∞ (true values
v_w	-159^{+40}_{-49}	-191^{+57}_{22}	-200
b_w	135^{+52}_{-54}	117^{+45}_{-46}	150
C_w	$0.4^{+0.4}_{-0.1}$	$0.32^{+0.24}_{-0.04}$	0.4
N_w	$15.1^{+1.2}_{-0.5}$	$15.3^{+1.1}_{-0.6}$	14.8
b_g	194^{+64}_{-41}	176^{+36}_{-21}	200
N_g	$14.3^{+0.1}_{-0.1}$	$14.38^{+0.05}_{-0.20}$	14.5

Note. — The median, the 84th and 16th percentile deviations of the PDFs of parameters from the median are given in the table. Note that our composite AGN spectrum has a SNR/Å$\sim$ 24 and bin size 0.3 Å and our model can successfully recover, within the 1σ, information from spectrum with signal-to-noise comparable to our data.

5.3.5 Checking the simple wind model with simulated data

Here we present the results of fitting our the simple model with simulated data. We simulated data with signal-to-noise per angstrom of 24 or 48 and with wavelength bin size of 0.3Å. Our composite AGN spectrum has a SNR/Å$\sim$ 24 and bin size 0.3Å. Table 5.5 and Figure 5.5 present the result of fitting the model to the simulated data.

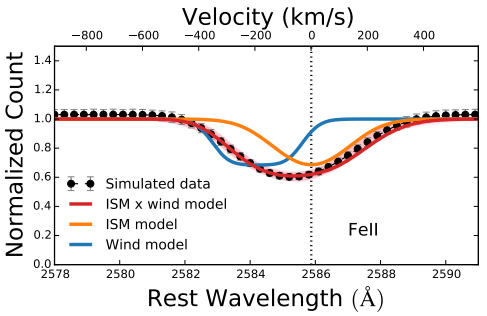

(a) Simulated data S/N/Å=48

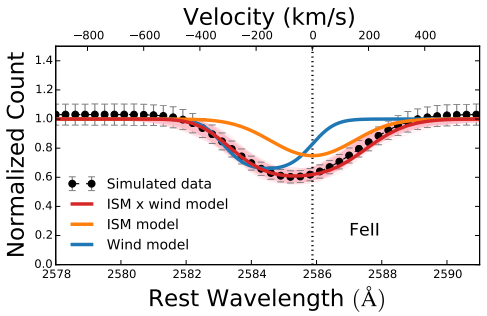

(b) Simulated data S/N/Å=24

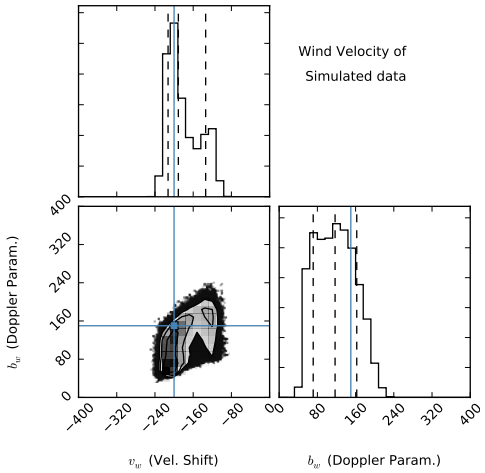

(c) Simulated data S/N/Å=48

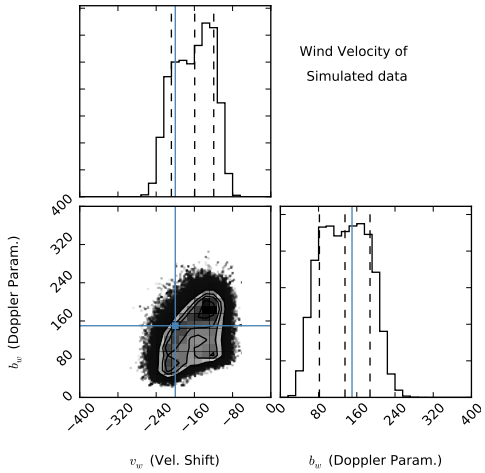

(d) Simulated data S/N/Å=24

Figure 5.20:. Results of fitting the wind model to simulated data. On the top panels, the simulated data are shown as black points with the error bars. The red curves are median-convolved wind models while the pink shades are 500 randomly-drawn wind models from the posterior probability distributions of the model parameters. The orange curves are the unconvolved ISM components of the models while blue curves are the unconvolved wind components. The histograms show the marginalized posterior probability distributions of wind velocities and wind doppler dispersion parameters. The dashed lines on the histograms indicate the median, 16th and 84th percentile values. The blue lines indicate the true input parameters. The model recovers the input parameters within a 1σ errors.

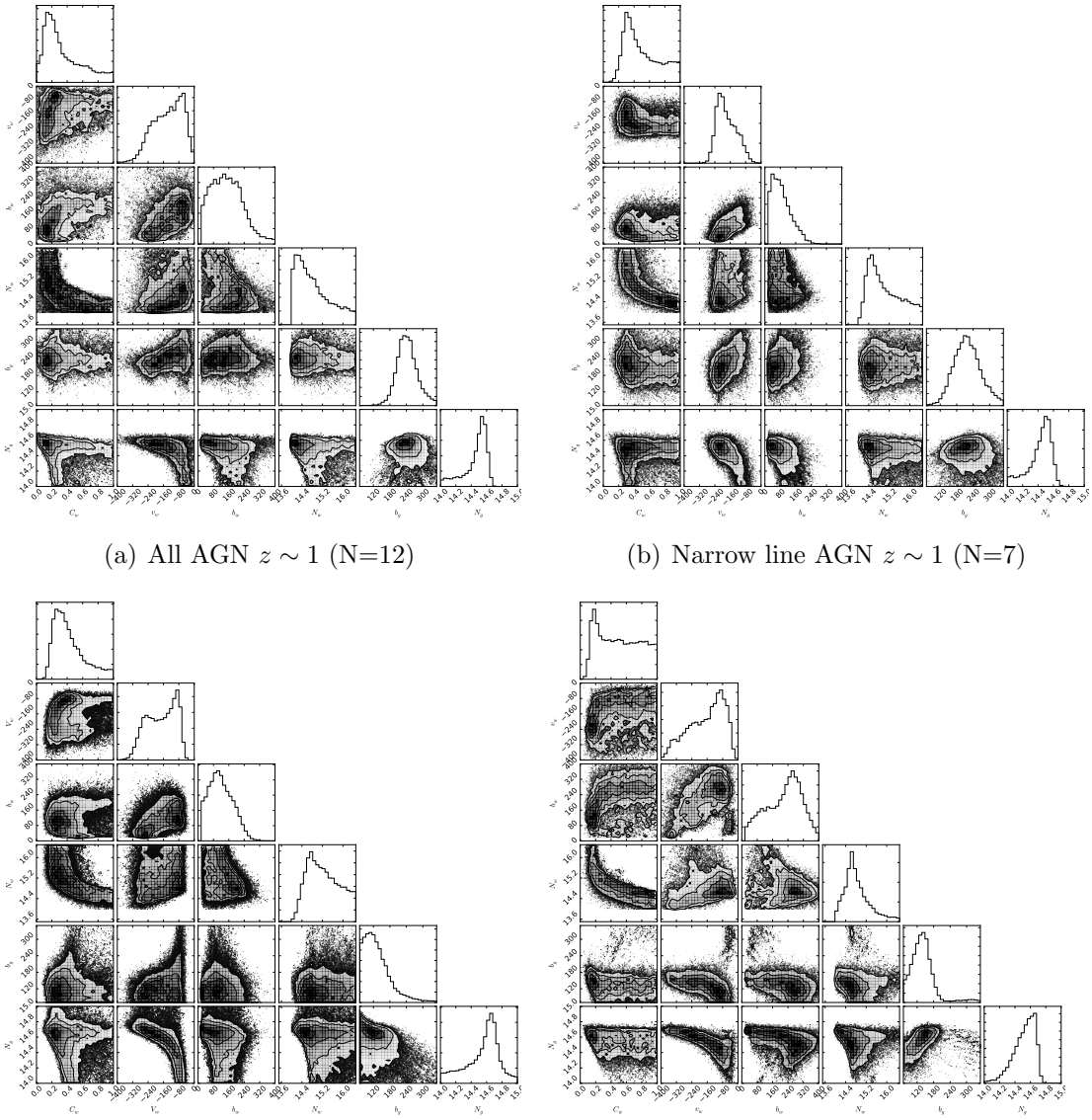

(a) All AGN $z \sim 1$ (N=12)

(b) Narrow line AGN $z \sim 1$ (N=7)

(c) AGN $z \sim 0.5$ (N=6)

(d) SF $z \sim 1$ (N=12)

Figure 5.21:. The joint posterior probability distributions of the wind model parameters. They are from top-to-bottom (or left-to-right): the covering fraction of the wind, C_w, the velocity centroid shifts of the wind, v_w, the Doppler broadening parameters of the wind, b_w, column density of the wind, N_w, the Doppler parameter of the gas in the galaxy, b_g, and the column density of the gas in the galaxy, N_g. Contours show the 0.5, 1, 1.5, and 2σ of the joint posterior probability distribution of a given two parameters. The histograms show the marginalized posterior probability distributions the parameters. Notice the correlation between some of the parameters. The results of this figure are summarized in table 4.3.

Bibliography

Ackermann, M., et al. 2014, ApJ, 793, 64

Aguirre, A., Hernquist, L., Schaye, J., Weinberg, D. H., Katz, N., & Gardner, J. 2001, ApJ, 560, 599

Aihara, H., et al. 2011, ApJS, 193, 29

Aird, J., et al. 2010, MNRAS, 401, 2531

Akritas, M. G., Murphy, S. A., & LaValley, M. P. 1995, Journal of the American Statistical Association, 90, 170

Alatalo, K., Cales, S. L., Appleton, P. N., Kewley, L. J., Lacy, M., Lisenfeld, U., Nyland, K., & Rich, J. A. 2014, ApJ, 794, L13

Alatalo, K., et al. 2011, ApJ, 735, 88

—. 2016, ApJ, 827, 106

Alexander, D. M., & Hickox, R. C. 2012, New A Rev., 56, 93

Alexander, D. M., et al. 2003, AJ, 126, 539

Arav, N., Borguet, B., Chamberlain, C., Edmonds, D., & Danforth, C. 2013, MNRAS, 436, 3286

Armus, L., et al. 2009, PASP, 121, 559

Ashby, M. L. N., et al. 2009, ApJ, 701, 428

Assef, R. J., et al. 2012, ArXiv e-prints

Baldry, I. K., Glazebrook, K., Brinkmann, J., Ivezić, Ž., Lupton, R. H., Nichol, R. C., & Szalay, A. S. 2004, ApJ, 600, 681

Baldwin, J. A., Phillips, M. M., & Terlevich, R. 1981, PASP, 93, 5

Balmaverde, B., et al. 2016, A&A, 585, A148

Balogh, M. L., Miller, C., Nichol, R., Zabludoff, A., & Goto, T. 2005, MNRAS, 360, 587

Balogh, M. L., Morris, S. L., Yee, H. K. C., Carlberg, R. G., & Ellingson, E. 1999, ApJ, 527, 54

Barnes, J. E., & Hernquist, L. 1996, ApJ, 471, 115

Barnes, J. E., & Hernquist, L. E. 1991, ApJ, 370, L65

Barro, G., et al. 2011, ApJS, 193, 30

—. 2013, ApJ, 765, 104

Bekki, K., Couch, W. J., Shioya, Y., & Vazdekis, A. 2005, MNRAS, 359, 949

Bekki, K., Shioya, Y., & Couch, W. J. 2001, ApJ, 547, L17

Bell, E. F., et al. 2004, ApJ, 608, 752

—. 2006, ApJ, 640, 241

—. 2012, ApJ, 753, 167

Bennert, N., Canalizo, G., Jungwiert, B., Stockton, A., Schweizer, F., Peng, C. Y., & Lacy, M. 2008, ApJ, 677, 846

Benson, A. J., Bower, R. G., Frenk, C. S., Lacey, C. G., Baugh, C. M., & Cole, S. 2003, ApJ, 599, 38

Bernardi, M., Roche, N., Shankar, F., & Sheth, R. K. 2011, MNRAS, 412, L6

Bertram, T., Eckart, A., Fischer, S., Zuther, J., Straubmeier, C., Wisotzki, L., & Krips, M. 2007, A&A, 470, 571

Blake, C., et al. 2004, MNRAS, 355, 713

Blanton, E. L., Randall, S. W., Clarke, T. E., Sarazin, C. L., McNamara, B. R., Douglass, E. M., & McDonald, M. 2011, ApJ, 737, 99

Blanton, M. R., & Roweis, S. 2007, AJ, 133, 734

Böhm, A., et al. 2013, A&A, 549, A46

Bolatto, A. D., Wolfire, M., & Leroy, A. K. 2013, ARA&A, 51, 207

Bordoloi, R., et al. 2014, ApJ, 794, 130

Borguet, B. C. J., Arav, N., Edmonds, D., Chamberlain, C., & Benn, C. 2013, ApJ, 762, 49

Borguet, B. C. J., Edmonds, D., Arav, N., Dunn, J., & Kriss, G. A. 2012, ApJ, 751, 107

Boselli, A., Cortese, L., Boquien, M., Boissier, S., Catinella, B., Lagos, C., & Saintonge, A. 2014, A&A, 564, A66

Bournaud, F., et al. 2008, A&A, 486, 741

Bourne, M. A., Zubovas, K., & Nayakshin, S. 2015, MNRAS, 453, 1829

Bower, R. G., Benson, A. J., & Crain, R. A. 2012, MNRAS, 422, 2816

Brammer, G. B., et al. 2009, ApJ, 706, L173

Brinchmann, J., Charlot, S., White, S. D. M., Tremonti, C., Kauffmann, G., Heckman, T., & Brinkmann, J. 2004, MNRAS, 351, 1151

Brinchmann, J., Pettini, M., & Charlot, S. 2008, MNRAS, 385, 769

Brown, M. J. I., et al. 2009, ApJ, 703, 150

Bruzual, G., & Charlot, S. 2003, MNRAS, 344, 1000

Bruzual A., G. 1983, ApJ, 273, 105

Bundy, K., et al. 2010, ApJ, 719, 1969

Buyle, P., Michielsen, D., De Rijcke, S., Pisano, D. J., Dejonghe, H., & Freeman, K. 2006, ApJ, 649, 163

Cales, S. L., et al. 2011, ApJ, 741, 106

Calzetti, D., Armus, L., Bohlin, R. C., Kinney, A. L., Koornneef, J., & Storchi-Bergmann, T. 2000, ApJ, 533, 682

Canalizo, G., & Stockton, A. 2001, ApJ, 555, 719

—. 2013, ApJ, 772, 132

Cappellari, M., et al. 2006, MNRAS, 366, 1126

Carniani, S., et al. 2015, A&A, 580, A102

Catinella, B., et al. 2010, MNRAS, 403, 683

—. 2012, A&A, 544, A65

Cattaneo, A., et al. 2007, MNRAS, 377, 63

Cen, R. 2012, ApJ, 755, 28

Chabrier, G. 2003, PASP, 115, 763

Chakrabarti, S., Fenner, Y., Cox, T. J., Hernquist, L., & Whitney, B. A. 2008, ApJ, 688, 972

Chamberlain, C., & Arav, N. 2015, MNRAS, 454, 675

Chang, T.-C., van Gorkom, J. H., Zabludoff, A. I., Zaritsky, D., & Mihos, J. C. 2001, AJ, 121, 1965

Charlot, S., & Fall, S. M. 2000, ApJ, 539, 718

Chary, R., & Elbaz, D. 2001, ApJ, 556, 562

Cheng, J. Y., Faber, S. M., Simard, L., Graves, G. J., Lopez, E. D., Yan, R., & Cooper, M. C. 2011, MNRAS, 412, 727

Cheung, E., et al. 2012, ApJ, 760, 131

Chilingarian, I. V., & Zolotukhin, I. Y. 2012, MNRAS, 419, 1727

Choi, E., Ostriker, J. P., Naab, T., & Johansson, P. H. 2012, ApJ, 754, 125

Churchill, C. W., Mellon, R. R., Charlton, J. C., Jannuzi, B. T., Kirhakos, S., Steidel, C. C., & Schneider, D. P. 2000, ApJ, 543, 577

Cicone, C., et al. 2014, A&A, 562, A21

Cid Fernandes, R., Stasińska, G., Mateus, A., & Vale Asari, N. 2011, MNRAS, 413, 1687

Ciotti, L., & Ostriker, J. P. 2007, ApJ, 665, 1038

Cisternas, M., et al. 2011, ApJ, 726, 57

Coil, A. L., Weiner, B. J., Holz, D. E., Cooper, M. C., Yan, R., & Aird, J. 2011, ApJ, 743, 46

Combes, F., et al. 2013, A&A, 558, A124

Couch, W. J., & Sharples, R. M. 1987, MNRAS, 229, 423

Cox, D. R. 1972, JRSS, 34, 187

Cresci, G., et al. 2015, ApJ, 799, 82

Croton, D. J., et al. 2006, MNRAS, 365, 11

Darg, D. W., et al. 2010, MNRAS, 401, 1043

Dasyra, K. M., Bostrom, A. C., Combes, F., & Vlahakis, N. 2015, ApJ, 815, 34

Davé, R., Finlator, K., & Oppenheimer, B. D. 2011, MNRAS, 416, 1354

Davies, R. I., Müller Sánchez, F., Genzel, R., Tacconi, L. J., Hicks, E. K. S., Friedrich, S., & Sternberg, A. 2007, ApJ, 671, 1388

Davis, T. A., et al. 2014, MNRAS, 444, 3427

De Lucia, G., Poggianti, B. M., Halliday, C., Milvang-Jensen, B., Noll, S., Smail, I., & Zaritsky, D. 2009, MNRAS, 400, 68

Debuhr, J., Quataert, E., & Ma, C.-P. 2012, MNRAS, 420, 2221

Dekel, A., & Birnboim, Y. 2006, MNRAS, 368, 2

Dekel, A., & Burkert, A. 2014, MNRAS, 438, 1870

Dekel, A., et al. 2009, Nature, 457, 451

Del Moro, A., et al. 2016, MNRAS, 456, 2105

Di Matteo, T., Springel, V., & Hernquist, L. 2005, Nature, 433, 604

Diamond-Stanic, A. M., Moustakas, J., Tremonti, C. A., Coil, A. L., Hickox, R. C., Robaina, A. R., Rudnick, G. H., & Sell, P. H. 2012, ApJ, 755, L26

Diamond-Stanic, A. M., & Rieke, G. H. 2010, ApJ, 724, 140

Doeleman, S. S., et al. 2008, Nature, 455, 78

Donley, J. L., et al. 2012, ApJ, 748, 142

Donoso, E., et al. 2012, ApJ, 748, 80

Downes, D., & Solomon, P. M. 1998, ApJ, 507, 615

Dressler, A., & Gunn, J. E. 1983, ApJ, 270, 7

Dressler, A., Oemler, Jr., A., Poggianti, B. M., Gladders, M. D., Abramson, L., & Vulcani, B. 2013, ApJ, 770, 62

Edmonds, D., et al. 2011, ApJ, 739, 7

Ellison, S. L., Patton, D. R., Mendel, J. T., & Scudder, J. M. 2011, MNRAS, 418, 2043

Erb, D. K., Quider, A. M., Henry, A. L., & Martin, C. L. 2012, ApJ, 759, 26

Evans, A. S., Frayer, D. T., Surace, J. A., & Sanders, D. B. 2001, AJ, 121, 1893

Fabello, S., Kauffmann, G., Catinella, B., Giovanelli, R., Haynes, M. P., Heckman, T. M., & Schiminovich, D. 2011, MNRAS, 416, 1739

Faber, S. M., et al. 2003, in Proc. SPIE, Vol. 4841, Instrument Design and Performance for Optical/Infrared Ground-based Telescopes, ed. M. Iye & A. F. M. Moorwood, 1657–1669

Faber, S. M., et al. 2007, ApJ, 665, 265

Fabian, A. C. 1999, MNRAS, 308, L39

—. 2012, ARA&A, 50, 455

Fabian, A. C., Sanders, J. S., Allen, S. W., Crawford, C. S., Iwasawa, K., Johnstone, R. M., Schmidt, R. W., & Taylor, G. B. 2003, MNRAS, 344, L43

Falkenberg, M. A., Kotulla, R., & Fritze, U. 2009, MNRAS, 397, 1940

Fang, J. J., Faber, S. M., Koo, D. C., & Dekel, A. 2013, ArXiv e-prints

Fang, J. J., Faber, S. M., Salim, S., Graves, G. J., & Rich, R. M. 2012, ApJ, 761, 23

Feigelson, E. D., & Nelson, P. I. 1985, ApJ, 293, 192

Ferrarese, L., & Merritt, D. 2000, ApJ, 539, L9

Feruglio, C., Maiolino, R., Piconcelli, E., Menci, N., Aussel, H., Lamastra, A., & Fiore, F. 2010, A&A, 518, L155

Fischer, J., et al. 2010, A&A, 518, L41

Foreman-Mackey, D., Hogg, D. W., Lang, D., & Goodman, J. 2013, PASP, 125, 306

Förster Schreiber, N. M., et al. 2014, ApJ, 787, 38

Fox, A. J., et al. 2015, ApJ, 799, L7

Franx, M., van Dokkum, P. G., Schreiber, N. M. F., Wuyts, S., Labbé, I., & Toft, S. 2008, ApJ, 688, 770

French, K. D., Yang, Y., Zabludoff, A., Narayanan, D., Shirley, Y., Walter, F., Smith, J.-D., & Tremonti, C. A. 2015, ApJ, 801, 1

Fukugita, M., Ichikawa, T., Gunn, J. E., Doi, M., Shimasaku, K., & Schneider, D. P. 1996, AJ, 111, 1748

Gabor, J. M., & Bournaud, F. 2014, MNRAS, 441, 1615

Gabor, J. M., Davé, R., Oppenheimer, B. D., & Finlator, K. 2011, MNRAS, 417, 2676

García-Burillo, S., et al. 2014, A&A, 567, A125

—. 2015, A&A, 580, A35

Geach, J. E., et al. 2014, Nature, 516, 68

Genel, S., et al. 2014, MNRAS, 445, 175

Genzel, R., et al. 2014, ApJ, 796, 7

Georgakakis, A., et al. 2008, MNRAS, 385, 2049

Geréb, K., Morganti, R., Oosterloo, T. A., Hoppmann, L., & Staveley-Smith, L. 2015, A&A, 580, A43

Ghez, A. M., et al. 2008, ApJ, 689, 1044

Gillessen, S., Eisenhauer, F., Fritz, T. K., Bartko, H., Dodds-Eden, K., Pfuhl, O., Ott, T., & Genzel, R. 2009, ApJ, 707, L114

Gladders, M. D., López-Cruz, O., Yee, H. K. C., & Kodama, T. 1998, ApJ, 501, 571

Goto, T. 2007, MNRAS, 377, 1222

Goto, T., Kawai, A., Shimono, A., Sugai, H., Yagi, M., & Hattori, T. 2008, MNRAS, 386, 1355

Graham, A. W., & Scott, N. 2013, ApJ, 764, 151

Granato, G. L., De Zotti, G., Silva, L., Bressan, A., & Danese, L. 2004, ApJ, 600, 580

Grogin, N. A., et al. 2011, ApJS, 197, 35

Groves, B. A., Heckman, T. M., & Kauffmann, G. 2006, MNRAS, 371, 1559

Guo, F., & Mathews, W. G. 2012, ApJ, 756, 181

Guo, Y., et al. 2013, ApJS, 207, 24

Hainline, K. N., Shapley, A. E., Greene, J. E., & Steidel, C. C. 2011, ApJ, 733, 31

Hainline, K. N., Shapley, A. E., Greene, J. E., Steidel, C. C., Reddy, N. A., & Erb, D. K. 2012, ApJ, 760, 74

Halsel, D. 2012, Statistics for Censored Environmental Data, 2nd edn. (Wiley)

Hao, C. N., Xia, X. Y., Mao, S., Wu, H., & Deng, Z. G. 2005, ApJ, 625, 78

Harrington, D. P., & Fleming, T. R. 1982, Biometrika, 69, 553

Harrison, C. M., Alexander, D. M., Mullaney, J. R., & Swinbank, A. M. 2014, MNRAS, 441, 3306

Harrison, C. M., et al. 2016, MNRAS, 456, 1195

Hayward, C. C., Jonsson, P., Kereš, D., Magnelli, B., Hernquist, L., & Cox, T. J. 2012, MNRAS, 424, 951

Hayward, C. C., Kereš, D., Jonsson, P., Narayanan, D., Cox, T. J., & Hernquist, L. 2011, ApJ, 743, 159

Hayward, C. C., Torrey, P., Springel, V., Hernquist, L., & Vogelsberger, M. 2014a, MNRAS, 442, 1992

Hayward, C. C., et al. 2014b, MNRAS, 445, 1598

Heckman, T. M., & Best, P. N. 2014, ARA&A, 52, 589

Hlavacek-Larrondo, J., Fabian, A. C., Edge, A. C., Ebeling, H., Sanders, J. S., Hogan, M. T., & Taylor, G. B. 2012, MNRAS, 421, 1360

Ho, L. C. 2008, ARA&A, 46, 475

Holt, J., Tadhunter, C. N., & Morganti, R. 2008, MNRAS, 387, 639

Hopkins, P. F. 2012, MNRAS, 420, L8

Hopkins, P. F., & Hernquist, L. 2006, ApJS, 166, 1

Hopkins, P. F., & Hernquist, L. 2009, The Astrophysical Journal, 698, 1550

Hopkins, P. F., Hernquist, L., Cox, T. J., Di Matteo, T., Robertson, B., & Springel, V. 2006, ApJS, 163, 1

Hopkins, P. F., Hernquist, L., Cox, T. J., & Kereš, D. 2008, ApJS, 175, 356

Hopkins, P. F., Kereš, D., Murray, N., Hernquist, L., Narayanan, D., & Hayward, C. C. 2013, MNRAS, 433, 78

Hopkins, P. F., Kocevski, D. D., & Bundy, K. 2014, MNRAS, 445, 823

Hopkins, P. F., et al. 2010, ApJ, 715, 202

Huang, M.-L., & Kauffmann, G. 2014, MNRAS, 443, 1329

Husemann, B., Scharwächter, J., Bennert, V. N., Manieri, V., Woo, J.-H., & Kakkad, D. 2015, ArXiv e-prints

Husemann, B., Wisotzki, L., Sánchez, S. F., & Jahnke, K. 2013, A&A, 549, A43

Hwang, H. S., & Geller, M. J. 2013, ArXiv e-prints

Ishibashi, W., & Fabian, A. C. 2012, MNRAS, 427, 2998

Izotov, Y. I., Guseva, N. G., Fricke, K. J., & Henkel, C. 2011, A&A, 536, L7

Jahnke, K., Kuhlbrodt, B., & Wisotzki, L. 2004, MNRAS, 352, 399

Jahnke, K., & Macciò, A. V. 2011, ApJ, 734, 92

Jonsson, P., Cox, T. J., Primack, J. R., & Somerville, R. S. 2006, ApJ, 637, 255

Jonsson, P., Groves, B. A., & Cox, T. J. 2010, MNRAS, 403, 17

Kaplan, E. L., & Meier, P. M. 1958, JASA, 53

Karouzos, M., Woo, J.-H., & Bae, H.-J. 2016, ApJ, 819, 148

Kartaltepe, J. S., et al. 2007, ApJS, 172, 320

Kauffmann, G., & Haehnelt, M. 2000, MNRAS, 311, 576

Kauffmann, G., & Heckman, T. M. 2009, MNRAS, 397, 135

Kauffmann, G., Heckman, T. M., De Lucia, G., Brinchmann, J., Charlot, S., Tremonti, C., White, S. D. M., & Brinkmann, J. 2006, MNRAS, 367, 1394

Kauffmann, G., et al. 2003a, MNRAS, 341, 33

—. 2003b, MNRAS, 341, 54

—. 2003c, MNRAS, 346, 1055

Kaviraj, S., Kirkby, L. A., Silk, J., & Sarzi, M. 2007, MNRAS, 382, 960

Kelson, D. D., & Holden, B. P. 2010, ApJ, 713, L28

Kennicutt, R. C., Lee, J. C., Akiyama, S., Funes, J. G., & Sakai, S. 2005, in American Institute of Physics Conference Series, Vol. 783, The Evolution of Starbursts, ed. S. Hüttmeister, E. Manthey, D. Bomans, & K. Weis, 3–16

Kennicutt, Jr., R. C. 1998, ARA&A, 36, 189

Kereš, D., Katz, N., Weinberg, D. H., & Davé, R. 2005, MNRAS, 363, 2

Kewley, L. J., & Dopita, M. A. 2002, ApJS, 142, 35

Kewley, L. J., Dopita, M. A., Sutherland, R. S., Heisler, C. A., & Trevena, J. 2001, ApJ, 556, 121

King, A., & Pounds, K. 2015, ARA&A, 53, 115

King, A. R., Zubovas, K., & Power, C. 2011, MNRAS, 415, L6

Klein, J. P., & Moeschberger, M. L. 2005, Survival analysis: techniques for censored and truncated data (Springer Science & Business Media)

Knapen, J. H., & James, P. A. 2009, ApJ, 698, 1437

Kocevski, D. D., et al. 2012, ApJ, 744, 148

—. 2015, ApJ, 814, 104

Koekemoer, A. M., et al. 2011, ApJS, 197, 36

Kormendy, J., & Ho, L. C. 2013, ARA&A, 51, 511

Kornei, K. A., Shapley, A. E., Martin, C. L., Coil, A. L., Lotz, J. M., Schiminovich, D., Bundy, K., & Noeske, K. G. 2012, ApJ, 758, 135

Kriek, M., van Dokkum, P. G., Labbé, I., Franx, M., Illingworth, G. D., Marchesini, D., & Quadri, R. F. 2009, ApJ, 700, 221

Kriek, M., van Dokkum, P. G., Whitaker, K. E., Labbé, I., Franx, M., & Brammer, G. B. 2011, ApJ, 743, 168

Krug, H. B., Rupke, D. S. N., & Veilleux, S. 2010, ApJ, 708, 1145

Ku, W. H.-M., Helfand, D. J., & Lucy, L. B. 1980, Nature, 288, 323

Lacy, M., et al. 2004, ApJS, 154, 166

Laird, E. S., et al. 2009, ApJS, 180, 102

Lake, S. E., Wright, E. L., Petty, S., Assef, R. J., Jarrett, T. H., Stanford, S. A., Stern, D., & Tsai, C.-W. 2012, AJ, 143, 7

Lamastra, A., Bianchi, S., Matt, G., Perola, G. C., Barcons, X., & Carrera, F. J. 2009, A&A, 504, 73

Lanz, L., Hayward, C. C., Zezas, A., Smith, H. A., Ashby, M. L. N., Brassington, N., Fazio, G. G., & Hernquist, L. 2014, ApJ, 785, 39

Larson, K. L., et al. 2016, ArXiv e-prints

Law, D. R., Steidel, C. C., Shapley, A. E., Nagy, S. R., Reddy, N. A., & Erb, D. K. 2012, ApJ, 759, 29

Lee, J. C., Kennicutt, Jr., R. C., Funes, S. J. J. G., Sakai, S., & Akiyama, S. 2009, ApJ, 692, 1305

Lee, L., & Lee, M. L. 2015

Leroy, A. K., et al. 2013, AJ, 146, 19

Lintott, C., et al. 2011, MNRAS, 410, 166

Liu, G., Zakamska, N. L., & Greene, J. E. 2014, MNRAS, 442, 1303

Liu, G., Zakamska, N. L., Greene, J. E., Nesvadba, N. P. H., & Liu, X. 2013, MNRAS, 436, 2576

Liu, X., Shen, Y., & Strauss, M. A. 2012, ApJ, 745, 94

Lotz, J. M., Jonsson, P., Cox, T. J., Croton, D., Primack, J. R., Somerville, R. S., & Stewart, K. 2011, ApJ, 742, 103

Lotz, J. M., Jonsson, P., Cox, T. J., & Primack, J. R. 2010, MNRAS, 404, 575

MacArthur, L. A. 2005, ApJ, 623, 795

Madau, P., & Dickinson, M. 2014, ARA&A, 52, 415

Magorrian, J., et al. 1998, AJ, 115, 2285

Mantel, N. 1966, Cancer chemotherapy reports. Part 1, 50, 163

Martig, M., Bournaud, F., Teyssier, R., & Dekel, A. 2009, ApJ, 707, 250

Martin, C. L., & Bouché, N. 2009, ApJ, 703, 1394

Martin, C. L., Shapley, A. E., Coil, A. L., Kornei, K. A., Bundy, K., Weiner, B. J., Noeske, K. G., & Schiminovich, D. 2012, ApJ, 760, 127

Martin, D. C., et al. 2005, ApJ, 619, L1

—. 2007, ApJS, 173, 342

Martinez, R. L. M. C. 2007, Diagnostics for choosing between Log-rank and Wilcoxon tests (ProQuest)

Mateos, S., et al. 2012, MNRAS, 426, 3271

McConnell, N. J., & Ma, C.-P. 2013, ApJ, 764, 184

McElroy, R., Croom, S. M., Pracy, M., Sharp, R., Ho, I.-T., & Medling, A. M. 2015, MNRAS, 446, 2186

McNamara, B. R., & Nulsen, P. E. J. 2007, ARA&A, 45, 117

McQuinn, K. B. W., et al. 2010, ApJ, 721, 297

Mendel, J. T., Simard, L., Ellison, S. L., & Patton, D. R. 2013, MNRAS, 463

Mineo, S., Gilfanov, M., Lehmer, B. D., Morrison, G. E., & Sunyaev, R. 2014, MNRAS, 437, 1698

Morganti, R., Tadhunter, C. N., & Oosterloo, T. A. 2005, A&A, 444, L9

Muñoz-Mateos, J. C., et al. 2009, ApJ, 701, 1965

Mullaney, J. R., Alexander, D. M., Fine, S., Goulding, A. D., Harrison, C. M., & Hickox, R. C. 2013, MNRAS, 433, 622

Müller-Sánchez, F., Prieto, M. A., Hicks, E. K. S., Vives-Arias, H., Davies, R. I., Malkan, M., Tacconi, L. J., & Genzel, R. 2011, ApJ, 739, 69

Muratov, A. L., Kereš, D., Faucher-Giguère, C.-A., Hopkins, P. F., Quataert, E., & Murray, N. 2015, MNRAS, 454, 2691

Murray, N., Quataert, E., & Thompson, T. A. 2005, ApJ, 618, 569

Narayanan, D., Krumholz, M., Ostriker, E. C., & Hernquist, L. 2011, MNRAS, 418, 664

Narayanan, D., et al. 2008, ApJS, 176, 331

—. 2010, MNRAS, 407, 1701

Nenkova, M., Sirocky, M. M., Nikutta, R., Ivezić, Ž., & Elitzur, M. 2008, ApJ, 685, 160

Nesvadba, N. P. H., Lehnert, M. D., De Breuck, C., Gilbert, A. M., & van Breugel, W. 2008, A&A, 491, 407

Nesvadba, N. P. H., Lehnert, M. D., Eisenhauer, F., Gilbert, A., Tecza, M., & Abuter, R. 2006, ApJ, 650, 693

Newman, J. A., et al. 2013, ApJS, 208, 5

Noeske, K. G., et al. 2007, ApJ, 660, L43

Norton, S. A., Gebhardt, K., Zabludoff, A. I., & Zaritsky, D. 2001, ApJ, 557, 150

Oke, J. B., et al. 1995, PASP, 107, 375

Oppenheimer, B. D., Davé, R., Kereš, D., Fardal, M., Katz, N., Kollmeier, J. A., & Weinberg, D. H. 2010, MNRAS, 406, 2325

Osterbrock, D. E. 1989, Astrophysics of gaseous nebulae and active galactic nuclei (University Science Books)

Pawlik, M. M., Wild, V., Walcher, C. J., Johansson, P. H., Villforth, C., Rowlands, K., Mendez-Abreu, J., & Hewlett, T. 2016, MNRAS, 456, 3032

Peng, C. Y. 2007, ApJ, 671, 1098

Peng, C. Y., Ho, L. C., Impey, C. D., & Rix, H.-W. 2002, AJ, 124, 266

Piconcelli, E., Jimenez-Bailón, E., Guainazzi, M., Schartel, N., Rodríguez-Pascual, P. M., & Santos-Lleó, M. 2005, A&A, 432, 15

Poggianti, B. M., Bridges, T. J., Komiyama, Y., Yagi, M., Carter, D., Mobasher, B., Okamura, S., & Kashikawa, N. 2004, ApJ, 601, 197

Poggianti, B. M., Smail, I., Dressler, A., Couch, W. J., Barger, A. J., Butcher, H., Ellis, R. S., & Oemler, Jr., A. 1999, ApJ, 518, 576

Poggianti, B. M., & Wu, H. 2000, ApJ, 529, 157

Pontzen, A., & Governato, F. 2012, MNRAS, 421, 3464

Pracy, M. B., Kuntschner, H., Couch, W. J., Blake, C., Bekki, K., & Briggs, F. 2009, MNRAS, 396, 1349

Prochaska, J. X., Kasen, D., & Rubin, K. 2011, ApJ, 734, 24

Prochaska, J. X., Lau, M. W., & Hennawi, J. F. 2014, ApJ, 796, 140

Quintero, A. D., et al. 2004, ApJ, 602, 190

Reines, A. E., & Volonteri, M. 2015, ApJ, 813, 82

Roche, N., Bernardi, M., & Hyde, J. 2009, MNRAS, 398, 1549

Rodríguez, M. I., Villar-Martín, M., Emonts, B., Humphrey, A., Drouart, G., García Burillo, S., & Pérez Torres, M. 2014, A&A, 565, A19

Roos, O., Juneau, S., Bournaud, F., & Gabor, J. M. 2015, ApJ, 800, 19

Rosario, D. J., et al. 2013, ArXiv e-prints

Rowlands, K., Wild, V., Nesvadba, N., Sibthorpe, B., Mortier, A., Lehnert, M., & da Cunha, E. 2015, MNRAS, 448, 258

Rubin, K. H. R., Prochaska, J. X., Koo, D. C., Phillips, A. C., Martin, C. L., & Winstrom, L. O. 2014, ApJ, 794, 156

Rupke, D. S., Veilleux, S., & Sanders, D. B. 2005a, ApJ, 632, 751

—. 2005b, ApJS, 160, 87

Rupke, D. S. N., & Veilleux, S. 2013, ApJ, 768, 75

Saintonge, A., et al. 2011, MNRAS, 415, 32

—. 2012, ApJ, 758, 73

Salim, S. 2014, Serbian Astronomical Journal, 189, 1

Salim, S., Fang, J. J., Rich, R. M., Faber, S. M., & Thilker, D. A. 2012, ApJ, 755, 105

Salim, S., et al. 2007, ApJS, 173, 267

—. 2009, ApJ, 700, 161

Sanders, D. B., & Mirabel, I. F. 1996, ARA&A, 34, 749

Sanders, D. B., Soifer, B. T., Elias, J. H., Madore, B. F., Matthews, K., Neugebauer, G., & Scoville, N. Z. 1988, ApJ, 325, 74

Sandstrom, K. M., et al. 2013, ApJ, 777, 5

Sarzi, M., Kaviraj, S., Nedelchev, B., Tiffany, J., Shabala, S. S., Deller, A. T., & Middelberg, E. 2016, MNRAS, 456, L25

Sato, T., Martin, C. L., Noeske, K. G., Koo, D. C., & Lotz, J. M. 2009, ApJ, 696, 214

Scannapieco, E., & Oh, S. P. 2004, ApJ, 608, 62

Schawinski, K., Simmons, B. D., Urry, C. M., Treister, E., & Glikman, E. 2012, MNRAS, 425, L61

Schawinski, K., Thomas, D., Sarzi, M., Maraston, C., Kaviraj, S., Joo, S.-J., Yi, S. K., & Silk, J. 2007, MNRAS, 382, 1415

Schawinski, K., Virani, S., Simmons, B., Urry, C. M., Treister, E., Kaviraj, S., & Kushkuley, B. 2009a, ApJ, 692, L19

Schawinski, K., et al. 2009b, ApJ, 690, 1672

—. 2014, MNRAS, 440, 889

Schweizer, F. 1982, ApJ, 252, 455

Scoville, N., & Norman, C. 1988, ApJ, 332, 163

Scoville, N. Z., Frayer, D. T., Schinnerer, E., & Christopher, M. 2003, ApJ, 585, L105

Sell, P. H., et al. 2014, MNRAS, 441, 3417

Sen, P. K. 1968, JASA, 63, 1379

Shih, H.-Y., Stockton, A., & Kewley, L. 2013, ApJ, 772, 138

Shioya, Y., Bekki, K., & Couch, W. J. 2001, ApJ, 558, 42

Sijacki, D., Springel, V., Di Matteo, T., & Hernquist, L. 2007, MNRAS, 380, 877

Silk, J., & Nusser, A. 2010, ApJ, 725, 556

Silk, J., & Rees, M. J. 1998, A&A, 331, L1

Silverman, J. D., et al. 2011, ApJ, 743, 2

Singh, R., et al. 2013, A&A, 558, A43

Smith, J. D. T., et al. 2007, ApJ, 656, 770

Snyder, G. F., Cox, T. J., Hayward, C. C., Hernquist, L., & Jonsson, P. 2011, ApJ, 741, 77

Solomon, P. M., Downes, D., Radford, S. J. E., & Barrett, J. W. 1997, ApJ, 478, 144

Somerville, R. S., Hopkins, P. F., Cox, T. J., Robertson, B. E., & Hernquist, L. 2008, MNRAS, 391, 481

Spoon, H. W. W., et al. 2013, ApJ, 775, 127

Springel, V., Di Matteo, T., & Hernquist, L. 2005a, ApJ, 620, L79

—. 2005b, MNRAS, 361, 776

Springel, V., & Hernquist, L. 2003, MNRAS, 339, 289

Stern, D., et al. 2005, ApJ, 631, 163

—. 2012, ApJ, 753, 30

Strateva, I., et al. 2001, AJ, 122, 1861

Sturm, E., et al. 2011, ApJ, 733, L16

Sun, A.-L., Greene, J. E., Zakamska, N. L., & Nesvadba, N. P. H. 2014, ApJ, 790, 160

Swinbank, A. M., Balogh, M. L., Bower, R. G., Hau, G. K. T., Allington-Smith, J. R., Nichol, R. C., & Miller, C. J. 2005, ApJ, 622, 260

Swinbank, A. M., Balogh, M. L., Bower, R. G., Zabludoff, A. I., Lucey, J. R., McGee, S. L., Miller, C. J., & Nichol, R. C. 2012, MNRAS, 420, 672

Tang, Y., Giavalisco, M., Guo, Y., & Kurk, J. 2014, ApJ, 793, 92

Thacker, R. J., Scannapieco, E., & Couchman, H. M. P. 2006, ApJ, 653, 86

Tombesi, F., Meléndez, M., Veilleux, S., Reeves, J. N., González-Alfonso, E., & Reynolds, C. S. 2015, Nature, 519, 436

Toomre, A., & Toomre, J. 1972, ApJ, 178, 623

Treister, E., Schawinski, K., Urry, C. M., & Simmons, B. D. 2012, ApJ, 758, L39

Tremaine, S., et al. 2002, ApJ, 574, 740

Tremonti, C. A., Moustakas, J., & Diamond-Stanic, A. M. 2007, ApJ, 663, L77

Tremonti, C. A., et al. 2004, ApJ, 613, 898

Trump, J. R., Hsu, A. D., Fang, J. J., Faber, S. M., Koo, D. C., & Kocevski, D. D. 2013, ApJ, 763, 133

Trump, J. R., et al. 2014, ApJ, 793, 101

Turnbull, B. W. 1976, JRSS, 290

van der Wel, A., et al. 2011, ApJ, 730, 38

Vasudevan, R. V., & Fabian, A. C. 2007, MNRAS, 381, 1235

Veilleux, S., Cecil, G., & Bland-Hawthorn, J. 2005, ARA&A, 43, 769

Veilleux, S., & Osterbrock, D. E. 1987, ApJS, 63, 295

Veilleux, S., et al. 2013, ApJ, 776, 27

Villar-Martín, M., Arribas, S., Emonts, B., Humphrey, A., Tadhunter, C., Bessiere, P., Cabrera Lavers, A., & Ramos Almeida, C. 2016, MNRAS, 460, 130

Villar Martín, M., Emonts, B., Humphrey, A., Cabrera Lavers, A., & Binette, L. 2014, MNRAS, 440, 3202

Villar-Martín, M., et al. 2013, MNRAS, 434, 978

Villforth, C., et al. 2014, MNRAS, 439, 3342

Volonteri, M. 2010, A&A Rev., 18, 279

Wake, D. A., van Dokkum, P. G., & Franx, M. 2012, ApJ, 751, L44

Weinberger, R., et al. 2016, ArXiv e-prints

Weiner, B. J., et al. 2009, ApJ, 692, 187

Whitaker, K. E., Kriek, M., van Dokkum, P. G., Bezanson, R., Brammer, G., Franx, M., & Labbé, I. 2012, ApJ, 745, 179

Whitaker, K. E., et al. 2014, ApJ, 795, 104

Wild, V., Charlot, S., Brinchmann, J., Heckman, T., Vince, O., Pacifici, C., & Chevallard, J. 2011a, MNRAS, 417, 1760

Wild, V., Heckman, T., & Charlot, S. 2010, MNRAS, 405, 933

Wild, V., Kauffmann, G., Heckman, T., Charlot, S., Lemson, G., Brinchmann, J., Reichard, T., & Pasquali, A. 2007, MNRAS, 381, 543

Wild, V., Walcher, C. J., Johansson, P. H., Tresse, L., Charlot, S., Pollo, A., Le Fèvre, O., & de Ravel, L. 2009, MNRAS, 395, 144

Wild, V., et al. 2011b, MNRAS, 410, 1593

Williams, R. J., Quadri, R. F., Franx, M., van Dokkum, P., & Labbé, I. 2009, ApJ, 691, 1879

Wong, O. I., et al. 2012, MNRAS, 420, 1684

Woo, J., Dekel, A., Faber, S. M., & Koo, D. C. 2015, MNRAS, 448, 237

Wright, E. L., et al. 2010, AJ, 140, 1868

Wuyts, S., et al. 2007, ApJ, 655, 51

—. 2011, ApJ, 742, 96

Wyder, T. K., et al. 2007, ApJS, 173, 293

Xia, X. Y., et al. 2012, ApJ, 750, 92

Xue, Y. Q., et al. 2011, ApJS, 195, 10

Yamauchi, C., & Goto, T. 2005, MNRAS, 359, 1557

Yan, R., & Blanton, M. R. 2012, ApJ, 747, 61

Yan, R., Newman, J. A., Faber, S. M., Konidaris, N., Koo, D., & Davis, M. 2006, ApJ, 648, 281

Yan, R., et al. 2009, MNRAS, 398, 735

Yang, Y., Zabludoff, A. I., Zaritsky, D., Lauer, T. R., & Mihos, J. C. 2004, ApJ, 607, 258

Yang, Y., Zabludoff, A. I., Zaritsky, D., & Mihos, J. C. 2008, ApJ, 688, 945

Yesuf, H. M., Faber, S. M., Trump, J. R., Koo, D. C., Fang, J. J., Liu, F. S., Wild, V., & Hayward, C. C. 2014, ApJ, 792, 84

York, D. G., et al. 2000, AJ, 120, 1579

Young, L. M., et al. 2011, MNRAS, 414, 940

Zabludoff, A. I., Zaritsky, D., Lin, H., Tucker, D., Hashimoto, Y., Shectman, S. A., Oemler, A., & Kirshner, R. P. 1996, ApJ, 466, 104

Zakamska, N. L., Gómez, L., Strauss, M. A., & Krolik, J. H. 2008, AJ, 136, 1607

Zakamska, N. L., & Greene, J. E. 2014, MNRAS, 442, 784

Zakamska, N. L., et al. 2016, MNRAS, 459, 3144

Zhu, G. B., et al. 2015, ApJ, 815, 48

Zubovas, K., & King, A. 2012, ApJ, 745, L34

Zubovas, K., King, A. R., & Nayakshin, S. 2011, MNRAS, 415, L21

Zwaan, M. A., Kuntschner, H., Pracy, M. B., & Couch, W. J. 2013, MNRAS, 432, 492